

# **Influence of ice-nucleating particles on tropical convection**

**Rachel Elizabeth Hawker**

Submitted in accordance with the requirements for the degree  
of Doctor of Philosophy

University of Leeds

School of Earth and Environment

January 2021

## **Declaration of Authorship**

The candidate confirms that the work submitted is her own, except where work which has formed part of jointly authored publications has been included. The contribution of the candidate and the other authors to this work has been explicitly indicated below. The candidate confirms that appropriate credit has been given within the thesis where reference has been made to the work of others. The authorship statements below are restated at the beginning of each chapter for clarity.

Chapter 2 is based on collaborative work from the paper “Hawker, R., Miltenberger, A., Wilkinson, J., Hill, A., Shipway, B., Cui, Z., Cotton, R., Carslaw, K., Field, P. and Murray, B.: The temperature dependence of ice-nucleating particle concentrations affects the radiative properties of tropical convective cloud systems, *Atmos. Chem. Phys.*, 21(7), 5439–5461, doi:10.5194/acp-21-5439-2021, 2021.” which is published in the journal ‘*Atmospheric Chemistry and Physics*’. At the time of first submission of this thesis the manuscript was in review.

REH is the lead author of the paper and the work presented in Chapter 2. REH wrote the paper and conducted all analysis shown in figures. REH, AKM, KSC, PRF and BJM contributed to the design, development and direction of the study. REH and AKM set up and ran the UM-CASIM simulations presented in the paper. REH processed and analysed the UM-CASIM datasets and compared the simulation data to observations. JMW, AAH and BJS built and maintained the Met-Office CASIM model used to run the simulations. ZC and RJC provided processed aircraft data from the ICE-D b933 flight and helped with the comparison of model data with aircraft measurements. REH, AKM, JMW, AAH, ZC, RJC, KSC, PRF and BJM edited the manuscript.

Chapter 3 is based on collaborative work from the manuscript ‘Effect of ice-nucleating particles and Hallett-Mossop ice production rates on anvil cirrus from deep convection’ which is in preparation for submission. The candidate is the lead author and the full author list is as follows: Rachel E. Hawker, Annette K. Miltenberger, Jill S. Johnson, Jonathan M. Wilkinson, Adrian A. Hill, Ben J. Shipway, Paul R. Field, Benjamin J. Murray, Ken S. Carslaw.

## II

REH, AKM, JSJ, PRF and KSC contributed to the design, development and direction of the study. AKM and REH set up a default deep convective simulation in the MONC-CASIM model. JSJ provided the base R code needed for the uncertain input parameter combination selection and to carry out the statistical emulation and uncertainty analysis, and provided advice about statistical emulation and uncertainty analysis throughout. REH carried out the model development in the MONC-CASIM code to build the base case simulation and allow for the perturbations to the uncertain input parameters determined by the sampling design, used and modified the R code to select the uncertain input parameter combinations, ran all MONC-CASIM simulations presented here, conducted all analysis and wrote the manuscript. JMW, AAH and BJS built and maintained the Met-Office MONC-CASIM model used to run the simulations. REH, AKM, JSJ, BJM, PEF and KSC edited the manuscript.

The candidate confirms that the work presented in Chapter 4 is her own and that appropriate credit has been given where reference has been made to the work of others. I am thankful to Kirsty J. Pringle and Ulrike Proske for help running the GLOMAP-mode model, to Jesus Vergara-Temprado for writing the parameterisation of ice-nucleating particle number concentrations from the GLOMAP-mode model (presented in Vergara-Temprado et al. (2017)), to Alberto Sanchez-Marroquin for helpful discussions, and to Annette K. Miltenberger, Paul R. Field, Benjamin J. Murray and Ken S. Carslaw for guidance with the study design and manuscript development.

This copy has been supplied on the understanding that it is copyright material and that no quotation from the thesis may be published without proper acknowledgement.

The right of Rachel Elizabeth Hawker to be identified as Author of this work has been asserted by Rachel Elizabeth Hawker in accordance with the Copyright, Designs and Patents Act 1988.

© 2018 The University of Leeds and Rachel Elizabeth Hawker

## **Acknowledgements**

Firstly I would like to say a sincere thank you to my supervisors, Benjamin Murray, Ken Carslaw, Paul Field, and Annette Miltenberger, for their support and guidance throughout this PhD. They have at all times been available for meetings, challenged me with insightful and difficult questions, and invested significant time in reading and providing constructive feedback on my work. I would like to say an additional thanks to Annette Miltenberger for her patience and generosity with her time and expertise at the start of this project. None of the work presented here would have been possible without her commitment to making sure I developed both the technical skills and the background knowledge needed to produce this research.

I'm grateful to my research groups, the Cloud Modellers Group, the Aerosol Modellers Group, and the Ice Nucleation Group, all of whom helped to create a very supportive and enjoyable community within the department. A special thanks to Jill Johnson, Dan Grosvenor, Hamish Gordon and Robin Stevens for always taking time to discuss problems, ideas and questions, as well as frequently providing code or resources to help me with particular problems. Jill Johnson in particular contributed a huge amount of expertise critical for the development of Chapter 3 of this thesis for which I'm very grateful.

Thanks to all the friends I made in Leeds who helped make the city a homely and fun place, especially my fellow 2016 School of Earth and Environment postgraduate starters who provided an instant support network from our very first day, and Kirsten Cameron who is always looking out for me. I'm also grateful for my friends and relatives at home in Ireland, I feel very lucky to have my home in such a wonderful community, and for the support of friends scattered over the UK and the globe.

Thank you to the European Research Council (ERC, grant 648661 MarineIce) for providing the funding for this project. I acknowledge the Natural Environment Research Council (NERC,

## IV

grant NE/M00340X/1) who funded the Ice in Clouds-Dust field campaign on which much of this project is based. I also acknowledge the use of Monsoon, a collaborative High Performance Computing facility funded by the Met Office and NERC, and the use of JASMIN, the UK collaborative data analysis facility.

Finally, thank you to my family, my parents, Janet and Phil, my brother, Dan, and my sister, Chloe, for their constant unwavering support.

## Thesis abstract

Convective clouds are key components of the global hydrological cycle with important roles in atmospheric energy and heat transfer. Within the mixed-phase region of convective clouds, ice crystals can form when an aerosol particle, termed an ice-nucleating particle (INP), catalyses the freezing of supercooled liquid droplets, or when existing ice hydrometeors facilitate the formation of new ice crystals via secondary ice production mechanisms (SIP). A large number of parameterisations of INP number concentrations are used in atmospheric models but the effect on convective cloud properties of INP parameterisation choice is not known. Firstly, I test the effect of INP parameterisation choice on a tropical convective cloud field in a regional model with advanced microphysics. The daytime domain outgoing radiation is sensitive to INP parameterisation choice and the differences between parameterisations can be as large as the effect of removing INP altogether. In particular, the temperature dependence of the INP parameterisation is important and determines cloud microphysical properties even in the presence of SIP via the Hallett-Mossop process. Next, I examine the effect of INP and the Hallett-Mossop process on the properties of an idealised deep convective cloud using a Latin hypercube sampling method and statistical emulation. At high INP number concentrations, the anvil ice crystal number concentration decreases sharply. At weak INP temperature dependencies, which increase INP number concentrations at warm mixed-phase temperatures, significant increases in anvil extent and anvil ice crystal size occur as a result of enhanced Hallett-Mossop ice production and more extensive cloud glaciation. Finally, INP transport across the tropical Atlantic, the region of interest for this thesis, is found to be overestimated in a global aerosol model. Overall, the results further our understanding of the effects of INP in convective clouds and indicate the importance of quantifying INP number concentrations at all mixed-phase temperatures and improving the representation of cloud glaciation in climate models.

# Table of Contents

Declaration of Authorship	I
Acknowledgements	III
Thesis abstract	V
Table of Contents	VI
List of figures	IX
List of tables	XI
Abbreviations	XII
<b>Chapter 1: Motivation and background information</b>	<b>1</b>
1.1. Weather and climate prediction	1
1.2. Clouds	3
1.2.1. Why do clouds matter?	3
1.2.2. Cloud phase	5
1.2.3. Convective clouds in weather and climate models	6
1.3. Processes affecting the amount of ice in convective clouds	10
1.3.1. Aerosol-cloud interactions	10
1.3.2. Cloud droplet formation	13
1.3.3. Homogeneous ice nucleation	16
1.3.4. Heterogeneous ice nucleation	16
1.3.5. Secondary ice production and tropical cloud glaciation	21
1.4. Parameterisation of ice-nucleating particles	24
1.4.1. Measurement and quantification of ice-nucleating particle number concentrations	24
1.4.2. Time-dependent/stochastic heterogeneous freezing parameterisations	26
1.4.3. Time independent/deterministic heterogeneous freezing parameterisations	28
1.5. Effect of INP in convective clouds	31
1.6. Research questions	35
1.6.1. Chapter 2: The effect of INP parameterisation choice on the radiative properties of a complex deep convective cloud field	35
1.6.2. Chapter 3: Influence of ice-nucleating particles and Hallett-Mossop ice production rates on anvil cirrus from deep convection	36

1.6.3. Chapter 4: Simulation of dust and K-feldspar INP transport across the tropical Atlantic by a global aerosol model	37
<b>Chapter 2: The effect of INP parameterisation choice on the radiative properties of a complex deep convective cloud field</b>	<b>39</b>
2.1. Abstract	40
2.2. Introduction	41
2.3. Methods	45
2.3.1. Model set-up	45
2.3.2. The observed case	57
2.4. Results	58
2.4.1. Effect of INP and INP parameterisation on outgoing radiation	58
2.4.2. Effect of INP and INP parameterisation on outgoing radiation from cloudy regions	62
2.4.3. Effect of INP and INP parameterisation on cloud fraction	69
2.4.4. Effect of INP and INP parameterisation on cirrus anvils	71
2.4.5. Importance of secondary ice production	73
2.5. Limitations of this modelling study	76
2.6. Conclusions	80
2.7 Appendix	83
<b>Chapter 3: Influence of ice-nucleating particles and Hallett-Mossop ice production rates on anvil cirrus from deep convection</b>	<b>86</b>
3.1. Abstract	87
3.2. Introduction	88
3.3. Methods	93
3.3.1. Model set-up and simulation design	93
3.3.2. Input parameters and their uncertainty ranges	99
3.3.4. Selection of uncertain input parameter combinations	103
3.3.5. Statistical emulation of the model output	105
3.4. Results	108
3.4.1. Anvil cloud properties	108
3.4.2. Importance of the Hallett-Mossop process and its interaction with $\lambda$ [INP]	127
3.5. Limitations of this modelling study	131
3.6. Discussion and Conclusions	133

3.7. Appendix	139
<b>Chapter 4: Simulation of dust and K-feldspar INP transport across the tropical Atlantic in a global aerosol model</b>	<b>141</b>
4.1. Abstract	142
4.2. Introduction	143
4.3. Methods	149
4.3.1. Overall approach	149
4.3.2. Model Description	151
4.3.3. Observational data	154
4.3.4. MERRA-2 dust reanalysis dataset	157
4.4. Results	159
4.4.1. Simulation of INP number concentrations by GLOMAP during B-ICE	159
4.4.2. Importance of marine organic INP for the INP number concentrations at Barbados	181
4.4.3. Impact of driving meteorology on GLOMAP INP and dust predictions	183
4.5. Conclusions	189
4.6. Appendix	193
<b>Chapter 5: Conclusions</b>	<b>196</b>
5.1. Summary of major findings	196
5.1.1. Chapter 2: The effect of INP parameterisation choice on the radiative properties of a complex deep convective cloud field	196
5.1.2. Chapter 3: Influence of ice-nucleating particles and Hallett-Mossop ice production rates on anvil cirrus from deep convection	199
5.1.3. Chapter 4: Simulation of dust and K-feldspar INP transport across the tropical Atlantic by a global aerosol model	202
5.1.4. Overall influence of INP on convective clouds from both regional (Chapter 2) and idealised (Chapter 3) simulations	204
5.2. Key limitations of this thesis	206
5.3. Main findings and implications of this research	213
<b>References</b>	<b>217</b>

## List of figures

### Chapter 1.

Figure 1.1. Mechanisms of primary ice nucleation from Kanji et al. (2017)	15
Figure 1.2. Variability in atmospheric ice-nucleating particle number concentrations from Kanji et al. (2017)	18
Figure 1.3. Mechanisms of secondary ice production from Korolev and Leisner (2020)	23

### Chapter 2.

Figure 2.1. Modelled conditions of Chapter 2 simulations	46
Figure 2.2. INP parameterisations and Cape Verde INP number concentrations	49
Figure 2.3. MODIS images and simulated outgoing longwave radiation	55
Figure 2.4. Comparison of simulated and observed cloud conditions	56
Figure 2.5. Effect of INP and SIP on TOA domain-mean daytime outgoing radiation	60
Figure 2.6. Effect of INP on TOA domain-mean daytime outgoing shortwave and longwave radiation	61
Figure 2.7. INP and outgoing radiation from cloudy regions	64
Figure 2.8. In-cloud microphysical profiles	65
Figure 2.9. Effect of INP on temperature, relative humidity and updraft speed	67
Figure 2.10. Outgoing radiation from cloudy regions and INP parameterisation slope	68
Figure 2.11. Cloud fraction and INP parameterisation slope	70
Figure 2.12. Vertical composition of cloud and effect of INP and SIP on cloud anvils	72
Figure 2.13. Schematic of the main effects of INP parameterisation slope and SIP	76
Figure A2.1. Simulated outgoing shortwave radiation	83
Figure A2.2. Effect of SIP on TOA domain-mean daytime outgoing shortwave and longwave radiation	84

### Chapter 3.

Figure 3.1. Initial conditions of the idealised deep convective cloud simulation	94
Figure 3.2. Cloud evolution	95
Figure 3.3. Time series of simulated surface precipitation and maximum cloud top height	97

Figure 3.4. Base case and maximum range of perturbation of INP parameterisation slope and INP number concentration	102
Figure 3.5. Uncertain input parameter combinations used in the cloud model	106
Figure 3.6. Simulated anvil ICNC and heterogeneous and homogeneous ice particle production rates	109
Figure 3.7. Emulator validation and variance-based sensitivity analysis of ICNC and heterogeneous and homogeneous ice particle production rates	111
Figure 3.8. Emulator response surfaces of ICNC and heterogeneous and homogeneous ice particle production rates	113
Figure 3.9. Simulated anvil ice crystal effective radius and driving processes	116
Figure 3.10. Regime change in anvil ice crystal effective radius and driving processes	119
Figure 3.11. Emulator validation and variance-based sensitivity analysis of anvil effective radius and driving processes	121
Figure 3.12. Emulator response surfaces of anvil effective radius and driving processes	123
Figure 3.13. Simulated anvil cloud fraction and driving processes	125
Figure 3.14. Regime change in anvil cloud fraction and driving processes	126
Figure 3.15. Importance of ice production in the Hallett-Mossop region	129
Figure 3.16. Schematic showing the key effects of the perturbations to the uncertain input parameters	137
Figure A3.1. Source of ice crystals in the Hallett-Mossop region of the simulated deep convective cloud	139
<b>Chapter 4.</b>	
Figure 4.1. Measured and simulated INP number concentrations at Barbados	159
Figure 4.2. Global distribution of surface INP number concentrations	161
Figure 4.3. Schematic depiction of model behaviour and uncertainties affecting simulated INP number concentration	163
Figure 4.4. Observed and simulated daily surface dust concentrations in July and August 2017	165
Figure 4.5. Box plots of simulated and observed surface dust mass concentrations in July and August at Barbados and at Miami	166
Figure 4.6. Comparison of global surface dust mass concentrations in MERRA-2 satellite reanalysis and GLOMAP for August 2017	169

Figure 4.7. Comparison of global column integrated dust mass concentrations in MERRA-2 satellite reanalysis and GLOMAP for August 2017	170
Figure 4.8. Comparison of GLOMAP dust mass concentration profiles to lidar observations from the 2013 SALTRACE ship campaign (Ansmann et al., 2017)	172
Figure 4.9. Global distribution of the mass fraction of dust in aerosol and of K-feldspar in aerosol	176
Figure 4.10. Measured and simulated INP number concentrations at Ragged Point, Barbados adjusted to assume 1% volume fraction of K-feldspar in aerosol	177
Figure 4.11. Contribution of accumulation mode aerosol to K-feldspar INP number concentrations	179
Figure 4.12. Importance of marine organic INP at a temperature of $-10^{\circ}\text{C}$	182
Figure 4.13. Sensitivity of simulated INP number concentrations at Ragged Point, Barbados to driving meteorology dataset	184
Figure 4.14. Sensitivity of surface INP concentrations to driving meteorology dataset	187
Figure 4.15. Comparison of monthly simulated and observed dust mass concentrations at Barbados and Miami for 2001	188
Figure A4.1. Locations of the profiles shown in Figure 4.8	193
Figure A4.2. Importance of marine organic INP at a temperature of $-37^{\circ}\text{C}$	194

## List of tables

### Chapter 1.

Table 1.1. Summary of a selection of ice nucleation parameterisations available for use in numerical weather prediction models	29
--	----

### Chapter 3.

Table 3.1. List of target output variables discussed in this study and the criteria used to extract their values from the simulation output	98
Table 3.2. The base case, minimum and maximum values of the uncertain input variables perturbed in this study	104

### Chapter 4.

Table 4.1. GLOMAP simulations carried out and discussed in this chapter	150
---	-----

## Abbreviations

<b>[INP]<sub>MAX</sub></b>	Factor applied to the base case INP number concentration profile in Chapter 2
<b>A13</b>	Atkinson et al., 2013
<b>AEROCOM</b>	Aerosol Model Intercomparison
<b>AERONET</b>	Aerosol Robotic Network
<b>AGAGE</b>	Advanced Global Atmospheric Gases Experiment
<b>AOD</b>	Aerosol Optical Depth
<b>AVHRR</b>	Advanced very-high-resolution radiometer
<b>B-ICE</b>	Barbados Ice-nucleating particle Concentration Experiment
<b>C86</b>	Cooper 1986
<b>CASIM</b>	Cloud AeroSol Interacting Microphysics scheme
<b>CCN</b>	Cloud condensation nuclei
<b>CD</b>	Cloud droplet
<b>CDNC</b>	Cloud droplet number concentration
<b>CIP</b>	Cloud Imaging Probes
<b>CMIP</b>	Coupled Model Intercomparison Project Phase
<b>D10</b>	DeMott et al., 2010
<b>DMT</b>	Droplet Measurement Technique
<b>ECMWF</b>	European Centre for Medium-Range Weather Forecasts
<b>ERA</b>	ECMWF Re-Analysis
<b>GLOMAP</b>	Global Model of Aerosol Processes
<b>GOCART</b>	Goddard Chemistry, Aerosol, Radiation, and Transport
<b>H19</b>	Harrison et al., 2019
<b>HM-rate</b>	Rate of splinter production per milligram rimed by the Hallett-Mossop process
<b>IC</b>	Ice crystal
<b>ICE-D</b>	Ice in Clouds Experiment – Dust
<b>ICNC</b>	Ice crystal number concentration
<b>INP</b>	Ice-nucleating particle
<b>K-feldspar</b>	Potassium feldspar
<b>LEM</b>	Large Eddy Model
<b>Lidar</b>	Light Detection and Ranging

### XIII

<b>M92</b>	Meyers et al., 1992
<b>MERRA-2</b>	Modern-Era Retrospective analysis for Research and Applications
<b>MISR</b>	Multi-angle Imaging Spectroradiometer
<b>MODIS</b>	Moderate Resolution Imaging Spectroradiometer
<b>MONC</b>	Met Office NERC Cloud Model
<b>N12</b>	Niemand et al., 2012
<b>NoINP</b>	Simulation without active ice nucleation
<b>NWP</b>	Numerical weather prediction
<b>PCASP</b>	Passive Cavity Aerosol Spectrometer Probe
<b>POLIPHON</b>	Polarization Lidar Photometer Networking
<b>S</b>	Snow
<b>SAL</b>	Saharan Air Layer
<b>SALTRACE</b>	Saharan Aerosol Long-range Transport and Aerosol–Cloud Interaction Experiment
<b>SEM-EDS</b>	Scanning Electron Microscopy with Energy Dispersive Spectroscopy
<b>SIP</b>	Secondary ice production
<b>SOCRATES</b>	Suite of Community RAdiative Transfer codes based on Edwards and Slingo
<b>SODA2</b>	System for OAP Data Analysis
<b>TOA</b>	Top-of-atmosphere
<b>UM</b>	Unified Model
<b>WP</b>	Water path
<b>XRD</b>	X-ray diffraction
$\lambda_{\text{[INP]}}$	INP parameterisation slope $d(\log_{10}[\text{INP (m}^{-3}\text{)]})/dT(\text{ }^{\circ}\text{C})$
<b><math>\mu\text{L-NIPI}</math></b>	Microlitre Nucleation by Immersed Particle Instrument

# Chapter 1: Motivation and background information

## 1.1. Weather and climate prediction

Understanding the Earth's atmosphere is critical for the daily life and future planning of civilians, organisations and governments. Accurate weather forecasts are vital for issuing advance warning of, and ensuring safety during, extreme weather events, mitigating the impact of weather such as very heavy rainfall, and informing civilians and economic sectors of imminent weather conditions for planning of commercial and leisure activities (Bauer et al., 2015). Furthermore, accurate representation of the Earth System in climate models is important for planning for future changes in climate that may require mitigation, such as sea level rise.

Models are theoretical representations of real or imaginary processes and systems. In the early 20<sup>th</sup> century it was proposed that the laws of physics could be used to predict the weather (Abbe, 1901; Bauer et al., 2015; Bjerknes, 1904). This suggestion prompted the birth and subsequent development of numerical weather prediction and in the 1950s, an electronic computer was used for the first time to predict the weather in hindcasts (Bauer et al., 2015; Charney et al., 1950) and not long afterwards, the first real-time forecasts were produced (Bauer et al., 2015; Bolin, 1955).

Today, numerical models can simulate most components of the Earth System including the atmosphere, ocean, sea ice and vegetation (Neumann et al., 2019). Every day numerical weather models (NWP) solve a complex system of non-linear differential equations at approximately half a billion points per timestep, allowing the prediction of the weather on scales from 100s of metres to 1000s of kilometres in the immediate future to weeks or months ahead (Bauer et al., 2015). Advances in weather modelling have typically been incremental

with steady advances in understanding and enhancing forecast accuracy and affordability over time: for example today's 6 day forecast is as accurate as the 5 day forecast 10 years ago (Bauer et al., 2015).

The complex systems of equations in numerical weather prediction and climate models don't encapsulate the full complexity of the real-world atmosphere or Earth System due to, for example, computational affordability restrictions, and therefore rely on many simplifications or parameterisations to represent processes that cannot be resolved within model grid boxes (Bauer et al., 2015). Deciding which atmospheric and Earth System processes to parameterise and to what extent is a major challenge for modellers, most significantly because finding the optimal balance between 'physical realism, linearity and computational affordability' (Lopez, 2007) is extremely difficult. This is particularly true when trying to represent processes and systems for which there is a lack of fundamental physical understanding or where observational data is sparse or non-existent (Bauer et al., 2015).

Atmospheric processes operate at scales from the molecular to 1000s of kilometres so at all grid resolutions, some processes will require parameterisation. As grid resolution increases, the complexity of the model generally increases on the assumption that more realistic and complex representations of all atmospheric processes will lead to greater accuracy in model predictive power. However, where processes must be simplified in some way, the decisions about which aspects of the real-world complexity to represent in detail are often made without a systematic 'investment gain' analysis (Yano et al., 2018). This leads to models representing huge complexity in some processes with consequences for computational time and cost without this additional complexity adding any value to the model forecast or predictive power compared to a simple parameterisation (Yano et al., 2018).

Addition of complexity to NWP models can be justified if it leads to direct improvement in the model predictive power or enhances our understanding of the climate and weather system

which can indirectly lead to forecasting improvement in the future. Making informed decisions about the complexity required for each process in numerical weather and climate models requires both an understanding of the underlying physical process and the impact of different representations of the process in question on the system of interest. This thesis examines the effects of the parameterisation of ice-nucleating particles (INP), aerosols with the ability to catalyse ice formation (Vali et al., 2015), on tropical convective clouds with the aim to understand the potential benefits of an enhanced understanding of INP properties for the representation of these climatically important clouds.

## **1.2. Clouds**

### **1.2.1. Why do clouds matter?**

Clouds are suspensions of liquid droplets and frozen crystals in the atmosphere. They are essential components of the global hydrological cycle and play an important role in energy and heat transfer in the atmosphere. They provide the majority of the Earth's freshwater in the form of liquid or solid precipitation and, as such, are vital to the planet's habitability. They are a part of our everyday life due to the role they play in weather, for example, in determining how much sunlight and rain we experience.

Clouds are key aspects of the global radiative budget through the reflection and absorption of incoming and outgoing radiation. Clouds reflect incoming shortwave radiation, i.e. from sunlight, inducing cooling, and absorb outgoing longwave radiation from the Earth's surface, causing warming. The balance between how much shortwave radiation is reflected by clouds (cloud albedo), and how much clouds reduce outgoing longwave radiation (a greenhouse effect) determines whether clouds have an overall cooling or warming effect on the Earth's

atmosphere and is the most important cloud property for climate prediction. It is estimated that overall the cloud albedo effect outweighs the cloud greenhouse effect and thus clouds cause a net cooling of the Earth's atmosphere of  $\sim 18 \text{ W m}^{-2}$  relative to a cloud free atmosphere (Zelinka et al., 2017).

However, clouds present challenges for both numerical weather prediction in the present and for prediction of future climates. For example, cloud processes operate across multiple scales, from nanometres to areas spanning 1000s of kilometres across the Earth's surface. Accurately representing processes at all relevant scales is extremely challenging in any model and one has to rely on simplified statistical representations of processes occurring at scales smaller than those resolved by the model numerics. Furthermore, our observational records of clouds remains relatively scarce making validation of climate and numerical weather model representations of clouds difficult. While forecasts produced by numerical weather models have been assessed against observations for accuracy for decades, clouds are generally not included in these assessments because their spatial and temporal heterogeneity makes verification against observations challenging (Pincus et al., 2008). Where cloudiness and precipitation are evaluated (e.g. by the ECMWF), performance remains much poorer than for the "larger-scale" dynamics variables, such as, for example, geopotential height.

Changes in atmospheric composition due to anthropogenic activity, in the form of global warming due to enhanced carbon dioxide concentrations or changes in aerosol sources, can cause changes in cloudiness and the amount of cooling they induce. The impact of anthropogenic activity on clouds is very uncertain because both the effect of warmer atmospheric temperatures, and the effect of altered aerosol concentrations and composition on cloud properties, are complicated and difficult to quantify. Cloud feedbacks, changes in cloud properties due to rising global temperatures that can amplify or dampen the global temperature increase, may be as large as  $2.0 \text{ W m}^{-2} \text{ }^{\circ}\text{C}$  (Zelinka et al., 2017). In idealised simulations of an

aquaplanet, i.e. simulations that didn't have to account for the interactions of clouds with land, ice, the biosphere or aerosols, the uncertainties in the response of clouds to global warming remained as large as they were in comprehensive Earth System Models (Medeiros et al., 2008; Stevens and Bony, 2013). The effect of aerosol-cloud interactions is currently the largest source of uncertainty in the IPCC Assessment of the eventual magnitude of the atmospheric temperature increase due to climate change (Boucher et al., 2013).

### **1.2.2. Cloud phase**

The balance of liquid and ice in mixed-phase clouds is important for cloud development, precipitation, lifetime and radiative properties. Ice particles tend to be more efficient collectors of liquid drops than cloud droplets, meaning frozen particles grow faster than liquid particles resulting in faster precipitation development in clouds with higher glaciation. Enhanced precipitation formation can result in the faster dissipation of a cloud with more ice and thus a shorter lifetime and lower overall cloud cover. Clouds with higher ice fraction tend to be thinner and to reflect less sunlight due to a reduction in the number of particles and an increase in particle size relative to a clouds containing more supercooled liquid water (Tan et al., 2016).

Tan et al. (2016) found that accurate representation of cloud phase in GCMs is important for constraining the equilibrium climate sensitivity to climate change. Cloud phase is an important component of potential 'cloud opacity feedbacks', the changes in cloud reflectivity to incoming shortwave or cloud absorption of outgoing longwave radiation due to global temperature rises. These cloud opacity feedbacks are 'highly uncertain' (Boucher et al., 2013) due in part to difficulty representing cloud phase and cloud microphysics in climate models (Zelinka et al., 2017).

Despite its climatic importance and its relevance for precipitation forecasts, cloud phase is not well constrained in weather or climate models in part due a lack of understanding of mixed-phase ice processes (Komurcu et al., 2014; Murray et al., 2020). Komurcu et al. (2014) found that there were large differences in the representation of cloud phase in six global climate models, and that all the models tested produced too much cloud glaciation at mixed-phase temperatures. Cloud phase is notoriously poorly represented in weather and climate models for a number of reasons including a lack of physical understanding of ice formation, strongly simplified representation of cloud glaciation in models, and difficulties observing and therefore validating mode representation of cloud phase (e.g. Cesana et al., 2015; Komurcu et al., 2014).

### **1.2.3. Convective clouds in weather and climate models**

Convective clouds are formed by warm, buoyant air rising relative to its surroundings. Unequal thermal heating of the air at the Earth's surface by solar radiation can cause an air parcel to become warmer and less dense than its surrounds. As this less dense air rises, it cools and water can form creating a cloud. The latent heat release from condensation, and freezing at higher altitudes, can further increase the buoyancy of a rising air parcel. Deep convective clouds in the tropics can extend from temperature greater than 30 °C to temperatures lower than -50 °C, i.e. from the boundary layer to beyond the tropopause, and can have horizontal radii greater than 1000 km<sup>2</sup>. Deep convective clouds are characterised by a convective core where air rises in strong updrafts of up to 50 m s<sup>-1</sup> (Frank, 1977; Musil et al., 1986; Xu et al., 2001), and powerful downdrafts at the edges of the convective cell caused by falling precipitation and evaporative cooling. Some cloud mass may be 'overshot' into the stratosphere by the momentum of the convective core's vertical motion, but the majority of cloud will spread out where the cloud hits the tropopause to form an optically thin layer of cloud called an anvil. At

the surface, air is pulled into the convective core due to displacement from the rising thermals, while very strong surface winds, called cold pool outflows, can occur where downdrafts hit the surface (e.g. Trzeciak et al., 2017).

Stevens and Bony (2013) assert that “an inadequate representation of clouds and moist convection is the main limitation in current representations of the climate system”, due to the fact that these processes operate on scales well below the GCM spatial resolution. These processes are particularly problematic in the tropics where they are especially dominant. The tropics are the largest contributor to uncertainty between models in CMIP5 simulations of global aquaplanet precipitation and radiation responses to climate change, with not only the magnitude, but the sign of precipitation responses differing between models (Medeiros et al., 2008; Stevens and Bony, 2013). The accurate representation of tropical convection is important for understanding weather and climate. For example, tropical Atlantic deep convective clouds are important for the development of tropical storms and hurricanes, and may play a role in the modulation of sea surface temperatures (Ramanathan and Collins, 1991), changes to which have been linked to changes in the African and Indian monsoon (Kucharski et al., 2007, 2009), precipitation over North America (e.g. Kushnir et al., 2010), Antarctic sea ice distribution (Li et al., 2014), and Amazon rainfall (Yoon and Zeng, 2010) and wildfire anomalies (Fernandes et al., 2011).

### **1.2.3.1. Unresolved convection**

The dilemma of representing unresolved processes on the resolved scale is encapsulated by the challenge of representing convective clouds in numerical weather prediction and climate models. At grid spacings greater than 10 km, convection is represented by so called convection parameterisations because processes triggering convection as well as the dynamics of these clouds occur at the micro- to mesoscale (Prein et al., 2015). In these cases, as many of the

governing processes occur in small fractions of the gridscale, it is assumed that all convection is unresolved (Bauer et al., 2015). However, these parameterisations are relatively ‘crude’ (Prein et al., 2015) and involve strong simplification of processes that are highly variable in space and time (Lopez, 2007) with implications for the physical properties, such as moisture and momentum transport, precipitation generation and cloud cover, that the parameterisations represent.

Uncertainty in convective representation has consequences for many aspects of weather and climate prediction. Parameterisations of updraft triggering, entrainment and detrainment of convective plumes (de Rooy et al., 2013) and convective precipitation efficiency (Renno et al., 1994) cause some of the largest uncertainties in projected large-scale parameters such as climate sensitivity (Knight et al., 2007; Prein et al., 2015; Sanderson et al., 2008; Sherwood et al., 2014). Furthermore, they interact with other parameterisations of microphysical and radiative processes causing further uncertainty (Prein et al., 2015). As a result, there is increasing interest in moving towards operational weather prediction modelling at a grid spacing of 1 km (Neumann et al., 2019; Prein et al., 2015) both globally and in regional simulations, where parameterisation of convection becomes unnecessary as most of the transient dynamics are resolved (Neumann et al., 2019).

### **1.2.3.2. Resolved convection**

However, even at 1 km grid spacing, not all convective processes, such as embedded small scale convective plumes, are resolved (Bauer et al., 2015). Furthermore, at 1 km grid spacing, the parameterisation of cloud microphysical processes becomes critical to accurate representation of cloud processes. The microphysics in convective clouds is particularly complex relative to stratiform clouds (Prein et al., 2015; Pruppacher and Klett, 1978), and therefore challenging to parameterise, due to stronger updrafts in convective clouds supporting

mixed-phase (ice and liquid) processes and a wide variety of hydrometeor types including ice crystals, snow, graupel, cloud droplets, rain and hail (Prein et al., 2015).

The microphysics of deep convective clouds are particularly difficult to accurately represent in climate and weather models due to the amount, complexity and variety of scales of processes occurring within them. Cloud droplets can form rapidly as the air in the convective core rises and cools. These cloud droplets contribute to the warm rain process whereby collision-coalescence between cloud, rain and drizzle drops can rapidly form precipitation-sized droplets. Once formed and elevated to colder altitudes cloud droplets can undergo heterogeneous or homogeneous freezing to form ice crystals. In water subsaturated cloud regions, such as the downdrafts of deep convective clouds, ice crystals can grow rapidly at the expense of cloud droplets via the Wegener-Bergeron-Findeisen process (e.g. Cui et al., 2006).

Ice crystals can grow rapidly to form graupel, where further riming of cloud droplets can cause rime splintering and the production of more ice crystals. Ice crystals can also coagulate to form snow particles. Rain, graupel and snow particles are heavier and will precipitate more readily than cloud or small ice particles producing sometimes very intense precipitation. Convective clouds can have multiple regions of updraft which can facilitate or enhance secondary ice production. Falling graupel and large droplets are also important for enhancing secondary ice production. Many microphysical processes parameterised in a global or convection permitting model can add considerable uncertainty to the simulated cloud state, and this uncertainty is compounded by process interactions. Furthermore, the accurate representation of dynamics is critical for the accurate representation of cloud microphysics. For example, Wellmann et al. (2018) found very large differences in the contribution of various microphysical and environmental parameters to the uncertainty in the development of an idealised deep convective cloud depending on whether the cloud was initiated using a warm bubble, a cold pool, or a mountain ridge. The relative importance of dynamics, environmental conditions and

cloud microphysics, and their interactions, in convective clouds is an ongoing area of research (e.g. Fan et al., 2016; Miltenberger et al., 2018a, 2018b; Miltenberger and Field, 2020; Wellmann et al., 2020).

## **1.3. Processes affecting the amount of ice in convective clouds**

### **1.3.1. Aerosol-cloud interactions**

Aerosols are particles suspended in the atmosphere that are either emitted from the Earth's surface (primary aerosol) or formed in situ from precursor gases which can nucleate forming new particles (secondary aerosol) (Pruppacher and Klett, 1978). Primary aerosols can be emitted naturally in the form of, for example, mineral dust from deserts (Knippertz and Todd, 2012), ash and sulphates from volcanic eruptions (Marshall et al., 2019; Mills et al., 2016; Sawyer et al., 2011) or organic matter and sea salt from sea spray (Vignati et al., 2010). Primary aerosol particles can also be emitted from anthropogenic activity in the form of, for example, black carbon from combustion (Streets et al., 2001), organic carbon from biomass burning (Bond et al., 2004), and sulphate and nitrate aerosols from shipping (Matthias et al., 2010). Fossil fuel burning (Huang et al., 2015), biogenic emissions of volatile organic compounds such as isoprene (Carlton et al., 2009) and volcanoes (Cole-Dai, 2010) are important sources of the precursor gases for secondary aerosol formation.

Aerosols are important drivers of climate. Aerosols can scatter and absorb incoming and outgoing short-wave and long-wave radiation, affecting the Earth's energy balance and changing albedo (Carslaw et al., 2013; Twomey, 1991). The impact of aerosol scattering and absorption on climate is known as the aerosol direct effect. For example, changes in the Earth's

albedo due to increased sulphate aerosols following large volcanic eruptions has been cited as a trigger for large scale climate change including periods of glaciation (Macdonald and Wordsworth, 2017).

Aerosols can also affect climate by affecting cloud radiative properties which in turn alters the Earth's albedo (Feingold and McComiskey, 2016; Twomey, 1991). These aerosol effects are called adjustments to aerosol-cloud interactions (previously termed the indirect effect) (Boucher et al., 2013). Specifically, aerosols can act as cloud condensation nuclei (CCN) and an increase in the number of aerosol particles in a cloud with no changes in the available moisture for condensation will increase the cloud droplet number concentration and decrease cloud droplet size. A cloud with more smaller droplets will scatter and reflect incoming solar radiation more effectively than a cloud with less larger droplets leading to a cooling effect (Carslaw et al., 2013). Cloud lifetime can also be increased in clouds with more small cloud droplets due to the suppression of the warm rain process (Lohmann, 2006) which can prolong this cooling effect.

Aerosols can also cause changes in atmospheric temperature and relative humidity which can affect cloud formation in what are called cloud adjustments to aerosol radiative forcing (previously termed the semi-direct effect) (Boucher et al., 2013). For example, absorption of solar radiation by soot particles and consequently reduced relative humidity reduced daytime cloud cover by trade cumulus clouds over the Indian Ocean by between 25 and 40% (Ackerman et al., 2000). The same effect has been demonstrated for marine stratocumulus clouds (Johnson et al., 2004).

Aerosol cloud interactions via the indirect and the semi-direct effect are currently the largest source of uncertainty in climate forcing estimates by the IPCC (Boucher et al., 2013), and these interactions become even more complicated than described above when we consider mixed-phase clouds and the potential for aerosol to affect ice formation processes. As well as acting

as CCN, aerosols can act as INP (Lohmann et al., 2016), aerosols that can initiate the freezing of a cloud droplet between 0 and  $\sim -38^{\circ}\text{C}$ . Given the important implications of aerosol-cloud interactions for climate and potentially also for weather prediction, understanding the role of aerosols in controlling mixed-phase cloud processes, including in ice formation, is an important challenge for atmospheric scientists. This thesis focuses on understanding the impact of INP, and particularly mineral dust, in determining the properties of tropical convective clouds.

### **1.3.1.1. Mineral dust**

Mineral dust from the world's deserts is an important global aerosol type (Choobari et al., 2014; DeMott et al., 2003; Prospero, 1996; Tang et al., 2016) with an atmospheric dust loading of approximately 19.2 Tg, compared to 7.5 Tg for the next largest loading, sea spray (Tang et al., 2016; Textor et al., 2006). Dust uplift in summer is associated with a wide range of meteorological conditions. Both dry (e.g. African Easterly Jet, Harmattan winds), and moist wind systems (e.g. monsoon circulation, cold pools) are known to be important (Knippertz and Todd, 2012; Schwendike et al., 2016a). Summertime dust events tend to reach heights of 4 to 6 km due to a tall boundary layer, high insolation, and the upward shift of the Intertropical Convergence Zone (ITCZ) (Gläser et al., 2015).

The tropical Atlantic, the region of interest in this thesis, is particularly influenced by high dust loading from the Sahara; North Africa accounts for 55% of global dust emissions (Ginoux et al., 2012). Saharan dust contributes 30-40% of Caribbean summertime aerosol volume (Groß et al., 2016) and has been observed acting as efficient INP over Florida (DeMott et al., 2003) demonstrating that dust can influence cloud properties thousands of kilometres from source (Tang et al., 2016; Vergara-Temprado et al., 2017).

### **1.3.2. Cloud droplet formation**

Atmospheric droplet formation relies on the presence of deliquesced soluble aerosol particles (Lohmann et al., 2016). CCN are aerosol particles upon which cloud droplets can form. CCN particles provide a liquid surface upon which water vapour can condense removing the need for formation of a liquid critical nucleus from the vapour phase, and thus reducing the condensation energy barrier. These particles take up liquid water in sub-saturated conditions via hygroscopic growth.

The potential for an aerosol to act as a CCN depends on both size and solute concentration. The Kelvin effect states that the smaller the droplet, the larger the equilibrium vapour pressure due to increased surface tension associated with curved surfaces. The Raoult effect refers to the decrease in equilibrium vapour pressure due to solute effects. Kohler Theory describes the competing nature of these two effects.

Models use parameterisations to represent droplet activation. The primary determinant of these schemes is generally updraft velocity (e.g. Abdul-Razzak and Ghan, 2000; Fountoukis and Nenes, 2005; Shipway and Abel, 2010; Twomey, 1959). A hygroscopicity parameter is used to describe effect of particle composition via the solute effect (Petters and Kreidenweis, 2007). Completely insoluble particles have a hygroscopicity parameter of 0, representing an inability to grow in size via deliquescence.

#### **1.3.2.1. Dust as CCN**

In mixed-phase clouds, most INP are expected to be subject to immersion freezing and therefore activate as CCN prior to heterogeneous nucleation (Ansmann et al., 2008; De Boer et al., 2011; Kanji et al., 2017). Therefore, for dust particles to be atmospherically relevant as INP particles, they should also act as CCN. In models, dust is normally assumed to be insoluble but small fractions of soluble components can enhance the ability of dust particles to act as

CCN by increasing their hygroscopicity parameters (Kelly et al., 2007). However, these soluble components have been deemed insufficient explanation for the demonstrated ability of dust to act as CCN (Karydis et al., 2012) and as a result, Kumar et al. (2009) highlighted the importance of including adsorption effects in consideration of CCN activity. Kumar et al. (2011) developed a new activation parametrisation that considers both Kohler Theory and adsorption effects via the Frenkel-Halsey-Hill adsorption activation theory (FHH). Dry generated dust samples, generally the larger of a bimodal dust size distribution, are expected to follow activation by FHH, while the smaller of the dust size modes, made up predominately of wet generated clays and minerals, will be dominated by solute effects (Kumar et al., 2011)

The effects of dust on CCN concentration depends on both dust concentration and its impact on other CCN species. Karydis et al. (2017) found that dust particles increased cloud droplet number concentration (CDNC) by up to 20% over the Sahara, but decreased CDNC by a comparable amount over areas with high anthropogenic aerosol loading. Dust particles with a high FHH contribution to activation are less prevalent CCN in low saturation environments (Karydis et al., 2012), because they are not subject to sub-saturated deliquescence on the same scale as small soluble particles. Due to their large size, dust particles require more water condensation onto their surface for activation than smaller droplets. Their presence in an aerosol population can thus reduce supersaturation and cloud droplet number, particularly if they take up considerable amounts of water but do not activate (Barahona et al., 2010). The effect of dust on CCN concentrations can have implications for cloud properties. For example, increased CCN number concentrations are understood to suppress the warm rain process by reducing the size of cloud droplets (e.g. Campos Braga et al., 2017; Konwar et al., 2012). However, if dust particles large enough to act as giant CCN are present in an aerosol population, they can form large drizzle droplets and form precipitation earlier (Posselt and Lohmann, 2008).

Karydis et al. (2017) report that global average CDNC decreases by 10% when adsorption is accounted for, while changes are less for particle solubility effects. Kelly et al. (2007) found that the impact of dust particle addition to CDNC in an air mass predominantly containing fine ammonium sulphate varied depending on updraft speeds. Sulfate uptake on the surface of dust particles increases CCN ability because of an increase in solubility (e.g. Gibson et al., 2007), but can reduce the overall CCN sized particles available due to a concurrent reduction in fine sulfate (Manktelow et al., 2009). In deep convective clouds, updrafts are often high enough to reduce water vapour competition and increase dust's contribution to activation (Anderson et al., 2005; LeMone et al., 1980).

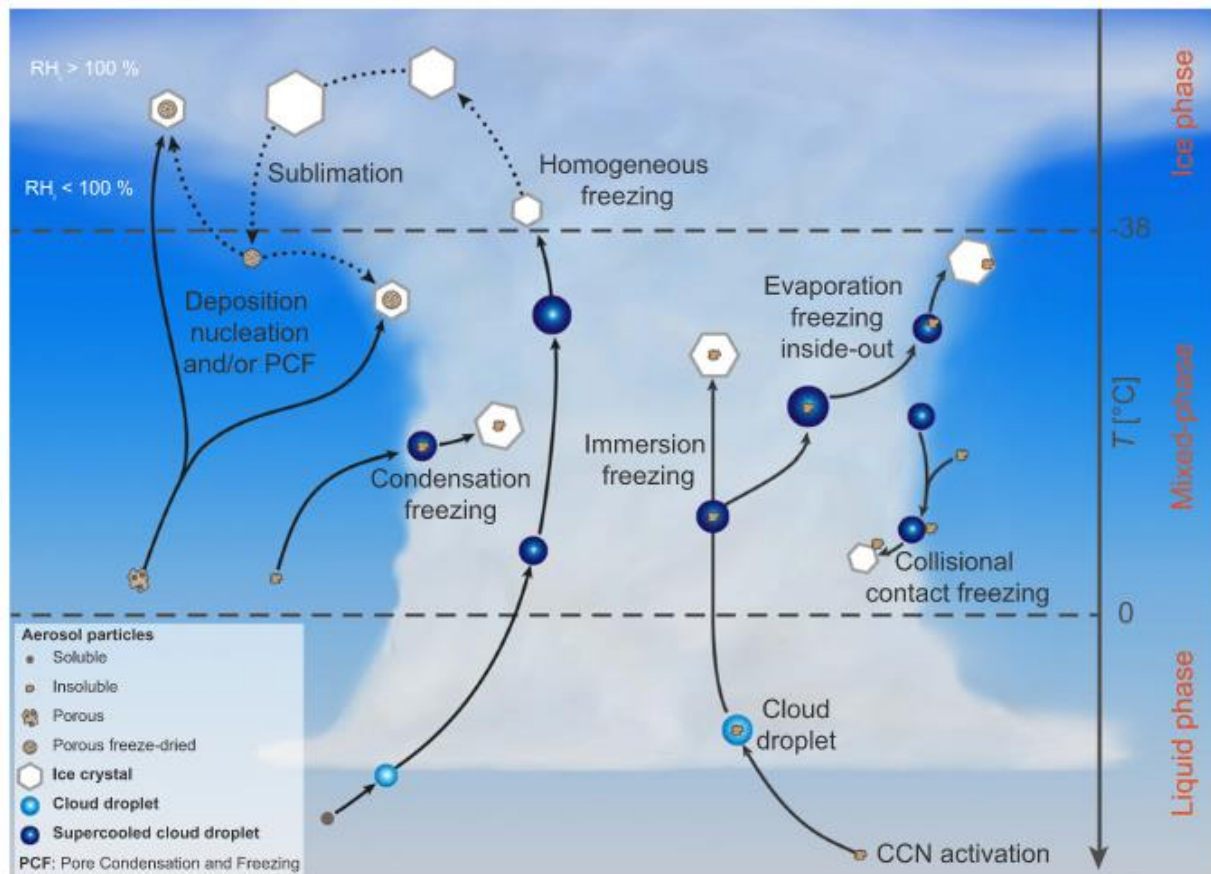


Figure 1.1. Mechanisms of primary ice nucleation in clouds from Kanji et al. (2017) (Fig 1-1, page 1.2, © American Meteorological Society. Used with permission).

### **1.3.3. Homogeneous ice nucleation**

Ice nucleation in the atmosphere can be homogeneous or heterogeneous. Homogeneous nucleation occurs below  $\sim -33^{\circ}\text{C}$  (Herbert et al., 2015). It involves the spontaneous growth of an ice germ within a droplet that leads to instantaneous freezing of the entire droplet. Nucleation of the initial cluster occurs when the thermodynamic conditions cause the Gibbs free energy barrier to drop low enough for phase transition. In the case of homogeneous droplet freezing, a thermodynamically stable cluster of ice forms within a metastable droplet. This subsequently causes freezing of the whole droplet (Lohmann et al., 2016).

### **1.3.4. Heterogeneous ice nucleation**

Heterogeneous ice nucleation occurs at temperatures between 0 and  $\sim -38^{\circ}\text{C}$  in the presence of INP. INP are generally rare in aerosol populations. INPs lower the energy barrier required for critical cluster formation by providing a surface upon which ice embryos can form. Theoretically, if an ice embryo forms on a solid surface, its shape will resemble that of a spherical cap rather than a full sphere, therefore its volume for the same radius is reduced, thus reducing the number of water molecules needed to join the embryo before it reaches its critical radius (Lohmann et al., 2016). Commonly known INPs are mineral dust particles (e.g. DeMott et al., 2003), bioaerosols (e.g. Diehl et al., 2002) and marine organics (Wilson et al., 2015).

Heterogeneous ice nucleation can occur via immersion, contact, condensation, and deposition freezing. Immersion freezing occurs when an INP is enclosed in a water droplet which then freezes when ambient conditions change to allow it. In the atmosphere, immersion freezing can occur after an aerosol particle has been activated as a CCN. Contact freezing occurs when collision of an INP with a water droplet initiates freezing at the INP-water interface. Condensation freezing takes place when freezing occurs simultaneously with the formation of

liquid water on the surface of an INP (Vali et al., 2015). Deposition nucleation occurs when water vapour is directly deposited as ice on the surface of an INP. This does not generally occur in mixed phase or low level clouds, and there is speculation as to the mechanism's existence. Condensation of liquid in unobservable quantities may occur prior to ice formation, or liquid may be present in cavities of the INP (Campbell and Christenson, 2018; Marcolli, 2014; Vali et al., 2015). Within mixed phase clouds, the majority of INP are expected to activate as CCN prior to ice formation and be subject to immersion freezing (Ansmann et al., 2008; De Boer et al., 2011; Westbrook and Illingworth, 2013). Mechanisms of primary ice formation in mixed-phase clouds are illustrated in Figure 1.1 (Kanji et al., 2017).

#### **1.3.4.1. Variability in atmospheric INP number concentrations**

INP number concentrations in the atmosphere are extremely variable and difficult to predict. The spread in INP number concentrations from observational measurements spans between three and six orders of magnitude at any one temperature (Kanji et al., 2017) (Figure 1.2), and large variability persists even in measurements of individual regions or aerosol populations (Boose et al., 2016b; Kanji et al., 2017; Lacher et al., 2018). For example, measurements of INP in the Saharan Air Layer at  $-33^{\circ}\text{C}$  have 4 orders of magnitude variation in number concentrations (Boose et al., 2016b) and measurements of INP number concentration in cloud and precipitation samples at  $-5^{\circ}\text{C}$ , i.e. a temperature very relevant for secondary ice production by the Hallett-Mossop process (Section 1.3.5), can vary from  $10^{-6}$  to  $0.1 \text{ L}^{-1}$  (Kanji et al., 2017; Petters and Wright, 2015). The large spread in observational INP data would not be problematic if INP number concentrations were easy to predict based on well-constrained atmospheric or aerosol properties. However, specific INP concentrations show only limited predictability from some aerosol size descriptors, such as aerosol surface area (Lacher et al., 2018), and very little predictability from meteorological variables such as pressure and temperature (Boose et al., 2016a; Lacher et al., 2018) and aerosol composition descriptors (Lacher et al., 2018). INP

number concentration of  $1 \text{ L}^{-1}$  have been recorded in coastal and open ocean mid- to high-latitudes at temperatures as cold as  $-35^\circ\text{C}$  and as warm as  $-10^\circ\text{C}$  (Murray et al., 2020), i.e. despite temperature being one of the strongest predictors of INP number concentration that is readily available in atmospheric models, similar INP number concentrations can occur at nearly all mixed-phase temperatures in remote locations with few aerosol sources.

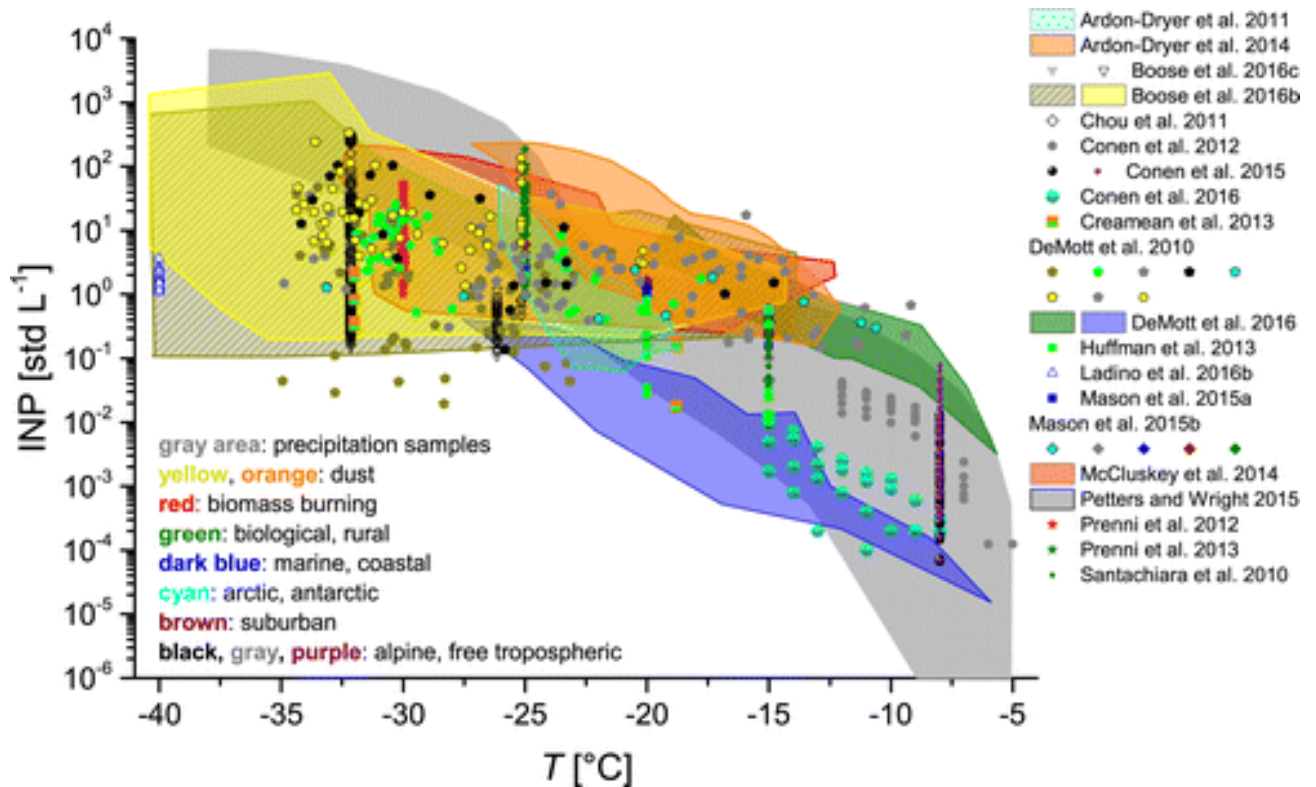


Figure 1.2. Variability in atmospheric ice-nucleating particle number concentrations from Kanji et al. (2017) (Fig 1-10, page 1.18, © American Meteorological Society. Used with permission).

Even for materials of similar and known mineralogy, measurements of ice nucleating efficiency can span several orders of magnitude: There is seven orders of magnitude variation in laboratory measurements of ice nucleation active site densities ( $n_s$ ) for different types of feldspar at  $-15^\circ\text{C}$  (Atkinson et al., 2013; Harrison et al., 2016; Peckhaus et al., 2016). While K-feldspar has been shown to more ice-active than other feldspars explaining this variability (Harrison et al., 2016), most models do not contain detailed information about the composition

of mineral dusts (in fact, many don't track information about broader aerosol type separating mineral dusts from for example, black carbon) meaning this variability in ice-nucleating ability between aerosols of different composition cannot currently be easily represented.

#### **1.3.4.2. Characteristics of ice nucleating particles**

INP are rarer in the atmosphere than CCN particles. The characteristics that make an aerosol particle capable of or efficient at nucleating ice is not well understood. Most INP, including mineral dusts (DeMott et al., 2003; Niemand et al., 2012), components of mineral dust such as K-feldspar (Atkinson et al., 2013; Harrison et al., 2016) and volcanic ash (Maters et al., 2019), are insoluble owing to the requirement for a solid surface on which an ice embryo can form (Lohmann et al., 2016). There is growing evidence that ice nucleation on solid surfaces favours imperfections or deformations on the particle surface. Locations on an aerosol particle where ice nucleation is favoured are termed active sites. These sites have been theorised to be, for example, surface pits (Holden et al., 2019), hydrophilic sites (Freedman, 2015), or lattice mismatches (Kulkarni et al., 2015) that reduce the contact angle between the INP surface and the spherical ice cap that must form for heterogeneous ice nucleation to occur (Lohmann et al., 2016).

It has also been theorised that the ability of an INP surface to hydrogen bond with water molecules can enhance ice-nucleating ability in, for example, aluminosilicate clay particles (Freedman, 2015). Particle structure is likely an important component driving the distribution of active sites. For example, the crystallinity of tephra was found to be of importance for the ice-nucleating activity of volcanic ash (Maters et al., 2019) and surface defects in K-feldspars were found to be preferential locations for active sites (Kiselev et al., 2016). The exact mechanism by which these sites facilitate ice nucleation is not understood limiting our ability

to predict the ice-nucleating ability of specific aerosol types without explicit testing and measurement.

It has recently been demonstrated that soluble particles in the form of small biological macromolecules, for example, pollen (Pummer et al., 2012), organics from soil (O'Sullivan et al., 2015), and marine organic aerosol (McCluskey et al., 2018; Wilson et al., 2015) can be efficient INP. This ice-nucleating ability may be attributed to hydrogen bonds between the water molecules and the macromolecule functional groups (e.g. –OH or amino groups) (Kanji et al., 2017). These macromolecules may also play a role in the ice-nucleating ability of insoluble aerosols such as soil or dust particles via adsorption on the insoluble surface (O'Sullivan et al., 2016) and the resultant formation of an active site that facilitates ice nucleation (Kanji et al., 2017).

#### **1.3.4.3. Mineral dust as INP**

The atmospheric importance of INP particles depends both on their ability to nucleate ice as well as their prevalence in the atmosphere. Aerosols which comprise only a minor component of atmospheric aerosols are unlikely to be atmospherically relevant regardless of their ice-nucleating ability. Mineral dust is an important INP due to both its demonstrated efficiency at nucleating ice particularly at low temperatures (e.g. Atkinson et al., 2013; Niemand et al., 2012) and a dominant presence in the atmosphere (Ginoux et al., 2012; Vergara-Temprado et al., 2017).

The nucleation efficiency of dust has been related to surface characteristics, or active sites (Harrison et al., 2016; Holden et al., 2019; Kiselev et al., 2016) and varies between mineralogies (Atkinson et al., 2013; Harrison et al., 2016). Ice nucleating ability can also be affected by atmospheric processing; the coating of dust with soluble material during processing may obscure ice active sites (Möhler et al., 2008). Acid processing has been reported to both

reduce (Sullivan et al., 2010b) and enhance INP efficiency (Sullivan et al., 2010a). Material can be accumulated on the surface of dust particles prior to emission, during transport or during cloud processing. Such materials can affect the particle ice-nucleating ability. If the accumulated materials have higher ice-nucleating efficiency than dust, they can increase the temperature at which heterogeneous freezing occurs, as has been shown for biological materials such as pollen, bacteria and fungi (Augustin-Bauditz et al., 2016; Chen et al., 2021; O'Sullivan et al., 2016). These effects are not well understood and are often not represented in models.

Dust's ice nucleating ability has been argued to have a global impact on cloud phase with less supercooled liquid in dusty regimes (Tan et al., 2014). Furthermore, several studies suggest convective invigoration due to dust acting as CCN and INP; the release of latent heat from condensation or freezing increases buoyancy and updrafts (e.g. Corr et al., 2016; Van Den Heever et al., 2011) leading to deeper clouds (Altaratz et al., 2014). This invigoration can increase cloud cover in the subtropical Atlantic (Koren et al., 2005, 2010). Kishcha et al. (2016) find that Saharan dust is responsible for an asymmetrical cloud cover with 20% higher values in the Northern tropical Atlantic than in the Southern tropical Atlantic.

### **1.3.5. Secondary ice production and tropical cloud glaciation**

Ice crystal concentrations in clouds have been recorded at much greater concentrations than the concentrations of INPs (Fridlind et al., 2007; Heymsfield and Willis, 2014; Ladino et al., 2017; Lawson et al., 2015; Mossop, 1985; Pruppacher and Klett, 1978). Lasher-Trapp et al. (2016) found INP concentrations were three to four orders of magnitude lower than graupel concentrations in tropical convective clouds between  $-5$  and  $-8^{\circ}\text{C}$  in the Western tropical Atlantic. In the same campaign (ICE-T) some ice crystal concentrations exceeded  $100\text{L}^{-1}$  at sampling temperatures between  $-6$  and  $-10^{\circ}\text{C}$  in multithermal clouds with tops of around -

14°C. This implies the existence of secondary ice production (SIP) (Field et al., 2017). A SIP is 'a mechanism or process that produces new ice crystals in the presences of pre-existing ice without requiring the action of an ice nucleating particle (or homogeneous freezing) (Field et al., 2017).

The most well-known SIP is the Hallett-Mossop process, or rime splintering (HM) (Hallett and Mossop, 1974). HM occurs between -3 and -8°C. During riming of snowflakes or graupel particles, splinters are produced. Debated explanations for splintering include a thermal shock induced by the temperature difference between the original drop and the rimed particle (Dong and Hallett, 1989; Field et al., 2017), or the protrusion of liquid from the main droplet through cracks caused by pressure build-up (Field et al., 2017; Mossop et al., 1974).

Other suggested SIP mechanisms include large droplet shattering, sublimation fragmentation, the break-up of ice-crystals following crystal-crystal collisions, fragmentation due to thermal shock and activation of INPs in transient supersaturation (Field et al., 2017; Korolev and Leisner, 2020). A detailed description of all of these suggested mechanisms is beyond the scope of this thesis but a schematic showing their general theorised operation is shown in Figure 1.3 (Korolev and Leisner, 2020). Collision fragmentation has been demonstrated between needles (Knight, 2012) and between graupel particles (Takahashi et al., 1995). Droplet shattering via bubble bursting, jetting, cracking, and breakup has been demonstrated in experiments where droplets were levitated in an electrodynamic balance (EDB) and secondary ice production upon contact with a small ice particle was observed with a high-speed camera (Lauber et al., 2018). These mechanisms are less understood than the Hallett-Mossop process, and are only recently beginning to be represented in a limited number of cloud resolving models (Sullivan et al., 2018). Their representation may be important for accurate representation of clouds in which the conditions for the Hallett-Mossop process are not met (Korolev et al., 2020) or where ICNC exceed INP number concentrations at temperatures lower than 8°C (Lauber et al., 2018).

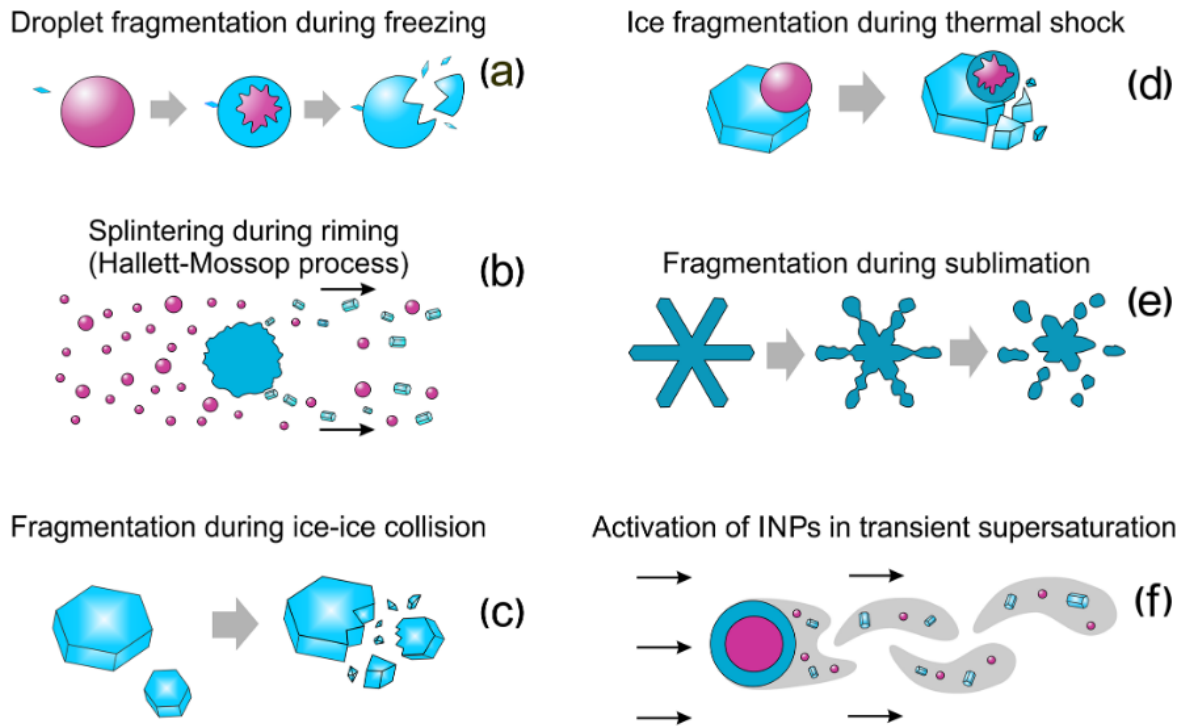


Figure 1.3. Diagram of SIP mechanisms thought to be relevant for mixed-phase clouds from Korolev and Leisner (2020): droplet fragmentation (a), the Hallett-Mossop process (b) fragmentation ice–ice collisions (c), ice fragmentation due to thermal shock (d), sublimation fragmentation (e), and activation of INPs in the transient supersaturation (f). Blue indicates ice phase and pink indicates liquid phase. Reproduced from (Korolev and Leisner, 2020).

The relative importance of INP number concentrations and ice production by SIP is not well quantified and likely varies between cloud types. The large discrepancy between observed ICNC and INP number concentrations has led to the suggestion that INP are not important for ice formation in tropical convective clouds or are only relevant up to a certain threshold needed to initiate ice formation (Beard, 1992; Crawford et al., 2012; Huang et al., 2017; Sullivan et al., 2018). The concentration of INP needed to initiate SIP in tropical maritime clouds is not certain. Very low concentrations of homogeneously or heterogeneously frozen crystals frozen in-situ or sedimented from upper levels may be enough (Beard, 1992; Field et al., 2017). An ICNC as low as  $0.01 \text{ L}^{-1}$  and  $0.002 \text{ L}^{-1}$  have been cited as enough to initiate the Hallett-Mossop process (Crawford et al., 2012; Huang et al., 2017) and ice-ice collisional breakup (Sullivan et

al., 2018) respectively. In deep convective clouds, these low thresholds may be reached by sedimenting homogeneously frozen crystals in the absence of INP. Conversely, Sullivan et al. (2018) found that there was no meaningful threshold of ice needed for initiation of the Hallett-Mossop process or droplet shattering with CCN concentrations and thermodynamic conditions being more important. However, the impact of INP may be more in deep convective clouds where stronger updrafts limit the dominance of SIP mechanisms and the anvil is susceptible to cold temperature INP number concentrations (Sullivan et al., 2018). Owing to the difficulty sampling deep convective clouds with updrafts strong enough to present difficulties for aircraft, most of the observational data of the Hallett-Mossop process was measured in comparatively shallow convective clouds with cloud top temperatures above  $-20^{\circ}\text{C}$  (e.g. Lasher-Trapp et al., 2016; Lloyd et al., 2019).

## **1.4. Parameterisation of ice-nucleating particles**

### **1.4.1. Measurement and quantification of ice-nucleating particle number concentrations**

The representation of ice nucleation in models relies on parameterisations developed from measurements of the ice-nucleating ability of aerosols or materials relevant for atmospheric aerosols. In order to measure INP number concentrations, some studies introduce an aerosol sample to a water saturation in, for example, cloud chambers (e.g. DeMott et al., 2015; Niemand et al., 2012) or continuous flow diffusion chambers (CFDCs) (e.g. Welti et al., 2009) and then observe number concentration of ice crystals formed at each temperature. These types of studies are advantageous because each cloud droplet contains a single aerosol particle

meaning the instruments are efficient in detecting INP particles active at very low temperatures (Kanji et al., 2017; Vergara Temprado, 2017).

Other studies suspend the aerosol sample in water, forming droplets containing numerous aerosol particles. These droplets are cooled down on a cold stage and the fraction of frozen droplets at each temperature is used to calculate an INP number concentration for the aerosol sample (Atkinson et al., 2013; Harrison et al., 2016, 2019; Price et al., 2018; Wilson et al., 2015). These suspension techniques are more effective at detecting low INP efficiencies at high temperatures owing to the large amount of aerosol suspended in each droplet (Kanji et al., 2017; Vergara Temprado, 2017).

INP parameterisations have been developed both from field samples of in-situ aerosols and also from components of aerosols with atmospheric relevance. For example, the behaviour of mineral dusts as INP has been parameterised from samples of surface dust or soil particles (Field et al., 2006; Kulkarni and Dobbie, 2010) sedimented atmospheric dust (Niemand et al., 2012), dusty airmasses measured in-situ (Price et al., 2018) as well as from dust ‘surrogates’ such as Arizona Test Dust (Möhler et al., 2006), and pure mineral dust components such as kaolinite, montmorillonite or illite (Welti et al., 2009). Parameterisations can also be based on multiple particle types; the parameterisation developed by DeMott et al. (2010) is based on long-term INP in-situ field measurements from predominately continental regions.

Representing the large variability in INP number concentrations (Section 1.3.4.1.) is a substantial challenge for weather and climate modellers. The chosen parameterisation of ice nucleation may impact cloud properties and resultant radiative forcing, even if aerosol concentrations are unchanged (Eidhammer et al., 2009; Fan et al., 2010b; Liu et al., 2018; Takeishi and Storelvmo, 2018). The most commonly used parameterisations can be divided into two categories based on whether they treat ice nucleation as a time-dependent, stochastic

process or as a time-independent, deterministic process. Table 1 summarises a few well-known parameterisations.

#### **1.4.2. Time-dependent/stochastic heterogeneous freezing parameterisations**

Parameterisations that account for the time-dependence of ice nucleation are stochastic and can be based on classical nucleation theory (CNT). The stochastic approach attempts to account for the dependence of ice nucleation on temperature, aerosol characteristics, and time. CNT was originally developed to describe homogeneous ice nucleation and related the nucleation rate coefficient, i.e. ‘the probability, or observed frequency, of ice nucleation events in unit volume of supercooled liquid or supersaturated vapor within a unit of time’, to the properties of supercooled water and the rate at which molecules were added to the ice embryos (Vali et al., 2015).

CNT has been adapted to describe heterogeneous freezing by accounting for a contact angle which describes the ability of the aerosol surface to nucleate ice (Hoose et al., 2010; Seinfeld and Pandis, 2006; Vali et al., 2015). The contact angle parameter allows the formation of ice at warmer temperatures than those of homogeneous freezing by lowering the energy barrier for the formation of a critical germ size by the addition of molecules to small agglomerates of ice (subcritical germs) on the ice nucleus surface (Hoose et al., 2010). The smaller the contact angle, the more efficient the aerosol sample at nucleating ice. CNT derived stochastic parameterisations of ice nucleation have been developed for multiple aerosol types to account for differences in nucleating ability between samples. For example, Hoose et al. (2010) developed CNT based parameterisations for mineral dust, soot, bacteria, and fungal spores using different contact angles for each species and accounting for their different activation energies required for critical germ formation. Mineral dust was assigned a contact angle of

30.98°, while soot was assigned an angle of 40.17° in the immersion freezing parameterisations to represent the higher ice-nucleating ability of mineral dust (Hoose et al., 2010).

Stochastic descriptions of ice nucleation using CNT representing single or multiple contact angles have been developed. When parameterisations use a single contact angle, it is assumed that droplets containing the same number of particles from a sample of aerosol, each droplet has the exact same probability of freezing in time if left long enough. A disadvantage of using a single contact angle is an inability to account for differences in ice-nucleating ability between particles from the same sample. For example, there is mounting evidence that ice-nucleating ability of mineral dusts and insoluble aerosols is determined by randomly distributed sites, such as surface pits (Holden et al., 2019), hydrophilic sites (Freedman, 2015), or lattice mismatches (Kulkarni et al., 2015), on the aerosol surface (Hiranuma et al., 2014; Holden et al., 2019; Kiselev et al., 2016). These ice active sites and their random, or at least not well understood or quantified, distribution means that two droplets containing the equal numbers of particles from the same aerosol population can have very different probabilities of freezing based on their particle specific concentration of active sites (Vergara Temprado, 2017). The stochastic approach using a single contact angle does not account for this difference in freezing probabilities.

Multi-component stochastic models were developed to address this issue and use a frequency distribution of contact angles to account for particle-to-particle variability in ice-nucleating ability (Eidhammer et al., 2009; Marcolli et al., 2007; Niedermeier et al., 2015; Vali et al., 2015). However these parameterisations typically add a large amount of computational expense and complexity to model simulations (Kanji et al., 2017).

### **1.4.3. Time independent/deterministic heterogeneous freezing parameterisations**

Most atmospheric models describe ice nucleation using a deterministic approach that neglect the time dependence of nucleation. All simulations presented in this thesis were conducted using deterministic parameterisations. Some widely employed parameterisations base the ice nucleating particle concentration of an aerosol population on temperature only (Cooper, 1986; Meyers et al., 1992). These solely temperature dependent parameterisations were developed by fitting a function to INP or ice-crystal number concentrations and neglect any dependence on aerosol number, surface area or surface characteristics when used in atmospheric models. Other deterministic parameterisations account for the aerosol size distribution or aerosol properties in their calculation of INP number concentrations. For example, DeMott et al. (2010) calculates the INP number concentrations from the number of aerosol particles with diameters greater than 0.5  $\mu\text{m}$  using a parameterisation fitted to CFDC measurements. Most recently developed parameterisations generally account for the site specificity of ice nucleation whereby there are preferred locations (or active sites) on the surface of the ice-nucleating aerosol with a higher probability of inducing freezing than the rest of the surface (Atkinson et al., 2013; Holden et al., 2019; Kiselev et al., 2016; Niemand et al., 2012; Vali et al., 2015). Such site specific deterministic parameterisations have been developed for, for example, feldspar (Atkinson et al., 2013), desert dust (Niemand et al., 2012) and Arizona test dust (Niedermeier et al., 2010). The assumed active site density of these parameterisations is then multiplied with the surface area of the modelled aerosol population to obtain an INP number concentration.

Table 1.1. Summary of a selection of ice nucleation parameterisations available for use in numerical weather prediction models.

Parameterisation	Samples and measurement instruments	Reported freezing mechanism*	Parameterisation equation is dependent on	Temperature range
<b>Cooper, 1986</b>	Literature data of in-cloud ice concentrations	Immersion, contact and condensation	- Temperature	≈-5 to -30 °C
<b>Meyers et al., 1992</b>	Aircraft measurements, CFDC	Deposition and condensation	- Ice super saturation - Temperature	-7 to -20 °C
<b>DeMott et al., 2010</b>	Aircraft and ground-based. CFDC	Immersion, deposition, condensation	- Temperature - Aerosol number concentration (d>0.5um)	-9 to -35 °C
<b>Hoose et al., 2010</b>	Classical Nucleation Theory	Immersion, contact and deposition	- Ambient parameters - Temperature - Particle radius and nucleation ability - Activation energy	0 to -38 °C
<b>Niemand et al., 2012</b>	Surface dust samples. AIDA chamber.	Immersion	- Temperature - Aerosol number concentration per size bin - Particle surface area	-12 to -36 °C
<b>Atkinson et al., 2013</b>	Pure minerals. Droplet freezing and microscopy	Immersion	- Temperature (used to calculate $n_s$ in parametrisation) - Aerosol size distribution.	-5 to -25 °C
<b>Niedermeier et al., 2015</b>	1 pure feldspar sample, Leipzig Aerosol Cloud Interaction Simulator	Immersion	- Particle surface area. - Average active sites per droplet - Temperature - Probability of a drop being liquid. - Time - Material characteristics	-20 to -40 °C
<b>Peckhaus et al., 2016</b>	Surface feldspar samples, droplet freezing technique (cooling ramp and isothermal experiments)	Immersion	- Particle surface area - Temperature - Probability of a drop being liquid. - Time - Material characteristics	-2 to -38 °C

\*reported freezing mechanism may differ from measured freezing mechanism as understanding of heterogeneous ice nucleation has improved (Vali et al., 2015).

The site-specific deterministic approach assumes that there is a surface density of active sites on a particle that can initiate freezing below a characteristic temperature. Freezing will always occur as soon as the particle is cooled to this characteristic temperature regardless of particle history (Kanji et al., 2017). There is no time dependence. The simplicity of excluding a time

dependence means that such deterministic parameterisations are more common than stochastic parameterisations in atmospheric models. However, when applied in atmospheric models, extrapolation beyond their measured range from which they were calculated is required for many common deterministic parameterisations (Table 1.1) to represent all altitudes and temperatures, something which has been shown to produce unreliable results (Hoose and Möhler, 2012).

Site-specific deterministic approaches also assume that site density remains constant over the entire size distribution, i.e. small particles have the same probability of having an active site as large particles. However, some materials with high ice-nucleating ability show variations in composition with size (Perlwitz et al., 2015b) that may affect the ability of the deterministic approach to describe their site density (Kanji et al., 2017). Furthermore, while time is thought to be of secondary importance relative to temperature and aerosol properties for nucleation (Atkinson et al., 2013; Marcolli, 2014; Niemand et al., 2012; Wilson et al., 2015), it is known to play some role in determining when nucleation occurs and as such neglecting it completely is undesirable.

There are other issues with commonly used deterministic parameterisations, the impact of which is not understood. Parameterisations based on in cloud ice-crystal number concentrations, such as Cooper (1986) may be affected by ice precipitating from higher altitudes or ice produced via secondary ice production mechanisms (see Section 1.3.5). This would cause an overestimation of atmospheric INP number concentrations. The parameterisation of Meyers et al. (1992) is described as a deposition and condensation freezing parameterisation and is often used as such alongside an immersion freezing parameterisation in modelling studies (Deng et al., 2018; Fan et al., 2010b, 2010a; Gibbons et al., 2018). However, the method by which this parameterisation was derived, from aircraft continuous flow diffusion chamber measurements (Meyers et al., 1992), means that there is no reason to

believe the concentrations measured were from any particular mechanism of heterogeneous ice nucleation. As most ice crystals in convective clouds are generated from immersion freezing (Ansmann et al., 2008; De Boer et al., 2011; Westbrook and Illingworth, 2013), it is likely that the parameterisation actually describes immersion freezing. Studies that have used the Meyers et al. (1992) parameterisation alongside another immersion freezing parameterisation (Deng et al., 2018; Fan et al., 2010b, 2010a; Gibbons et al., 2018) may have inadvertently doubled their INP concentrations.

## **1.5. Effect of INP in convective clouds**

The effect of INP and changing INP number concentrations on convective clouds is poorly quantified. Studies finding both only minor and also major impacts on convective clouds have been reported. Some observational and modelling studies suggest that INP concentrations are not a key determinant of convective cloud properties, and the influence of secondary and homogeneous freezing far outweighs that of heterogeneous freezing. Observed ICNC has often exceeded INP number concentrations by orders of magnitude in clouds with warm ( $> -16$  °C) cloud top temperatures (Fridlind et al., 2007; Heymsfield and Willis, 2014; Ladino et al., 2017; Lawson et al., 2015) implying that INP concentrations are not a key determinant of cloud ICNC (Korolev et al., 2020; Ladino et al., 2017). In such cases secondary ice production has been cited as the most likely dominant ice production process. A ‘buffering’ effect is suggested whereby INP number concentrations are irrelevant beyond the threshold needed to initiate secondary freezing (Ladino et al., 2017; Phillips et al., 2007; Sullivan et al., 2018).

Some studies have shown that the concentration of primary ice needed to initiate the Hallett-Mossop process (Hallett and Mossop, 1974), the most well-known secondary production mechanism, is as low as  $0.01 \text{ L}^{-1}$  (Crawford et al., 2012; Huang et al., 2017), a concentration

that could be achieved via INP or homogeneous freezing. In deep convective clouds, where ice production by homogeneous freezing dominates (Phillips et al., 2005), secondary production may be primarily initiated by sedimenting homogeneously frozen crystals. Many field campaigns aiming to measure SIP target young convective clouds where sedimenting ice crystals are assumed not to be present (e.g. Lasher-Trapp et al., 2016; Lloyd et al., 2019) so the extent to which INP are important for initiating SIP in deep convective clouds is not known. Modelling by Sullivan et al. (2018) with a parcel model found that INP number concentration were much less important than CCN concentrations and thermodynamic conditions for the initiation of the Hallett-Mossop process and the consequent multiplication of cloud ice number concentrations.

On the other hand, some modelling studies indicate that changes in INP concentrations can cause substantial changes to cloud properties (Deng et al., 2018; Fan et al., 2010b; Gibbons et al., 2018). Heterogeneous freezing rates have been shown to contribute uncertainty to some cloud microphysical properties including ICNC along with updraft speed (Johnson et al., 2015b) and precipitation rates (Wellmann et al., 2018). Where changes to INP concentrations have been found to have a substantive impact on cloud properties, the results have frequently been conflicting. For example, increases in INP concentration have been shown to both increase (Fan et al., 2010b; Gibbons et al., 2018) and decrease (Gibbons et al., 2018) deep convective anvil extent, discrepancies which stem from INP having different microphysical effects in different case studies.

Increasing INP concentrations can lead to enhanced updrafts with greater freezing rates in the mixed-phase regime (Fan et al., 2010b; Gibbons et al., 2018) increasing transport of moisture to the anvil region. Conversely, increased INP freezing can consume liquid at lower altitude levels causing a reduction in transport of liquid to the homogeneous temperature regime with increased INP number concentration (van den Heever et al., 2006; Phillips et al., 2005, 2007).

Similarly, increases in INP concentration in deep convective clouds have been found to both increase or decrease anvil ICNCs (Fan et al., 2010b; Gibbons et al., 2018; van den Heever et al., 2006; Phillips et al., 2005, 2007), convective rainfall (Gibbons et al., 2018; Rosenfeld et al., 2011), the size and number of snow particles (Gibbons et al., 2018) and cloud radar reflectivity (Gibbons et al., 2018; Min et al., 2009).

The effect of INP in deep convective clouds can be dependent on other cloud and environmental properties. The CCN number concentration can affect both the availability of supercooled droplets for heterogeneous freezing, and their droplet size, which affects the efficiency of heterogeneous freezing, and subsequently the riming efficiency of frozen hydrometeors (Altaratz et al., 2014). Higher CCN number concentrations lead to a reduced warm rain process and a subsequent reduction of rain drops available to become instant rimers within the heterogeneous and Hallett-Mossop ice production regimes (Phillips et al., 2002). A stronger warm rain process and the resultant enhancement in latent heat release from rain freezing, riming and ice depositional growth can also cause cloud invigoration, which can increase rates of heterogeneous and homogeneous freezing at upper cloud altitudes (Altaratz et al., 2014; Fan et al., 2007).

The interaction of cloud dynamics, microphysics and different freezing mechanisms can also be important for deep convectively generated anvils causing implications for climate (due to the persistence of anvil clouds in the atmosphere long after the convective clouds that forms them have decayed (Luo and Rossow, 2004)). For example, Heymsfield et al. (2005) found that different ice particle size distributions exist in the anvil and convective core of a deep convective cloud depending on whether cloud updrafts are low enough to allow the suppression of homogeneous ice formation due to the diffusional and accretional growth of large graupel or ice crystals formed at mixed-phase temperatures.

The global radiative effect of INP due to impacts on cloud phase has been estimated globally, the results have been inconclusive with different results for different models (DeMott et al., 2010; Komurcu et al., 2014; Shi and Liu, 2019; Storelvmo et al., 2011) and the radiative impact of changing INP number concentrations in convective clouds is not well understood. Analysis of observational satellite data suggests that outgoing longwave radiation in the maritime tropics may be reduced by up to  $16 \text{ W m}^{-2}$  due to INP particles shifting cloud glaciation to higher temperatures, but this may not be the case in deep convective clouds with ice water paths exceeding  $40 \text{ g m}^{-2}$  (Min and Li, 2010).

Furthermore, most studies of INP impacts on deep convective clouds have focused on the impact of increasing INP number concentrations (Carrió et al., 2007; Connolly et al., 2006; Deng et al., 2018; Ekman et al., 2007; Fan et al., 2010a; Gibbons et al., 2018; van den Heever et al., 2006; Phillips et al., 2005) but global simulations and experiments on Antarctic mixed-phase clouds indicate that INP parameterisation choice can have a large impact on cloud radiative effects (e.g. DeMott et al., 2010; Vergara-Temprado et al., 2018). The differences between parameterisations that use the same aerosol number concentrations are the intercept term (the ice-nucleating ability or particle number at  $0^\circ\text{C}$ ) and the temperature dependence of the INP number concentrations, i.e.  $\text{dlog}_{10}[\text{INP}]/\text{dT}$  (referred throughout this thesis as the slope of the INP parameterisation).

Aerosol type and efficiency determines the INP parameterisation slope: marine organic INP are more efficient at warm temperatures than mineral dust INP and as a result have a shallower slope (Atkinson et al., 2013; Niemand et al., 2012; Wilson et al., 2015). In a simulated cloud, different temperature dependencies between INP parameterisations causes changes in the ice crystal formation and droplet depletion with altitude with implication for cloud microphysical responses (Takeishi and Storelvmo, 2018). The role of INP temperature dependence in deep convective clouds is not well understood despite its potential importance for cloud properties.

For example, INP with high efficiencies at warm temperatures (or shallow INP parameterisation slopes), such as marine organics (Wilson et al., 2015), may exert substantial control over cloud properties via their role in initiating SIP mechanisms (Crawford et al., 2012; Huang et al., 2017; Sullivan et al., 2018) despite these aerosol types having a lower atmospheric prevalence than mineral dust (Vergara-Temprado et al., 2017)

## **1.6. Research questions**

### **1.6.1. Chapter 2: The effect of INP parameterisation choice on the radiative properties of a complex deep convective cloud field**

Firstly, this thesis will address the effect of INP and INP parameterisation choice on tropical convection. Convective cloud systems in the maritime tropics play a critical role in global climate and weather, but accurately representing mixed-phase ice processes within these clouds persists as a major challenge for weather and climate modelling. In Chapter 2, I use a regional model with an advanced double-moment microphysics scheme to quantify the effect of INP on the radiative properties of a complex tropical Atlantic deep convective cloud field. This work aims to elucidate the relative importance of heterogeneous and secondary ice production for tropical convective clouds. The specific questions addressed by Chapter 2 are:

- a) What is the radiative effect of INP and INP parameterisation choice in a complex tropical convective cloud field?
- b) What is the effect of SIP (via the Hallett-Mossop process) and its interaction with INP parameterisation choice on the outgoing radiation of the cloud field?
- c) What is the relative importance of INP and SIP (via the Hallett-Mossop process) for the radiative properties of a complex convective cloud field?

## **1.6.2. Chapter 3: Influence of ice-nucleating particles and Hallett-**

### **Mossop ice production rates on anvil cirrus from deep convection**

Secondly, this thesis will examine the relative importance of absolute INP number concentration, the temperature dependency of INP number concentration (or INP parameterisation slope), and the rate of splinter production by the Hallett-Mossop process in determining the anvil properties of an idealised deep convective cloud. The formation of ice crystals in the mixed phase cloud region is important for deep convective cloud glaciation and anvil properties (Deng et al., 2018; Fan et al., 2013; Gibbons et al., 2018), which are crucial in determining the overall cloud radiative effect of deep convective clouds. New ice-crystals are formed in the mixed-phase cloud region by heterogeneous ice nucleation and SIP, for example, by the Hallett-Mossop process. The representation of these ice formation processes is highly uncertain. In this study, I use Latin hypercube sampling and statistical emulation to investigate the joint impact of INP absolute number concentration, INP temperature dependence, and the Hallett-Mossop ice production rate for the anvil properties of an idealised deep convective cloud. This work aims to further our fundamental understanding of mixed-phase ice processes in deep convective clouds and determine the potential importance of accurate representation of these processes for cloud anvil and radiative properties. The specific questions addressed by Chapter 3 are:

- a) How does INP number concentration, INP parameterisation slope, and Hallett-Mossop splinter production rate affect the anvil properties of an idealised deep convective cloud?
- b) What is the relative importance of INP number concentration, INP parameterisation slope, and Hallett-Mossop splinter production rate for the development and resultant anvil properties of an idealised deep convective cloud?

- c) Are statistical emulation and variance-based sensitivity analysis useful tools for the assessment of uncertainty in parameterisations of mixed-phase ice formation in deep convective clouds?

### **1.6.3. Chapter 4: Simulation of dust and K-feldspar INP transport across the tropical Atlantic by a global aerosol model**

Lastly, this thesis will examine the ability of the Global Model of Aerosol Processes (GLOMAP), a global aerosol model, to represent dust and INP transport across the tropical Atlantic. The accurate representation of heterogeneous ice nucleation in global models relies on accurate emission and transport of ice-nucleating aerosols such as mineral dust. In Chapter 4, INP number and dust mass concentrations simulated by GLOMAP are compared to field measurements and possible sources of error within the model are explored. Specifically, Chapter 4 will address the following questions:

- a) How well does the GLOMAP aerosol model simulate the INP number concentrations measured during the 2017 Barbados Ice-nucleating particle Concentration Experiment field campaign at Ragged Point, Barbados?
- b) Can discrepancies between measured and GLOMAP simulated INP number concentrations be attributed to discrepancies between measured and simulated dust export from North Africa over the tropical Atlantic?
- c) Can discrepancies between measured and GLOMAP simulated INP number concentrations be attributed to discrepancies between the measured and simulated feldspar content of aerosol?



## Chapter 2: The effect of INP parameterisation choice on the radiative properties of a complex deep convective cloud field

Chapter 2 is based on collaborative work from the journal article “Hawker, R., Miltenberger, A., Wilkinson, J., Hill, A., Shipway, B., Cui, Z., Cotton, R., Carslaw, K., Field, P. and Murray, B.: The temperature dependence of ice-nucleating particle concentrations affects the radiative properties of tropical convective cloud systems, *Atmos. Chem. Phys.*, 21(7), 5439–5461, doi:10.5194/acp-21-5439-2021, 2021.” which is published in the journal ‘*Atmospheric Chemistry and Physics*’. The candidate is the lead author and the full author list is as follows:

**Rachel E. Hawker<sup>\*1</sup>, Annette K. Miltenberger<sup>2</sup>, Jonathan M. Wilkinson<sup>3</sup>, Adrian A. Hill<sup>3</sup>, Ben J. Shipway<sup>3</sup>, Zhiqiang Cui<sup>1</sup>, Richard J. Cotton<sup>3</sup>, Ken S. Carslaw<sup>1</sup>, Paul R. Field<sup>1, 3</sup>, Benjamin J. Murray<sup>1</sup>**

1. Institute for Climate and Atmospheric Science, University of Leeds, Leeds, LS2 9JT, United Kingdom.

2. Institute for Atmospheric Physics, Johannes Gutenberg University Mainz, Mainz, 55128, Germany.

3. Met Office, Exeter, EX1 3PB, United Kingdom.

Author contributions: Rachel E. Hawker, Annette K. Miltenberger, Ken S. Carslaw, Paul R. Field and Ben J. Murray contributed to the design, development and direction of the study. Rachel E. Hawker and Annette K. Miltenberger set up and ran the UM-CASIM simulations presented in the paper. Rachel E. Hawker processed and analysed the UM-CASIM datasets and compared the simulation data to observations. Jonathan M. Wilkinson, Adrian A. Hill and Ben J. Shipway built and maintained the Met-Office CASIM model used to run the simulations. Zhiqiang Cui and Richard J. Cotton provided processed aircraft data from the ICE-D b933 flight and helped with the comparison of model data with aircraft measurements. Rachel E. Hawker wrote the chapter and the associated paper. Rachel E. Hawker, Annette K. Miltenberger, Jonathan M. Wilkinson, Adrian A. Hill, Zhiqiang Cui, Richard J. Cotton, Ken S. Carslaw, Paul R. Field and Ben J. Murray edited the manuscript.

## 2.1. Abstract

Convective cloud systems in the maritime tropics play a critical role in global climate, but accurately representing aerosol interactions within these clouds persists as a major challenge for weather and climate modelling. We quantify the effect of ice-nucleating particles (INP) on the radiative properties of a complex tropical Atlantic deep convective cloud field using a regional model with an advanced double-moment microphysics scheme. Our results show that the domain-mean daylight outgoing radiation varies by up to  $18 \text{ W m}^{-2}$  depending on the chosen INP parameterisation. The key distinction between different INP parameterisations is the temperature dependence of ice formation, which alters the vertical distribution of cloud microphysical processes. The controlling effect of the INP temperature dependence is substantial even in the presence of Hallett-Mossop secondary ice production and the effects of secondary ice formation depend strongly on the chosen INP parameterisation. Our results have implications for climate model simulations of tropical clouds and radiation, which currently do not consider a link between INP particle type and ice water content. The results also provide a challenge to the INP measurement community, since we demonstrate that INP concentration measurements are required over the full mixed-phase temperature regime, which covers around 10 orders of magnitude in INP concentration.

## 2.2. Introduction

Deep convective clouds are important drivers of local, regional and global climate and weather (Arakawa, 2004; Lohmann et al., 2016). They produce substantial precipitation (Arakawa, 2004) and the associated phase changes release latent heat that helps to drive global atmospheric circulation (Fan et al., 2012). Convective clouds have a direct impact on climate through interactions with incoming shortwave and outgoing longwave radiation (Lohmann et al., 2016), for example by producing radiatively important long-lived cirrus clouds (Luo and Rossow, 2004). The clouds extend from the warmer lower levels of the atmosphere where only liquid exists to the top of the troposphere where only ice exists (Lohmann et al., 2016). Between these levels is the mixed-phase region where both liquid and ice coexist and interact (Seinfeld and Pandis, 2006). Within the mixed-phase region, primary ice particles can form heterogeneously through the freezing of cloud droplets by ice-nucleating particles (INP). The importance and relative contribution of heterogeneous freezing to ice crystal number concentrations (ICNC) and resultant cloud properties, such as cloud reflectivity, is very uncertain (Cantrell and Heymsfield, 2005; Kanji et al., 2017). This uncertainty stems from the difficulty of predicting INP number concentrations (Kanji et al., 2017; Lacher et al., 2018) as well as the difficulty of quantifying complex interactions between heterogeneous freezing and other ice production mechanisms (Crawford et al., 2012; Huang et al., 2017; Phillips et al., 2005).

Understanding the effects of INP on convective clouds presents substantial challenges. Measurements indicate that INP number concentrations can vary by as much as six orders of magnitude at any one temperature due to variations in, for example, aerosol source, chemical or biological composition, surface morphology and degree of chemical weathering (DeMott et al., 2010; Kanji et al., 2017). Large variability exists even in measurements of individual regions or aerosol populations (Boose et al., 2016b; Kanji et al., 2017; Lacher et al., 2018). For

example, there are four orders of magnitude variation in summertime measurements of INP number concentrations in the Saharan Air Layer at  $-33^{\circ}\text{C}$  (Boose et al., 2016b). Even for particles of similar and known mineralogy, measurements of ice-nucleation efficiency can span several orders of magnitude: The spread in laboratory measurements of ice nucleation active site densities ( $n_s$ ) for different types of feldspar spans seven orders of magnitude at  $-15^{\circ}\text{C}$  (Atkinson et al., 2013; Harrison et al., 2016, 2019; Peckhaus et al., 2016). Our ability to understand and quantify such variability in INP concentrations has improved as more measurements have been made. Although INP concentrations do not simply correlate with meteorological variables such as pressure and temperature (Boose et al., 2016a; Lacher et al., 2018; Price et al., 2018), aerosol surface area (Lacher et al., 2018) and diameter (DeMott et al., 2015) provide some predictability and global models based on known INP-active materials show reasonable skill in simulating global INP concentrations (Shi and Liu, 2019; Vergara-Temprado et al., 2017).

It is known from model simulations that changes in INP number concentration affect the microphysical properties and behaviour of deep convective clouds (Deng et al., 2018; Fan et al., 2010a, 2010b; Gibbons et al., 2018; Takeishi and Storelvmo, 2018). However, in these model studies perturbations to INP number concentrations have predominantly involved uniform increases in aerosol or INP concentrations with all simulations using the same INP parameterisation (Carrió et al., 2007; Connolly et al., 2006; Deng et al., 2018; Ekman et al., 2007; Fan et al., 2010a; Gibbons et al., 2018; van den Heever et al., 2006; Phillips et al., 2005), i.e. the temperature dependence of INP number concentrations has not been altered. Where different INP parameterisations have been used (Eidhammer et al., 2009; Fan et al., 2010b; Liu et al., 2018; Takeishi and Storelvmo, 2018), the results have in most cases been interpreted in terms of the overall increase in INP number concentration (Fan et al., 2010b; Liu et al., 2018; Takeishi and Storelvmo, 2018).

However, there are important structural differences between different INP parameterisations that have not yet been explored in detail. For example, currently available and regularly used parameterisations of INP vary substantially in the dependence of INP activity on temperature. We hypothesise that the difference in the temperature dependence of INP number concentrations between parameterisations will be particularly important for deep convective clouds because heterogeneous ice formation occurs over a very wide temperature range from just below 0 to around  $-38^{\circ}\text{C}$  in the mixed-phase region of these clouds. For the same dust particle concentration, predicted INP concentrations can increase by up to three orders of magnitude from  $-15$  to  $-20^{\circ}\text{C}$  (corresponding to approximately 1 km altitude change) using an INP parameterisation with a steep temperature dependence (lower INP concentrations at high temperatures and higher INP concentrations at low temperatures) (Atkinson et al., 2013), but by less than one order of magnitude using an INP parameterisation with a shallower dependence (DeMott et al., 2010; Meyers et al., 1992). We hypothesise that such large differences in ice production rates between INP parameterisations are likely to affect cloud properties. In simulations of deep convective clouds over North America (Takeishi and Storelvmo, 2018) there were differences in the magnitude and altitude of droplet depletion depending on INP parameterisation choice (Bigg, 1953; DeMott et al., 2010, 2015).

Uncertainty in mixed-phase cloud properties is compounded further by a lack of quantification of the interaction of heterogeneous freezing with other ice production mechanisms. Ice crystals in the mixed-phase region can also be formed by secondary ice production (SIP) from existing hydrometeors (Field et al., 2017) and droplets can freeze homogeneously below around  $-33^{\circ}\text{C}$  (Herbert et al., 2015). In observations of convective clouds with relatively warm cloud-top temperatures (Fridlind et al., 2007; Heymsfield and Willis, 2014; Ladino et al., 2017; Lasher-Trapp et al., 2016; Lawson et al., 2015), ICNC has frequently exceeded INP number concentrations by several orders of magnitude, suggesting that secondary ice production is the

dominant small-ice formation mechanism in mixed-phase regions (Ladino et al., 2017). The importance of heterogeneous ice production relative to secondary and homogeneous freezing has therefore been questioned (Ladino et al., 2017; Phillips et al., 2007) and it has been proposed that INP concentrations may only be relevant up to a threshold needed to initiate SIP (Ladino et al., 2017; Phillips et al., 2007), a value that may be as low as  $0.01 \text{ L}^{-1}$  (Crawford et al., 2012; Huang et al., 2017) for the Hallett-Mossop process (Hallett and Mossop, 1974). If this is the case, in clouds where SIP may also be initiated by the primary freezing of a few large ( $\sim 1 \text{ mm}$ ) droplets in a rising parcel (Field et al., 2017), INP number concentrations may be largely irrelevant to cloud ice properties. The effect of INP and INP parameterisation on convective cloud properties must therefore be examined with consideration for the presence of, and interactions with, SIP.

Here we explore how the choice of INP parameterisation affects the properties of a large and realistic cloud field containing clouds at all levels as well as deep convective systems in the eastern tropical Atlantic with a focus on the top of atmosphere (TOA) outgoing radiation. The eastern tropical Atlantic is an ideal location in which to examine the role of INP concentrations in convective cloud systems because, owing to its position at the interface between the Saharan Air Layer and the Inter Tropical Convergence Zone, it is subject to both high levels of convective activity and high loadings of desert dust, a relatively well-defined INP type (e.g. DeMott et al., 2003; Niemand et al., 2012; Price et al., 2018).

The chapter is structured as follows: Section 2.3 details our model set-up and the case study our simulations are based on. Section 2.4 presents our results. First, we determine how the presence of INP alters the radiative properties of the cloud field (Section 2.4.1). We then examine how the properties of the simulated cloud field, including cloud shortwave reflectivity (Section 2.4.2), cloud fraction (Section 2.4.3) and anvil extent (Section 2.4.4), depend on the choice of INP parameterisation. In particular, we examine the importance of the dependence

of INP number concentration on temperature, referred to as INP parameterisation slope herein, as a major factor that determines cloud properties. We also examine the effect on cloud properties of the inclusion of SIP due to the Hallett-Mossop process (Section 2.4.5). Section 2.5 details the limitations of this study and Section 2.6 discusses the study conclusions and the outlook for the future.

## **2.3. Methods**

### **2.3.1. Model set-up**

#### **2.3.1.1. Regional domain and initial conditions**

Simulations described in this chapter were performed using the Unified Model (UM) version 10.8 (GA6 configuration) (Walters et al., 2017). The UM is a numerical weather prediction model developed by the UK Met Office. We use a regional nest within the global model simulation (Figure 2.1a), which has a grid spacing of 1 km (900\*700 grid points) and 70 vertical levels. Meteorology of the driving global model is based on operational analysis data. Within the nested domain, the Cloud AeroSol Interacting Microphysics scheme (CASIM) is employed to handle cloud microphysical properties. A global model simulation (UM vn 8.5, GA6 configuration, N512 resolution (Walters et al., 2017)) is used to initialise the nested simulation at 00:00 on the 21st of August 2015 and is used throughout the simulation for the boundary conditions.

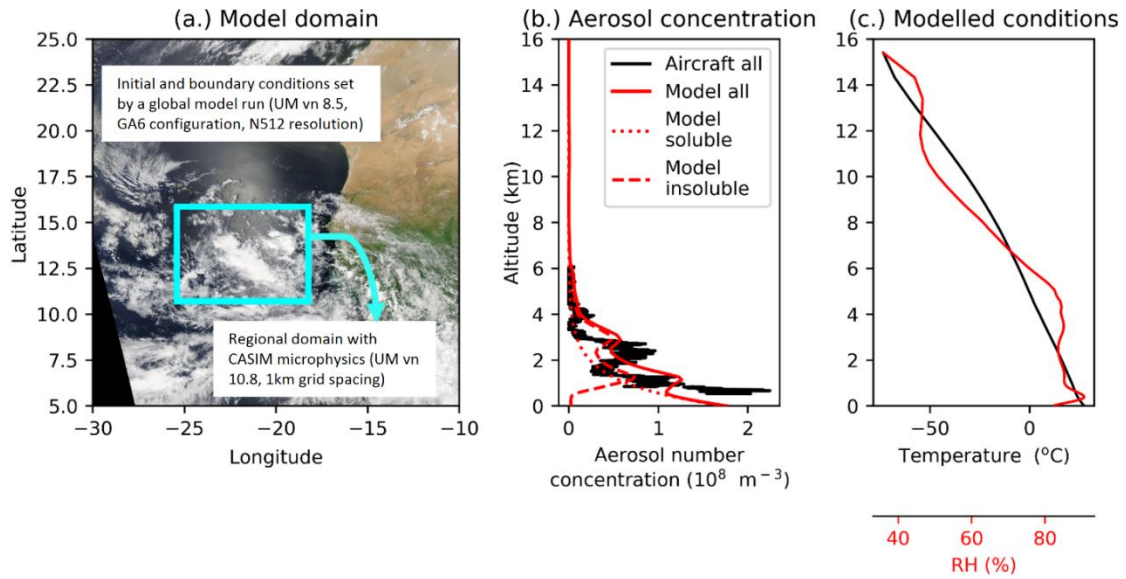


Figure 2.1. Modelled domain location and resolution details (a), observed (black line) and modelled (red lines) aerosol concentrations (b), and mean modelled domain-mean temperature and relative humidity profiles (c). The observed aerosol profile shown in b was measured using the Passive Cavity Aerosol Spectrometer Probe (PCASP) which captures aerosols between  $0.1$  and  $3\mu\text{m}$  in size. The insoluble aerosol profile shown in b is extracted from a regional UM v10.3 simulation (8 km grid spacing, CLASSIC dust scheme). The modelled aerosol profiles are applied throughout the regional domain shown in (a) at the start of the simulation (00:00 21<sup>st</sup> August 2015) and at the boundaries throughout. INP concentrations in the D10, N12 and A13 simulations are linked to the insoluble aerosol profile shown in b. The image shown in (a) is moderate resolution imaging spectroradiometer (MODIS) Corrected Reflectance imagery produced using the MODIS Level 1B data and downloaded from the NASA Worldview website.

The 21st of August 2015 was chosen for simulation to coincide with flight b933 of the Ice in Clouds Experiment – Dust (ICE-D) July-August 2015 field campaign that targeted convective clouds extending to and beyond the freezing level. The aerosol profile measured during flight b933 (Figure 2.1b) was used to derive the aerosol profiles prescribed over the nested domain at the beginning of the simulation and are constantly applied at the boundaries. Model profiles were calculated as follows: The UM v10.3 was used to simulate a domain comprising the entire tropical Atlantic and West Africa. This simulation was initiated on the 18<sup>th</sup> August 2015

with a grid spacing of 8 km using the UM operational one-moment microphysics (i.e. not CASIM) and the CLASSIC aerosol scheme with a 6-bin dust model (Johnson et al., 2015a). On the day of the b933 flight (21<sup>st</sup> August 2015), a dust layer was present between 2 and 3 km altitude. Comparison to MODIS AOD data indicates agreement between the model and observations (not shown). This UM v10.3 simulation was used to calculate the average dust profile (mass and number concentration) over the CASIM domain on the 21<sup>st</sup> of August 2015 and these dust profiles are applied in the nested domain as the insoluble aerosol profiles (Figure 2.1b). The approximate difference between the dust aerosol profile provided by the UM regional simulation and the observed aerosol profile measured during flight b933 (comprising both insoluble and soluble particles) is used as the soluble aerosol profile (Figure 2.1b). The profiles shown in Figure 2.1b and applied in our simulations represent our best estimate of the aerosol environment within which the clouds sampled during flight b933 of the ICE-D campaign formed. However, as the atmosphere is heterogeneous with many coexisting air masses, it is possible that the aerosol profiles were measured in a separate air mass to those in which the clouds formed. The inability to sample the exact air mass in which sampled clouds formed, due to instrumental limitations and the fact that the aerosol environment is disturbed by the cloud formation, is a key limitation of modelling studies linked to observational campaigns. The simulations are 24 hours in length.

### **2.3.1.2. CASIM microphysics**

CASIM is a multi-moment bulk scheme, which is configured to be two-moment in this work. Both number concentration and mass concentration for each of the five hydrometeor classes (cloud droplets, rain droplets, ice crystals (or cloud ice), graupel, snow) are prognostic variables. The model set-up is very similar to that used in Miltenberger et al. (2018) including

the parameter choices within CASIM. CASIM has been used and tested previously in simulations of coastal mixed-phase convective clouds (Miltenberger et al., 2018b), South-East Pacific stratocumulus clouds (Grosvenor et al., 2017), Southern Ocean supercooled shallow cumulus (Vergara-Temprado et al., 2018), midlatitude cyclones (McCoy et al., 2018) and CCN-limited Arctic clouds (Stevens et al., 2018).

Cloud droplet activation is parameterised according to Abdul-Razzak and Ghan (2000). The soluble accumulation mode aerosol profile shown in Figure 2.1b is used for cloud droplet activation and a simplistic CCN activation parameterisation is included for the insoluble aerosol mode (Abdul-Razzak and Ghan, 2000) that assumes a 5% soluble fraction on dust. Scavenging of CCN or INP is not represented. Condensation is represented using saturation adjustment meaning that where liquid is present at the end of a timestep, the specific humidity is adjusted to be the equilibrium saturation over water and the grid box temperature and liquid mass is adjusted accordingly. If only frozen hydrometeors are present in a grid box, saturation is treated explicitly. Collision-coalescence, riming of ice crystals to graupel and aggregation of ice crystals to snow is represented. Rain drop freezing is described using the parameterisation of Bigg (1953). Deposition onto ice is treated explicitly allowing ice particles to grow in the presence of liquid. However, due to the saturation adjustment treatment of condensation, the Wegener-Bergeron-Findeisen process is not present in exactly the same way as one would expect in a real cloud. For reference, the modelled domain-mean out-of-cloud temperature and relative humidity are shown in Figure 2.1c. The model time-step is 5 seconds.

Heterogeneous ice nucleation is represented using 5 different parameterisations: Cooper (1986) (C86), Meyers et al. (1992) (M92), DeMott et al. (2010b) (D10), Niemand et al. (2012) (N12) and Atkinson et al. (2013) (A13) (Figure 2.2). C86 and M92 calculate an INP number concentration based on temperature and are independent of aerosol concentration. D10 calculates an INP number concentration from temperature and the number concentration of

insoluble dust aerosol with a diameter greater than  $0.5 \mu\text{m}$ . N12 and A13 calculate an INP concentration from the temperature dependent active surface site density and the surface area of insoluble dust aerosol ( $n_s$ ). For A13, a potassium-feldspar fraction of 0.25 is assumed. This is the upper recommended fraction (Atkinson et al., 2013) which was deemed appropriate because of the study region's exposure to Saharan dust outflow.

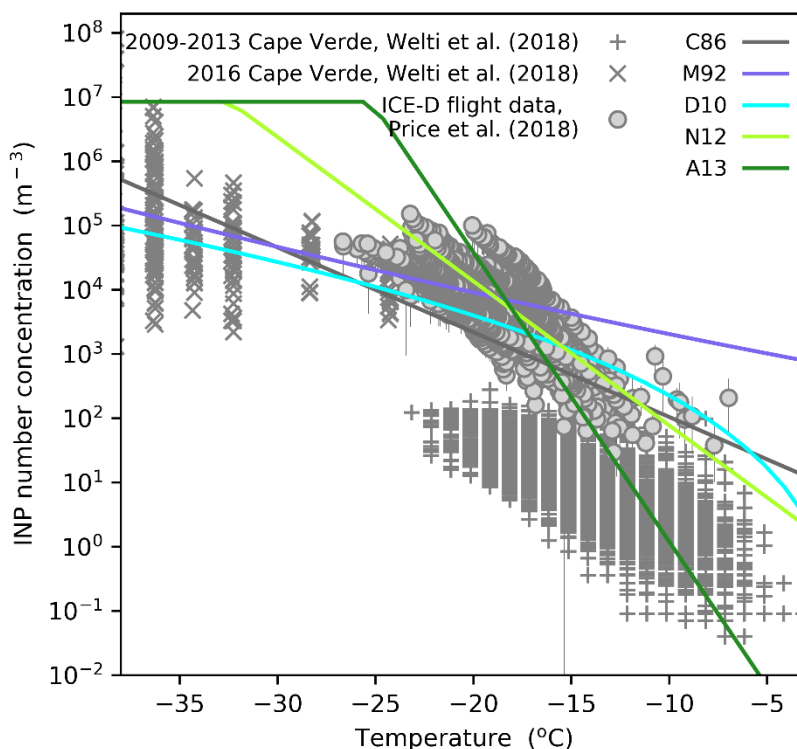


*Figure 2.2. The five heterogeneous freezing parameterisations tested in this study (C86, M92, D10, N12, A13) compared to INP number concentrations measured in the eastern tropical Atlantic (Price et al., 2018; Welte et al., 2018). Parameterisations are shown for the aerosol concentrations at approximately the first freezing level in our simulations ( $\sim 8 \text{ cm}^{-3}$ ). D10, N12 and A13 are dependent on aerosol concentrations, while C86 and M92 are not dependent on aerosol concentration.*

M92 is described as a deposition and condensation freezing parameterisation (Meyers et al., 1992) and is often used alongside an immersion freezing parameterisation in modelling studies (Deng et al., 2018; Fan et al., 2010b, 2010a; Gibbons et al., 2018). However, the M92

parameterisation is based on aircraft continuous flow diffusion chamber measurements and those measurements should capture all relevant nucleation mechanisms (see Vali et al., 2015). To represent nucleation at conditions relevant for clouds with liquid water present, we have set the saturation term in the M92 parameterisation to water saturation. One simulation is conducted with no active heterogeneous ice nucleation representation (NoINP).

The INP parameterisations inspect the conditions (temperature, cloud droplet number, ICNC) and aerosol concentrations within a gridbox and use that information to predict an ice production rate via heterogeneous freezing. The supercooled droplets are depleted by the freezing parameterisation, but scavenging of INPs is not represented. Homogeneous freezing of cloud droplets is parameterised according to Jeffery and Austin (1997). Secondary ice production (SIP) is represented using an approximation of the Hallett-Mossop process which occurs between  $-2.5$  and  $-7.5^{\circ}\text{C}$ . The efficiency of the Hallett-Mossop process increases from  $-2.5$  and  $-7.5^{\circ}\text{C}$  to 100% at  $-5^{\circ}\text{C}$ . The ice splinters produced by the representation of the Hallett-Mossop process are the smallest allowable size of ice in the model (i.e.  $10^{-18}$  kg, volume radius  $\sim 0.11$   $\mu\text{m}$ ). Splinters are produced from rime mass of snow and graupel.

The rate of splinter production per rimed mass is prescribed with 350 new ice splinters produced per milligram of rime at  $-5^{\circ}\text{C}$ . This rate of splinter production by the Hallett-Mossop process is based on the best available estimate of the efficacy of the mechanism (Connolly et al., 2006; Hallett and Mossop, 1974; Mossop, 1985). A maximum splinter production rate of 350 per milligram of rimed material has been measured in a number of laboratory studies (Hallett and Mossop, 1974; Mossop, 1985) and has been applied as the best estimate of Hallett-Mossop ice production in previous modelling studies (Connolly et al., 2006), although other rates have also been measured (Heymsfield and Mossop, 1984; Saunders and Hosseini, 2001). In-situ cloud observations have frequently observed ICNC that could be explained by the Hallett-Mossop process, but the mechanism underlying the Hallett-Mossop process as well as

the ice particle production rate remain uncertain and not well quantified (Field et al., 2017). Uncertainties regarding the rate of splinter production by Hallett-Mossop are an important consideration that will be investigated in Chapter 3; this chapter however study only explores the structural uncertainty of the presence/absence of the Hallett-Mossop process as currently understood. Other mechanisms of SIP such as collision fragmentation, droplet shattering and sublimation fragmentation have been proposed (Field et al., 2017), but are not represented in these simulations, in part because they are very poorly defined and it is not clear how important they are. Other studies have attempted to model some of these additional SIP processes (Phillips et al., 2018; Sullivan et al., 2018) but that was beyond the scope of this study.

### **2.3.1.3. Cloud radiation**

The radiative processes are represented by the Suite of Community RAdiative Transfer codes based on Edwards and Slingo (SOCRATES) (Edwards and Slingo, 1996; Manners et al., 2017), which considers cloud droplet number and mass, as well as ice crystal and snow water paths for the calculation of cloud radiative properties. It does not explicitly consider changes in ice crystal or snow number concentration or size (though changes in number and size will affect mass concentrations which are considered), and does not consider any changes to rain or graupel species. The cloud droplet single scattering properties are calculated from the cloud droplet mass and effective radius in each gridbox using the equations detailed in Edwards and Slingo (1996). Snow and ice are combined to form one ice category for the purposes of the radiation calculations. The single scattering properties of this snow and ice category are calculated from their combined mass and the ambient temperature. The parameterisation of bulk optical properties of snow and ice used in the model is detailed in Baran et al. (2014).

The radiative properties (shortwave, longwave and total radiation) are calculated for daylight hours only, i.e. 10:00-17:00 UTC. This is because owing to the length of our simulation (24 hours), when spin-up time is excluded from the analysis, there isn't a full night-time period available. Therefore, we felt it was fairest to calculate the radiative effects from the simulation period comprising the daylight hours only. For all other modelled properties presented, except when plotted against a corresponding radiative property, values are calculated for the last 14 hours of the simulation, i.e. from 10:00 - 24:00. The sensitivity of analysis to time period selection was tested and found to have little impact.

Changes to outgoing radiation from cloudy regions and changes in cloud fraction both contribute to the total overall change in outgoing radiation between two simulations. The contributions from changes in outgoing radiation from cloudy regions and cloud fraction to the overall radiative differences between simulations were calculated separately as described below. The cloudy regions contribution, i.e. the difference in outgoing radiation between two cloudy regions due to changes in cloud albedo or thickness ignoring any changes in cloud fraction, ( $\Delta Rad_{REFL}$ ) to a domain radiative difference between a sensitivity simulation (s) and a reference simulation (r) ( $s - r$ ) is calculated using Eq. (1).

$$\Delta Rad_{REFL} = cf_r \times \Delta Rad_{cl} \quad (1)$$

where  $cf_r$  is the cloud fraction of simulation r and  $\Delta Rad_{cl}$  is the change in outgoing radiation from cloudy areas only between simulations ( $s - r$ ). The reference run (r) in Sections 2.4.1 – 2.4.4 refers to the NoINP simulation while the sensitivity run (s) are simulations which include an INP parameterisation. In Section 2.4.5, the reference run (r) refers to a simulation which has no representation of SIP and the sensitivity run (s) to a simulation which includes SIP due to the Hallett-Mossop process. The contribution of cloud fraction changes, i.e. the change in radiation that can be attributed to an area of clear sky in simulation s becoming cloudy in

simulation r or vice versa, to the total change in domain outgoing radiation ( $\Delta Rad_{CF}$ ) is calculated using Eq. (2).

$$\Delta Rad_{CF} = (Rad_{r,cl} - Rad_{r,cs}) \times \Delta cf \quad (2)$$

Where  $Rad_{r,cl}$  is the mean outgoing radiation from cloudy regions in simulation r and  $Rad_{r,cs}$  is the mean outgoing radiation from clear sky regions in simulation r and  $\Delta cf$  is the difference in domain cloud fraction between simulations s and r (s-r). There is interaction between the outgoing radiation from cloudy regions and cloud fraction changes ( $\Delta Rad_{INT}$ ) which is calculated in Eq (3).

$$\Delta Rad_{INT} = \Delta Rad_{cl} \times \Delta cf + \Delta Rad_{cs} \times (1 - cf_s) \quad (3)$$

Where  $\Delta Rad_{cs}$  is the change in mean outgoing radiation from clear sky areas between simulations s and r and  $cf_s$  is the cloud fraction of simulation s.

The total outgoing radiation difference between simulations s and r ( $\Delta Rad_{s-r}$ ) is therefore calculated as shown in Eq. (4).

$$\Delta Rad_{s-r} = Rad_s - Rad_r = \Delta Rad_{REFL} + \Delta Rad_{CF} + \Delta Rad_{INT} \quad (4)$$

The interaction term  $\Delta Rad_{INT}$  was found to be negligible and was therefore ignored for the purpose of this paper.

#### 2.3.1.4. Model simulations

The conducted simulations are as follows:

- Five simulations with different heterogeneous ice nucleation parameterisations (C86, M92, D10, N12 and A13) ((Figure 2.2) with a representation of the Hallett-Mossop process (SIP active).

- One simulation with no heterogeneous ice nucleation (NoINP), but with a representation of the Hallett-Mossop process (SIP active).
- Five simulations with different heterogeneous ice nucleation parameterisations (C86, M92, D10, N12 and A13) (Figure 2.2.) without a representation of the Hallett-Mossop process (SIP inactive).

The INP number concentration ([INP]) predicted by the five INP parameterisations (C86, M92, D10, N12, A13) are compared with the available measurements from the study region (Price et al., 2018; Welti et al., 2018) in Figure 2.2, including those taken during the ICE-D field campaign (Price et al., 2018). All parameterisations are in reasonable agreement with the measurements (and with each other) at around  $-17^{\circ}\text{C}$ , but deviate strongly at higher and lower temperatures. It should be noted that all parameterisations tested in this work were developed between specific temperature ranges and extrapolation beyond these temperatures adds uncertainty. However, for the purposes of this paper and to allow a direct comparison between parameterisations, all parameterisations have been applied between  $0$  and  $-37^{\circ}\text{C}$ . Importantly, the INP parameterisation slopes of the chosen parameterisations span the range used within regional models (from a shallow  $d\log_{10}[\text{INP} (\text{m}^{-3})]/dT(^{\circ}\text{C}) = -0.07$  in M92 (Meyers et al., 1992) to a steep  $d\log_{10}[\text{INP}(\text{m}^{-3})]/dT (^{\circ}\text{C}) = -0.45$  in A13 (Atkinson et al., 2013)). For the correlation analysis where model outputs were plotted against parameterisation slope ( $d\log_{10}[(\text{m}^{-3})]/dT(^{\circ}\text{C})$ ), a straight line was fitted to the D10 parameterisation between  $-3$  and  $-37^{\circ}\text{C}$  to obtain an approximate INP parameterisation slope. Other temperature ranges were tested and were found to have no notable effect on results.

When analysing the simulation output, cloudy grid boxes were classed as those containing more than  $10^{-5} \text{ kg kg}^{-1}$  condensed water from cloud droplets, ice crystals, graupel and snow. Rain was not included to ensure analysis did not include areas below cloud base. Other cloud thresholds were tested and found to have no notable effect on the results. For cloud

categorisation into low, mid and high clouds, model vertical columns containing cloudy grid boxes were categorised by cloud altitude. Low cloud occurs below 4km, mid cloud between 4 and 9 km and high cloud above 9 km. Columns with cloudy grid boxes in two or more cloud categories were classified as mixed category columns according to the vertical placement of the cloudy grid boxes, e.g. low/high for columns containing cloud below 4 km and above 9 km. 4 and 9 km were chosen as the low/mid and mid/high division points because they are just below two well-defined peaks in cloud base heights (not shown) and roughly correspond to the beginning of the heterogeneous and homogeneous freezing regions, respectively.

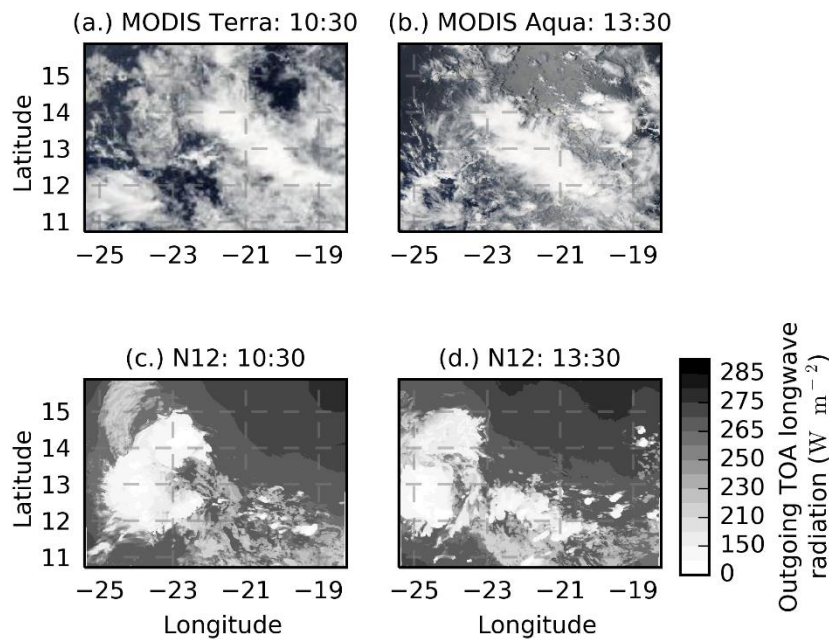


*Figure 2.3. Cloud field evolution. MODIS Terra (a) and Aqua (b) corrected reflectance images of the modelled domain for the 21st of August 2015 and the corresponding simulated top of atmosphere outgoing longwave radiation for the N12 simulation (c, d). Note that the colour bar relates to panels c and d only. Images shown in (a) and (b) are moderate resolution imaging spectroradiometer (MODIS) Corrected Reflectance imagery produced using the MODIS Level 1B data and downloaded from the NASA Worldview website.*

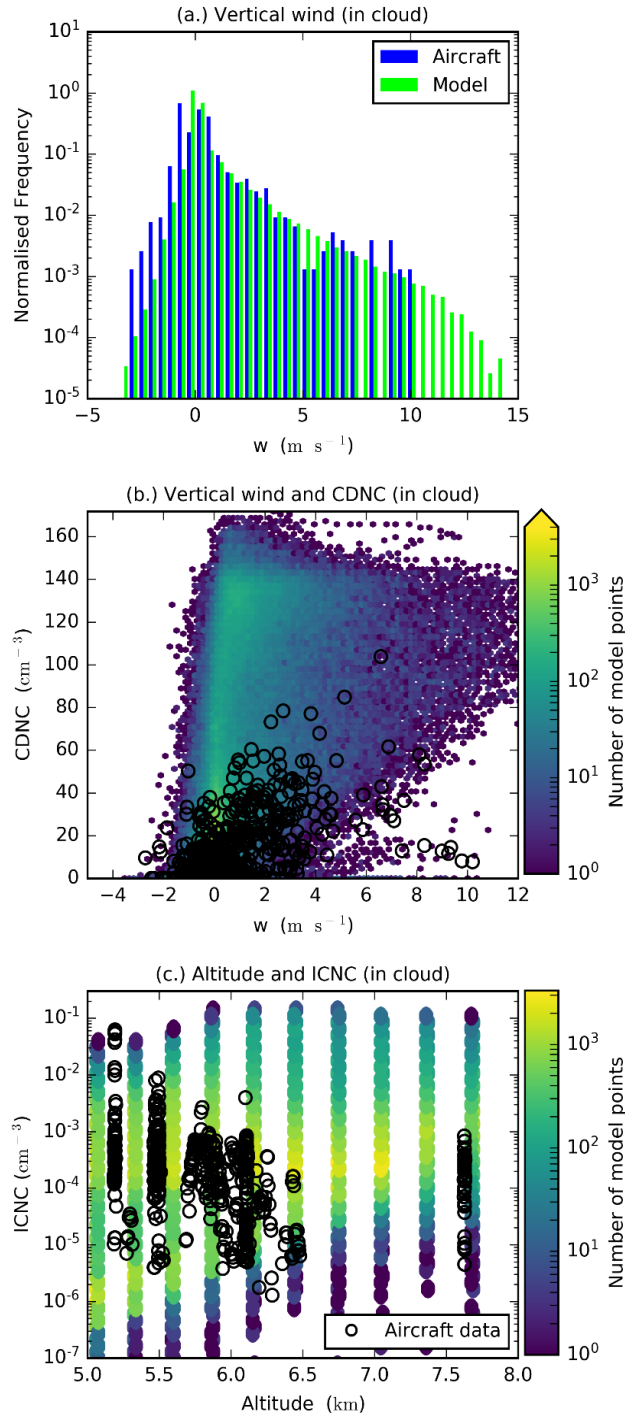


Figure 2.4. Comparison of observed conditions from the b933 ICE-D field campaign flight on the 21st August 2015 and the modelled conditions. Vertical wind speed from the model and aircraft data (a), a 2D histogram of modelled vertical wind against cloud droplet number concentration (CDNC) (b) and altitude plotted against ice crystal number concentration (ICNC) (c) with the aircraft data overlaid. Modelled values are selected from clouds between 10 and 150  $\text{km}^2$  in size from the N12 simulation.

### 2.3.2. The observed case

MODIS visible images of the 21<sup>st</sup> August 2015 are shown in Figure 2.3 (a, b) alongside snapshots of the TOA outgoing longwave radiation in one of our simulations (c, d). The simulated cloud field has more cloud-free areas than the satellite images but in general produces clouds similar to those shown in the satellite image and in approximately the correct location. Overall the simulations produce a complex and realistic cloud field. Snapshots of the simulated model TOA outgoing shortwave radiation are shown in Figure A2.1 of the appendix (Section 2.7).

In-situ measurements of cloud and aerosol properties were made using the UK FAAM Bae-146 research aircraft, which was flown from Praia, Cape Verde Islands. An extensive suite of in-situ aerosol and cloud particle instruments were operated onboard the aircraft and are described in detail in Lloyd et al. (2019). The aircraft penetrated the growing convective clouds at a range of altitudes from just below the freezing level up to  $-20^{\circ}\text{C}$ . In order to show that the model reproduces the observed conditions, the observational data were compared to the conditions in modelled clouds of similar size to those the aircraft flew in ( $10 - 150 \text{ km}^2$ ) where a comparison was thought appropriate.

Comparisons of a selection of simulated cloud properties with aircraft data are shown in Figure 2.4. In-cloud measurements from the aircraft were selected using the same total water content threshold as for the model data ( $10^{-5} \text{ kg kg}^{-1}$ ). Note that observational data only samples clouds along the 1D flight path, while model results include all grid points inside the selected clouds.

The vertical wind and cloud droplet and ice number concentrations are shown Figure 2.4. The vertical wind speeds from the model and aircraft measurements agree well (Figure 2.4a). The aircraft data exhibit less measurements of vertical wind speeds above  $10 \text{ m s}^{-1}$  but that is expected since the aircraft was purposefully not flown in very high updraft speeds. The aircraft

cloud droplet number concentration (CDNC), measured using a Droplet Measurement Technique (DMT) cloud droplet probe, falls predominantly in the regions of parameter space most highly populated by model data when plotted against vertical wind speed (Figure 2.4b). Note that the simulated points in Figure 2.4b represent values of CDNC and updraft speed in all cloudy gridboxes, not just those at cloud base. The updraft speed is collocated with CDNC and therefore does not necessarily represent the updraft speed at which the cloud droplets were activated. The higher CDNC values exhibited in the model data may be due to the higher updraft speeds which were not measured by the aircraft. The observed ICNC was derived from measurements using the DMT Cloud Imaging Probes (CIP-15 and CIP-100) and the Stratton Park Engineering Company Stereoscopic optical array probe covering a size range from 10 to 6200  $\mu\text{m}$  using the SODA2 (System for OAP Data Analysis) processing code to reconstruct ice particle images that are fully contained within the probe sample volume. Because of uncertainties in the optical array probe sample volume for very small images, only ice particle images greater than 100  $\mu\text{m}$  were included. The aircraft ICNC fall almost entirely within the range of the model values (Figure 2.4c).

## **2.4. Results**

### **2.4.1. Effect of INP and INP parameterisation on outgoing radiation**

We first examine the effect of INP parameterisation on the outgoing radiation relative to the simulation where the only source of primary ice production was through homogeneous freezing (NoINP). Ice crystals formed via homogeneous freezing, which have been sedimented to lower levels can indirectly initiate ice production via the Hallett-Mossop process once converted to snow or graupel. When contrasting the effect of different INP parameterisations in Section 2.4.1 to Section 2.4.5, the Hallett-Mossop process was always active including in the NoINP

simulation. As stated in Section 2.3.1.3, the radiation code is represented by SOCRATES (Edwards and Slingo, 1996; Manners et al., 2017), and responds to changes in cloud droplet number and cloud droplet, ice crystal and snow mass. The results detailed below relate to either the domain-wide properties or all in-cloud regions within the domain. This means that the results describe the direct and indirect changes, for example changes to the Hallett-Mossop ice production, occurring due to the presence of INP across all cloud present in the domain, including low-level liquid clouds, mixed-phase clouds without a convective anvil and very deep convective clouds with an anvil. The effects of INP parameterisation and SIP on convective anvils are discussed in Section 2.4.4 and 2.4.5.

Domain-mean TOA outgoing radiation (daylight hours, shortwave plus longwave) is enhanced by the inclusion of INP in all cases (Figure 2.5a). The enhancement in outgoing radiation varies between  $2.6 \text{ W m}^{-2}$  for D10 and  $20.8 \text{ W m}^{-2}$  for A13 relative to the NoINP simulation. There is a variation of up to  $18.2 \text{ W m}^{-2}$  depending on the chosen representation of heterogeneous ice nucleation, which shows that the INP parameterisation can affect outgoing radiation as much as excluding or including heterogeneous freezing altogether.

Bear in mind that SIP was active (SIP active) in the simulations summarised in Figure 2.5a, including in the NoINP simulation in which the Hallett-Mossop process can be initiated by settling ice-phase hydrometeors (either by settling homogeneously frozen ice crystals subsequently converted to snow or graupel, or by settling snow or graupel formed from homogeneously frozen ice crystals at upper cloud levels), indicating that these cloud systems are sensitive to INP even in the presence of SIP. This is consistent with a comparatively small change in TOA radiation when SIP is active relative to when it is inactive (Figure 2.5b and 3c) (we discuss the role of SIP in more detail in Section 2.4.5).

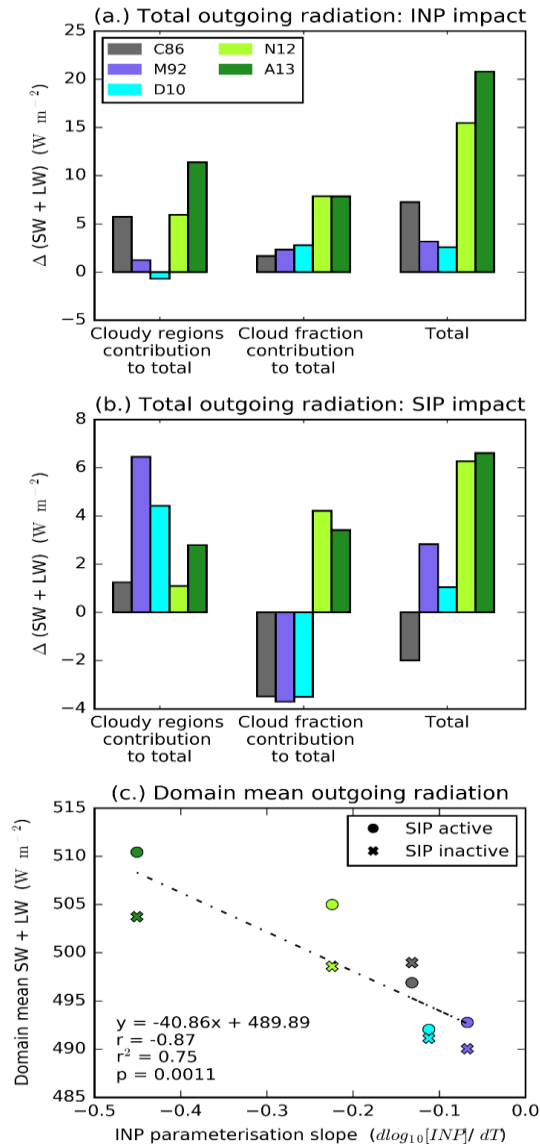


Figure 2.5. Effect of INP and secondary production on TOA outgoing radiation. Effect of INP parameterisation (a) and SIP (a representation of the Hallett-Mossop process) (b) on domain-mean daytime TOA outgoing radiation and total domain-mean daytime TOA outgoing radiation plotted against INP parameterisation slope (c). In (a), the change from the NoINP simulation is shown (INP - NoINP) with SIP active. In (b), the change from SIP active to SIP inactive is shown (SIP active - SIP inactive). A positive value indicates more TOA outgoing radiation when INP or SIP are active. In (a) and (b), the relative contributions of changes in outgoing radiation from cloudy regions (left) and cloud fraction (middle) to the total radiative effect (right) are shown (calculation described in Section 2.3.1.3). In addition to the simulated values, a regression line ( $n=10$ ) is shown in (c) along with its associated statistical descriptors.

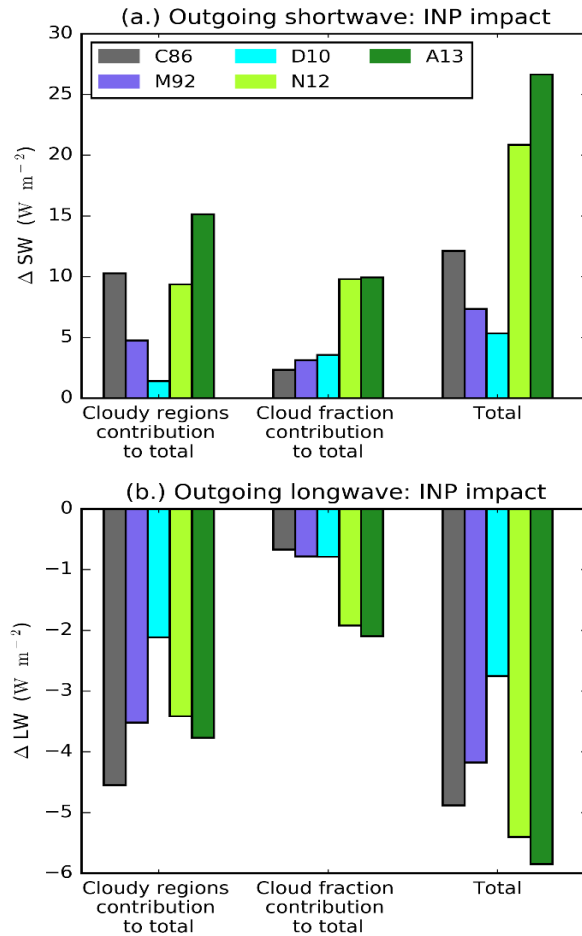


Figure 2.6. Effect of INP on domain-mean daytime outgoing TOA shortwave and longwave radiation. The change from the NoINP simulation is shown (INP - NoINP). A positive value indicates more outgoing radiation when INP are present. The contributions of changes in outgoing radiation from cloudy regions (left) and cloud fraction (middle) to the total radiative forcing (right) are also shown.

The slope of the INP parameterisation (i.e. the dependence of INP number concentration on temperature,  $d\log_{10}[\text{INP}]/dT$ ) is a key determinant of the outgoing radiation. There is a statistically significant correlation between INP parameterisation slope and total TOA outgoing radiation ( $r^2 = 0.75$ ,  $p < 0.01$ ,  $n = 10$ ) (Figure 2.5c). The difference in radiation between the NoINP and the simulations where INP are present are caused mainly by changes to outgoing shortwave radiation (Figure 2.6a). The inclusion of INP enhances outgoing shortwave radiation by between  $5.3 W m^{-2}$  for D10 and  $26.6 W m^{-2}$  for A13 (Figure 2.6a). Differences in outgoing

longwave radiation are comparatively small ( $-2.7 \text{ W m}^{-2}$  for D10 to  $-5.8 \text{ W m}^{-2}$  for A13; Figure 2.6b) due to similar cloud top heights between simulations of these thermodynamically limited clouds.

Changes in outgoing radiation due to the presence of INP are caused by a combination of changes to the outgoing radiation from cloudy regions, caused by changes in cloud structure and microphysical properties, and changes to domain cloud fraction, whose contributions to the total radiative difference are shown in Figure 2.5a (left and centre). In order to appreciate the reasons for these trends, we will now take a closer look at the effect of INP on outgoing radiation from cloudy regions only (Section 2.4.2) and changes to the domain cloud fraction (Section 2.4.3).

### **2.4.2. Effect of INP and INP parameterisation on outgoing radiation from cloudy regions**

Here we discuss the changes in outgoing radiation from cloudy regions only due to INP parameterisation choice. Daytime outgoing radiation from cloudy regions increases due to INP for all but one INP parameterisation (Figure 2.7a). The absolute change in outgoing radiation from cloudy regions is between  $-0.8$  (D10) and  $+28.1$  (A13)  $\text{W m}^{-2}$ , and the larger values are a result of large increases in reflected shortwave (up to  $+37.2 \text{ W m}^{-2}$ ) and relatively moderate decreases in outgoing longwave radiation (up to  $-11.1 \text{ W m}^{-2}$ ) from cloudy regions. The above absolute changes in outgoing radiation from cloudy regions contribute between  $-0.7$  and  $+11.4 \text{ W m}^{-2}$  to the domain-mean change in outgoing radiation due to the presence of INP (Figure 2.5a, cloudy regions contribution).

The enhancement of outgoing radiation from cloudy regions due to INP is caused primarily by increases in cloud condensate relative to the NoINP simulation (Figure 2.7b). When INP are

included in a simulation, snow and cloud droplet water path are enhanced, causing increases in total cloud condensate, despite decreases (in all except A13) in ice crystal water path due to a reduction in ice crystal number and mass concentrations caused by a reduction in the availability of cloud droplets for homogeneous freezing. Snow, cloud droplets and ice crystals are the hydrometeors that affect outgoing radiation in CASIM and the combined water path of these three species is significantly positively correlated with cloud shortwave reflectivity ( $r^2 = 0.62$ ,  $p < 0.01$ ,  $n = 11$ ) (Figure 2.7c). In-cloud microphysical profiles of secondary and homogeneous ice particle production, ICNC and ice crystal, snow and graupel mass concentrations are shown in Figure 2.8. Profiles of the difference in out-of-cloud temperature and relative humidity, and in in-cloud updraft speed, between simulations including INP and the NoINP simulation are shown in Figure 2.9.

The mechanism for the INP induced increase in cloud condensate and consequently cloud shortwave reflectivity shown in Figure 2.7 is as follows: When heterogeneous ice nucleation is active, liquid is consumed in the warmer regions of mixed-phase clouds because of increased heterogeneous ice nucleation (Figure 2.2) and SIP (Figure 2.8a). The resultant additional ice crystals in mixed-phase regions (Figure 2.8c, d) facilitate riming causing increases in snow and graupel (Figure 2.8e, f), increasing snow water path and reflectivity in mixed-phase and ice clouds. At the same time, the enhanced production of relatively heavy snow and graupel increases precipitation which on melting to form rain below the freezing level and subsequent evaporation below 4 km, reduces out-of-cloud temperature and increases relative humidity (Figure 2.9a, b). This leads to increases in water path in low-level liquid clouds and thus an enhancement in their shortwave reflectivity.

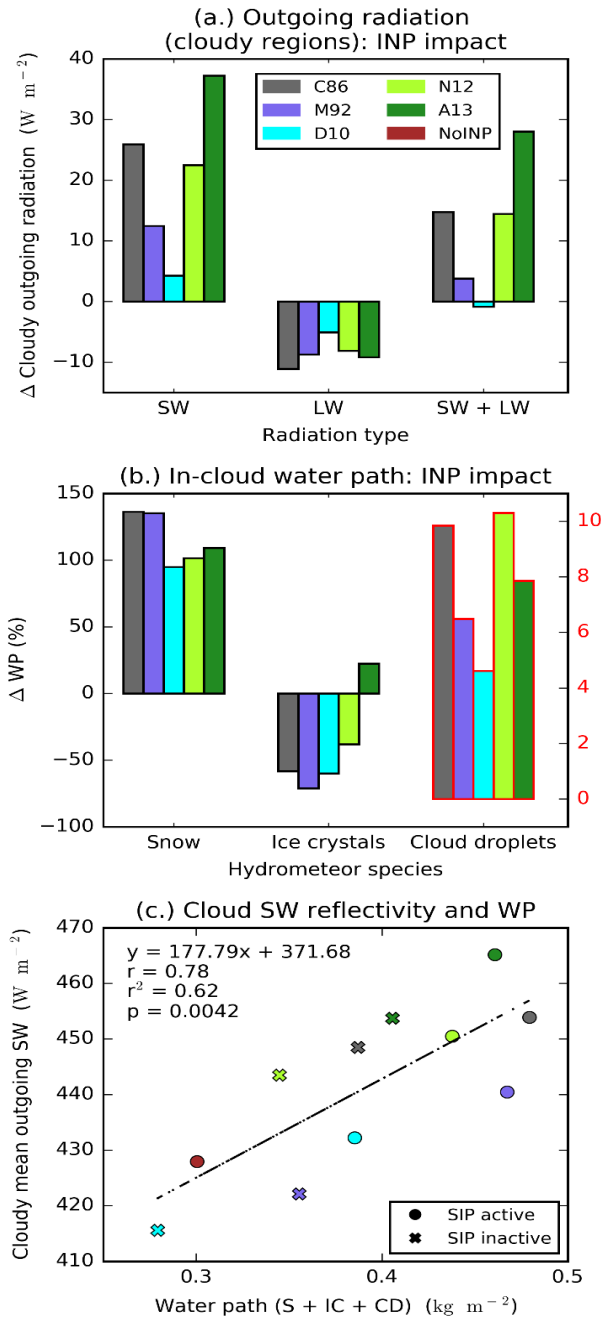


Figure 2.7. INP and outgoing radiation from cloudy regions. Absolute change in outgoing shortwave, longwave and total radiation from cloudy regions relative to the NoINP simulation (a), the percentage change in water path (WP) associated with snow (S), ice crystals (IC) and cloud droplets (CD) relative to the NoINP simulation (b), and mean daytime outgoing shortwave from cloudy regions plotted against the sum of S, IC and CD water paths (c). Note different scale for CD water path in (b). In addition to the simulated values, a regression line ( $n=11$ ) is shown in (c) along with its associated statistical descriptors.

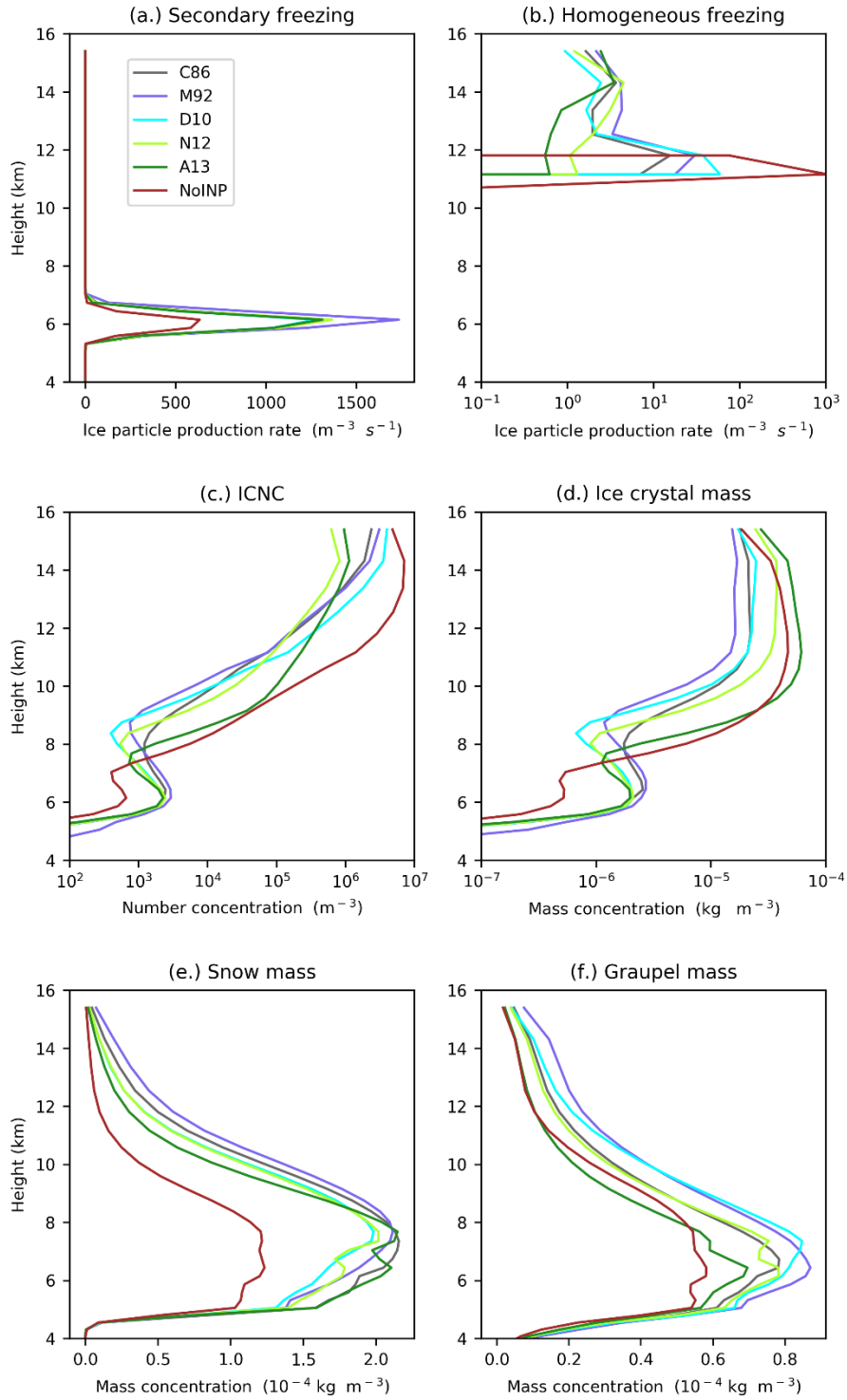


Figure 2.8. Profiles of some microphysical properties of the simulated clouds. Mean in-cloud ice particle production rates from secondary (a) and homogeneous (b) freezing, ICNC (c), ice crystal (d), snow (e), and graupel (f) mass concentrations.

However, increases in total cloud condensate alone cannot account for the differences in outgoing radiation from cloudy regions between simulations using different INP parameterisations, which are caused by a combination of cloud microphysical responses. We find that outgoing radiation from cloudy regions is significantly negatively correlated with INP parameterisation slope ( $r^2 = 0.63$ ,  $p < 0.01$ ,  $n = 10$ ) (Figure 2.10a), i.e. simulations using a steep INP parameterisation have a higher outgoing radiation from cloudy regions. This result makes sense when we consider the relationships between INP parameterisation slope and a multitude of cloud microphysical properties affecting cloud radiative properties.

In particular, a steep INP parameterisation results in a mixed-phase cloud region characterised by a higher ice crystal water path aloft ( $r^2 = 0.80$ ,  $p < 0.01$ ,  $n = 10$ ; Figure 2.10b) and higher cloud droplet number concentrations at the bottom of the mixed-phase region ( $r^2 = 0.89$ ,  $p < 0.01$ ,  $n = 10$ ; Figure 2.10c) when compared to shallower parameterisations. A steeper INP parameterisation slope allows increased transport of liquid to upper cloud levels due to lower rates of heterogeneous freezing at the mid-bottom region of the mixed-phase cloud (lower supercooling, Figure 2.2) and SIP at high temperatures (Figure 2.8a). This, combined with higher INP concentrations at low temperatures (Figure 2.2), increases ICNC and ice crystal mass concentrations at upper mixed-phase altitudes, as well as enhancing the lifetime of liquid cloud droplets at lower altitudes in the mixed-phase region when compared to shallower INP parameterisations.

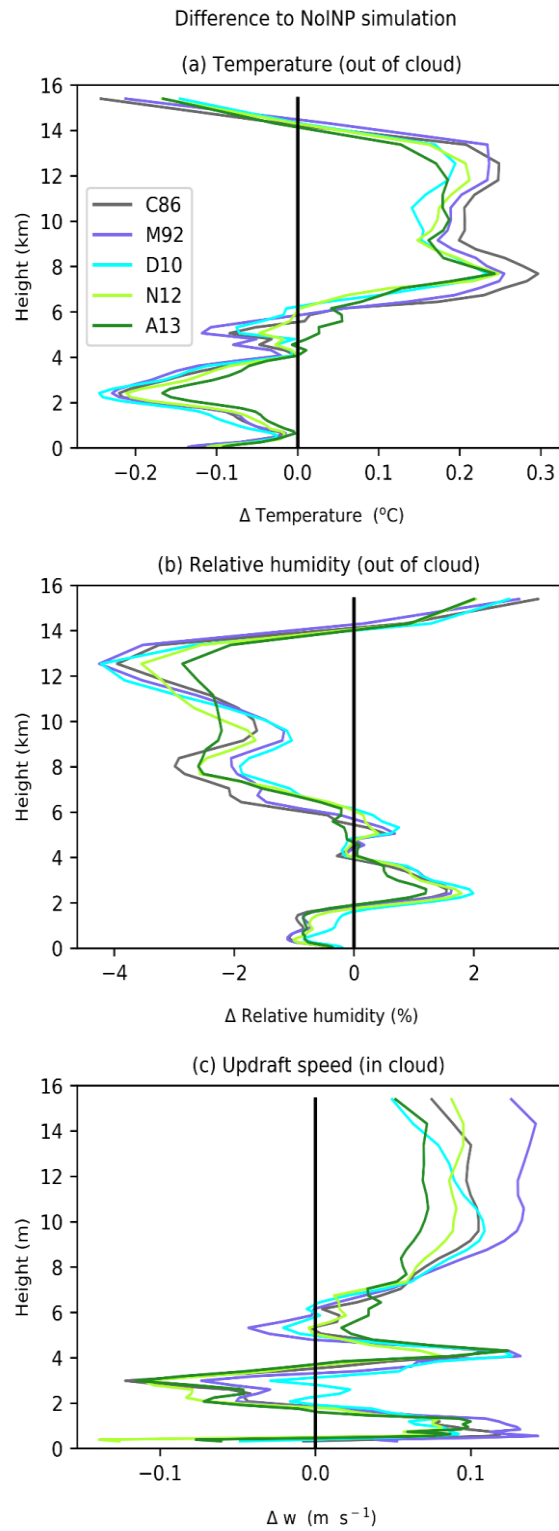


Figure 2.9. Effect of INP on domain-mean out of cloud temperature (a) and relative humidity (b), and in-cloud updraft speed (c). The difference from the NoINP simulation is shown, a positive value indicates a higher value when INP is present.

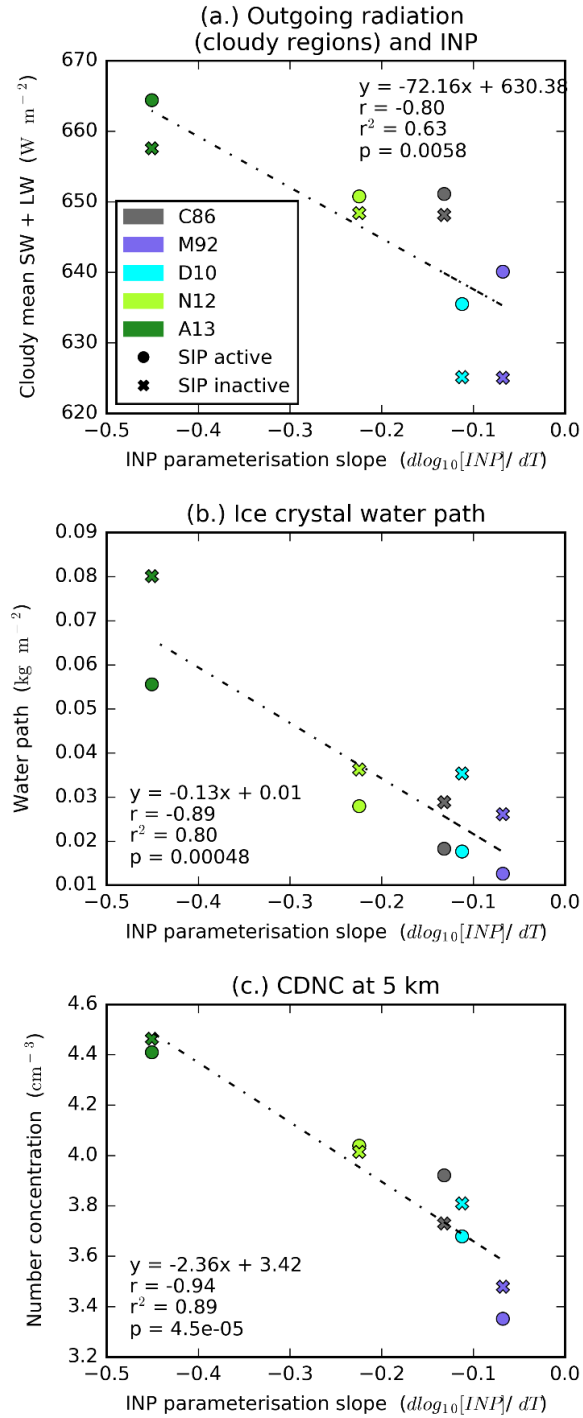


Figure 2.10. Outgoing radiation from cloudy regions and INP parameterisation slope. Scatter plots of INP parameterisation slope and total daytime outgoing radiation from cloudy regions (a), in-cloud mean ice crystal (cloud ice only) water path (b), and in-cloud cloud droplet number concentrations at the start of the mixed-phase region (5 km) (c). Also shown are the respective regression lines ( $n=10$ ) and associated statistical descriptors.

### 2.4.3. Effect of INP and INP parameterisation on cloud fraction

Overall cloud fraction is increased by INP for all INP parameterisations and these increases in cloud fraction contribute about as much to changes in domain-mean radiation as the changes in outgoing radiation from cloudy regions (Figure 2.5a, cloud fraction contribution). Increases in domain cloud fraction due to INP are driven by cloud cover increases in the warm and mixed-phase regions of the cloud (~ 4 -6 km), offset somewhat by decreases in the cloud fraction due to reduced homogeneous freezing in the ~ 10 - 14 km regime (Figure 2.11a).

Cloud fraction increases at mid-levels (4-9 km) occur because heterogeneous ice nucleation induces an increase in precipitation-sized particles (snow and graupel) which sediment to lower levels and moisten the atmosphere by evaporation (Figure 2.9a, b). This increases new cloud formation and may prolong the lifetime of existing cloud cells. Additionally, increased droplet freezing and riming in the mixed-phase cloud region releases latent heat and invigorates cloud development with increases in updraft speed just above 4 km (Figure 2.9c). The increased cloud fraction at mid-levels due to INP are partially offset by a reduced cloud fraction above 10 km (Figure 2.11a) which is caused by an INP induced enhancement in freezing and riming in the mixed-phase region reducing moisture transport to the homogeneous freezing regime and consequently ICNC (Figure 2.9c).

The effects of INP on the altitude profile of cloud fraction are strongest for shallow INP parameterisation slopes, which have a freezing profile most different to that of the NoINP simulation (Figure 2.11a). At 5 km, the shallowest parameterisation (M92) causes the largest increase in cloud fraction, while the steepest parameterisation (A13) causes the smallest ( $r^2 = 0.83$ ,  $p < 0.05$ ,  $n = 5$ ). At 12 km, the order is reversed, and steep parameterisations exhibit the highest cloud fraction of simulations with active INP ( $r^2 = 0.94$ ,  $p < 0.01$ ,  $n = 5$ ).

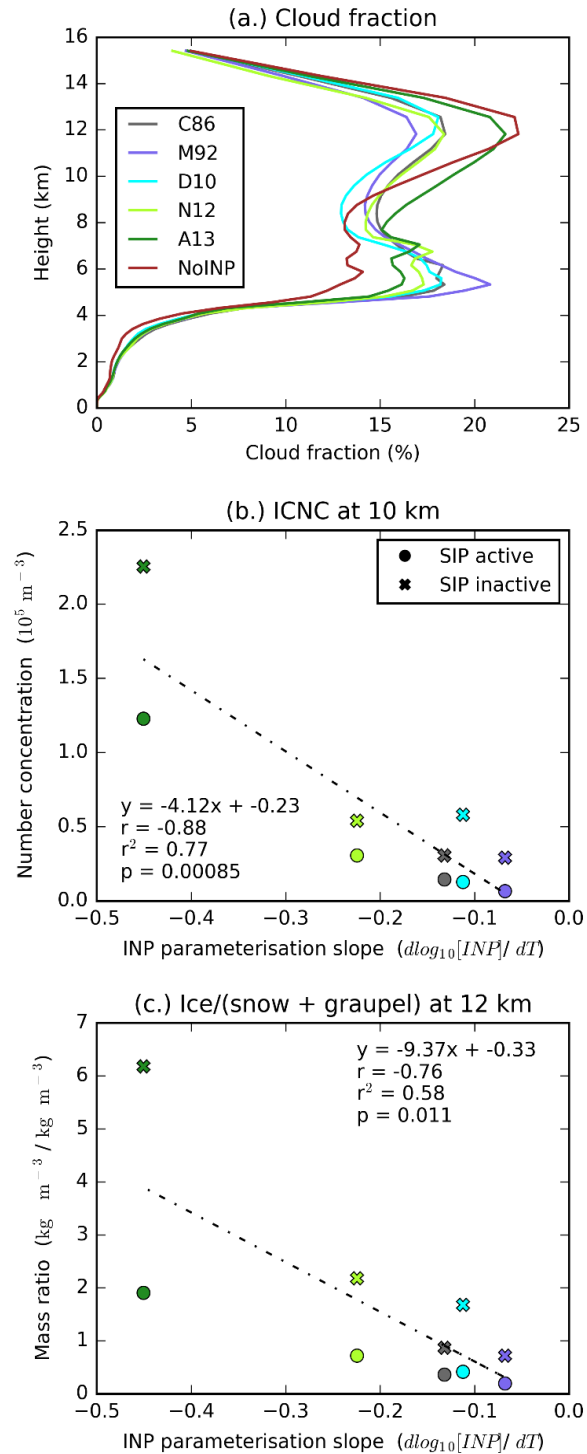


Figure 2.11. Cloud fraction and INP parameterisation slope. Domain-mean cloud fraction profile (a), INP parameterisation slope plotted against ice crystal number concentration at 10 km (b) and mass ratio of ice crystals to snow plus graupel at 12 km (c). Also shown in (b) and (c) are the respective regression lines ( $n=10$ ) and associated statistical descriptors.

The largest cloud fraction-induced increases in outgoing radiation relative to the NoINP simulation (Figure 2.5a) are seen in simulations using steeper INP parameterisations because these simulations exhibit higher cloud fractions at high altitudes (~12 km), translating into the higher total cloud fraction. These slope dependent changes in cloud fraction are explained by a relationship between cloud fraction and several microphysical properties affecting cloud fraction. For example, steeper INP parameterisations produce higher ICNC at the top of the mixed-phase region (10 km) as well as higher ratios of ice crystal mass to snow and graupel mass within the homogeneous freezing region (12 km) (Figure 2.11b, c). A higher number and mass of ice crystals relative to those of larger precipitation-sized hydrometeors with the steepest parameterisations results in lower frozen hydrometeor sedimentation, a longer cloud lifetime and a higher cloud fraction.

#### **2.4.4. Effect of INP and INP parameterisation on cirrus anvils**

Our results show that the INP parameterisation affects the properties and spatial extent of cirrus anvils. We define cirrus anvils to be regions where cloud is present above 9 km only (further details available in Sect. 2.3.1.4). 2D aerial images of cloud categorisation (Figure 2.12a-f) show well-defined regions of anvil cloud (light blue - H) surrounding a large convective system containing clouds at a range of altitudes from <4 km to >9 km. There are clearly differences in the extent and position of cloud categories between simulations (Figure 2.12a -f).

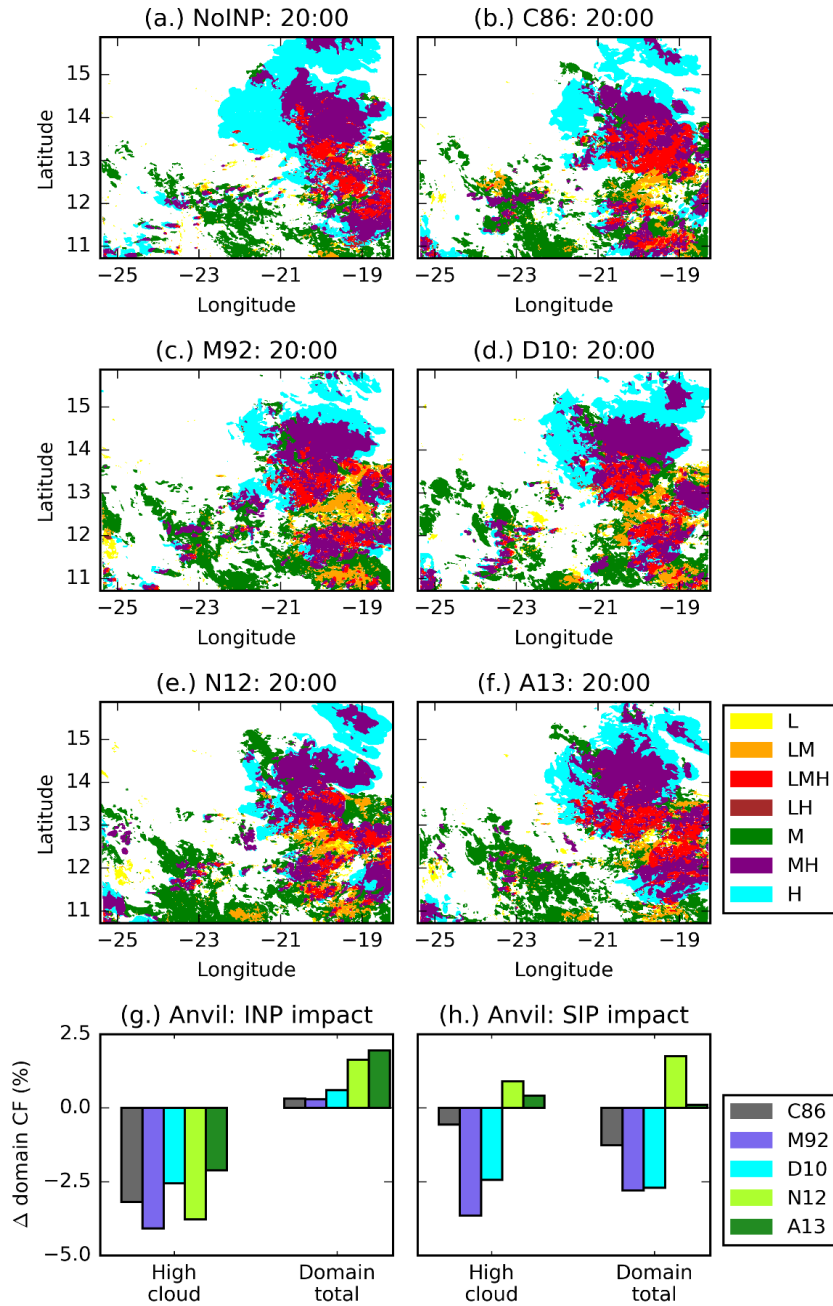


Figure 2.12. Vertical composition of cloud. 2D distribution of cloud type at 20:00 for all six SIP active simulations (a-f), as well as anvil and domain cloud fraction change due to INP (g) and due to SIP (h). Clouds are categorised according to their altitude into low (L, <4 km), mid (M, 4-9 km) and high (H, >9 km) levels and mixed category columns if cloud (containing more than  $10^{-5}$  kg kg<sup>-1</sup> condensed water from cloud droplets, ice crystals, snow and graupel) was present in more than one of these levels (a more detailed description can be found in Sect. 2.1.4). A positive value in (g) or (h) indicates higher values when INP (g) or SIP (h) are active.

The presence of INP reduces convective anvil extent by between 2.1 and 4.1% of the domain area depending on the choice of INP parameterisation (Figure 2.12 g), corresponding to a decrease in anvil cloud of between 22 and 53% relative to the NoINP simulation (not shown). The reduction in anvil extent in the presence of INP is caused by increased liquid consumption at all mixed-phase levels, due to heterogeneous freezing, enhanced SIP and increased graupel and snow production, reducing the availability of cloud droplets for homogeneous freezing (Figure 2.8b), reducing ICNC at cloud-top, and reducing cloud fraction at high altitudes (Figure 2.11a) and cloud anvil extent (Figure 2.12g).

Reductions in anvil extent caused by INP are somewhat offset by the overall increases in cloud fraction across the domain (Figure 2.12g). However, it is possible that the effect of INP and INP parameterisation choice on anvil cloud fraction, and the contribution of anvil cloud to overall cloud fraction and radiative changes, would become larger with a longer analysis period. This is because detrained convective anvils can persist longer in the atmosphere than the convective core that creates them (e.g. Luo and Rossow, 2004; Mace et al., 2006), but this is beyond the scope of the current study.

#### **2.4.5. Importance of secondary ice production**

It has been argued that the observed (or derived) primary ice particle production rate is unimportant for convective cloud properties when secondary ice production (SIP) is active (e.g. Fridlind et al., 2007; Heymsfield and Willis, 2014; Ladino et al., 2017; Lawson et al., 2015) because primary ice crystal concentrations are often overwhelmed by ice crystals formed via SIP (Field et al., 2017). However, the results shown in Figure 2.5a (in which the simulations included SIP) do not support this argument. We find that the microphysical and radiative

properties of the cloud field depend strongly on the properties of the INP even when SIP due to the Hallett-Mossop process occurs. Furthermore, the effect of including SIP on daylight domain-mean outgoing radiation varies between  $-2.0 \text{ W m}^{-2}$  and  $+6.6 \text{ W m}^{-2}$  (Figure 2.5b), showing that the presence of the Hallett-Mossop process has a smaller effect than the INP parameterisation and that the sign and magnitude of this effect depends on the INP parameterisation. The mean effect on daylight domain-mean outgoing radiation of including INP is  $+9.8 \text{ W m}^{-2}$  whereas the mean effect of including SIP via the Hallett-Mossop process is  $+2.9 \text{ W m}^{-2}$ . Therefore, rather than primary ice being simply overwhelmed by SIP, it actually determines how SIP affects cloud microphysics. The changes in domain-mean outgoing shortwave and longwave due to the inclusion of the Hallett-Mossop process can be seen in Figure A2.2 in the appendix (Section 2.7). Other mechanisms of SIP have been proposed (Field et al., 2017; Korolev and Leisner, 2020; Lauber et al., 2018) and the impact of INP on cloud properties in the presence of these mechanisms, particularly those present at temperatures below  $10^\circ\text{C}$  such as droplet shattering (Lauber et al., 2018), should be tested in future but was beyond the scope of the present study.

The effect of SIP on the radiative properties of the cloud field is dependent on INP parameterisation choice, both in magnitude and sign of change (Figure 2.5b). SIP makes the clouds more reflective independent of the chosen parameterisation (Figure 2.5b, cloudy regions contribution) due to increases in snow and cloud droplet water path. N12 and A13 have the largest overall radiative response to SIP because changes to the radiative forcing from cloudy regions and cloud fraction contributions act to increase outgoing radiation (Figure 2.5b). However, the cloud fraction response to SIP is opposite for C86, M92 and D10 meaning the cloudy regions and cloud fraction contributions act in opposite directions, reducing the total radiative forcing.

The different response of the domain cloud fraction to the presence of SIP is caused by substantial variation between simulations in the anvil cloud extent (Figure 2.12h), from an increase of 10% (+0.9% of the domain area) in N12 to a decrease of 40% (-3.6% of the domain area) in M92 (Figure 2.12h). These non-uniform changes in cloud fraction and outgoing radiation can be explained by differences in the response of cloud freezing profiles to SIP due to variations in INP parameterisation slope. For all INP parameterisations, the Hallett-Mossop process consumes liquid in the Hallett-Mossop cloud region and therefore reduces the availability of liquid at higher altitudes. For shallower parameterisations such as M92 this causes a reduction in the amount of cloud droplets reaching the homogeneous freezing regime and thereby reduces ICNC and cloud anvil spatial extent.

However, in simulations using a steep parameterisation, almost all available droplets are frozen heterogeneously before they reach the homogeneous regime (see reduced homogeneous ice production rates in N12 and A13 in Figure 2.8b). Therefore, in simulations using a steeper parameterisation, such as N12, a reduction in liquid availability due to SIP occurs at the top of the heterogeneous freezing regime, reducing the availability of liquid for riming, causing a reduction in frozen hydrometeor size at high altitudes, a reduction in hydrometeor sedimentation and an increase in anvil extent.

The effects of INP parameterisation slope and the Hallett-Mossop process on the simulated cloud field properties are summarised in Figure 2.13. Overall, our simulations show that INP parameterisation choice, and particularly the temperature dependence of the INP parameterisation, are important determinants of cloud field micro- and macrophysical properties, even when SIP is active. We also find that the choice of INP parameterisation affects the cloud field response to SIP.

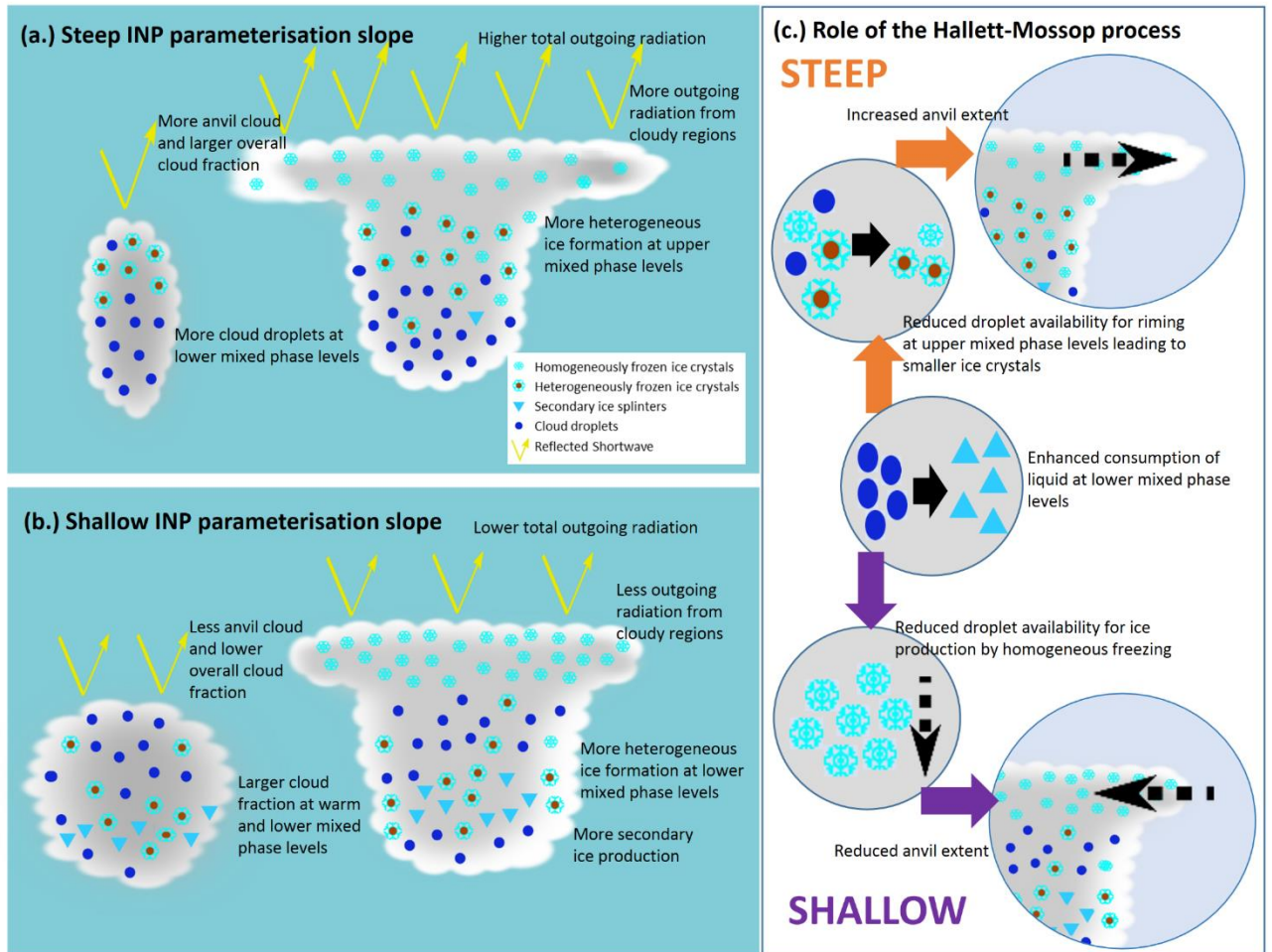


Figure 2.13. Schematic of the main effects of INP parameterisation slope (i.e. a steep (a) or shallow (b) temperature dependence of INP number concentrations) and the role of the Hallett-Mossop process on the simulated cloud field (c).

## 2.5. Limitations of this modelling study

The lack of consideration of ice and snow particle number by the SOCRATES radiation scheme is an important limitation of the results presented here. Changes to ICNC (Figure 2.8c), without a co-occurring change in ice crystal mass concentrations, will not be reflected in modelled radiative fluxes. However, our results are still very relevant for climate model simulations as climate models do not typically account for ICNC in their radiation calculations and have frequently been shown to poorly represent ice crystal mass concentrations (Baran et al., 2014;

Waliser et al., 2009). The SOCRATES representation of radiation with a dependence on ice mass is a more accurate and realistic representation of radiation than is seen in many climate models which often derive bulk optical properties using empirically derived deterministic relationships between ice particle size and environmental temperature and/or ice water content (Baran et al., 2014; Edwards et al., 2007; Fu et al., 1999; Gu et al., 2011). However, the effect of INP parameterisation on deep convective clouds radiative properties using a radiation code that considers ice particle number should be explored in future studies. The sensitivity of the cloud field to the chosen INP parameterisation and SIP indicates the importance of accurately representing ice water content in climate models and linking this ice water content to ice-nucleating particle type.

Another limitation of the SOCRATES radiation code is its lack of consideration of rain and graupel particles. The effects of these hydrometeors are expected to be less than that of ice, snow and cloud droplets as they precipitate faster and therefore have a shorter lifetime. Furthermore, the effect of graupel on the tropical longwave radiative effect has been found to be negligible and dwarfed by that of snow (Chen et al., 2018). The global radiative effect of rain has also been found to be small in the vast majority of cases even at high temporal and spatial resolution (Hill et al., 2018). The effect of the incorporation of these hydrometeors into radiative transfer parameterisations should however be tested in future studies.

Future work should also conduct a similar experiment including the night-time radiative fluxes in the analysis. This would enhance the importance of changes in the longwave outgoing radiation relative to the shortwave radiation. Our simulation length prohibited us from including all night-time hours in our analysis once spin-up was excluded, and therefore the radiative effects of INP and SIP presented apply only to the daytime hours. The effect of including the night-time hours in the calculation of the effect of INP and SIP on outgoing longwave radiation was tested and found to cause no notable differences.

The use of both aerosol-dependent (D10, N12, A13) and solely-temperature dependent (C86, M92) parameterisations in this study means that we have examined the radiative sensitivity of a complex cloud field to a larger variety of INP parameterisations used in weather and climate models than if we had exclusively used parameterisations that consider aerosol concentration. However, this experimental design has limitations. For example, due to the lack of aerosol dependence of the C86 and M92 schemes a 'presumed' dust concentration is implicitly present in these two cases and remains uniform throughout the simulation period. The effect of INP parameterisation choice on convective cloud field properties should also be examined with the inclusion of aerosol scavenging but this was beyond the scope of this study.

Raindrop freezing was parameterised according to Bigg (1953). This parameterisation is volume and temperature based, and is therefore inconsistent with the changes in the heterogeneous freezing parameterisation of cloud droplets detailed in this chapter. Ideally the treatment of raindrops would be consistent with that of cloud droplets and this should be addressed in future studies. In studies, such as this, where processing is inactive, the rate of raindrop freezing should be linked to the interstitial aerosol concentration. Where processing is active, raindrop freezing would ideally take into account the accumulation of INP in large droplets due to the collision and accumulation of multiple aerosol-containing cloud droplets. For example, Paukert et al. (2017) developed a two-moment microphysical scheme that allows for the aerosol dependent heterogeneous freezing of raindrops by tracking the number of aerosol particles accumulated in raindrops by accretion, self-collection, and auto-conversion. This was beyond the scope of the current study but would be the 'gold standard' approach for future studies.

Our results showed that an enhancement in cloud updraft strength due to increased freezing was partly responsible for cloud fraction increases in the mixed-phase region. Cloud invigoration due to aerosols has been documented previously (e.g. Fan et al., 2010a, 2010b,

2012; van den Heever et al., 2006; Tao et al., 2012) and is most frequently discussed in relation to increased CCN concentrations or an overall aerosol increase (i.e. affecting both CCN and INP concentrations) (e.g. Altaratz et al., 2014; Fan et al., 2012; Lerach et al., 2008; Seifert and Beheng, 2006; Wang, 2005). However, cloud invigoration due to enhanced INP concentrations and the associated increased latent heat release of heterogeneous freezing has also been documented (Altaratz et al., 2014; Fan et al., 2010a, 2010b; van den Heever et al., 2006). Here, we see an invigoration effect due to changes in the altitude of ice formation with different heterogeneous ice formation parameterisations. The relative importance and strength of this invigoration relative to changes that would be induced from CCN changes should be examined in future studies.

This study utilised our best estimate of ice production by the Hallett-Mossop process (Connolly et al., 2006; Hallett and Mossop, 1974; Mossop, 1985), the most well-studied SIP mechanism, to try and understand the effect of the process, as currently understood, on deep convective cloud properties. The work indicates that INP concentrations at all mixed phase temperatures can be important for cloud properties even in the presence of the Hallett-Mossop process, and that the impact of the Hallett-Mossop process depends on INP number concentrations. The dependence of the rate of ice production by the Hallett-Mossop process on INP number concentrations (Figure 2.8a) in particular highlights that the role of SIP in clouds may be dependent on INP. However, the rate of ice production by the Hallett-Mossop process is very uncertain and other mechanisms of SIP have also been proposed (Field et al., 2017). We recommend that similar studies examining the effect of INP should be conducted with the inclusion of other proposed SIP mechanisms. In particular, Lloyd et al. (2019) suggests that droplet shattering may be occurring in the clouds sampled during the ICE-D field campaign. However, this was beyond the scope of the present study due in part to the lack of quantification and parameterisations for these other mechanisms (Field et al., 2017). The work presented in

Chapter 3 will attempt to overcome some of the above caveats by using statistical emulation (Johnson et al., 2015b) to examine the interacting effects of dust number concentration, INP parameterisation slope and SIP in an idealised deep convective cloud.

## 2.6. Conclusions

We quantified the effect of INP parameterisation choice on the radiative properties of a deep convective cloud field using a regional model with advanced double-moment capabilities. The simulated domain exceeds 600,000 km<sup>2</sup> and therefore captures the effects of INP and INP parameterisation on a typical large, complex and heterogeneous convective cloud field. The presence of INP increases domain-mean daylight TOA outgoing radiation by between 2.6 and 20.8 W m<sup>-2</sup> and the choice of INP parameterisation can have as large an effect on cloud field properties as the inclusion or exclusion of INP. These effects are evident even in the presence of SIP due to the Hallett-Mossop process, refuting the hypothesis that INP is irrelevant beyond a minimum concentration needed to initiate the Hallett-Mossop process (Crawford et al., 2012; Ladino et al., 2017; Phillips et al., 2007). Furthermore, the effects of SIP on the cloud field properties are strongly dependent on INP parameterisation choice. Both the magnitude and direction of change in cloud fraction and total outgoing radiation due to SIP varies according to INP parameterisation choice. Microphysical alterations to cloud properties are important contributors to radiative differences between simulations, in agreement with previous studies documenting the effect of aerosol-cloud interactions to the radiative forcing by deep convective clouds (Fan et al., 2013). For example, increasing cloud condensation nuclei concentrations, with no perturbations to INP, was shown to increase cloud albedo and cloud fraction, deepen clouds and increase TOA outgoing radiation by 2-4 W m<sup>-2</sup> (Fan et al., 2013). Here we find that even for the same aerosol and CCN concentrations, just altering the relationship between

aerosol concentration and ice-nucleating ability can cause changes in daylight TOA outgoing radiation of up to  $18.2 \text{ W m}^{-2}$  in our domain.

Our results indicate that the slope of the INP parameterisation with respect to temperature ( $d\log_{10}[\text{INP}]/dT$ ) is particularly important: Outgoing total radiation, along with many cloud field and microphysical properties affecting radiation, were significantly correlated with INP parameterisation slope. Best practise for accurately representing INP number concentrations based on current knowledge is to utilise parameterisations that link aerosol number and particle size to INP number concentration (e.g. D10, N12, A13) but that is not enough without also using a parameterisation in which the temperature dependence of the INP number concentrations matches reality; the largest differences in domain outgoing radiation existed in this study between simulations using aerosol dependent parameterisations (D10 and A13). These large variations in outgoing radiation between simulations using different aerosol dependent INP parameterisations justifies investment in observational campaigns to more effectively constrain the range of expected INP concentrations and parameterisation slopes in the Saharan dust outflow region, and other regions dominated by maritime deep convective activity.

The significance of the slope of the INP parameterisation indicates the potential importance of accounting for differences in aerosol composition in modelling studies. For example, INP derived from marine organics (Wilson et al., 2015) have a shallower slope than mineral dust INP (Atkinson et al., 2013; Niemand et al., 2012). Furthermore, real-world INP concentrations are known to have complex temperature dependencies with biological INP, such as soil borne fungus and plant related bacteria, making significant contributions at the warmest temperatures and mineral components being more important at lower temperatures (O'Sullivan et al., 2018). The ice-nucleating temperature dependence of mineral dust (and other aerosol types) can also be substantially altered by the adsorption of biological material such as ice-nucleating

macromolecules from fungi, pollen and bacteria on particle surfaces complicating the picture further (Augustin-Bauditz et al., 2016; Chen et al., 2021; O’Sullivan et al., 2016). The vast majority of models do not account for the complex multi-component composition of aerosol populations and individual aerosol particles which determines the real world ice-nucleating temperature dependence. The work here suggests that the presence of biological INP might be to reduce liquid water transport to the upper levels of the cloud, reducing cirrus anvil extent, but also to increase low cloud fraction. Nevertheless, measurements in the eastern tropical Atlantic indicate that biological INP in the Saharan dust plumes is at most a minor contribution and that the parameterisations with shallow slopes in Figure 2.2 likely produce too much glaciation at warm temperatures (e.g. Price et al., 2018).

The results presented here also present a new framework for understanding the effect of SIP by identifying a potential relationship between the effect of the Hallett-Mossop process and INP parameterisation slope. The significance of INP parameterisation slope also highlights the importance of characterising the INP concentration across the entirety of the mixed-phase temperature range rather than just at one temperature, or in a narrow temperature range, as is common in many field campaigns. For example, in the ICE-D field campaign, INP concentrations at temperatures above  $-7$  and below  $-27^{\circ}\text{C}$  were not measurable due to experimental and sampling constraints (Price et al., 2018). Measuring INP over the entire mixed-phase temperature range, throughout which deep convective clouds extend, conceivably covering around 10 orders of magnitude in INP number concentration, represents a major experimental challenge. This issue is compounded by the fact that INP spectra cannot reliably be extrapolated to higher or lower temperatures since our underpinning physical understanding of what makes an effective nucleation site is lacking (Coluzza et al., 2017; Holden et al., 2019; Kanji et al., 2017; Kiselev et al., 2016). This work demonstrates the importance of solving these problems and measuring INP number concentrations across the entirety of the mixed-

phase temperature spectrum, as has been demonstrated in previous work (e.g. Liu et al., 2018; Takeishi and Storelvmo, 2018).

## 2.7. Appendix

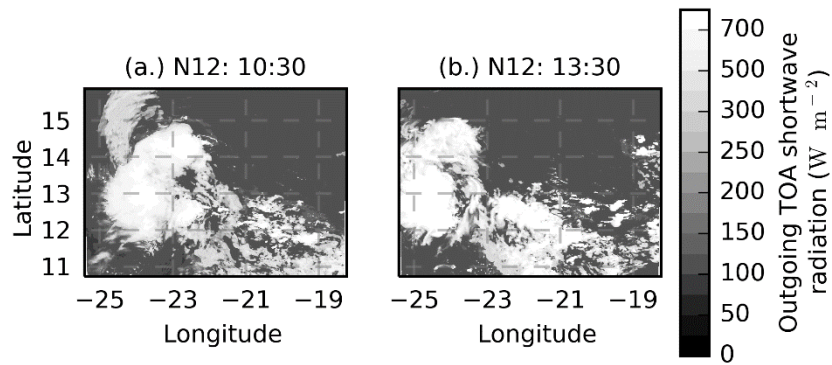


*Figure A2.1. The cloud field. Simulated top of atmosphere outgoing shortwave radiation for the N12 simulation at 10:30 (a) and 13:30 (b).*

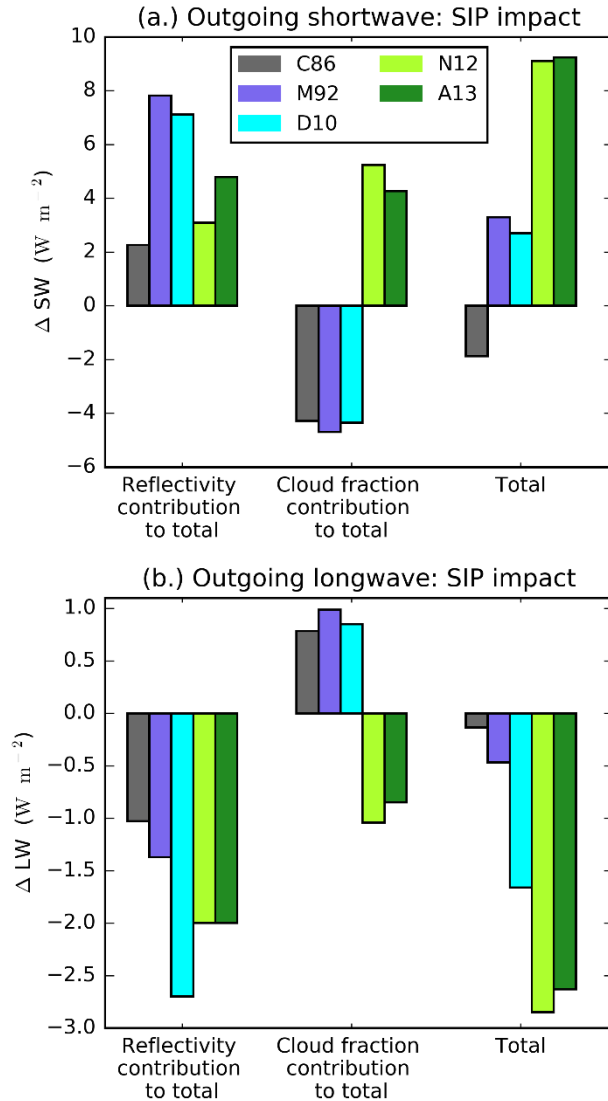


Figure A2.2. Effect of the Hallett-Mossop process on domain-mean daytime outgoing TOA shortwave and longwave radiation. The change from the SIP inactive simulation is shown (SIP active – SIP inactive). A positive value indicates more outgoing radiation when the Hallett-Mossop process is active. The contributions of changes in outgoing radiation from cloudy regions (left) and cloud fraction (middle) to the total radiative forcing (right) are also shown.



## Chapter 3: Influence of ice-nucleating particles and Hallett-Mossop ice production rates on anvil cirrus from deep convection

Chapter 3 is based on collaborative work from the manuscript ‘Effect of ice-nucleating particles and Hallett-Mossop ice production rates on anvil cirrus from deep convection’ which is in preparation for submission. The candidate is the lead author and the full author list is as follows:

**Rachel E. Hawker\*<sup>1</sup>, Annette K. Miltenberger<sup>2</sup>, Jill S. Johnson<sup>1</sup>, Jonathan M. Wilkinson<sup>3</sup>, Adrian A. Hill<sup>3</sup>, Ben J. Shipway<sup>3</sup>, Paul R. Field<sup>1,3</sup>, Benjamin J. Murray<sup>1</sup>, Ken S. Carslaw<sup>1</sup>**

1. Institute for Climate and Atmospheric Science, University of Leeds, Leeds, LS2 9JT, United Kingdom.

2. Institute for Atmospheric Physics, Johannes Gutenberg University Mainz, Mainz, 55128, Germany.

3. Met Office, Exeter, EX1 3PB, United Kingdom.

Author contributions: Rachel E. Hawker, Annette K. Miltenberger, Jill S. Johnson, Ken S. Carslaw, Paul R. Field and Benjamin J. Murray contributed to the design, development and direction of the study. Annette K. Miltenberger and Rachel E. Hawker set up a default deep convective simulation in the MONC-CASIM model. Jill S. Johnson provided the base R code needed for the uncertain input parameter combination selection and to carry out the statistical emulation and uncertainty analysis, and provided advice about statistical emulation and uncertainty analysis throughout. Rachel E. Hawker carried out the model development in the MONC-CASIM code to build the base case simulation and allow for the perturbations to the uncertain input parameters determined by the sampling design, used and modified the R code to select the uncertain input parameter combinations, ran all MONC-CASIM simulations presented here, conducted all analysis and wrote the manuscript. Jonathan M. Wilkinson, Adrian A. Hill and Ben J. Shipway built and maintained the Met-Office CASIM model used to run the simulations. Rachel E. Hawker, Annette K. Miltenberger, Jill S. Johnson, Ken S. Carslaw, Paul R. Field and Benjamin J. Murray edited the manuscript.

### 3.1. Abstract

The formation of ice crystals in the mixed-phase region of deep convective clouds is important for cloud glaciation and anvil properties, which in turn affect cloud radiative properties. Small ice crystals in the mixed-phase cloud region can be formed by two mechanisms: heterogeneous ice nucleation by ice-nucleating particles (INP) and secondary ice production (SIP) by, for example, the Hallett-Mossop process. The representation of these ice formation processes in cloud and numerical weather prediction models is highly uncertain. We use a Latin hypercube sampling method and statistical emulation to quantify the effect of varying INP number concentration, INP parameterisation slope (i.e. the temperature dependence of the INP number concentration in the mixed-phase temperature region) and the Hallett-Mossop splinter production rate on the anvil properties of an idealised deep convective cloud. Overall, the anvil ICNC is substantially reduced at high INP number concentrations owing to a reduction in homogeneous ice production when heterogeneous freezing becomes the dominant mechanism for primary ice production. Furthermore, at shallow INP parameterisation slopes, there is a sharp transition to a cloud regime with larger anvil ice crystals and a more extensive anvil. This regime shift is driven by more extensive cloud glaciation which is in part caused by higher INP number concentrations at warm mixed-phase temperatures in simulations with shallow INP parameterisations slopes enhancing the ice particle production by the Hallett-Mossop process. These enhanced ice particle production rates by the Hallett-Mossop process cause more extensive cloud glaciation and an invigoration effect due to enhanced latent heat release from Hallett-Mossop freezing and the resultant enhancement in riming, deposition, and snow and graupel formation. This enhances the vertical mass flux and condensate divergence at the outflow level. This work highlights the importance of quantifying the full spectrum of INP number concentrations across all mixed-phase altitudes, and furthers our understanding of the interactions of INP with secondary ice production mechanisms.

## 3.2. Introduction

Deep convective clouds are an important component of the global hydrological cycle and radiative budget (Lohmann et al., 2016; Massie et al., 2002). The anvil cirrus cloud they produce can persist in the atmosphere for several hours to a few days and therefore impact outgoing radiation for long after the deep convection has decayed (Luo and Rossow, 2004). However, accurately representing the spatial and temporal complexity of large convective systems and therefore convectively generated cirrus presents extensive challenges for atmospheric modelling (Prein et al., 2015).

Deep convective cloud systems extend vertically from the boundary layer to the tropopause and can have a horizontal radius of over 1000 km. They are dynamic and powerful systems with updraft speeds of up to  $50 \text{ m s}^{-1}$  (Frank, 1977; Musil et al., 1986; Xu et al., 2001). In addition, a multitude of different thermodynamic and microphysical conditions can exist within the same system. There is a scarcity of measurements of these climatically important clouds, particularly profile measurements within the convective core (Fan et al., 2016), and thus a scarcity of data with which to validate representations of deep convective clouds in models.

The myriad of competing microphysical processes operating within deep convective clouds, along with the difficulty in validating model simulations against observations, cause the simulation of deep convective clouds to be subject to a large number of parametric and structural uncertainties (Johnson et al., 2015b; Wellmann et al., 2018). In particular, mixed-phase microphysics presents a challenge for cloud modelling because it is critical for deep convective cloud properties and very poorly understood (Prein et al., 2015).

One of the largest uncertainties in quantifying aerosol-cloud interactions and the resultant climate impacts is the amount of, and balance between, liquid and ice in mixed-phase clouds. In particular, the representation of microphysical processes affecting cloud phase in tropical

convection contributes substantial uncertainty to the simulated climate response to global warming in climate models (Medeiros et al., 2008; Stevens and Bony, 2013). The representation of the amount of ice within deep convective clouds is also important for the representation of the amount and intensity of precipitation, the prediction of which is one of the most socially and economically important roles of numerical weather forecasting (Arakawa, 2004; Prein et al., 2015).

Within the mixed-phase region of deep convective clouds, the region between 0 and  $\sim -38^{\circ}\text{C}$  where both liquid and ice can coexist, we hypothesise that three variables controlling ice production strongly influence the partitioning of condensate into cloud liquid and ice. These are the total number concentration of potential INP (aerosol particles with the ability to initiate the freezing of cloud droplets at temperatures between 0 and  $-38^{\circ}\text{C}$ ), the temperature dependence of INP number concentration (the rate of increase in ambient INP number concentrations as temperature decreases from  $\sim 0$  to  $\sim -38^{\circ}\text{C}$ ) and the presence/absence or rate of ice production by secondary ice production mechanisms (SIP, whereby small ice particles are produced from existing hydrometeors).

The number concentration of potential INP in the atmosphere is extremely variable and depends on several interacting factors. For example, the export of Saharan dust, an efficient INP at temperatures below  $-15^{\circ}\text{C}$ , and the largest component by mass of the global aerosol budget (Tang et al., 2016; Textor et al., 2006), across the Atlantic Ocean varies hugely, depending on factors such as season (Ridley et al., 2012), desert soil moisture (Laurent et al., 2008), local wind speed (Grini et al., 2005; Laurent et al., 2008) and the occurrence and intensity of convection (Bou Karam et al., 2014; Marsham et al., 2011; Provod et al., 2016) both in source (Heinold et al., 2013) and transport regions (Sauter et al., 2019; Twohy and Twohy, 2015). As a result of variations in dust emission and transport, summertime INP

number concentrations in the Saharan Air Layer can vary by up to four orders of magnitude at  $-33^{\circ}\text{C}$  (Boose et al., 2016b).

Variations in INP number concentrations can impact cloud properties and cloud radiative forcing (Shi and Liu, 2019; Solomon et al., 2018). However, the reported effect of changes to INP number concentrations on cloud properties can be non-linear, counterintuitive or conflicting depending on the environmental conditions, magnitude of the tested perturbation, or study methodology (Deng et al., 2018; Fan et al., 2010b, 2010a; Gibbons et al., 2018; Hawker et al., 2021; van den Heever et al., 2006; Phillips et al., 2005, 2007).

A large number of aerosol types have been shown to have the ability to act as INP, including mineral dust (Atkinson et al., 2013; Niemand et al., 2012; Price et al., 2018; Welti et al., 2018), organic material in sea spray (McCluskey et al., 2018; Wilson et al., 2015), bacteria (Šantl-Temkiv et al., 2015), and pollen (Diehl et al., 2002). The temperature dependence of INP number concentration, which determines the concentration of INP at lower mixed-phase altitudes, depends, amongst other factors, on the aerosol type providing INP in a given scenario. For example, INP comprised of marine organics emitted with sea spray tend to have a shallower temperature dependence than INP comprised of mineral dusts which means they have a higher ice-nucleating ability at warm temperatures, but lower ice-nucleating ability at colder temperatures (DeMott et al., 2016; McCluskey et al., 2018; Wilson et al., 2015) (Atkinson et al., 2013; Niemand et al., 2012; Vergara-Temprado et al., 2017).

In numerical weather and climate models, which represent heterogeneous ice nucleation using parameterisations, the temperature dependence of INP number concentrations can be described by the slope of the INP parameterisation (i.e.  $d(\log_{10}[\text{INP}])/dT$  as described in Hawker et al. (2021)). The INP parameterisation slope depends on aerosol type (DeMott et al., 2010; Harrison et al., 2016, 2019) and any aging the aerosol has been subjected to (Boose et al., 2016b; Brooks et al., 2014) as well as aerosol properties yet to be fully understood, such as

surface morphology (Holden et al., 2019). The INP slope of any one aerosol population (composed of different INP types) is extremely uncertain and difficult to accurately predict without specific measurements. Variation in ice nucleation active site densities ( $n_s$ ) of even materials of similar mineralogy can span several orders of magnitude at any one temperature (Atkinson et al., 2013; Harrison et al., 2016, 2019). Also, variations in the temperature dependence of INP number concentration can affect the cloud development and the altitude at which liquid depletion occurs, as was noted by Takeishi and Storelvmo (2018). This difference in liquid depletion altitude has been shown to cause differences in hail amount, intensity, and size (Liu et al., 2018), anvil ice crystal number concentration (ICNC) (Takeishi and Storelvmo, 2018), and radiative forcing (Hawker et al., 2021) of convective clouds.

The formation of ice crystals within the mixed-phase regions in deep convective clouds occurs not only via heterogeneous freezing but also via SIP, whereby ice is produced from processes operating on existing ice particles (Field et al., 2017). Observational campaigns have long documented the existence of ice crystals at concentrations vastly exceeding the concentration of INP in clouds with relatively warm cloud top temperatures, indicating the presence of SIP mechanisms (Crawford et al., 2012; Field et al., 2017; Huang et al., 2017; Ladino et al., 2017; Lasher-Trapp et al., 2016). SIP can occur via processes such as rime splintering (i.e. the Hallett-Mossop process), droplet shattering, collision fragmentation, and sublimation fragmentation (Field et al., 2017; Korolev et al., 2020).

The most well-studied SIP mechanism is the Hallett-Mossop process by which small ice splinters are produced during the riming of liquid drops onto existing frozen hydrometeors (Crawford et al., 2012; Field et al., 2017; Hallett and Mossop, 1974; Ladino et al., 2017; Manton et al., 2008; Phillips et al., 2007). However, even the Hallett-Mossop process is relatively poorly defined and its importance disputed. A recent laboratory study failed to observe rime-splintering in conditions designed to stimulate the Hallett-Mossop process

(Emersic and Connolly, 2017), and some recent literature suggests that previous observations of ICNC attributed to the Hallett-Mossop process may have been indicative of other secondary ice formation mechanisms (Korolev et al., 2020). Nevertheless, as it is the only SIP mechanism that is currently represented in most numerical weather prediction (NWP) models, we focus on the uncertainty associated with the Hallett-Mossop process in this study.

In addition to the individual uncertainties in INP number concentration, ice-nucleating ability temperature dependence, and SIP rates, these three variables can also interact causing non-linear or counterintuitive changes in cloud properties, further motivating the exploration of their combined effects here. For example, the highest ice crystal production rate was shown to occur at intermediate INP concentrations and Hallett-Mossop rates (Crawford et al., 2012; Sullivan et al., 2017).

We use Latin hypercube sampling and an idealised cloud model coupled to a double-moment microphysics scheme to investigate the individual and interacting effects of the INP number concentration, the temperature dependence of INP number concentration across the full spectrum of mixed-phase temperatures, and the Hallett-Mossop ice production rate on the micro- and macro-physical properties of an idealised deep convective cloud. We use statistical emulation where appropriate to investigate the importance of these uncertain input parameters and their interactions with one another for the anvil properties of the simulated deep convective cloud. Statistical emulation is a powerful tool for analysing and understanding the behaviour of complex systems (Johnson et al., 2015b; Lee et al., 2011; Marshall et al., 2019; Wellmann et al., 2018) because it enables dense sampling over a defined parameter uncertainty space, leading to detailed response surfaces of system behaviour.

This chapter is structured as follows: Section 3.3 describes the idealised cloud model and the simulation set-up, as well as the methods used in our analysis. In Section 3.4, we examine the role of the uncertain input parameters in determining the ice crystal number concentration, ice

crystal size, and the cloud fraction of the simulated deep convective anvil cirrus. In Section 3.5, we detail the limitations of our study. Section 3.6 summarises the main findings and implications of this study.

### **3.3. Methods**

#### **3.3.1. Model set-up and simulation design**

This work utilised the Met Office NERC Cloud Model (MONC) which is an idealised cloud model developed from the Met Office Large Eddy Model (LEM) (Gray et al., 2001). Here, MONC is coupled to the Met Office Cloud AeroSol Interacting Microphysics (CASIM) module, which is a multi-moment bulk scheme that allows simulations of aerosol cloud interactions with advanced microphysical capabilities. MONC-CASIM has been used to investigate aerosol cloud interactions in nocturnal fog (Poku et al., 2019) and low-level clouds during the West African monsoon season (Dearden et al., 2018). CASIM has also been used with the Met Office Unified Model in regional simulations of coastal mixed-phase convective clouds (Miltenberger et al., 2018b, 2018a), South-East Pacific stratocumulus clouds (Grosvenor et al., 2017), Southern Ocean supercooled shallow cumulus (Vergara-Temprado et al., 2018), midlatitude cyclones (McCoy et al., 2018), and CCN-limited Arctic clouds (Stevens et al., 2018).

The simulations presented in this chapter use a grid box spacing of 250 m (500\*500 grid boxes) and 138 vertical levels. The model diagnostics are output every 5 minutes and the timestep is flexible to maintain model stability with a maximum value of 2 seconds and a minimum value of 0.01 seconds. MONC has a number of prognostic variables including u, v and w velocity

scalars, potential temperature and water vapour content. MONC-CASIM is configured to be two-moment in this work. The number and mass concentrations for cloud droplets, rain droplets, ice crystals (or cloud ice), graupel, and snow are prognostic variables. The prognostic aerosol variables utilised in this work are the soluble accumulation-mode aerosol mass and number concentrations and the coarse dust mass and number concentrations. The aerosol can be advected around but is not scavenged. The model boundary conditions are cyclical and as such scavenging the aerosol would result in a rapid removal of all aerosol from the simulation.

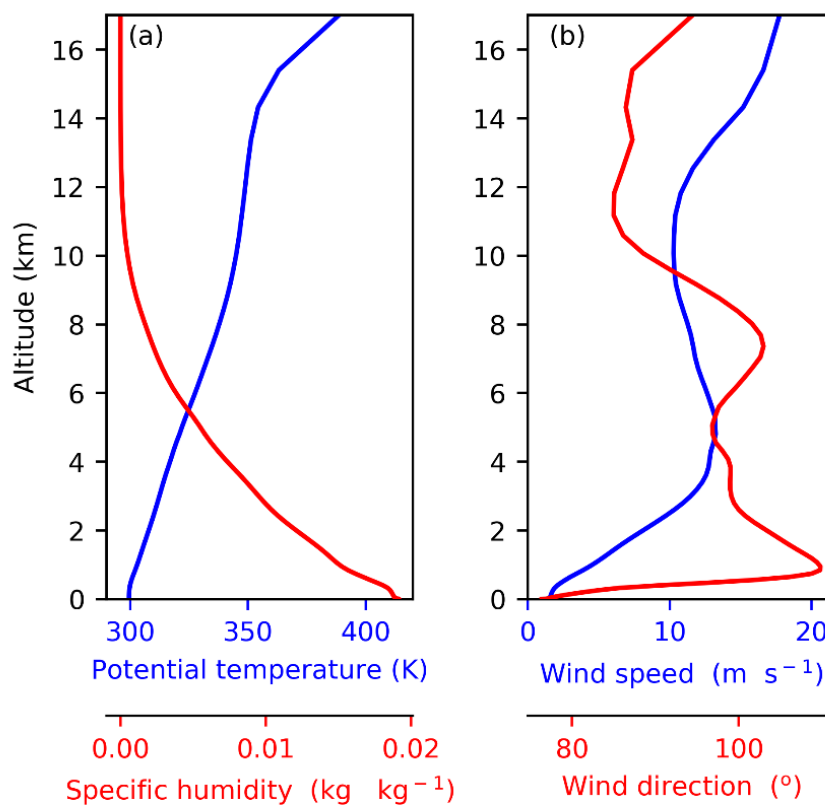


*Figure 3.1. Initial conditions. The potential temperature and specific humidity (a), and wind speed and direction (b) profiles used to initiate the model. The profiles shown were extracted from a Met-Office Unified Model simulation of a large deep convective cloud field in the maritime tropical Atlantic (described in Hawker et al. (2021)). The profiles were averaged over out-of-cloud areas between 1200 and 1800 UTC.*

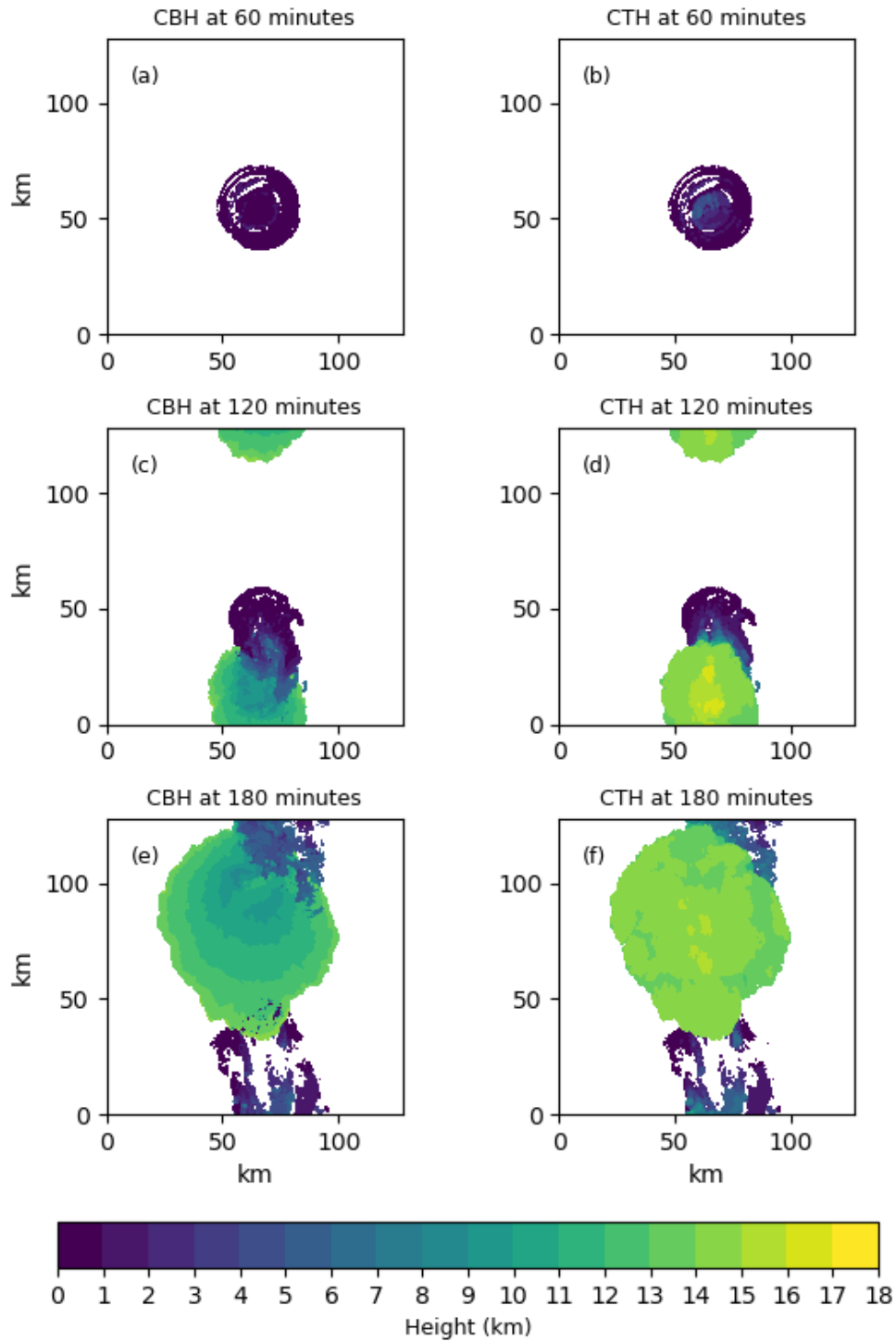
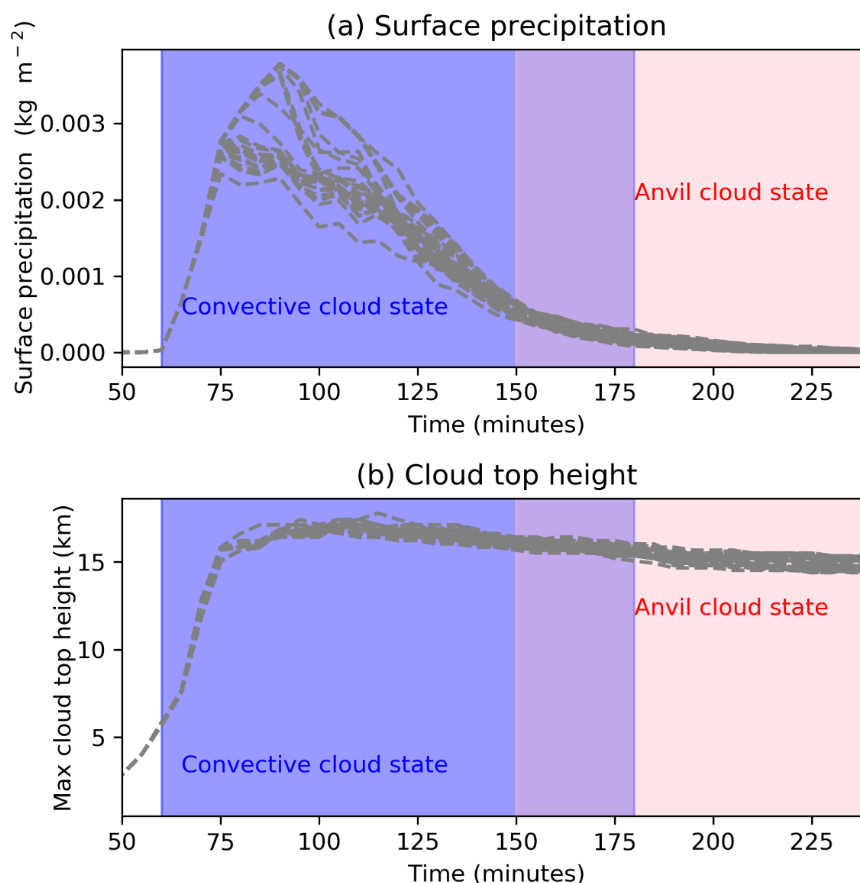


Figure 3.2. Cloud evolution. The cloud base height (CBH, a, c, e) and cloud top height (CTH, b, d, f) of the simulated convective cloud for the base case simulation.

The CASIM model configuration is very similar to that of Chapter 2 and Miltenberger et al. (2018a). Cloud droplet activation is parameterised according to Abdul-Razzak and Ghan, (2000). The soluble accumulation mode aerosol is used for cloud droplet activation and a simplistic CCN activation parameterisation is included for the insoluble aerosol mode (Abdul-Razzak and Ghan, 2000) that assumes a 5% soluble fraction on dust.

Condensation is represented using saturation adjustment meaning that where liquid is present at the end of a timestep, the specific humidity is adjusted to be the equilibrium saturation over water and the grid box temperature and liquid mass is adjusted accordingly. If only frozen hydrometeors are present in a grid box, saturation is treated explicitly. Collision-coalescence, riming of ice crystals to graupel and aggregation of ice crystals to snow is represented. Rain drop freezing is described using the parameterisation of Bigg (1953). Deposition onto ice is treated explicitly allowing ice particles to grow in the presence of liquid. However due to the saturation adjustment treatment of condensation, the Wegener-Bergeron-Findeisen process is not present in exactly the same way as one would expect in a real cloud.

We simulate a single deep convective cloud using the MONC-CASIM model. The cloud formation is initiated using a single warm bubble with a radius of 20 km, a height of 500 m and a temperature perturbation of 1.5°C. The model was initiated using mean profiles (u, v, w, theta, qv, and soluble accumulation aerosol number and mass concentration) extracted from a Met-Office Unified Model simulation of a deep convective cloud field sampled during the Ice in Clouds-Dust flight campaign on the 21st of August 2015 (out of cloud values between 12:00 and 15:00) (Hawker et al., 2021). Details of this simulation including comparisons to observations are available in Hawker et al. (2021). The environmental conditions used to initiate the model are shown in Figure 3.1.



*Figure 3.3. Simulated cloud properties. Evolution of surface precipitation (a) and maximum cloud top height (b) over time for all simulations included in this analysis. The convective and anvil cloud stages defined for the purposes of analysis are highlighted.*

The simulation produces a large convective cloud with an extensive anvil (Figure 3.2). Figure 3.3 shows that the cloud evolution for all simulations is similar with a large increase in surface precipitation (Figure 3.3a) from 60 minutes to up to 90 minutes and a decline that begins between 70 and 90 minutes. Similarly, the maximum cloud top height for most simulations peaks at around 120 minutes after which it declines slightly indicating a reduction in convective strength after this time (Figure 3.3b). It is important for statistical emulation (Section 3.3.5), where one value for each cloud response is extracted from the model, that the clouds in each simulation undergo similar lifecycles. We can see from Figure 3.3 that this is the case for the simulated deep convective cloud.

*Table 3.1. Target output variables. List of target output variables discussed in this study and the criteria used to extract their values from the simulation output.*

	<b>Output variables</b>	<b>Criteria</b>
<b>Anvil cloud stage</b>	Anvil ICNC, anvil ice crystal effective radius	Cloud condensate $> 1 \times 10^{-6} \text{ kg}^{-1} \text{ kg}^{-1}$ (i.e. in-cloud) Ice water path $> 0.04 \text{ kg m}^{-2}$ , Cloud base height $> 9 \text{ km}$ , Time period in simulation: 150-240 minutes.
	Cloud fraction	Mean peak in cloud fraction profile where cloud is where cloud condensate $> 1 \times 10^{-6} \text{ kg}^{-1} \text{ kg}^{-1}$ , Time period in simulation: 150-240 minutes.
<b>Convective cloud stage</b>	Ice particle production rates, accretion rates, hydrometeor water paths and column number concentrations, updraft speed	Cloud condensate $> 1 \times 10^{-6} \text{ kg}^{-1} \text{ kg}^{-1}$ (i.e. in-cloud), Time period in simulation: 60-180 minutes.

When extracting the diagnostic variables and single values to be used for analysis, results from 60 minutes to 180 minutes into the simulation are used to represent the convective cloud state. Sixty minutes is approximately the time when the cloud first reaches the mixed-phase cloud level where freezing can first occur ( $\sim 4 \text{ km}$ , Figure 3.2b) and therefore where the perturbations to the chosen uncertain input parameters (Section 3.3.2) start to cause divergence between simulations. When isolating the anvil stages of cloud development, we use the results from between 150 and 240 minutes into the simulation. Table 3.1 lists the target output response variables that are investigated and the time period from which they are extracted.

### 3.3.2. Input parameters and their uncertainty ranges

In this work, we investigate the effect of variations in absolute potential INP number concentration, INP parameterisation slope and the rate of ice production by the Hallett-Mossop process. For the purposes of this study, the magnitude of these three variables are varied using the following uncertain input parameters:

- Absolute potential INP number concentration or the total number of aerosol capable of nucleating ice is varied using  $[\text{INP}]_{\text{MAX}}$ .  $[\text{INP}]_{\text{max}}$  is the factor by which the profile of INP concentration at  $-38^{\circ}\text{C}$  in the base case is multiplied.
- INP parameterisation slope, termed  $\lambda_{[\text{INP}]}$  herein is the change in the  $\log_{10}$  of the INP number concentration per degree Celsius increase in temperature between  $-38$  and  $-3^{\circ}\text{C}$ , i.e.  $d(\log_{10}[\text{INP} (\text{m}^{-3})])/dT (^{\circ}\text{C})$  which is shortened to units of  $^{\circ}\text{C}^{-1}$  herein.
- Rate of ice production by the Hallett-Mossop process, termed **HM-rate** herein. This is the number of secondary ice splinters produced by the Hallett-Mossop process for every milligram of rimed material, shortened to units of  $\text{mg}^{-1}$  herein.

The representation of these uncertain input parameters in MONC and their range of potential values are described in the following Sections 3.3.2.1 to 3.3.2.3. The base case, minimum and maximum values of  $\lambda_{[\text{INP}]}$  and the INP concentration achieved by varying  $[\text{INP}]_{\text{MAX}}$  can be seen in Figure 3.4a, along with the base case INP number concentration profile which is perturbed using  $[\text{INP}]_{\text{MAX}}$  (Figure 3.4b). The combined perturbations of  $[\text{INP}]_{\text{MAX}}$  and  $\lambda_{[\text{INP}]}$  produce an INP parameterisation that is applied in the cloud model.

#### 3.3.2.1. Absolute potential INP concentration – $[\text{INP}]_{\text{MAX}}$

The base case coarse dust number aerosol profile applied in MONC is shown in Figure 3.4b. In the MONC model, the coarse dust aerosol can act as INP, and for the purposes of these

simulations, the ambient concentration of these particles is fixed as the INP concentration at -38°C. The profile shown in Figure 3.4b is the mean daily aerosol concentration, assumed to be predominately dust, in Cape Verde extracted from a 2015 Global Model of Aerosol Processes model (GLOMAP-mode; (Mann et al., 2010)) simulation run scaled to be approximately equal to the mean daily K-feldspar INP concentration from the same simulation (Vergara-Temprado et al., 2017). We use the scaled mean daily aerosol profile rather than the INP from the GLOMAP-mode itself, because the aerosol profile has both mass and number concentration information and this is not available for the GLOMAP-mode INP profile. The absolute INP number concentration is perturbed by multiplying the profile in Figure 3.4b by  $[\text{INP}]_{\text{MAX}}$  values between  $1 \times 10^{-4}$  and 200 to vary the potential INP number concentration. The minimum and maximum INP number concentrations the chosen  $[\text{INP}]_{\text{MAX}}$  values produce for the height of maximum aerosol concentrations in the base case (~3 km, Figure 3.4b) are shown in Figure 3.4a (black triangles) and correspond to the minimum and maximum values of observed INP from numerous collated field and laboratory measurements (Kanji et al., 2017).

### 3.3.2.2. INP parameterisation slope – $\lambda_{[\text{INP}]}$

$\lambda_{[\text{INP}]}$  is perturbed by varying the exponent (P) in equation (1) below, which determines the number of active sites ( $n_s$ ) per unit area of an aerosol population at temperature T, from -1.3 and -0.1. For this study, we define the number of active sites,  $n_s$ , as:

$$n_s = e^{P \times T + i} \quad (1)$$

where  $i$  is the intercept of the natural log of  $n_s$  at 0°C and T is the ambient temperature in degrees Celcius. The equation is a basic form of  $n_s$ -based INP parameterisations and is adapted from Niemand et al. (2012). In the Niemand et al. (2012) parameterisation, P is -0.517 and results in a  $\lambda_{[\text{INP}]}$  of  $\sim -0.22 \text{ } ^\circ\text{C}^{-1}$  shown as the base case  $\lambda_{[\text{INP}]}$  in Figure 3.4a. The minimum (steepest) value of  $\lambda_{[\text{INP}]}$  is  $-0.5646 \text{ } ^\circ\text{C}^{-1}$  (P=-1.3) which is slightly steeper than that of the

Atkinson et al. (2013) parameterisation based on K-feldspar. The maximum (shallowest) value of  $\lambda_{[INP]}$  is  $-0.0434 \text{ } ^\circ\text{C}^{-1}$  ( $P=-0.1$ ) which is slightly shallower than that of the Meyers et al. (1992) parameterisation. The minimum (steepest) and maximum (shallowest) slopes simulated in this work are shown in Figure 3.4a for an insoluble aerosol concentration of  $1 \text{ cm}^{-3}$  with a mean radius of  $1 \text{ }\mu\text{m}$ .

In addition to varying the exponent, the original Niemand et al. (2012) parameterisation was altered to allow the INP number concentration at  $-38^\circ\text{C}$  (determined by  $[INP]_{MAX}$ ) to be exactly equal to the insoluble aerosol number concentration. This avoids interdependence between the  $[INP]_{MAX}$  and  $\lambda_{[INP]}$  which can occur at low temperatures where the INP concentration plateaus at low temperatures at the aerosol concentration. This plateau can be seen in the Niemand et al. (2012) line in Figure 3.4a. Modification of the original Niemand et al. (2012) parameterisation allows the intercept ( $i$  in Equation 1) of the INP parameterisation to be calculated as follows:

$$i = (\ln N - \ln S) - (P \times (-38)) \quad (2)$$

Where  $N$  is the number of potential INP in  $\text{m}^{-3}$  and  $S$  is the surface area of the available INP in  $\text{m}^{-2}$ . The INP concentration at temperature  $T$  is therefore:

$$INP = n_s \times S \quad (3)$$

Heterogeneous freezing is active between  $-38$  and  $-3^\circ\text{C}$  in the MONC-CASIM model used in this work.

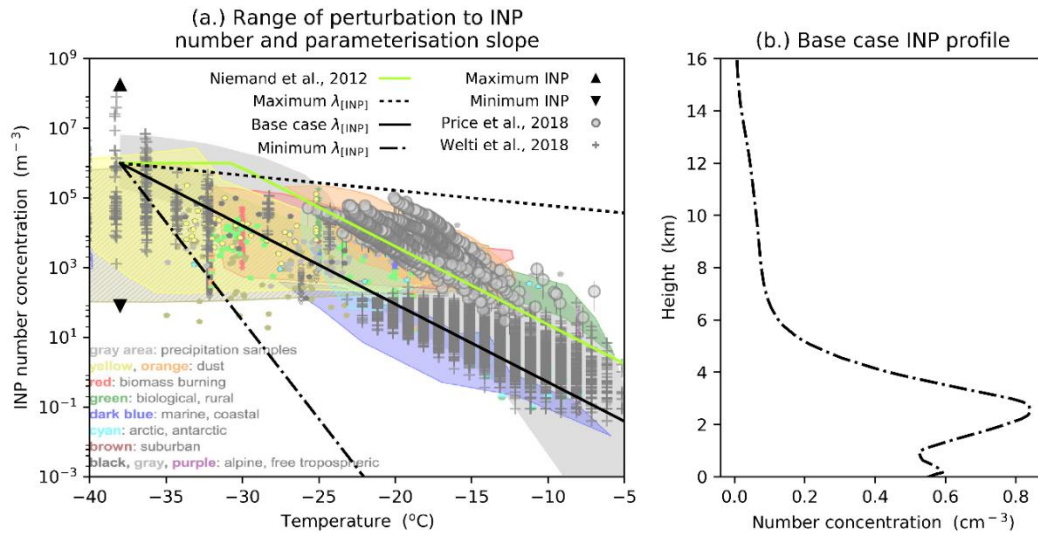


Figure 3.4. INP parameterisation slopes ( $\lambda_{[INP]}$ ) and potential INP profile (varied using  $[INP]_{MAX}$ ). The base case (black solid line), minimum or steepest (black dash-dotted line) and maximum or shallowest (black dashed line) perturbations to  $\lambda_{[INP]}$  are shown in (a) for an aerosol concentration of  $1\text{ cm}^{-3}$  and a radius of  $1\ \mu\text{m}$ , and the Niemand et al. (2012) parameterisation (light green solid line). The INP parameterisations are overlain on Figure 1-10 from Kanji et al. (2017) (© American Meteorological Society. Used with permission), showing observed INP concentrations along with some recent measurements from Cape Verde in grey (Price et al., 2018; Welti et al., 2018). Figure 3.1b shows the base case INP number concentration (at a temperature of  $-38^\circ\text{C}$ ) perturbed in this study. Also shown in Figure 3.1a is the maximum and minimum INP concentration at  $-38^\circ\text{C}$ , achieved by perturbing the profile shown in Figure 3.1b using  $[INP]_{MAX}$  (up- and downward pointing black triangles).

### 3.3.2.3. The Hallett-Mossop process ice production rate/HM-rate

The HM-rate in the model is varied from 1 to 1000 splinters per milligram of rimed liquid. The default value of ice production from the Hallett-Mossop process in MONC-CASIM is  $350\ \text{mg}^{-1}$ . This value is the best estimate of ice production based on a number of laboratory studies, and was frequently used in previous modelling studies (Connolly et al., 2006; Hallett and Mossop, 1974; Mossop, 1985). However, other rates have been reported. An upper limit of  $1000\ \text{mg}^{-1}$  aligns with previous modelling studies where the rate of ice production by the Hallett-Mossop

process was varied (Connolly et al., 2006). This upper limit also allows us to account somewhat for the possibility that the Hallett-Mossop process operating in real clouds is stronger than that observed in laboratory studies (Field et al., 2017; Korolev et al., 2020; Takahashi et al., 1995).

### 3.3.4. Selection of uncertain input parameter combinations

MONC was run with combinations of values of  $[\text{INP}]_{\text{MAX}}$ ,  $\lambda_{[\text{INP}]}$  and HM-rate from within the ranges shown in Table 3.2. These combinations of uncertain input parameters input into the cloud model were selected using a maximin Latin hypercube design algorithm. Latin hypercube sampling is based on the Latin Square and ensures optimum space filling (Johnson et al., 2015b; Lee et al., 2011; McKay et al., 2000) by maximising the minimum distance between points in the cube (Lee et al., 2011). The values of the uncertain input parameters used in every MONC simulation are shown in Figure 3.5. In total 73 simulations of the deep convective cloud were carried out. The values of  $\lambda_{[\text{INP}]}$  and HM-rate are selected by sampling on a linear scale while the values of  $[\text{INP}]_{\text{MAX}}$  are selected by sampling on a logarithmic scale. This is because INP number concentrations vary over multiple orders of magnitude (Figure 3.4a) and sampling  $[\text{INP}]_{\text{MAX}}$  on a linear scale would bias the design to higher INP number concentrations.

The INP parameterisations input to the cloud model as a result of the perturbations to the  $[\text{INP}]_{\text{MAX}}$  and  $\lambda_{[\text{INP}]}$  are shown in Figure 3.5d. As a result of not representing the plateauing of the parameterisation (as can be seen in the Niemand et al. (2012) line in Figure 3.4a) in order to avoid codependence between  $\lambda_{[\text{INP}]}$  and  $[\text{INP}]_{\text{MAX}}$ , we have large coverage of a region of parameter space with unrealistically low INP concentrations (light grey and pink dots in Figure 3.5a and light grey and pink lines in Figure 3.5d). Additional simulations in the ‘realistic’ regions of parameter space (shown by the red and black dots in Figure 3.5a and red and black

lines in Figure 3.5d) were conducted to compensate for this, and the values of the additional simulations were selected by augmenting points into the largest gaps in the realistic section of the original design.

*Table 3.2. Experiment design. The base case, minimum and maximum values of the variables perturbed in this study.*

<b>Uncertain parameter</b>	<b>Estimated base case</b>	<b>Minimum value of perturbation</b>	<b>Maximum value of perturbation</b>	<b>Perturbed on a log or linear scale?</b>
$\lambda_{[\text{INP}]}$ ( $d(\log_{10}[\text{INP} (\text{m}^{-3})])/dT(^{\circ}\text{C})$ ) [value of P in Eq. 1]	-0.2245 [-0.517]	-0.5646 [-1.3]	-0.0434 [-0.1]	Linear
$[\text{INP}]_{\text{MAX}}$ [approximate INP number concentration at peak aerosol layer ( $\text{cm}^{-3}$ )]	1 [0.82]	$1\text{e-}4$ [ $8.2 \times 10^{-3}$ ]	200 [164]	Log (base 10)
HM-rate (splinters produced per milligram rimed)	350	1	1000	Linear

The use of a maximin Latin hypercube to design the parameter combinations for the simulations cover the 3-d parameter space in an optimum manner. As a result we can evaluate the full effects of the parameters (individual and interacting) using traditional analysis on just the simulation data itself, as well as employing statistical emulation (described in Section 3.3.5) to analyse a more dense sampling of the uncertainty space.

### **3.3.5. Statistical emulation of the model output**

Statistical emulation is a “process by which the computer model is replaced by a statistical surrogate model that can be run more efficiently” (Lee et al., 2011). This approach has previously been used to look at deep convective cloud microphysical properties in a 3D model (Johnson et al., 2015), hail formation (Wellmann et al., 2018), nocturnal stratocumulus (Glassmeier et al., 2019) and aerosol forcing from volcanic eruptions (Marshall et al., 2019). In this study, as well as using traditional methods of analysis, we explore the usefulness of statistical emulation as a tool to understand the interacting effects of mixed-phase ice production mechanisms.

Statistical emulation involves creating a mapping from the input space (where the inputs have been sampled to ensure good coverage of the multi-dimensional parameter space) to an output variable of interest so that the values of the output variable in question can be estimated at all regions of parameter space within the input parameter ranges (Lee et al., 2011). In this study, we use a Gaussian process as the basis for the emulator (Johnson et al., 2015; Lee et al., 2011; Marshall et al., 2019).

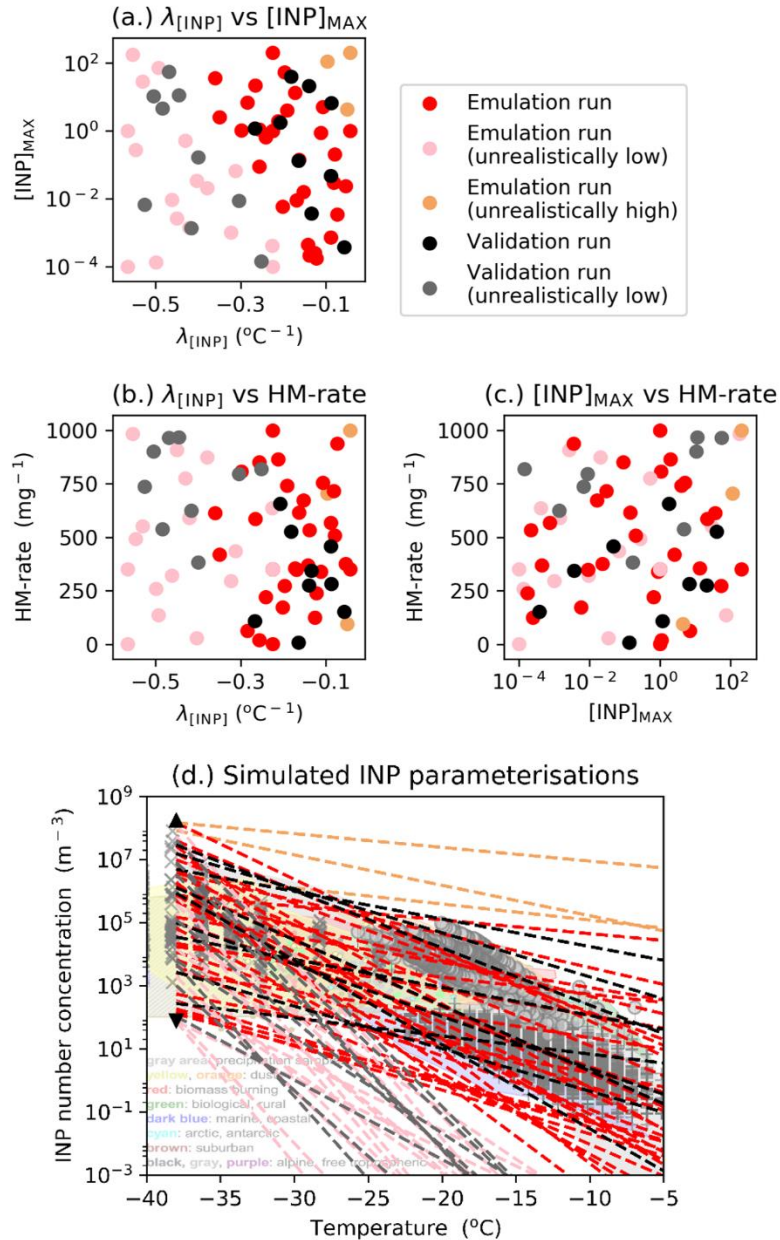


Figure 3.5. Experiment design. Values of the uncertain input parameter combinations used in the cloud model for the three uncertain input parameters ( $[INP]_{MAX}$  and  $\lambda_{[INP]}$  (a),  $\lambda_{[INP]}$  and HM-rate (b) and  $[INP]_{MAX}$  and HM-rate (c)). Shown in (d) is the resultant INP parameterisations arising due to the combination of perturbations to  $\lambda_{[INP]}$  and  $[INP]_{MAX}$  overlain on Figure 1-10 of Kanji et al. (2017) (© American Meteorological Society. Used with permission). The parameterisations shown in (d) are calculated for an INP number concentration of  $0.82 \text{ cm}^{-3}$  which is the peak INP number concentration for the base case ( $[INP]_{MAX} = 1$ ) profile shown in Figure 3.4d. Output from the simulations shown in red, pink and orange are used to build the emulator while output from the simulations shown in black or grey are used to validate the emulator results.

Statistical emulation has advantages over traditional one-at-a-time tests (where one variable is varied at predictable values from a control or base case while all other variables are held constant). Firstly, it allows the exploration of the effects of simultaneously perturbing multiple uncertain input parameters on output variables of interest across the entirety of reasonable parameter space for a much reduced number of complex simulations. Secondly, dense sampling via statistical emulation enables techniques such as variance-based sensitivity analysis to be applied, through which we can identify the input parameters that are contributing the most uncertainty to important output responses. This subsequently allows for the direction of resources towards quantifying and accurately representing those key parameters that contribute large amounts of uncertainty to output variables of interest.

An underlying assumption of the Gaussian process emulator is that the output of the cloud model varies smoothly and continuously. Based on this assumption, the emulator fits a smooth response surface that passes directly through each training point. To test whether the emulator can accurately predict the output of the cloud model, it is necessary to validate the prediction against output from simulations that have not been used to train the emulator. The simulations used to train and validate the emulator are shown in Figure 3.5 (a-c). Fifty-two simulations are used to train each emulator. This is well in excess of the thirty simulations recommended by Loepky et al. (2009), who states that 10 times the number of variable parameters is required. Eighteen additional simulations are used to validate the emulator. The model's output from these 18 simulations is compared with the mean and 95% confidence interval predicted by the emulator at those combinations of the uncertain input parameters.

Variance-based sensitivity analysis is used to measure the sensitivity of the cloud model outputs to the three uncertain input parameters and their interaction effects (Johnson et al., 2015b; Saltelli et al., 2000). The overall variance attributed to each input can be separated into the individual or main effect index of each input parameter and the total effect index which

comprises the variation attributed to the input parameter in question including due to interactions with other input parameters (Saltelli et al., 2000). The main effect index tells us the proportion of variance in the value of an output variable that could be minimized if the value of each individual input parameter was known exactly. The difference between the total and main effect indices of a parameter tells us how much variance in the output variable is determined by the input parameter in question interacting with other input parameters (Johnson et al., 2015b). In this work, the variance-based sensitivity analysis is carried out using the extended-FAST (Fourier Amplitude Sensitivity Test) approach detailed in Saltelli et al. (1999).

## **3.4. Results**

### **3.4.1. Anvil cloud properties**

We first examine the effect of variations in  $[\text{INP}]_{\text{MAX}}$ ,  $\lambda_{[\text{INP}]}$  and HM-rate on anvil cloud properties. We focus on the anvil ice properties in Sections 3.4.1.1 and 3.4.1.2 because anvil cloud can persist in the atmosphere longer than the deep convective cloud that forms it (and beyond the simulation period here) and is therefore climatically more important for cloud-radiation interactions. Tropical convectively produced cirrus can persist in the atmosphere for 1-2 days (Luo and Rossow, 2004) while the convective stage of the deep convective cloud simulated here has decayed after  $\sim 3$  hours. An anvil with more numerous, smaller crystals will persist longer in the atmosphere than one with fewer, larger crystals. In Section 3.4.1.3, we examine the simulated anvil cloud fraction and the microphysical properties controlling it. The anvil region of the cloud is defined as the cloudy regime occurring between 150 and 240 minutes in the simulations with a cloud base height greater than 9 km and an ice water path less than  $0.04 \text{ kg m}^{-2}$ . Other thresholds were tested and did not change the results substantially.

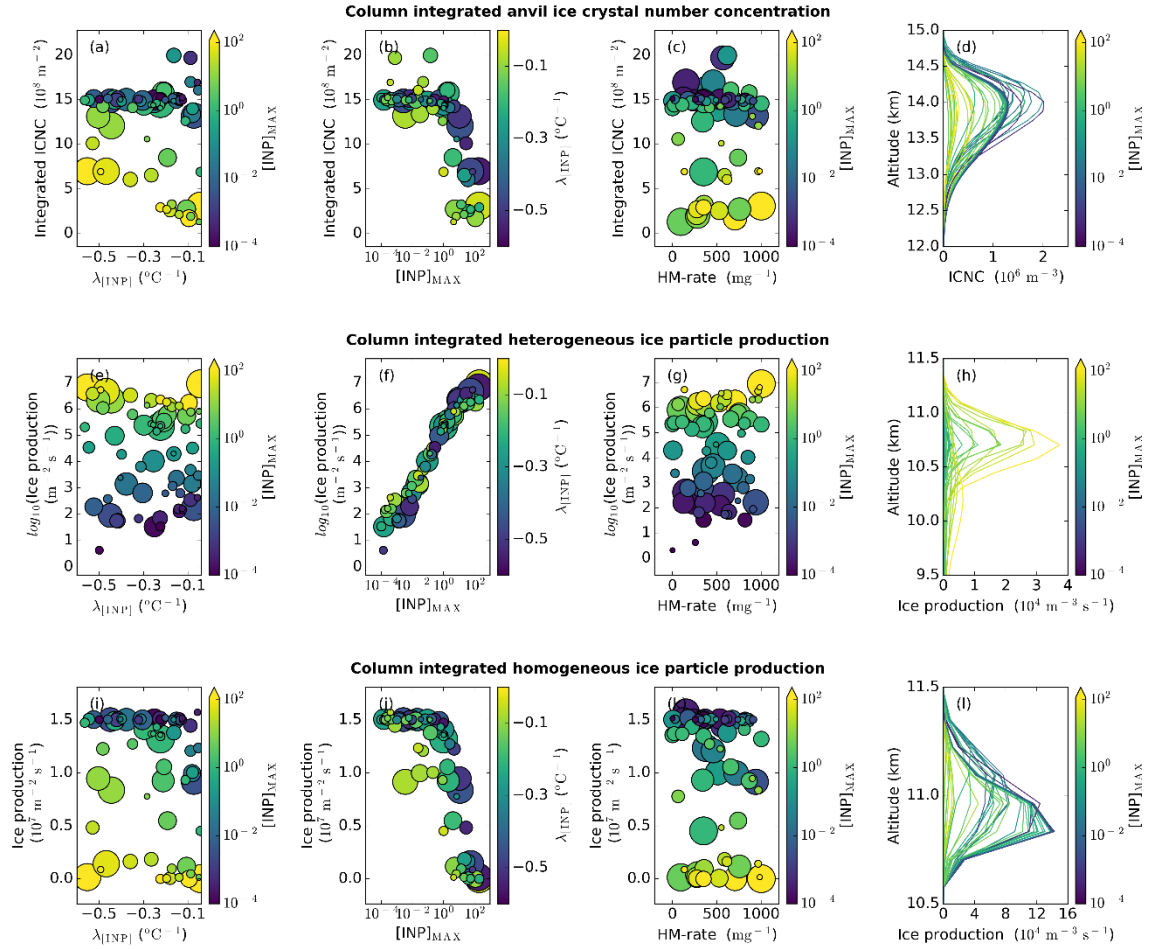


Figure 3.6. Anvil ICNC and ice particle production rates. Dependence of anvil ice crystal number concentration (a-d), ice particle production by heterogeneous freezing (e-h), and ice particle production by homogeneous freezing (i-l) on the three uncertain input parameters:  $\lambda_{[INP]}$  (a, e, i),  $[INP]_{MAX}$  (b, f, j), and HM-rate (c, g, k). In-cloud profiles of anvil ICNC (d), ice particle production by heterogeneous freezing (h), and ice particle production by homogeneous freezing (l) in all simulations coloured by  $[INP]_{MAX}$ . For panels (a), (e), and (i), the colour of the markers indicate  $[INP]_{MAX}$  and the marker size indicates HM-rate. For panels (b), (f), and (j), the colour of the markers indicate  $\lambda_{[INP]}$  and the marker size indicates the HM-rate. For panels (c), (g), and (k), the colour of the markers indicate  $[INP]_{MAX}$  and the marker size indicates the  $\lambda_{[INP]}$  value. Panels (a-d) are the average of the cloud property between 150 and 240 minutes (anvil stage) in the simulation, while panels (e-l) are the average of the relevant cloud property between 60 and 180 minutes (convective stage) in the simulations.

### 3.4.1.1. Anvil ice crystal number concentration

The integrated anvil ICNC (defined as the mean ICNC in cloudy columns occurring between 150 and 240 minutes with a cloud base height  $> 9$  km and an ice water path  $< 0.04$  kg m<sup>-2</sup>) from all simulations is shown in Figure 3.6 (a-c). Figure 3.6d shows the associated mean anvil ICNC profile in each simulation. Anvil ICNCs are predominately controlled by the value of  $[INP]_{MAX}$  (Figure 3.6 a-d), with a higher  $[INP]_{MAX}$  causing lower anvil ICNCs (Figure 3.6 b, d). Figure 3.6 d shows that the higher the  $[INP]_{MAX}$ , the lower the anvil ICNC at all anvil altitudes. This is because the higher the  $[INP]_{MAX}$ , the higher the rate of heterogeneous freezing at the top of the mixed phase cloud (Figure 3.6 e-h) which reduces homogeneous freezing rates (Figure 3.6 i-l).

The homogeneous and heterogeneous ice particle production rates shown in Figure 3.6 (e-l) are the mean values from cloudy columns (e-g, i-k) or cloudy grid boxes (h, l) between 60 and 180 minutes of the simulation. Homogeneous freezing is a stronger mechanism of ice crystal production than heterogeneous freezing with peak ice particle production rates of  $\sim 14 \times 10^4$  m<sup>-3</sup> s<sup>-1</sup> (Figure 3.6 l) compared to  $\sim 3.5 \times 10^4$  m<sup>-3</sup> s<sup>-1</sup> by heterogeneous freezing (Figure 3.6 h). Note that these rates are occurring in different simulations so the peak rates of heterogeneous and homogeneous ice particle production do not occur concurrently in the parameter uncertainty space.

INP parameterisation slope,  $\lambda_{[INP]}$ , plays a very minor secondary role in controlling anvil ICNC (Figure 3.6 a). Simulations with a high  $[INP]_{MAX}$  (more yellow markers in Figure 3.6a) have slightly lower anvil ICNC at shallow  $\lambda_{[INP]}$ . The chosen Hallett-Mossop splinter production rate has no notable impact on anvil ICNC regardless of the value of  $[INP]_{MAX}$  or  $\lambda_{[INP]}$ .

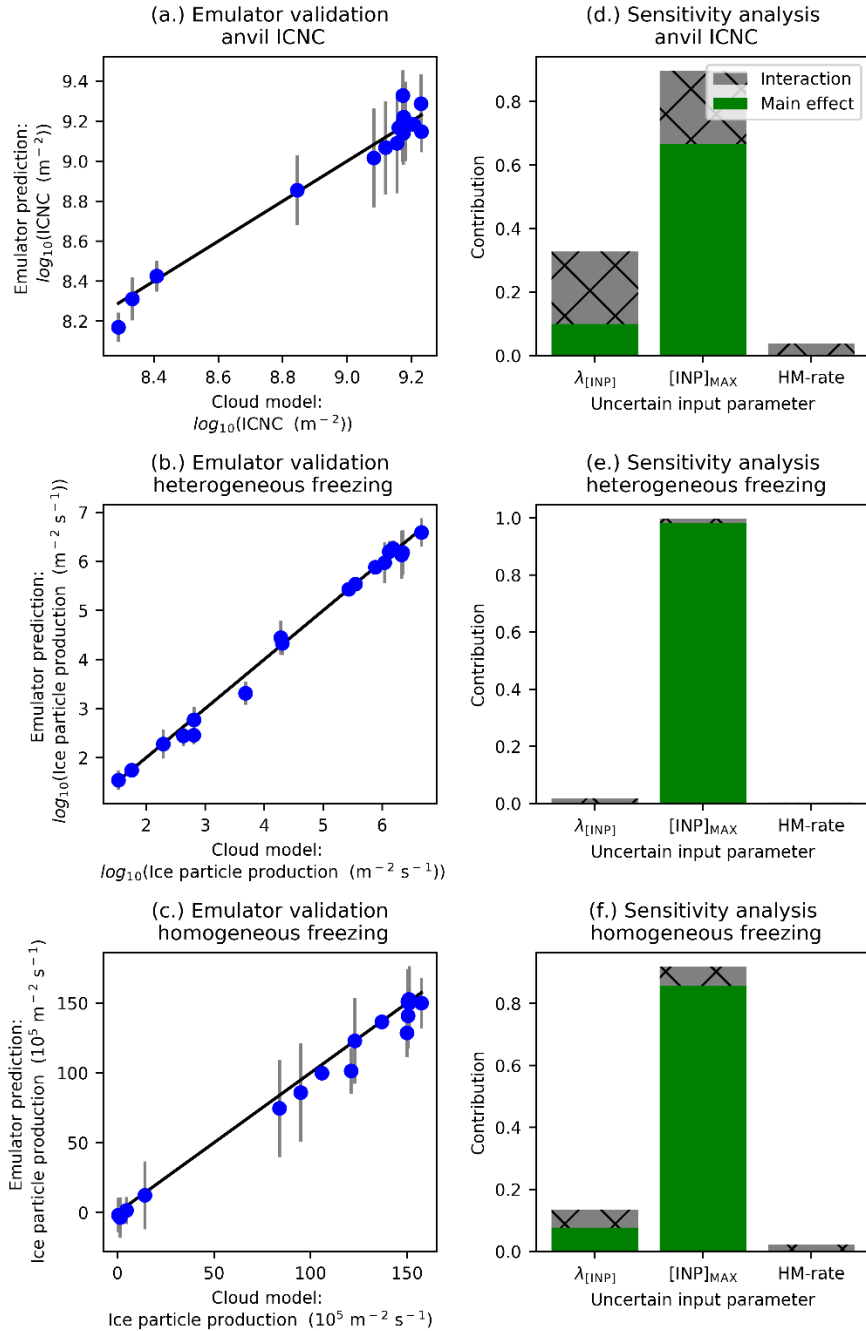


*Figure 3.7. Emulator validation and uncertain input contributions to output uncertainty. Validation of emulator results (a - c) and results of the variance-based sensitivity analysis (d - f) for anvil ICNC (a, b), ice particle production by heterogeneous freezing (c, d), and ice particle production by homogeneous freezing (e, f). In (a) - (c), the dots show the value of the validation run on the x-axis and the corresponding emulator mean prediction on the y-axis. 95% confidence intervals on the emulator predictions are also shown. An emulator that validates well will have dots close to the 1:1 line and small error bars.*

We now use statistical emulation to further examine the effects of our three uncertain input parameters ( $\lambda_{\text{INP}}$ ,  $[\text{INP}]_{\text{MAX}}$ , HM-rate) on anvil ICNC and convective heterogeneous and homogeneous ice particle production. Figure 3.7 (a - c) shows a comparison of the output from the validation simulations (shown in black and grey in Figure 3.5 a - d) with the corresponding emulator predictions at the same location in parameter space for anvil ICNC and convective heterogeneous and homogeneous ice crystal number production, along with 95% confidence intervals on the emulator predictions. All three outputs validate well with points close to or on the 1:1 line and small 95% confidence intervals that overlap the 1:1 line most of the time. This indicates that the emulator can capture the variability in the idealised cloud model well for the output variables in question.

Figure 3.7 (d - f) shows the results of variance-based sensitivity analysis and indicates the relative importance of the uncertain input parameters in controlling the variance in the value of the output variable in question. As was inferred from Figure 3.6,  $[\text{INP}]_{\text{MAX}}$  is the dominant input parameter controlling the variance of anvil ICNC and heterogeneous and homogeneous ice particle production rates, while  $\lambda_{\text{INP}}$  and interaction effects contribute a non-negligible, but secondary amount to the variance in anvil ICNC. Figure 3.7d indicates that  $[\text{INP}]_{\text{MAX}}$  is the key parameter driving the uncertainty in the anvil ICNC of the simulated deep convective cloud, contributing to over 60% of this output's uncertainty. Hence, the uncertainty in the anvil ICNC could be significantly reduced if the value of  $[\text{INP}]_{\text{MAX}}$  was to be known exactly. Similarly, this parameter is almost completely controlling the uncertainty in the column integrated heterogeneous ice particle production (Figure 3.7e), with no real contribution from the other parameters here. The interaction effects are relatively small for all three output variables accounting for only 30% of the variance in the anvil ICNC and less than 10% for the ice particle production by heterogeneous and homogeneous freezing.

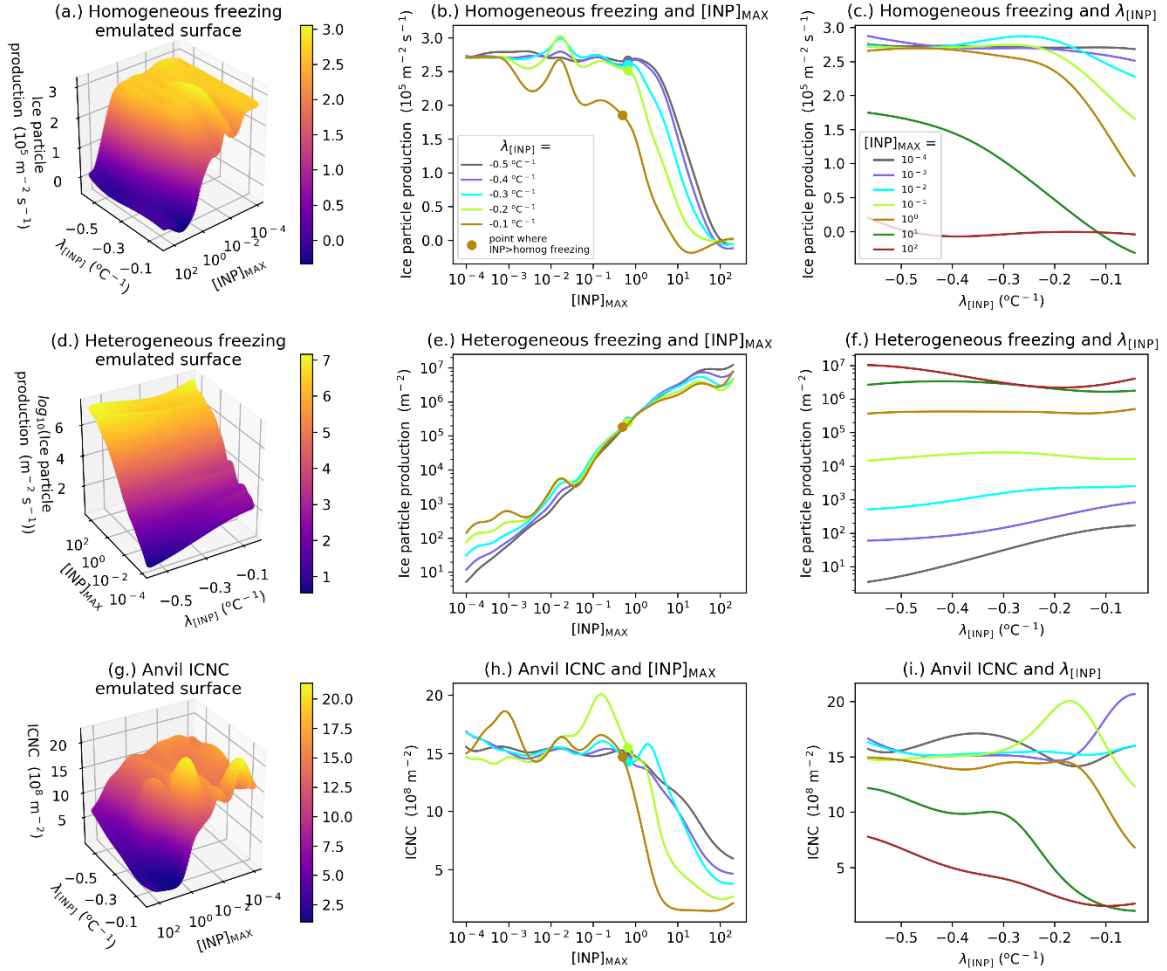


Figure 3.8. Emulator response surfaces. Prediction of ice particle production by homogeneous freezing (a, b, c), heterogeneous freezing (d, e, f), and anvil ICNC (g, h, i) by the emulator. Shown in (a), (d), and (g) are emulated response surfaces at a fixed HM-rate of 350 splinters  $\text{mg}^{-1}$  rimed. The colours indicate output values and are the same range and units as the z-axis. The line plots show the variation in predicted output value (y-axis) from these response surfaces for fixed  $\lambda_{[\text{INP}]}$  (b, e, h) and fixed  $[\text{INP}]_{\text{MAX}}$  (c, f, i).

Figure 3.8 (a, d, g) shows the emulator surfaces for homogeneous (a) and heterogeneous (d) ice particle production and anvil ICNC (g) at a fixed HM-rate of 350  $\text{mg}^{-1}$ . We hold the HM-rate constant because it had a minimal effect on the variance in the output variables (Figure 3.7d-f) and as such variations in its value do not alter the shape of the emulated surface substantially. It is important to note that the emulator response surface tracks through each cloud model point exactly and as such doesn't allow for 'noise' due to internal variability in

the cloud model output. As a result the emulator surfaces should be interpreted by examining the general smoothly varying trends rather than individual bumps which may be an artefact of the emulator fitting around a particular point.

Homogeneous freezing ice particle production is high and relatively constant between an  $[\text{INP}]_{\text{MAX}}$  of  $10^{-4}$  and 1 before decreasing rapidly when  $[\text{INP}]_{\text{MAX}}$  increases further (Figure 3.8a). The emulator response surface shows very little dependence on INP parameterisation slope apart from a slight decrease in homogeneous freezing rates at very shallow slopes above a  $\lambda_{[\text{INP}]}$  of  $-0.2 \text{ } ^\circ\text{C}^{-1}$ . Heterogeneous ice particle production increases relatively uniformly with increasing  $[\text{INP}]_{\text{MAX}}$ . At low  $[\text{INP}]_{\text{MAX}}$ , the heterogeneous ice particle production is highest for shallow  $\lambda_{[\text{INP}]}$  values, while at high  $[\text{INP}]_{\text{MAX}}$ , the heterogeneous ice particle production rates are highest at steep  $\lambda_{[\text{INP}]}$  values. The emulated anvil ICNC surface (Figure 3.8g) is very similar to that of homogeneous ice particle production (Figure 3.8a) with relatively uniform and high concentrations at  $[\text{INP}]_{\text{MAX}}$  values below 1 and sharp decreases as it moves towards higher  $[\text{INP}]_{\text{MAX}}$ .

Figure 3.8 (b, e, h) shows the average (mean) emulator response across the uncertainty range of  $[\text{INP}]_{\text{MAX}}$  of homogeneous (b) and heterogeneous (e) ice particle production and anvil ICNC (h) for different settings of  $\lambda_{[\text{INP}]}$  values (distinguished by line colours). In each line, the point where the rates of ice particle production by heterogeneous freezing first exceeds that of homogeneous freezing is marked. Homogeneous freezing is the dominant mechanism of cloud ice crystal production at  $[\text{INP}]_{\text{MAX}}$  values below 1 (Figure 3.8b) corresponding to an absolute INP number concentration of  $\sim 0.82 \text{ cm}^{-3}$  in the peak aerosol layer (Figure 3.4b) above which heterogeneous freezing becomes the dominant mechanism of ice crystal production for all  $\lambda_{[\text{INP}]}$  values (Figure 3.8e).

Homogeneous freezing is essentially completely shut off at an  $[\text{INP}]_{\text{MAX}}$  between 1 and 2 (Figure 3.8 b) meaning that at very high  $[\text{INP}]_{\text{MAX}}$  values all primary ice crystals in the

simulated deep convective cloud are formed via heterogeneous freezing. This is because heterogeneous freezing and subsequent processes in the mixed-phase region of the cloud significantly reduce the amount of cloud liquid reaching the homogeneous freezing altitude. Anvil ICNC decreases sharply as INP concentration increases as soon as heterogeneous freezing becomes the dominant mechanism of primary cloud ice production (Figure 3.8h). Based on the value of the peak INP number concentration shown in Figure 3.4b and assuming that the dust at 3 km of the applied profile is lifted to all levels of the simulated deep convective cloud, an INP number concentration of  $1 \text{ cm}^{-3}$  at any upper mixed-phase level may be enough to shut down homogeneous freezing.

Figure 3.8 (c, f, i) shows the average (mean) emulator response across the uncertainty range of  $\lambda_{\text{[INP]}}$  of homogeneous (c) and heterogeneous (f) ice particle production and anvil ICNC (i) for different settings of  $[\text{INP}]_{\text{MAX}}$  (distinguished by line colours). The ice particle production by homogeneous freezing is sensitive to  $\lambda_{\text{[INP]}}$  only at intermediate-high  $[\text{INP}]_{\text{MAX}}$  values between 1 and 10 (Figure 3.8c). Ice particle production by heterogeneous freezing is insensitive to changing  $\lambda_{\text{[INP]}}$  values except for a slight increase in heterogeneous freezing at low  $[\text{INP}]_{\text{MAX}}$  values where the rate of ice production is highest at shallow  $\lambda_{\text{[INP]}}$  (Figure 3.8f). Anvil ICNC is relatively insensitive to  $\lambda_{\text{[INP]}}$  values, except at high  $[\text{INP}]_{\text{MAX}}$  ( $>10$ ) where the highest anvil ICNCs occur at steep  $\lambda_{\text{[INP]}}$  values (Figure 3.8i).

Overall anvil ICNC is controlled predominately by INP number concentration ( $[\text{INP}]_{\text{MAX}}$ ) with a minor effect from the INP parameterisation slope ( $\lambda_{\text{[INP]}}$ ). The higher the  $[\text{INP}]_{\text{MAX}}$ , the lower the anvil ICNC. A shallow  $\lambda_{\text{[INP]}}$  can further reduce anvil ICNC, particularly at high  $[\text{INP}]_{\text{MAX}}$  values. The anvil ICNC is reduced substantially when the number of heterogeneously frozen ice crystals exceeds the number of homogeneously frozen ice crystals due to the efficient consumption of liquid at upper mixed-phase cloud levels before droplets can be frozen homogeneously.

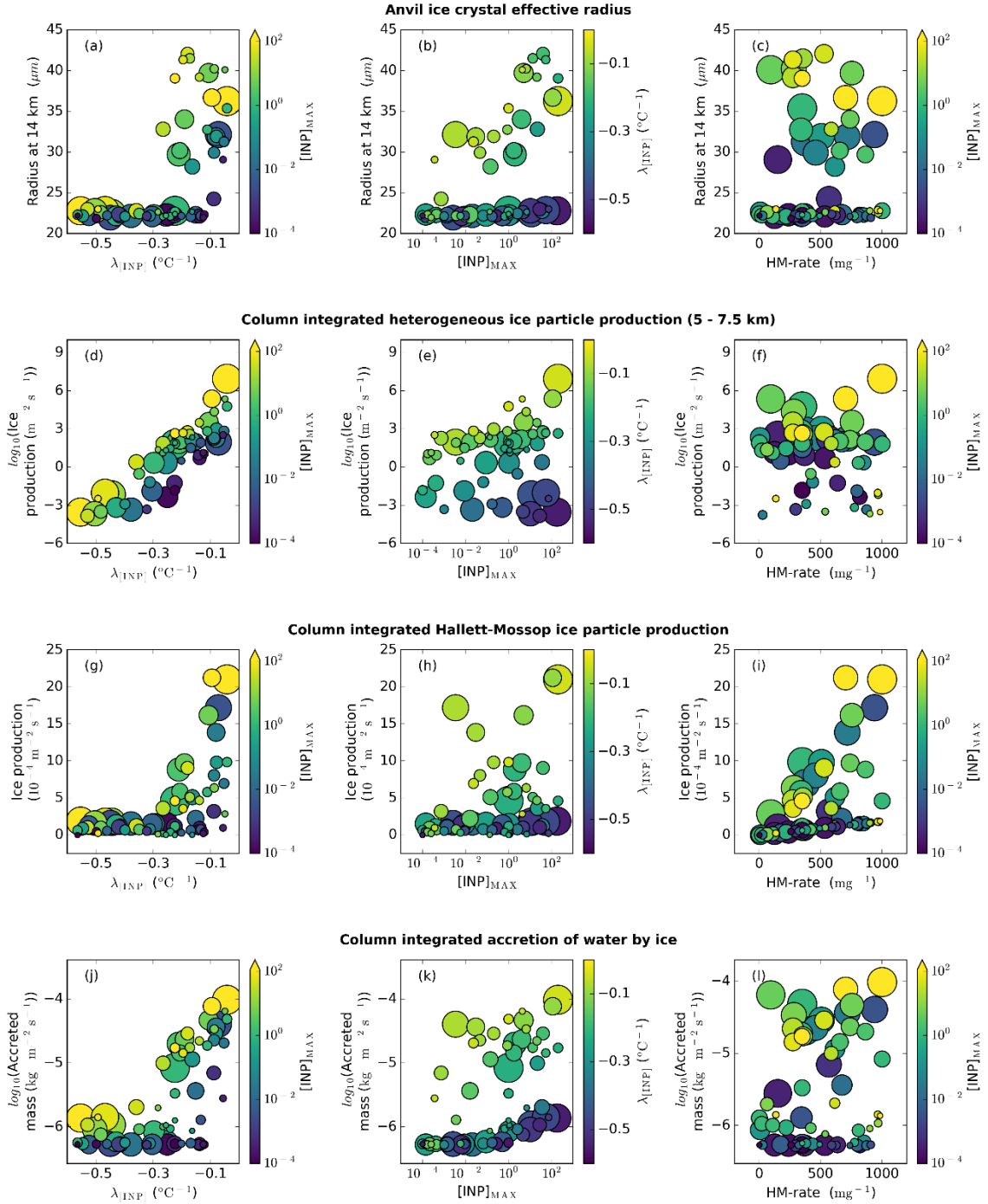


Figure 3.9. Anvil ice crystal size and driving processes. Dependence of anvil ice crystal effective radius (a-c), ice particle production by heterogeneous freezing between 5 and 7.5 km altitude (d-f), ice particle production by the Hallett-Mossop process (g-i), and the accretion of water by ice crystals (j-l) on the three uncertain input parameters:  $\lambda_{\text{INP}}$  (a, d, g, j),  $[\text{INP}]_{\text{MAX}}$  (b, e, h, k), and HM-rate (c, f, i, l). For the leftmost column, the colour of the markers indicates  $[\text{INP}]_{\text{MAX}}$  and the marker size indicates HM-rate. For the middle column, the colour of the markers indicate  $\lambda_{\text{INP}}$  and the marker size indicates the HM-rate. For the

*rightmost column, the colour of the markers indicate  $[INP]_{MAX}$  and the marker size indicates  $\lambda_{[INP]}$ . Panels (a-c) are the average of the cloud property between 150 and 240 minutes (anvil stage) in the simulation, while panels (d-l) are the average of the relevant cloud property between 60 and 180 minutes (convective stage) in the simulations.*

### **3.4.1.2. Anvil ice crystal size**

We now examine the impact of uncertainty in  $[INP]_{MAX}$ ,  $\lambda_{[INP]}$  and HM-rate on the anvil ice crystal effective radius (defined here as the ratio of the third to the second moments of the ice crystal size distribution). A larger ice crystal effective radius indicates that anvil ice particles will have a higher fall speed and lower lifetime, theoretically reducing the lifetime of the anvil cloud and reducing its radiative effect. The simulated ice crystal effective radius in the anvil cloud region at 14 km can be seen in Figure 3.9 (a-c). We used the effective radius at 14 km because it is the altitude of peak ICNC shown in Figure 3.6d.

Anvil ice crystal size exhibits two distinct regimes depending on the value of  $\lambda_{[INP]}$  which can be seen in Figure 3.9 (a-b). Simulations with a  $\lambda_{[INP]}$  shallower than approximately  $-0.3 \text{ }^\circ\text{C}^{-1}$  (Figure 3.9a) exhibit a large jump in ice crystal effective radius from under  $25 \text{ }\mu\text{m}$  to between  $27$  and  $45 \text{ }\mu\text{m}$ . In simulations with a shallow  $\lambda_{[INP]}$  and consequent jump in ice crystal size, the value of the effective radius is dependent on the  $[INP]_{MAX}$ , with simulations with larger  $[INP]_{MAX}$  values having a larger ice crystal size (Figure 3.9b). This indicates that while anvil ICNC was determined predominately by  $[INP]_{MAX}$ , ice crystal size is determined predominately by  $\lambda_{[INP]}$  with  $[INP]_{MAX}$  having a secondary role. This is because ice crystal size is more strongly affected than ICNC by the altitude of ice formation, the amount of liquid available for riming and the time available for deposition growth, and therefore is affected by the the INP number concentration at warm temperatures which is determined by  $\lambda_{[INP]}$ .

The mechanism for the increased ice crystal size at shallow  $\lambda_{[\text{INP}]}$  and high  $[\text{INP}]_{\text{MAX}}$  values is as follows: Ice crystals in clouds with higher  $[\text{INP}]_{\text{MAX}}$  and shallower  $\lambda_{[\text{INP}]}$  values have larger numbers of heterogeneously frozen crystals at warm mixed-phase temperatures (Figure 3.9 d-f). This increase in heterogeneously frozen ice crystals in the Hallett-Mossop region leads to an increase in ice particle production by the Hallett-Mossop process (Figure 3.9 g-i). We see a large increase of approximately one order of magnitude in ice particle production by the Hallett-Mossop process at shallow  $\lambda_{[\text{INP}]}$  (Figure 3.9g) and a bifurcation in the data because of this enhancement. The output data is split into two populations based on the  $\lambda_{[\text{INP}]}$  value, with each population or regime having a linear dependence on HM-rate (Figure 3.9i). Within the warmer temperature mixed-phase cloud region liquid is still available when crystals are frozen for riming. Therefore, with more heterogeneously frozen ice crystals at lower cloud altitude levels, there are higher riming rates (Figure 3.9 j-l), more ice crystal growth and larger ice crystal sizes.

Figure 3.9 (a, g, j) illustrate a regime change at shallow  $\lambda_{[\text{INP}]}$  values with large increases in anvil ice crystal size (a), Hallett-Mossop ice particle production (g) and accretion of water by ice (j) at values of  $\lambda_{[\text{INP}]}$  above approximately  $-0.3 \text{ }^\circ\text{C}^{-1}$ . This regime change is further illustrated in Figure 3.10 which shows the variation in anvil ice crystal effective radius (a), convective Hallett-Mossop ice particle production (b) and accretion of water by ice (c) with changing  $\lambda_{[\text{INP}]}$  and  $[\text{INP}]_{\text{MAX}}$  values. The value of all three output variables substantially increases in the upper right corner of parameter space which indicates simulations with shallow  $\lambda_{[\text{INP}]}$  and high  $[\text{INP}]_{\text{MAX}}$  values. The  $[\text{INP}]_{\text{MAX}}$  determines at what  $\lambda_{[\text{INP}]}$  the regime change occurs: At an  $[\text{INP}]_{\text{MAX}}$  of  $10^{-4}$ ,  $\lambda_{[\text{INP}]}$  must be greater than  $-0.1 \text{ }^\circ\text{C}^{-1}$  for the regime change to occur. At an  $[\text{INP}]_{\text{MAX}}$  greater than  $10^1$ , the regime change occurs when  $\lambda_{[\text{INP}]}$  is greater than  $-0.3 \text{ }^\circ\text{C}^{-1}$ . The regime change occurs in the same location of parameter space in all three variables (Figure 3.10). Simulations in the shallow  $\lambda_{[\text{INP}]}$  regime with a HM-rate above  $600 \text{ mg}^{-1}$  are highlighted

with a black outline and the lack of distinction in colour between simulations with a high HM-rate in the low  $[INP]_{MAX}$  and steep  $\lambda_{[INP]}$  regions indicate that a high HM-rate does not have the same effect in the cloud as a shallow  $\lambda_{[INP]}$ . However, simulations on the border of the regime transition seem more likely to have elevated ice effective radius and thus be in the shallow  $\lambda_{[INP]}$  regime if they have a high HM-rate.

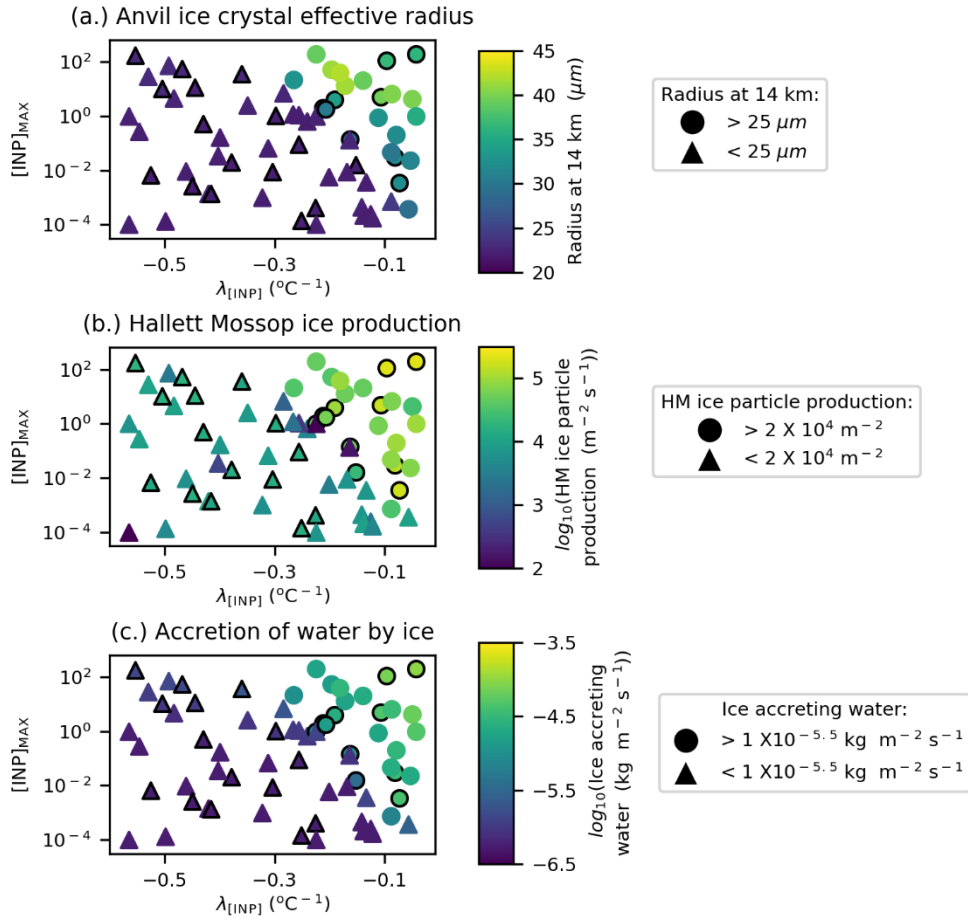


*Figure 3.10. Regime change in anvil ice crystal effective radius and driving processes. Variation in anvil ice crystal effective radius (a), ice particle production by the Hallett-Mossop process (b), and the accretion of water by ice crystals (c) due to variation in  $\lambda_{[INP]}$  and  $[INP]_{MAX}$ . Marker colours indicate the value of anvil ice crystal effective radius (a), ice particle production by the Hallett-Mossop process (b), and the accretion of water by ice crystals (c). Circular markers indicate an ice crystal effective radius above  $25 \mu m$  (a), an ice particle production rate by Hallett-Mossop over  $2 \times 10^4 m^{-2} s^{-1}$  (b), and a rate of water accretion by ice over  $1 \times 10^{-5.5} kg m^{-2} s^{-1}$  (c). Simulations with a HM-rate above 600 splinters  $mg^{-1}$  are indicated with a black outline.*

Statistical emulation of anvil ice crystal effective radius at 14 km, Hallett-Mossop ice particle production and accretion of water by ice crystals was attempted. Figure 3.11 (a - c) shows the validation of the emulator surface against the cloud model validation points. In all three cases the emulator does not validate as well as was seen in Figure 3.7 with larger 95% confidence intervals. Applying a nugget, or noise term, to allow the emulator to pass nearby to, rather than directly through, the training points (Johnson et al., 2011) was tested as a means to improve the validation. However, because the poorer validation occurs mainly as a result of the emulator struggling with the sharp transitions at shallow  $\lambda_{[INP]}$  values seen in Figure 3.9 (a, g, j), a nugget term did not change the results. Nevertheless in most cases the points are relatively close to the 1:1 line indicating that the emulator has some skill in predicting ice crystal size and the cloud development properties that control ice crystal size.

Figure 3.11 (d - f) shows the results of variance-based sensitivity analysis and indicates that for all three output variables here,  $\lambda_{[INP]}$  accounts for a large proportion of the variance with a main effect index of 30 to 60%. Interaction effects between the  $\lambda_{[INP]}$  and the  $[INP]_{MAX}$  account for around 20% of the uncertainty or variance in the anvil ice crystal size. This is in contrast to the emulated outputs shown in Figure 3.8 for anvil ICNC and heterogeneous and homogeneous ice particle production rates, in which  $[INP]_{MAX}$  accounted for nearly all of the uncertainty in the output value. The uncertainty in the anvil ice crystal size and the accretion of water by ice of the simulated cloud would be substantially reduced by knowing the values of  $\lambda_{[INP]}$  and  $[INP]_{MAX}$  exactly, while the uncertainty in the ice particle production rate by the Hallett-Mossop process would be substantially reduced by knowing the values of  $\lambda_{[INP]}$  and HM-rate exactly.

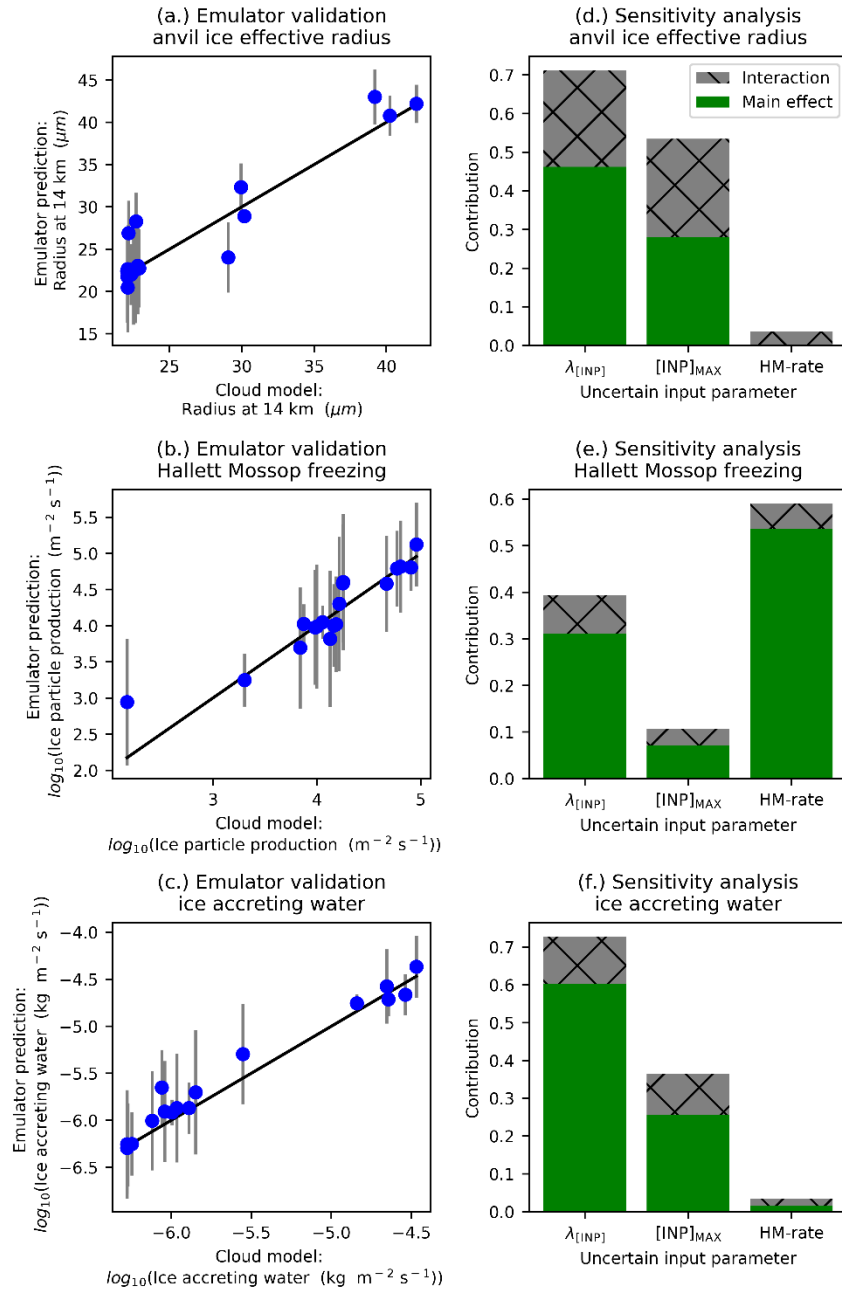


Figure 3.11. Emulator validation and uncertain input contributions to output uncertainty. Validation of emulator results (a - c) and results of the variance-based sensitivity analysis (d - f) for anvil effective radius at 14 km (a, b), ice particle production by the Hallett-Mossop process (c, d), and water accretion by ice (e, f). In (a) – (c) the dots show the value of the validation run on the x-axis and the corresponding emulator mean prediction on the y-axis. 95% confidence intervals of the emulator mean predictions are also shown. An emulator that validates well will have dots close to the 1:1 line and small error bars.

Figure 3.12 shows emulator response surfaces for anvil ice crystal effective radius at 14 km (a), ice particle production by the Hallett-Mossop process (b) and accretion of water by ice crystals (c). In (a) and (c), the Hallett-Mossop splinter production rate is held constant at 350 splinters  $\text{mg}^{-1}$  rimed. In (b), the  $[\text{INP}]_{\text{MAX}}$  is held constant at 1. The emulator response surfaces are noisier with more bumps than those shown in Figure 3.8. This is expected due to the larger 95% confidence intervals on the emulator predictions shown in Figure 3.11 (a – c). Emulation using a Gaussian process assumes that the uncertain input parameters cause changes in output variables that vary smoothly over the parameter space. This is not the case for the three variables emulated in Figure 3.12. For example, the ice particle production rate by the Hallett-Mossop process shows a distinct regime change at shallow  $\lambda_{[\text{INP}]}$  values with a sharp upwards bend in the emulator surface occurring at a  $\lambda_{[\text{INP}]}$  of approximately  $-0.2 \text{ }^\circ\text{C}^{-1}$  (Figure 3.11b). However, in general the response surfaces represent the trends seen in Figures 3.9 and 3.10 reasonably well. For example, the emulated response surfaces show increases with high  $[\text{INP}]_{\text{MAX}}$  and shallow  $\lambda_{[\text{INP}]}$  values that are also evident in Figures 3.9 and 3.10.

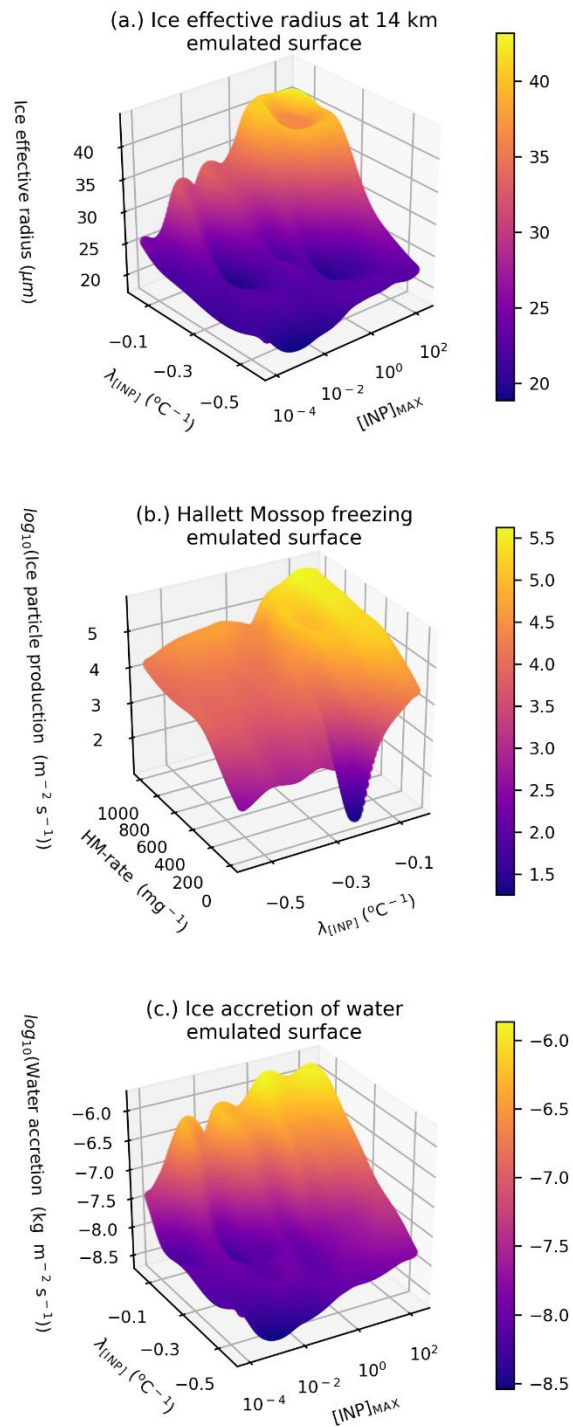
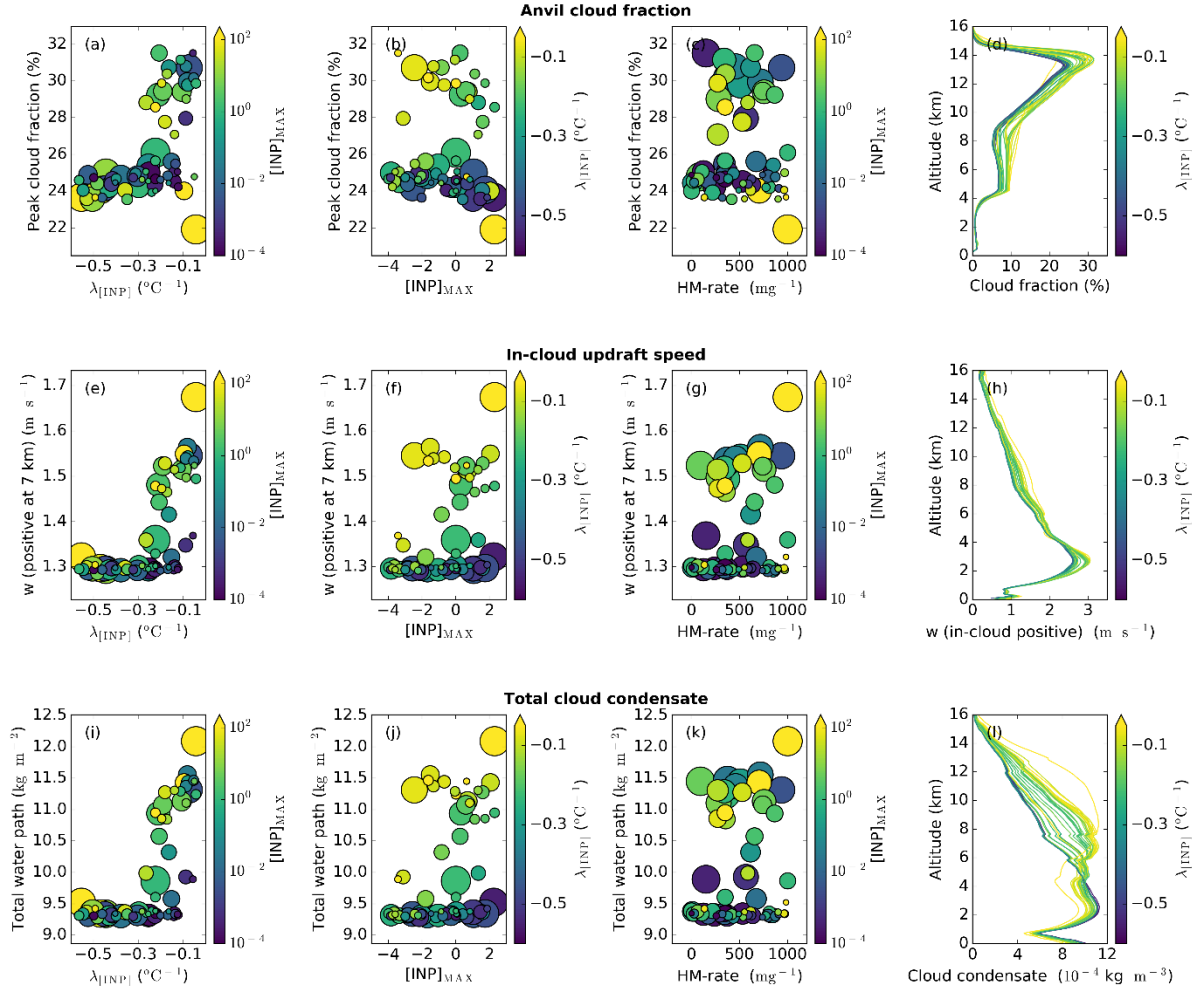


Figure 3.12. Emulator response surfaces. Prediction of ice effective radius (a), Hallett-Mossop ice production (b), and accretion of water (c) by the emulator. Shown in (a) and (c) are the emulated response surfaces at a fixed HM-rate of 350 splinters  $\text{mg}^{-1}$  rimed. Shown in (b) is the emulated response surface at a fixed  $[\text{INP}]_{\text{MAX}}$  of 1. The colours indicate output values and are the same range and units as the z-axis.

### 3.4.1.3. Anvil cloud fraction

Figure 3.13 shows the dependence of observed anvil cloud fraction (a-d), in-cloud updraft speed (e-h) and total cloud condensate amount (i-l) on the uncertain input parameters. Anvil cloud fraction is the mean of the peak cloud fraction that occurs between 180 and 240 minutes of the simulations (i.e. the peak of the profile shown in Figure 3.13d). A similar regime shift at shallow  $\lambda_{[INP]}$  values as was seen in the anvil ice crystal size is seen in all three of these output variables (Figure 3.13a, d, g) with simulations with a shallow  $\lambda_{[INP]}$  having an elevated cloud fraction. A small secondary dependence of cloud fraction on  $[INP]_{MAX}$  is evident with simulations in the shallow  $\lambda_{[INP]}$  regime, exhibiting reductions in cloud fraction from ~32% at low  $[INP]_{MAX}$  values to ~28% at higher  $[INP]_{MAX}$  values. The regime shift to high cloud fractions, updraft speed and cloud condensate occurs in the same shallow  $\lambda_{[INP]}$  and high  $[INP]_{MAX}$  region of parameter space (Figure 3.14) as was seen in anvil ice crystal size, Hallett-Mossop ice particle production and ice accretion rates (Figure 3.10).

Anvil cloud fraction is enhanced at shallow  $\lambda_{[INP]}$  values due to an invigoration effect caused by enhanced heterogeneous (Figure 3.9, d-f) and secondary freezing (Figure 3.9, g-i) and increased riming (Figure 3.9, j-l) in the mixed phase cloud region, and the resultant enhancement in latent heat release, updraft speeds (Figure 3.13, e, h), and vertical condensate mass transport (Figure 3.13 i, l). The enhancement in convective strength and the resultant increase in anvil size at shallow  $\lambda_{[INP]}$  values is large enough to compensate for the effect of increased ice crystal sizes (which would be expected to reduce anvil size due to increased ice fall speed) at shallow  $\lambda_{[INP]}$  values within the simulated time period. The importance of the anvil ice properties relative to the convective invigoration effect for anvil cloud fraction may change with a longer simulation period owing to the persistence of the anvil cloud after the decay of the convection that forms it.



*Figure 3.13. Anvil cloud fraction and driving processes. Dependence of anvil cloud fraction (a-d), in-cloud updraft speed at 7 km (e-h), and total cloud condensate (i-l) on the three uncertain input parameters:  $\lambda_{[INP]}$  (a, e, i),  $[INP]_{MAX}$  (b, f, j), and HM-rate (c, g, k). In-cloud profiles of anvil cloud fraction (d), in cloud updraft speed (h), and total cloud condensate (l) in all simulations are coloured by  $\lambda_{[INP]}$ . For panels (a), (e), and (i), the colour of the markers indicate  $[INP]_{MAX}$  and the marker size indicates the HM-rate. For panels (b), (f), and (j), the colour of the markers indicate  $\lambda_{[INP]}$  and the marker size indicates HM-rate. For panels (c), (g), and (k), the colour of the markers indicate  $[INP]_{MAX}$  and the marker size indicates  $\lambda_{[INP]}$ . Panels (a-d) are the average of the cloud property between 150 and 240 minutes (anvil stage) in the simulation, while panels (e-l) are the average of the relevant cloud property between 60 and 180 minutes (convective stage) in the simulations.*

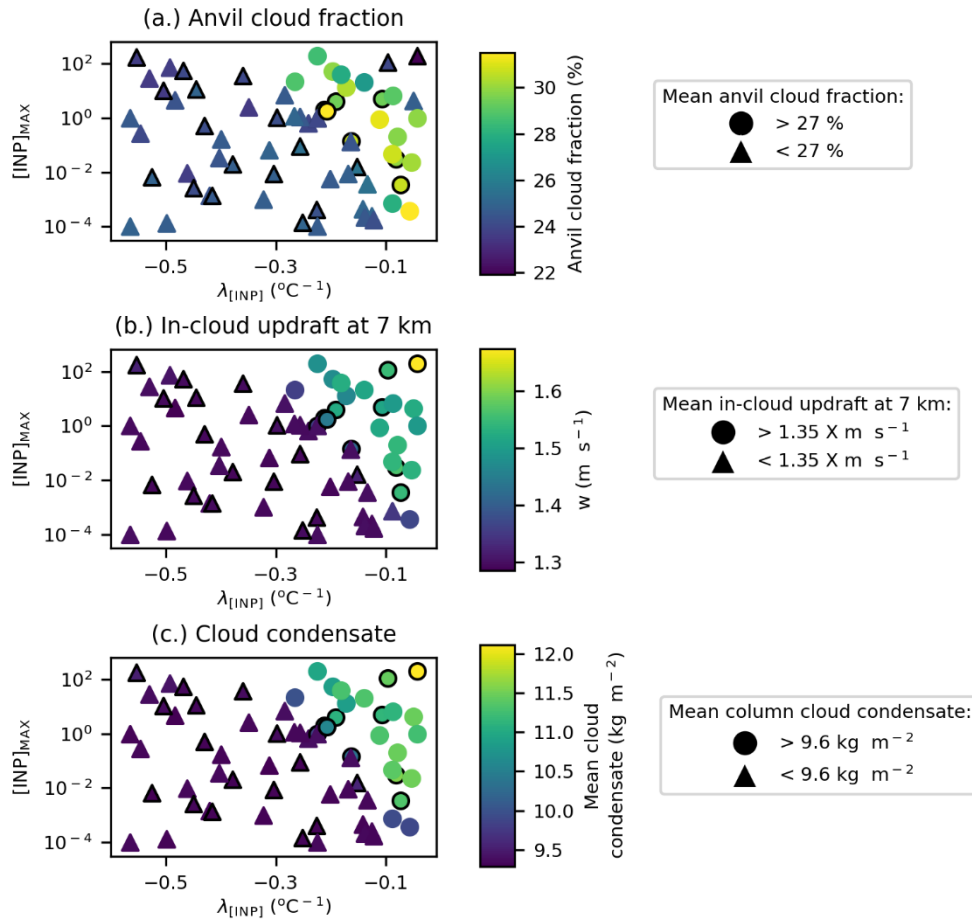


Figure 3.14. Regime change in anvil cloud fraction and driving processes. Variation in anvil cloud fraction (a), in-cloud updraft speed at 7 km (b), and total cloud water path (c) due to variation in  $\lambda_{[INP]}$  and  $[INP]_{MAX}$ . Marker colours indicate the value of the mean peak anvil cloud fraction (a), in-cloud updraft speed at 7 km (b) and total cloud water path (c). Circular markers indicate a cloud fraction above 27% (a), a mean in-cloud updraft speed above  $1.35 \text{ m s}^{-1}$  (b), and a water path over  $9.6 \text{ kg m}^{-2}$  (c). Simulations with a HM-rate above  $600 \text{ splinters mg}^{-1}$  are indicated with a black outline.

The small reduction of anvil cloud fraction within the shallow  $\lambda_{[INP]}$  regime with increasing  $[INP]_{MAX}$  (Figure 3.13b) can be attributed to the changes in anvil ice properties reported in Sections 3.4.1.1 and 3.4.1.2. At high  $[INP]_{MAX}$  values, ICNC is reduced (Figure 3.6b) and ice crystal size is increased (Figure 3.9b). Fewer and larger crystals will sediment out faster and therefore will spread out over a smaller horizontal area, reducing anvil fraction in simulations with high  $[INP]_{MAX}$  values. The chosen Hallett-Mossop splinter production rate has very little

impact on anvil cloud fraction (Figure 3.13c), updraft speeds (Figure 3.13g) or cloud condensate amount (Figure 3.13k).

Statistical emulation of anvil cloud fraction was attempted but the bifurcation of the output data into two distinct regimes depending on the value of  $\lambda_{\text{[INP]}}$  proved impossible to capture with the emulator, and validation of the emulation showed little predictive power (not shown). This indicates that although emulation is a powerful tool to aid in our understanding of cloud processes, traditional methods of analysis are still needed where there are sharp transitions such as those seen in Figure 3.14. It is not clear why the emulation of some variables with a two distinct regimes (such as ice crystal effective radius) worked relatively well and emulation of anvil cloud fraction did not. It may be because simulations exhibited both a sharp transition to a larger cloud fraction at high  $[\text{INP}]_{\text{MAX}}$  and shallow  $\lambda_{\text{[INP]}}$  values and within this regime there was a decrease with increasing  $[\text{INP}]_{\text{MAX}}$  and the emulator struggles to capture the complicated dependence on  $[\text{INP}]_{\text{MAX}}$ . Furthermore there is a notable outlier with one simulation with the highest  $[\text{INP}]_{\text{MAX}}$  and shallowest  $\lambda_{\text{[INP]}}$  having the lowest cloud fraction (Figures 3.13, 3.14) which may affect the emulation.

### **3.4.2. The importance of the Hallett-Mossop process and its interaction with $\lambda_{\text{[INP]}}$ .**

One notable feature of the results presented so far is the apparent lack of impact of uncertainty in the HM-rate on most output variables. For example, the results of the variance based sensitivity analysis shown in Figures 3.7 and 3.11 indicate that the HM-rate makes no significant contribution to the uncertainty in the value of anvil ICNC, heterogeneous or homogeneous freezing rates, anvil effective radius or ice accretion of water. Ice particle

production by the Hallett-Mossop process was the only output variable shown to have a notable dependence on the HM-rate, and up to 40% of the uncertainty in its value was attributed to variation in the  $\lambda_{\text{[INP]}}$  value owing to the role of  $\lambda_{\text{[INP]}}$  in determining the regime shift evident in Figures 3.9g and 3.10b. This regime shift induces an enhancement in the ice particle production by the Hallett-Mossop process of about 1 order of magnitude at shallow  $\lambda_{\text{[INP]}}$  values regardless of the value of HM-rate.

In most simulations over 99% of ice crystals in the Hallett-Mossop region (5 – 7.5 km) are formed via the Hallett-Mossop process and not via heterogeneous ice formation (Appendix Section 3.7: Figure A3.1). Figure A3.1 shows that only 7 of 73 simulations conducted have more than 10% of the ice particle production between 5 and 7.5 km occurring via heterogeneous ice nucleation rather than via the Hallett-Mossop process. Despite the apparent unimportance of the chosen HM-rate for the simulated cloud properties detailed in Section 3.4.1, many output variables, particularly those exhibiting a regime shift at shallow  $\lambda_{\text{[INP]}}$  and high  $[\text{INP}]_{\text{MAX}}$ , show a strong correlation with ice particle production in the Hallett-Mossop region of the cloud (Figure 3.15). This correlation indicates that the key role of INP slope in determining cloud properties can be partly attributed to its role in enhancing Hallett-Mossop ice particle production rates (Figure 3.9 g-i) which dominate ice production in the Hallett-Mossop regime (Section 3.7: Figure A3.1). Note that the simulations and correlation analysis shown Figure 3.15 comprise only simulations from the realistic region of parameter space (Figure 3.5).

Ice particle production by the Hallett-Mossop process is greatly enhanced at shallow  $\lambda_{\text{[INP]}}$  values due to both the larger availability of ‘seed’ ice crystals and the enhanced riming events that accompany these increased ICNCs. This indicates that INP particles can exert strong control over deep convective cloud properties even when heterogeneous freezing is not the dominant mechanism of ice production because they can alter the rate of ice production by SIP mechanisms (Figure 3.9 g-I, Figure 3.15 and Section 3.7: Figure A3.1).

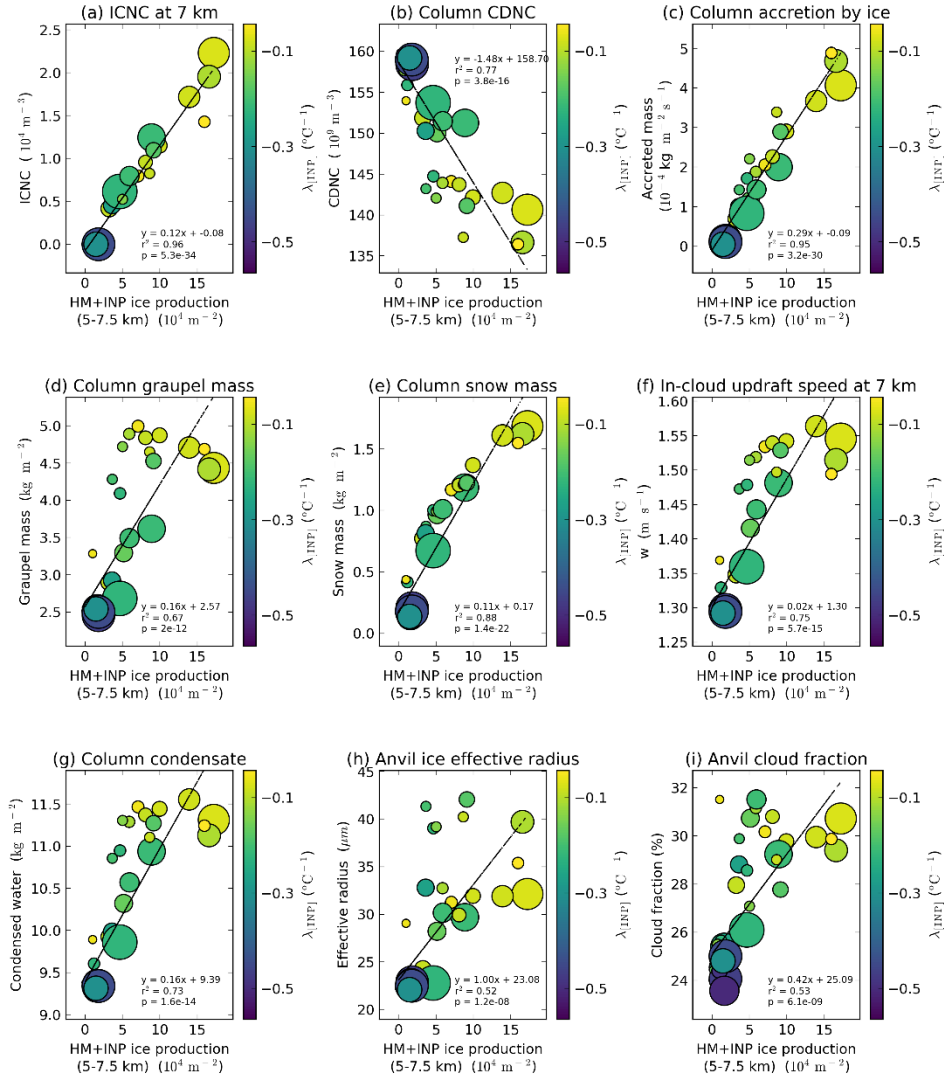


Figure 3.15. Importance of ice production by the Hallett-Mossop process. Dependence of cloud properties on ice particle production in the Hallett-Mossop regime (5 - 7.5 km) in the convective stage of cloud development (60 - 180 minutes). Shown is ICNC at 7 km (a), column cloud droplet number concentration (b), accretion of water by ice (c), graupel mass (d), snow mass (e), in-cloud updraft speed at 7 km (f), cloud condensate from cloud droplets, rain, ice crystals, snow and graupel (g), anvil ice crystal effective radius at 14 km (h), and anvil cloud fraction (i). The colour of the markers indicate  $\lambda_{[INP]}$  and the marker size indicate the HM-rate. Panels (a - g) are the average of the cloud property between 60 and 180 minutes (convective stage), while panels (h - i) are the average of the relevant cloud property in the simulations between 150 and 240 minutes (anvil stage) in the simulation. Simulations deemed as having unrealistically high or unrealistically low INP concentrations due to the combined perturbations of  $\lambda_{[INP]}$  and  $[INP]_{MAX}$  (as indicated in Figure 3.5) are not shown in this plot or included in the correlation analysis.

In particular, we note that high rates of ice particle production by the Hallett-Mossop process do not occur unless the  $\lambda_{\text{[INP]}}$  is shallow. This is evident from the lack of distinction between simulations with a HM-rate above or below 600 splinters  $\text{mg}^{-1}$  in Figures 3.10 and 3.14. This indicates that a steep  $\lambda_{\text{[INP]}}$  and a high HM-rate cannot have the same effect on the cloud properties as a shallow  $\lambda_{\text{[INP]}}$  regardless of the HM-rate. Furthermore, ICNCs at lower mixed phase altitudes, regardless of the freezing mechanism in question, can be key determinants of deep convective cloud properties and the properties of the convectively generated anvil (Figure 3.15).

Figure 3.15 indicates that as ice production by the Hallett-Mossop process increases due to increased INP number concentrations at shallow  $\lambda_{\text{[INP]}}$  values, mixed-phase ICNCs (Figure 3.15a) are increased and column cloud droplet number concentrations are reduced (Figure 3.15b). Due to the enhancement in ICNC in the lower mixed-phase region with shallower  $\lambda_{\text{[INP]}}$  and higher resultant Hallett-Mossop ice particle production, increases are seen in all mixed-phase freezing mechanisms including accretion of ice by water (Figure 3.15c), snow (Figure 3.13d) and graupel (Figure 3.15e) mass concentrations due to the well-documented enhanced effectiveness of liquid collection by frozen hydrometeors relative to liquid ones (Johnson, 1987; Phillips et al., 2005). Enhanced latent heat release by the increased freezing events from multiple pathways leads to increased updraft speeds (Figure 3.15f) and an overall increase in cloud formation (Figure 3.15g). Enhanced riming in the mixed phase region increases anvil ice crystal effective radius (Figure 3.15h) as more anvil ice crystals are formed via heterogeneous freezing and subject to riming than are formed via homogeneous freezing. The increased convective strength also leads to increased anvil cloud fraction (Figure 3.15i). The correlations shown in Figure 3.15 are particularly evident in simulations in the shallow  $\lambda_{\text{[INP]}}$  cloud regime indicating that the sensitivity of deep convective cloud properties to mixed-phase ice processes

may vary depending on ambient aerosol concentrations and the number and efficiency of the available ice-nucleating aerosol.

### **3.5. Limitations of this modelling study**

The role of  $\lambda_{\text{[INP]}}$  in determining the ice particle production by the Hallett-Mossop process highlights the importance of the interaction of INP number concentrations with SIP mechanisms. However the Hallett-Mossop process is not the only SIP mechanism that has been identified in convective clouds (Field et al., 2017; Korolev et al., 2020). Other SIP mechanisms, such as droplet shattering (Lauber et al., 2018), are not represented in our simulations and their impact has not been tested. We recommend that the effect of other SIP mechanisms, including those occurring at temperatures below  $-10^{\circ}\text{C}$  (Field et al., 2017; Lauber et al., 2018) on deep convective clouds be tested in similar studies as parameterisations become available.

The simulated cloud is single idealised case and as such the results cannot be directly extrapolated to more realistic convective cloud cases, where less idealised triggering mechanisms are at play (Wellmann et al., 2018, 2020) and different clouds in the population can interact (e.g. Chapter 2 and Hawker et al. (2021)). It was not feasible to conduct the necessary number of simulations required to study the impact of three uncertain input parameters on a larger more complicated cloud field due to time and cost restrictions. However, we believe the results presented here provide an interesting stepping stone to understanding the interacting effects of INP number concentrations, INP efficiency, and SIP on deep convective anvil properties and recommend similar studies be undertaken with more realistic cases in the future.

The chosen uncertain input parameters are just three of a multitude of microphysical parameters that contribute uncertainty to convective cloud processes which should be considered in future

work. For example, uncertainty in ice crystal number and mass concentrations were strongly affected by ice crystal shape in simulations of a continental deep convective cloud simulated using the 3D MAC3 model (Johnson et al., 2015b). Changes in CCN number concentrations have also been shown to have large effects on many microphysical processes, such as cloud invigoration, and resultant cloud properties, including the anvil extent, in deep convective clouds (e.g. Altaratz et al., 2014; Fan et al., 2010a, 2010b, 2012; Wang, 2005), none of which have been examined here. Uncertainty in environmental conditions that may affect the cloud properties, for example, the size and temperature perturbation value of the warm bubble initiating our deep convective cloud, or the potential temperature profile (Wellmann et al., 2018), have also not been addressed here.

In order to effectively decouple the  $[INP]_{MAX}$  and  $\lambda_{[INP]}$ , the INP number concentration at  $-38^{\circ}C$  was fixed to be equal to the coarse dust number concentration. This was necessary because a key assumption of the variance-based sensitivity analysis shown in Figures 3.7 and 3.11 is that the uncertain input parameters are independent of one another. However, decoupling the  $\lambda_{[INP]}$  and  $[INP]_{MAX}$  in this way means that the plateauing of the INP number concentrations at low temperatures and high aerosol concentrations, as can be seen in the Niemand et al. parameterisation in Figure 3.4a, is not represented in the simulations in this study (Atkinson et al., 2013; Niedermeier et al., 2015; Niemand et al., 2012). Therefore, the effect of a high  $[INP]_{MAX}$  and steep  $\lambda_{[INP]}$  on the cloud properties may be larger in reality than was found in this idealised study because of this design feature. This feature of our experiment design also means that combinations of INP number concentration and INP parameterisation slope causing unrealistically low INP concentrations at temperatures above  $-35^{\circ}C$  are very common in our sampling design. To compensate for this we conducted 22 additional simulations for use in the emulator design and 6 additional validation simulations in the realistic region of parameter space (red and black lines in Figure 3.5d). Our variance-based

sensitivity analysis is conducted over all simulated parameter space, including the unrealistic space shown in Figure 3.5.

It should also be borne in mind that INP concentration spectra often do not follow a simple logarithmic relationship. Instead, different INP species can contribute to different temperature regimes and different INP tend to have different temperature dependencies. For example, mineral dust tends to have a steep slope and dominates INP populations below around  $-15^{\circ}\text{C}$ , whereas, biological material can enhance the INP concentration in the HM regime (e.g. O’Sullivan et al., 2018). Hence, the INP concentration spectra in real clouds can be much more complex than those used in this model.

As in Chapter 2, raindrop freezing was parameterised according to Bigg (1953). This means the raindrop freezing is temperature and volume based and disconnected from the perturbations in  $[\text{INP}]_{\text{MAX}}$  and  $\lambda_{[\text{INP}]}$ . In a future study, the importance of raindrop freezing should at the very least be linked to the  $[\text{INP}]_{\text{MAX}}$  value or, if processing is active, perturbed using both  $[\text{INP}]_{\text{MAX}}$  and  $\lambda_{[\text{INP}]}$  using a two-moment scheme that accounts for the accumulation of aerosol in raindrops during collision (e.g. Paukert et al., 2017).

The ice properties of the convectively generated anvil were analysed and the implications for anvil lifetime and radiative effect theorised. However, the short length of our simulations due to computational limitations meant we did not examine the full lifecycle of the generated anvil. Conducting similar simulations covering a longer time period would address this limitation and is recommended for the future.

### **3.6. Discussion and Conclusions**

We quantify the impact of varying INP number concentration (via the  $[\text{INP}]_{\text{MAX}}$  uncertain input parameter), INP parameterisation slope ( $\lambda_{[\text{INP}]} = d\log_{10}[\text{INP}(\text{m}^{-3})]/dT(^{\circ}\text{C})$ ) and the Hallett-

Mossop splinter production rate (HM-rate, splinters produced per milligram rimed) on the anvil properties of an idealised deep convective cloud. A schematic of the main effects identified in this study is shown in Figure 3.16. Overall, the anvil ICNC is substantially reduced at high  $[INP]_{MAX}$  owing to a reduction in homogeneous ice production when heterogeneous freezing becomes the dominant mechanism for primary ice production. Furthermore, at shallow  $\lambda_{[INP]}$  values, there is a sharp transition to a cloud regime with larger anvil ice crystals and a more extensive anvil. This regime shift is driven by more extensive cloud glaciation which is in part caused by shallow  $\lambda_{[INP]}$  values enhancing the ice particle production by the Hallett-Mossop process.

We infer the possible implications of the uncertain input parameters on anvil lifetime based on the anvil ice crystal properties. Tropical cirrus can typically persist, and therefore affect radiation, in the atmosphere for days after the convective cloud that formed them has decayed (e.g. Luo and Rossow, 2004). An anvil with more numerous, smaller crystals will persist longer in the atmosphere than one with fewer, larger crystals. Our results indicate that a higher INP number concentration leads to both fewer and larger anvil ice crystals and a reduced cloud fraction. This implies that deep convection generated in an environment with a high concentration of ice-nucleating aerosol, such as in heavy dust events, may be less long-lived than those generated in pristine environments. Statistical emulation demonstrated that anvil ICNC declines sharply as soon as heterogeneous ice production becomes the dominant mechanism of ice crystal production in the cloud. This is due to the suppression of homogeneous freezing when liquid is consumed at lower altitudes by high heterogeneous freezing rates and subsequent mixed-phase processes, such as riming and deposition.

Uncertainty in the INP parameterisation slope ( $\lambda_{[INP]}$ ) had the largest effect on the properties of the simulated deep convective cloud out of the three uncertain input parameters. A regime shift occurs at a shallow  $\lambda_{[INP]}$  of between  $-0.3$  and  $-0.1$   $^{\circ}\text{C}^{-1}$  (the exact value of the transition depends

on the  $[\text{INP}]_{\text{MAX}}$  above which the deep convective cloud generates a larger anvil with bigger ice crystals (Figures 3.10, 3.14). At shallow  $\lambda_{[\text{INP}]}$  values, the anvil ice crystals are larger indicating that a cloud anvil formed in the presence of an INP population with high efficiency at warmer temperatures, e.g. marine organics (Wilson et al., 2015), will have a shorter lifetime than that formed in the presence of an INP population with a steeper temperature dependence. However, this effect is compensated for by the invigoration effect driven by higher rates of mixed-phase ice formation in simulations with shallow  $\lambda_{[\text{INP}]}$  values, which leads to larger condensate mass divergence in the upper troposphere and a larger anvil in the timescale simulated in this study. Future studies should cover the entire lifecycle of the generated deep convective cloud and anvil cirrus in order to quantify the resultant lifetime of the convective anvil due to compensation between these two effects of  $\lambda_{[\text{INP}]}$ .

The microphysical effects of the variations in INP number concentrations and INP parameterisation slope detailed here build on the results of Chapter 2 (also in Hawker et al. (2021)) and further our understanding of the role of these two uncertain inputs on deep convection. In both the complex cloud-field simulation of Hawker et al. (2021) and the idealised deep convective cloud presented here, INPs in the mixed-phase region enhance Hallett-Mossop ice particle production, and increase snow and graupel formation leading to an invigoration effect, more cloud condensate and an increased cloud fraction at mixed-phase cloud levels. INPs in the mixed-phase region also reduce homogeneous ice production leading to reduced overall column integrated ICNCs in both studies. Conversely, in the Hawker et al. (2021) study, shallow  $\lambda_{[\text{INP}]}$  values led to a reduced cloud fraction above 9 km due to reduced ice particle production by homogeneous freezing. In the deep convective cloud simulated here, a shallow  $\lambda_{[\text{INP}]}$  leads to an increased anvil cloud fraction due to an invigoration effect caused by enhanced ice formation and latent heat release in the mixed-phase cloud region. This indicates that the microphysical effects of INP and the interaction of INP with the Hallett-

Mossop process are relatively consistent between realistic and idealised case studies. However, the consequences of microphysical changes due to INP on the cloud macro-physical properties such as cloud fraction and outgoing radiation can be different depending on the specific conditions of the simulation and the type of cloud being perturbed. For example, the deep convective cloud simulated here was initiated with a relatively strong warm bubble perhaps predisposing the cloud fraction to be more sensitive to enhancements in an already strong convective updraft strength than the more realistic clouds in the Hawker et al. (2021) study indicating that this aspect still requires more clarification.

The regime shift at shallow  $\lambda_{\text{[INP]}}$  values could be in part attributed to the substantial enhancement of the rate of ice production in the lower mixed-phase region by the Hallett-Mossop process which induces more riming, higher snow and graupel production and stronger updrafts as a result of the increased freezing and latent heat release (Figure 3.15, Section 3.7: Figure A3.1). Ice particle production by the Hallett-Mossop process is enhanced at shallower  $\lambda_{\text{[INP]}}$  values due to both the larger availability of ‘seed’ ice crystals and the enhanced riming events that accompany these increased ICNC. Interestingly, the Hallett-Mossop ice particle production rate is controlled by both the HM-rate and  $\lambda_{\text{[INP]}}$ . A shallow  $\lambda_{\text{[INP]}}$  provides a large jump in Hallett-Mossop ice particle production of up to an order of magnitude, while the impact of the chosen HM-rate has an incremental, linear effect. Whether the interaction of INP with other SIP mechanisms that operate over different temperature ranges has a similar effect on SIP ice particle production rates should be explored in the future.

Statistical emulation is a powerful tool for helping to visualise and understand the relationships between cloud responses (Figure 3.8). However, the emulation struggles to accurately model cloud responses where there is a significant regime shift at shallow  $\lambda_{\text{[INP]}}$  (Figure 3.10,14). We therefore suggest that emulation be used alongside traditional analysis methods for the further study of the complex processes occurring within deep convective clouds, particularly where

sudden transitions or regime shifts are evident or likely. The use of Latin hypercube sampling to capture cloud responses in all realistic parameter space to multiple uncertain input parameters is very effective, even without undertaking statistical emulation of the simulation data.

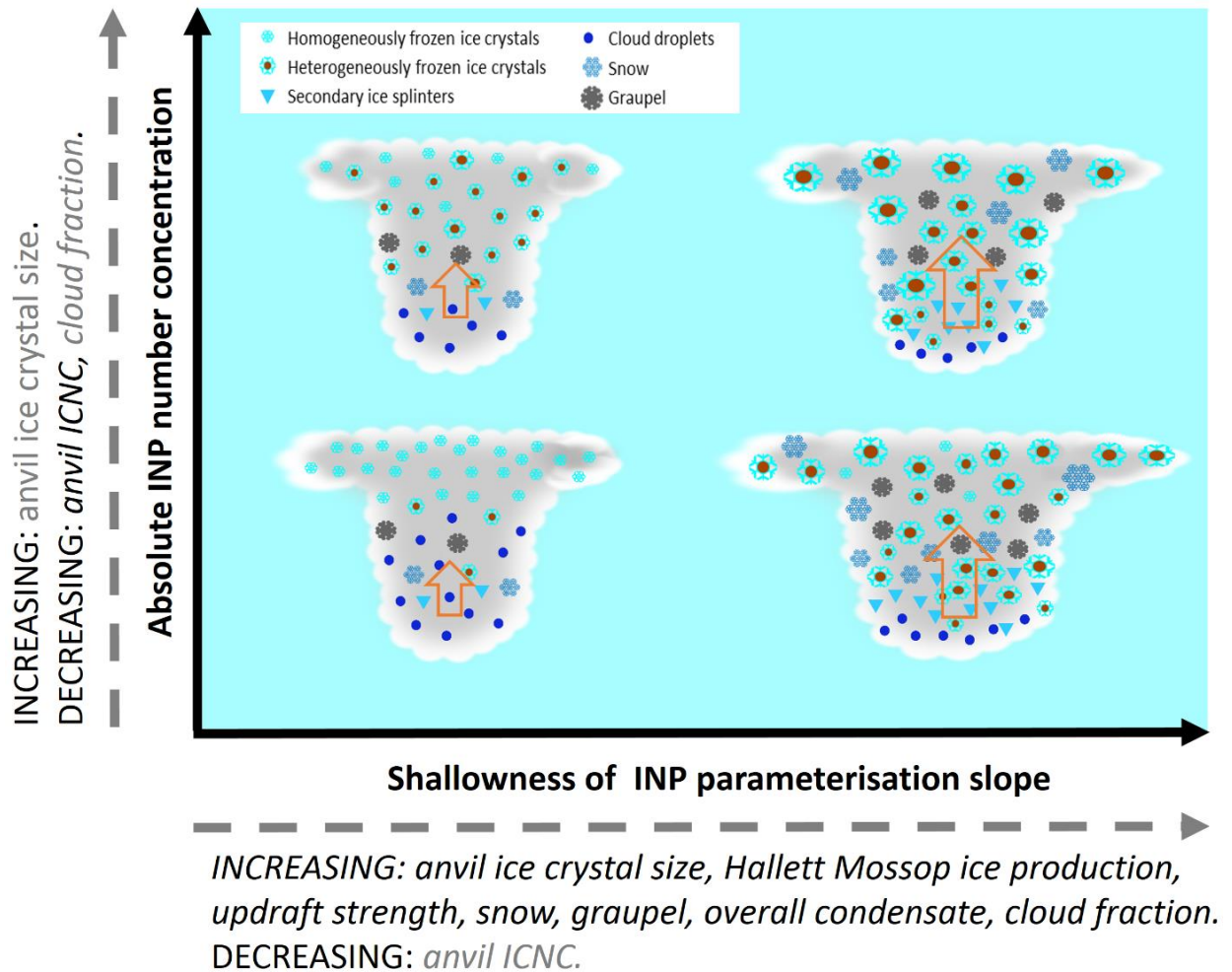


Figure 3.16. Summary of results. Schematic showing the key effects of the perturbations to absolute INP number concentration at  $-38\text{ }^{\circ}\text{C}$  ( $[INP]_{MAX}$ ) and INP parameterisation slope ( $\lambda_{[INP]}$ ) on the deep convective cloud simulated in this study. Output variables written along the x and y-axes in black indicate that they are primarily controlled by the uncertain input variable on that axes while grey writing indicates a secondary or smaller effect of the uncertain input variable in question.

This work highlights the complexity of interactions between mixed-phase ice processes and the challenge of representing them accurately in numerical weather prediction models. The potential for ice particle production by INP and SIP to impact anvil cirrus ice properties also presents a challenge for climate models. Climate models do not typically use INP number concentrations to determine ice water path and the resultant outgoing radiation, and this is an important area for future work (Baran et al., 2014; Waliser et al., 2009). The role of the temperature dependence of INP number concentration in determining the observed cloud properties indicates the importance of quantifying the concentration of INP at all mixed-phase temperatures, adding to work by, for example, Hawker et al. (2021), Liu et al. (2018), Shi and Liu (2019), and Takeishi and Storelvmo (2018). The importance of the temperature dependence of INP number concentrations indicates that accurately representing species accumulated on the surface of mineral dust may be of particular importance for the representation of the glaciation of deep convective clouds in the Saharan outflow regions: The ice-nucleating ability of mineral dust particles can be substantially enhanced by the accumulation of biological material from fungi, pollen and bacteria (Augustin-Bauditz et al., 2016; Chen et al., 2021; O'Sullivan et al., 2016). Furthermore, the temperature dependence of the INP parameterisation had a substantial effect on Hallett-Mossop ice particle production rates, indicating that heterogeneous freezing can be an important determinant of deep convective cloud properties even when it is not the dominant mechanism of ice formation.

### 3.7. Appendix

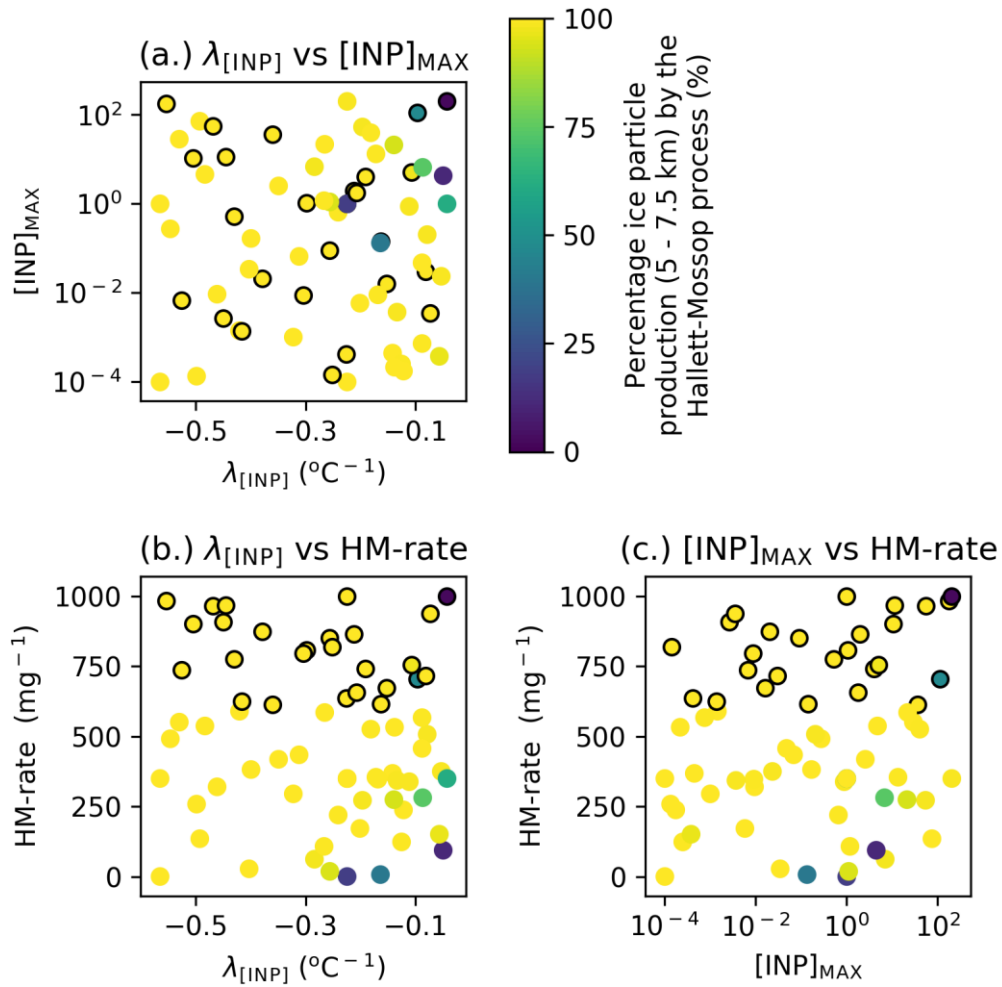


Figure A3.1. Source of ice crystals in the Hallett-Mossop region of the simulated deep convective cloud. Percentage of ice crystals produced between 5 and 7.5 km altitude that are produced from the Hallett-Mossop process [i.e. (Hallett-Mossop ice crystals / Hallett-Mossop and INP produced ice crystals)  $\times 100$ ]. Simulations with a HM-rate above 600 splinters  $\text{mg}^{-1}$  are indicated with a black outline.



## **Chapter 4: Simulation of dust and K-feldspar INP transport across the tropical Atlantic in a global aerosol model**

The candidate confirms that the work presented in Chapter 4 is her own and that appropriate credit has been given where reference has been made to the work of others. I am thankful to Kirsty J. Pringle and Ulrike Proske for assistance running the GLOMAP-mode model, to Jesus Vergara-Temprado for writing the parameterisation of ice-nucleating particle number concentrations from the GLOMAP-mode model (presented in Vergara-Temprado et al. (2017)), to Alberto Sanchez-Marroquin for helpful discussions, and to Annette K. Miltenberger, Paul R. Field, Benjamin J. Murray and Ken S. Carslaw for guidance with the study design and manuscript development.

## 4.1. Abstract

Mineral dust aerosol from the world's arid and semi-arid regions have important effects on climate through their direct effect on incoming and outgoing radiation and through their interactions with clouds. Dust aerosol can act as ice-nucleating particles (INP), initiating ice formation in the mixed-phase temperature regime. This ability has been attributed to mineral components of dust, such as potassium feldspar (K-feldspar), which have demonstrated efficiency at nucleating ice. Measurements of INP number concentration in Barbados provide a useful dataset to evaluate the transport of dust and K-feldspar INP from the Sahara across the tropical Atlantic to the Caribbean in the Global Model of Aerosol Processes (GLOMAP). GLOMAP is a global aerosol model that has previously been used to draw conclusions about the sources of INP when compared to field measurements. We find that GLOMAP overestimates the concentration of K-feldspar INP at Barbados but underpredicts the dust mass concentration relative to surface-based measurements, profiles of dust mass measured by lidar, and the MERRA-2 reanalysis dataset. The overprediction of K-feldspar INP can be explained by an overprediction of the K-feldspar aerosol fraction, perhaps driven by the model placing too much K-feldspar in the accumulation size mode relative to the coarse size mode. INP and dust mass prediction by GLOMAP are affected by the choice of driving meteorological reanalysis used in the model. Differences in INP number concentration at  $-10^{\circ}\text{C}$  can be as large as 200% in some places between simulations using the ERA-interim rather than the ERA-40 reanalysis dataset. Overall, a combination of direct atmospheric observations, measurements derived from satellite and remote sensing data, and model simulations are used to build a better understanding of the representation of dust and INP in GLOMAP.

## 4.2. Introduction

Mineral dusts emitted from the world's arid and semi-arid regions are a dominant component of global aerosol budgets with important effects on global radiative energy fluxes, climate, and weather. Mineral dust aerosol can directly affect global radiative fluxes through the scattering and absorption of incoming and outgoing radiation (e.g. Evan and Mukhopadhyay, 2010). It can affect cloud properties such as precipitation and albedo through its role as cloud condensation nuclei (CCN) (Karydis et al., 2012, 2017; Kumar et al., 2009) and ice-nucleating particles (INP) (e.g. Harrison et al., 2016; Niemand et al., 2012; Vergara-Temprado et al., 2018). These effects can include interaction with tropical storms and cyclones causing invigoration (Herbener et al., 2014; Khain et al., 2016; Lynn et al., 2016) or weakening (Fan et al., 2013; Lynn et al., 2016; Zhang et al., 2007). Upon sedimentation, through dry deposition or wet nucleation and impaction scavenging, mineral dust can alter ocean or soil biogeochemistry and productivity (Jickells et al., 2005; Mahowald et al., 2005) or alter the albedo of the surfaces it is deposited on, for example by darkening the surface of sea ice (Wittmann et al., 2017). The atmospheric dust cycle is complex with large and difficult to measure uncertainties across multiple spatial and temporal scales (Huneeus et al., 2011; Shao et al., 2011; Wu et al., 2020).

Dust emission from the surface occurs when the surface wind speed exceed a surface-specific threshold which depends on surface roughness, material grain size, and the amount of soil moisture (Engelstaedter et al., 2006). The difficulty of quantifying emission fluxes, the primary determinant of the atmospheric burden of mineral dust in the atmosphere, highlights the complexity and challenge of accurately representing the dust cycle in global models. Quantification of emission fluxes is challenging because of the heterogeneity of emission regions which have large changes in mineral composition and surface erodibility across short distances (Nickovic et al., 2012; Sweeney et al., 2011), the short lifetime of most emitted

mineral dust particles, and the remote desert location of most dominant emission regions making installation and monitoring of measurement equipment challenging (Engelstaedter et al., 2006). Estimations of global dust emissions from climate models are extremely variable with estimates from 15 different CMIP5 (Coupled Model Intercomparison Project Phase 5) models spanning from 735 to 8186 Tg yr<sup>-1</sup> (Wu et al., 2020). This large variation is attributable in part to some models considering only particles smaller than 16 µm and others considering particles as large as 63 µm. However, even among models considering only particles between 0.2 and 20 µm the dust emission flux ranges from 735 to 3598 Tg yr<sup>-1</sup> (Wu et al., 2020). The range of global estimated dust emissions from 15 Aerosol Model Intercomparison (AEROCOM) models are similarly varied (500 to 4400 Tg yr<sup>-1</sup>) (Huneus et al., 2011).

Owing to the dearth of direct measurements, constraint of emission fluxes relies on the validation of variables such as aerosol optical depth (AOD) which are dependent on dust emission and observable via remote sensing techniques (Engelstaedter et al., 2006; Huneus et al., 2011) or on reanalysis datasets which are produced using a combination of satellite and observed atmospheric conditions and model simulations (Randles et al., 2017; Wu et al., 2020). These remotely sensed or reanalysis datasets are subject to their own, often large, uncertainties further complicating the quantification of global dust emission fluxes (Huneus et al., 2011).

The global atmospheric dust burden depends on the amount of dust emitted into the atmosphere, the lifetime of atmospheric dust, and the amount removed via dry and wet deposition (Shao et al., 2011). The magnitude of all of these dust cycle components are very uncertain, leading to an unconstrained atmospheric dust flux estimated to be between 8 and 35.9 Tg yr<sup>-1</sup> (Shao et al., 2011). One thing that is not uncertain however is that the majority of the global atmospheric dust burden is emitted from North Africa (e.g. Ginoux et al., 2012; Huneus et al., 2011) before being transported westwards across the tropical Atlantic towards the Caribbean (e.g. Gläser et al., 2015; Huneus et al., 2011; Wu et al., 2020). Ginoux et al.

(2012) estimate that Northern Africa accounts for 55% of global dust emissions. In the summer, dust outbreaks can occur every 3-5 days and the emitted dust reaches the Caribbean in 1-2 weeks (Gläser et al., 2015; Huang et al., 2010; Prospero and Lamb, 2003); Huang et al. (2010) estimates using Moderate Resolution Imaging Spectroradiometer (MODIS) satellite data that dust in the Saharan Air Layer (SAL), a typically dry and dusty air mass situated between 2 and 6 km that transports dust from North Africa to the Caribbean (Chiapello et al., 1995; Dunion and Velden, 2004; Huang et al., 2010; Prospero and Carlson, 1972) travels at a speed of 1000 km day<sup>-1</sup>.

Emission and transport of dust from North Africa to the Caribbean is complicated but in general, the SAL is developed as follows: Dust is emitted via a number of pathways including synoptic scale systems, nocturnal low level jets, boundary layer convection, cold pool outflows and dust devils (Marsham et al., 2011). Solar heating over Africa leads to the generation of convection and subsequently a hot, dry and dusty mixed layer. As this air is transported over the tropical Atlantic, the moist, cold sea air undercuts it. The dusty layer is warm enough to allow the formation of an inversion above the moist trade winds leading to the persistence of the SAL across the entirety of the tropical Atlantic (Prospero and Carlson, 1972). There SAL is generally understood to have low relative humidity, but there is some evidence of dust transport over the Atlantic in moist air masses, particularly where emission is related to cold pools (Schwendike et al., 2016b; Trzeciak et al., 2017), as well as a low level transport route in Easterly trade winds which is strongest in the wintertime (Chiapello et al., 1995).

During transport, dust particles can interact with clouds affecting their cloud droplet number concentration (e.g. Karydis et al., 2017), glaciation state (e.g. Tan et al., 2014), updraft strength (e.g. Van Den Heever et al., 2011; Lynn et al., 2016), and precipitation (e.g. Min et al., 2009; Yin et al., 2002). However, the effect of mineral dust particles on clouds is not well understood. For example, the addition of large and predominately insoluble dust particles can increase

CDNC in relatively pristine air masses or decrease CDNC in polluted and continental air masses (Karydis et al., 2017), as well as potentially preventing cloud formation if they take up considerable amounts of water, lowering supersaturation, without activating to cloud droplets (Barahona et al., 2010).

Mineral dust is also an efficient and globally dispersed INP (Atkinson et al., 2013; Niemand et al., 2012; Vergara-Temprado et al., 2017) meaning it can affect cloud phase with implications for cloud opacity and lifetime 1000s of kilometres from source (e.g. Komurcu et al., 2014; Murray et al., 2020; Zelinka et al., 2017). For example, observations by Sassen et al. (2003) indicate that Saharan dust is capable of glaciating altocumulus clouds over Florida with relatively warm cloud top temperatures of  $-8.8^{\circ}\text{C}$  and the accurate representation of K-feldspar INP number concentrations was shown to be important in representing the lifetime and radiative forcing of mixed-phase clouds in the Southern Ocean (Vergara-Temprado et al., 2018)

The ice-nucleating ability of mineral dust is thought to be related to characteristics of the particle surface, known as active sites, and varies depending on the aerosol mineralogy (Atkinson et al., 2013; Harrison et al., 2016). The most ice-active mineral in desert dust is potassium feldspar (K-feldspar) (Atkinson et al., 2013; Harrison et al., 2016; Niedermeier et al., 2015) and the contribution of K-feldspar-containing particles to global INP number concentrations has been used as a proxy to estimate the contribution of desert dust to global INP (Vergara-Temprado et al., 2017). Quantifying both the ice-nucleating ability of mineral dust and the number concentration of dust particles in the atmosphere is a challenge for atmospheric modelers with implications for the glaciation state of the simulated clouds. There are several orders of magnitude difference in ice nucleation active site densities for different types of feldspar, a component of mineral dust that has been shown to have particularly high ice-nucleating ability, at any one temperature (Harrison et al., 2016; Peckhaus et al., 2016), and

measurements of INP number concentrations in the SAL show similar variation due to the variability of dust export (Boose et al., 2016b).

The Global Model of Aerosol Processes (GLOMAP) is a global aerosol model that has a bin (GLOMAP-bin) or a modal (GLOMAP-mode) representation of aerosol distributions. The GLOMAP-bin model has previously been used to estimate the role of dust on the sulfate burden of East Asian dust storms (Manktelow et al., 2009) and on the role of dust transport in supplying soluble iron to the ocean (Shi et al., 2011). More recently, the GLOMAP-mode model was used to predict the global concentration of mineral dust and marine organic INP (Vergara-Temprado et al., 2017) and this model version has been used to evaluate the sources of INP number concentrations measured in the Saharan outflow region (Price et al., 2018) and in Northern England (O'Sullivan et al., 2018). However, the representation of dust concentrations in the Saharan outflow region in either of the GLOMAP models (GLOMAP-mode or GLOMAP-bin) has not been assessed.

Global climate models have been shown to have varying degrees of accuracy in predicting surface dust concentrations with observations frequently up to, and in some cases exceeding, an order of magnitude difference to the observed values (Huneus et al., 2011; Wu et al., 2020). In Manktelow et al. (2009), the wind-dependent emissions in the East Asian dust source region in GLOMAP-bin needed to be increased by a factor of 6-14 to match the dust concentrations observed by the flight campaign. The accuracy of the representation of dust in the version of GLOMAP-mode used to estimate K-feldspar INP number concentrations has not been tested and whether a similar scaling factor is required for accurate dust transport and concentrations is not known.

Furthermore, there are a number of uncertainties in the representation of the feldspar fraction of mineral dust in GLOMAP and therefore in the parameterisation of K-feldspar INP number concentrations that have not been explored. For example, the accumulation mode feldspar

fraction (including all feldspar types, e.g. K, Na and Ca rich feldspars) of mineral dust in GLOMAP is based on the coarse mode ratio of feldspar to quartz despite differences between the two minerals that may cause discrepancies in the distribution of mass between size modes (Nickovic et al., 2012). These include susceptibility of feldspar to chemical reactions (e.g. Augustin-Bauditz et al., 2014; Harrison et al., in prep) and fragmentation during wet-sieving (Perlwitz et al., 2015a) compared to quartz. Measured INP number concentrations from the 2017 Barbados Ice-nucleating particle Concentration Experiment (B-ICE) campaign (Harrison et al., in prep) and collocated long-term measurements of surface dust mass concentrations (Zuidema et al., 2019), both at Ragged Point, Barbados, present an opportunity to assess the representation of dust and K-feldspar INP transport from North Africa across the tropical Atlantic. Barbados is ideally situated for this task as the location is generally representative of the year to year variability in dust export from the Sahara (Chiapello et al., 2005).

This chapter is structured as follows: In Section 4.3, I describe the methods, model and observational datasets used in this thesis chapter. In Section 4.4.1, I compare the INP number concentrations measured during B-ICE to the INP number concentrations predicted by GLOMAP. The model overestimates the measured INP number concentrations. I therefore examine two possible explanations: that GLOMAP overestimates dust export from the Sahara (Section 4.4.1.1) and that GLOMAP overestimates the K-feldspar fraction of dust exported to the Western tropical Atlantic (Section 4.4.1.2). Section 4.4.2 examines the relative importance of marine organic INP over the tropical Atlantic and Section 4.4.3 quantifies the effect of a change in driving meteorology on the simulated INP number concentrations over the tropical Atlantic. Conclusions and recommendations for further study are detailed in Section 4.5.

## 4.3. Methods

### 4.3.1. Overall approach

This thesis chapter evaluates the ability of Global Model of Aerosol Processes (GLOMAP-mode) to predict the INP concentrations observed in the 2017 B-ICE campaign at Ragged Point, Barbados. GLOMAP-mode, referred to as GLOMAP herein, is a global aerosol model, the original version of which is detailed in Mann et al. (2010) and was adapted by Vergara-Temprado et al. (2017) to represent INP from the K-feldspar component of desert dust and marine organics in sea spray.

Potential explanations for discrepancies between the observed and simulated INP concentrations are explored. The model output is compared to several observations and reanalysis products, including:

- INP number concentrations observed during the 2017 B-ICE campaign.
- Observed surface dust concentrations from Barbados and Miami observed and reported in Zuidema et al. (2019).
- Integrated column dust and surface dust mass concentrations from the Modern-Era Retrospective analysis for Research and Applications (MERRA-2) reanalysis product (Randles et al., 2017).
- Profile dust measurements from lidar observations during the 2013 Saharan Aerosol Long-range Transport and Aerosol–Cloud Interaction Experiment (SALTRACE) (Ansmann et al., 2017; Rittmeister et al., 2017; Weinzierl et al., 2017).

As the primary purpose of this chapter is to evaluate the model performance in simulating the INP concentrations observed at Barbados in July and August of 2017, the results mainly use a 2017 GLOMAP run for comparison to observations or MERRA-2 products. However,

GLOMAP was also run for May 2013 in order to compare the simulation output to lidar dust profile measurements presented in Ansmann et al. (2017).

*Table 4.1. GLOMAP simulations carried out and discussed in this chapter.*

<b>Time period for analysis</b>	<b>Spin-up time</b>	<b>Driving meteorology data-set</b>	<b>Purpose of simulation</b>	<b>Compared to</b>
<b>July-August 2017</b>	July 2016- July 2017	ERA-interim	Determine the ability of GLOMAP to predict INP number concentrations at Barbados	INP number concentrations from the B-ICE campaign  MERRA-2 reanalysis of surface and column dust concentrations  Surface dust observations from Zuidema et al. (2019)
<b>May 2013</b>	May 2012- May 2013	ERA-interim	Determine the skill of GLOMAP in predicting the vertical distribution of dust	Dust mass profiles from lidar measurements during SALTRACE (Ansmann et al., 2017)
<b>Entirety of 2001</b>	January 2000- January 2001	ERA-interim	Determine the effect of the driving meteorology reanalysis dataset on INP and dust representation in GLOMAP	Surface dust observations from Zuidema et al. (2019)
<b>Entirety of 2001</b>	January 2000- January 2001	ERA-40		

In Price et al. (2018) and Vergara-Temprado et al. (2017), INP number concentrations from a 2001 GLOMAP simulation were compared to field measurements from multiple years and from the 2015 Ice in Clouds-Dust (ICE-D) field campaign, respectively. This simulation used the ERA-40 reanalysis dataset to determine the model meteorology including wind, temperature, humidity and large-scale precipitation. However, the ERA-40 reanalysis dataset is unavailable after 2002 and the ERA-interim reanalysis dataset is used in the simulations detailed here instead to allow the use of year-specific meteorology. Two simulations of the entirety of 2001 using the ERA-40 and the ERA-interim reanalysis datasets are carried out to determine the effect of the change in driving meteorology dataset on INP and dust concentrations. The GLOMAP simulations carried out and reported in this chapter are shown in Table 4.1.

### **4.3.2. Model Description**

GLOMAP has a grid spacing of  $2.8^\circ$  and 31 pressure levels (Vergara-Temprado et al., 2017). In all simulations at least a year of spin-up is conducted prior to the analysis period. GLOMAP represents dust, K-feldspar, sea salt, black carbon, particulate organic matter, and sulphate. GLOMAP aerosol processes comprise seven internally mixed lognormal modes (soluble nucleation (mean diameter  $<10$  nm), soluble and insoluble Aitken (10-100 nm), soluble and insoluble accumulation (100-1000 nm), and soluble and insoluble coarse ( $>1000$  nm) modes). The mass concentrations of each of these aerosol components are represented individually in prognostic variables for each mode. The number concentrations are represented with a prognostic variable for each mode representing lognormal size distributions corresponding to the modal diameter ranges given above (Mann et al., 2010). GLOMAP represents new particle formation by gas-to-particle conversion, growth by coagulation and condensation of low-

volatility gases, scavenging by impaction below cloud and nucleation in cloud, and dry deposition. Ice clouds are assumed to glaciate at  $-15^{\circ}\text{C}$  and nucleation scavenging of soluble aerosol is suppressed in these clouds. Insoluble aerosol can be scavenged in glaciated clouds. Aerosol scavenging in GLOMAP is detailed in Browse et al. (2012). Ice-nucleation by the K-feldspar component of mineral dust (Atkinson et al., 2013) and by marine organics in sea spray (Wilson et al., 2015) are represented in GLOMAP (Vergara-Temprado et al., 2017).

#### **4.3.2.1. Representation of mineral dust INP**

GLOMAP dust emissions are derived from daily-varying emission fluxes provided by AEROCOM emissions data-base (Dentener et al., 2006; Mann et al., 2010; Vergara-Temprado et al., 2017). Emissions are based on simulations using near-surface winds from the year 2000 from the NASA Goddard Earth Observing System Data Assimilation System and prescribed to take place in the lowest model layer (Dentener et al., 2006) after which they can be advected around by the winds of the GLOMAP run in question. This means that dust emissions are not specific to the year in question and annual variations in mineral dust export due to meteorological variation is not fully represented in GLOMAP simulations. The effect of this has not previously been tested to my knowledge.

Both feldspar and dust are emitted into the insoluble accumulation and coarse modes and can then move into the soluble accumulation and coarse modes upon aging by condensation of sulphates and secondary organic aerosol. Feldspar is emitted as a fraction of the dust mass concentration based on a global dataset of soil mineral composition compiled by Nickovic et al. (2012). This global database provides soil feldspar content for the coarse particle mode. The fraction of feldspar in the accumulation mode is calculated by assuming the ratio of feldspar to

quartz is the same in both the accumulation and coarse modes of mineral dust (Nickovic et al., 2012).

INP number concentrations are parameterised based on the K-feldspar component of mineral dust as detailed in Vergara-Temprado et al. (2017). The INP parameterisation assumes that 35% of feldspar is K-feldspar and capable of nucleating ice. The value of  $n_s$ , the number of active sites per unit particle surface area (Vali et al., 2015), is calculated based on either the Atkinson et al. (2013) (A13) or the Harrison et al. (2019) (H19) parameterisation. The soluble accumulation aerosol mode is the only mode used in the calculation of INP number concentrations. The inclusion of the other feldspar modes was tested and found to make very little difference to INP number concentrations, particularly far from source where most particles have been aged (and are therefore in the soluble category) and larger coarse particles have largely been removed from the atmosphere.

#### **4.3.2.1. Representation of marine organic INP**

Sea salt aerosols are emitted in GLOMAP as a function of the simulated 10 m wind speed based on Gong (2003). Sea salt emissions, unlike dust emissions, are specific to the year in question and not fixed to year 2000 emissions. The sea spray particles are emitted into the soluble accumulation mode and can be removed by nucleation scavenging in precipitating clouds. An organic mass fraction of the sea spray is calculated from the wind speed and the chlorophyll content of seawater in a parameterisation described in Vergara-Temprado et al. (2017). The INP number concentration from marine organics is then calculated from this organic mass fraction using the parameterisation of Wilson et al. (2015) as is described in Vergara-Temprado et al. (2017).

### **4.3.2.3. GLOMAP driving meteorology by ERA-interim and ERA-40 reanalysis datasets**

The driving meteorology including winds and precipitation in GLOMAP is based on European Centre for Medium-Range Weather Forecasts (ECMWF) model reanalysis datasets. Depending on the year of simulation, GLOMAP can use the ERA-interim or ERA-40 reanalysis datasets. Reanalysis datasets assimilate observational data into model simulations to provide global coverage of best-guess atmospheric conditions (Mooney et al., 2011). ERA-interim dataset covers the period 1979-2019 and ERA-40 datasets covers the period 1957-2002. ERA-interim was developed to replace the ERA-40 dataset and uses 4-dimensional, rather than 3-dimensional, variational assimilation (Dee et al., 2011). One of the primary aims of the ERA-interim reanalysis dataset was to address problems with the ERA-40 hydrological cycle, including large overestimates of rainfall over the tropical oceans (Dee et al., 2011; Uppala et al., 2005). The horizontal resolution of ERA-interim corresponds to a grid spacing of 79 km, compared to 125 km in ERA-40), on a reduced Gaussian grid (Dee et al., 2011). The vertical resolution of ERA-40 and ERA-interim are the same with 60 vertical levels up to 0.1 hPa (Dee et al., 2011).

### **4.3.3. Observational data**

#### **4.3.3.1. Barbados Ice-nucleating particle Concentration Experiment (B-ICE)**

The B-ICE sampling campaign was carried out from the 24<sup>th</sup> July to the 24<sup>th</sup> August 2017 at Ragged Point, Barbados. Ragged Point is the most easterly point of Barbados and is therefore a prime location to sample air masses that may have been influenced by Saharan dust and have since been transported across the tropical Atlantic. The Ragged Point measurement site is home to an Advanced Global Atmospheric Gases Experiment (AGAGE) measurement location and

a 17 m sampling tower belonging to the University of Miami (Zuidema et al., 2019). Aerosol measurements were taken from the top of the sampling tower. The INP measurement techniques are detailed in Harrison et al. (in prep).

Aerosols were sampled on polycarbonate filters using MESA PQ100 aerosol samplers. The samples were analysed for ice-nucleating ability on site within a portable laboratory. Ice-nucleating experiments were carried out using the  $\mu\text{L-NIPI}$  which uses an immersion mode drop assay technique (as detailed in Harrison et al., 2016; O’Sullivan et al., 2018). The aerosol sample is immersed in water and  $\mu\text{L}$  liquid droplets from this suspension are cooled and the temperature of first ice formation is recorded using a high-definition webcam. The INP number concentration of the suspension and consequently the aerosol sample can then be calculated.

#### **4.3.3.2. Surface-level dust measurements**

The GLOMAP-simulated dust mass concentrations are compared to long-term observations from Barbados and Miami presented in Zuidema et al. (2019). The Barbados measurements were taken from the same University of Miami sampling tower at Ragged Point as the INP measurements in B-ICE. In Miami, sampling occurs at the top of a 16 m tower on a 12 m building at Biscayne Bay. In both locations, sampling occurs every day (weather permitting). Samples are collected on 20 cm  $\times$  25 cm Whatman-41 (W-41) filters with pumps at a flow rate of 1 m<sup>3</sup> min<sup>-1</sup> (Zuidema et al., 2019). This dataset only comprises samples when the airflow is from the open ocean to the East at speed greater than 1 m s<sup>-1</sup> to remove the influence of local sources (Zuidema et al., 2019) allowing us to assume that the sampled air comprises predominately of dust transported from North Africa.

#### 4.3.3.3. Dust mass concentration profiles

Saharan dust transported across the tropical Atlantic is the source of 30-40% of the summertime aerosol volume in the Caribbean (Groß et al., 2016). An important transport route for North African dust is through the SAL, a dust-laden air mass situated between 2 and 6 km (e.g. Gläser et al., 2015). Therefore, in order to understand dust transport and concentration representations in GLOMAP, it is important to investigate the vertical distribution of dust over the tropical Atlantic.

In order to assess the vertical distribution of dust in GLOMAP, I compare profiles of dust mass concentrations from the model to observations of dust made using a polarization/Raman lidar during the 2013 SALTRACE campaign (Ansmann et al., 2017; Rittmeister et al., 2017; Weinzierl et al., 2017). An additional GLOMAP model run covering May of 2013 is carried out for direct comparison to these observations (Table 4.1). The SALTRACE profile measurements use the so called POLIPHON (Polarization Lidar Photometer Networking) method to firstly identify different aerosol types in a column and also to estimate the mass of fine and coarse mode dust in any identified dust layers. A full description of this method is beyond the scope of this thesis but is detailed in full in Ansmann et al. (2017) and Mamouri and Ansmann (2017; 2014).

Polarization lidar allows for the identification of different aerosol types (e.g. dust, urban haze or smoke from biomass burning) using profiles of the particle backscatter coefficient and linear depolarization ratios. The POLIPHON method distinguishes between dust and non-dust particles, as well as between fine and coarse mode dust, using their different depolarization ratios at 532 nm (Ansmann et al., 2017; Mamouri and Ansmann, 2017). Next the measured backscatter coefficients are converted into light extinction coefficients allowing the calculation of height profiles of the dust extinction coefficient at 532 nm. These extinction coefficient profiles are then converted into mass concentrations using extinction-to-volume conversion

factors determined using a combination of observations from the Aerosol Robotic Network (AERONET) sun photometer and field campaigns with lidar/photometer in Mamouri and Ansmann (2017) and an assumed dust density of  $2.6 \text{ g cm}^{-3}$  (Ansmann et al., 2017). The 2013 SALTRACE POLIPHON dust profile observations are used alongside the MERRA-2 integrated column dust concentrations to determine the skill of GLOMAP in representing the vertical distribution of dust globally and particularly over the tropical Atlantic. The division between the fine and coarse mode aerosol by the POLIPHON method corresponds exactly to the division between the GLOMAP accumulation and coarse mode aerosol ( $1 \mu\text{m}$ ).

#### **4.3.4. MERRA-2 dust reanalysis dataset**

The Modern-Era Retrospective analysis for Research and Applications, Version 2 (MERRA-2) is an atmospheric reanalysis dataset produced by NASA's Global Modeling and Assimilation Office (Gelaro et al., 2017; Mccarty et al., 2016). The dataset spans from 1980 to the present day and uses combinations of observations (including direct ground-based observations, ground-based remotely sensed observations, satellite retrievals, derivations, and radiances), and model simulations to calculate global values for a number of environmental and climate properties that are not readily observed by satellites directly (Mccarty et al., 2016). MERRA-2 has an aerosol analysis dataset which includes dust. The Goddard Chemistry, Aerosol, Radiation, and Transport (GOCART) model aerosol module (Chin et al., 2002; Colarco et al., 2010) is coupled to the Goddard Earth Observing System, version 5 Data Assimilation System which allows the inclusion of aerosol mass tracers for dust, sea-salt, black and organic carbon, and sulphate (Randles et al., 2017). The Goddard Aerosol Assimilation System is used to assimilate bias-corrected AOD from a number of sources including AVHRR (Advanced very-high-resolution radiometer), MODIS (Moderate Resolution Imaging Spectroradiometer) Terra

and Aqua datasets, MISR (Multi-angle Imaging Spectroradiometer), and AERONET (Randles et al., 2017).

Dust is represented in GOCART with five non-interacting size bins. The dust mass mixing ratio tracers in GOCART are externally mixed. The dust emissions are dependent on wind speed and use a map of dust source locations (Ginoux et al., 2001). Dust is removed via dry deposition (including gravitational settling), large-scale wet removal, and convective scavenging (Randles et al., 2017). The MERRA-2 dust dataset utilised in this study are the monthly surface dust concentrations and integrated column dust mass which were sourced from the NASA Worldview website. These products are produced on a  $0.5^\circ \times 0.625^\circ$  latitude by longitude grid (Randles et al., 2017). For comparison to the dust mass concentrations simulated by GLOMAP, the MERRA-2 datasets were regridded using linear interpolation to the GLOMAP grid of  $2.8^\circ \times 2.8^\circ$  latitude by longitude. It should be noted that regridding may cause some error in the regridded dataset due to differences in the resolution of the two grids but in the examples presented in Section 4.4.1.1 the differences between the MERRA-2 and GLOMAP datasets were in general large enough that the regridding method would not have a large effect on the results. MERRA-2 surface dust concentrations and AOD has been previously compared to observed dust concentrations in a large Saharan dust event in April 2010 and over the entirety of the year 2010 and was found to compare well with high correlation between the MERRA-2 and observed values (Buchard et al., 2017). The MERRA-2 dataset surface dust concentrations were also found to have good agreement to observations at a number of other locations globally (Wu et al., 2020).

## 4.4. Results

### 4.4.1. Simulation of INP number concentrations by GLOMAP during B-ICE

A GLOMAP simulation was conducted to coincide with the 2017 B-ICE INP measurement campaign at Ragged Point, Barbados. The output of this simulation is compared to measured INP concentrations in the following section.

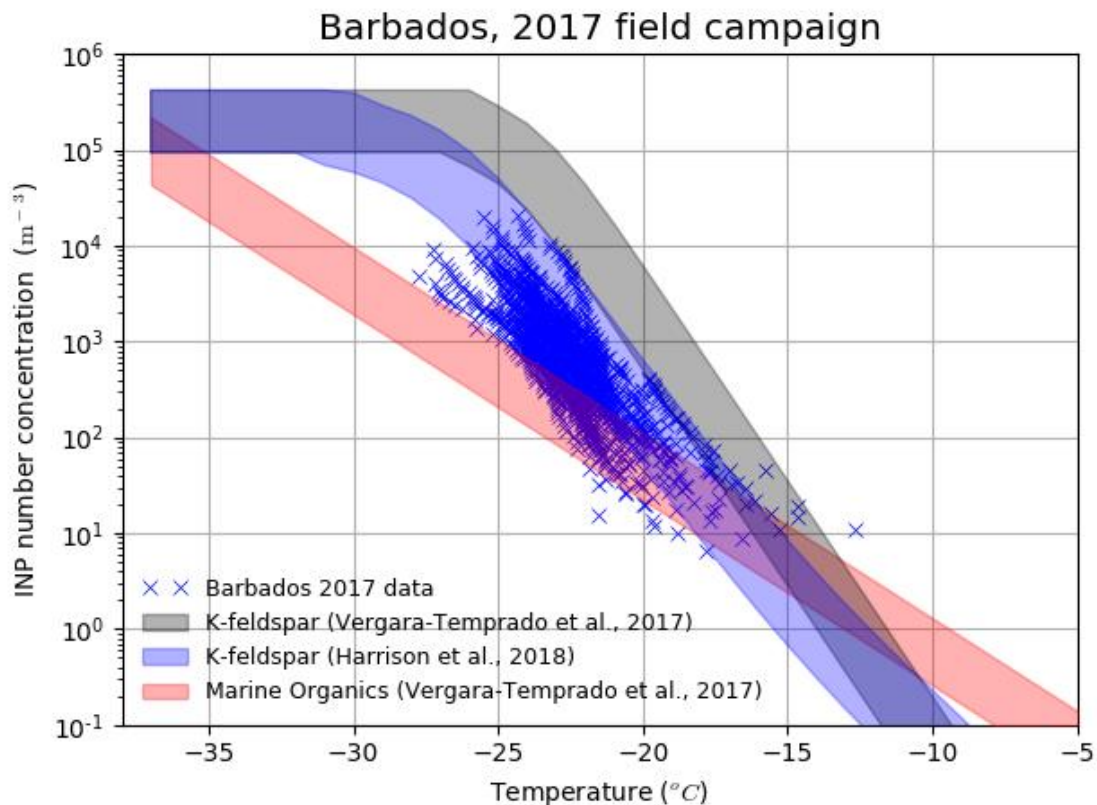


Figure 4.1. Measured and simulated INP number concentrations at Ragged Point, Barbados between the 20<sup>th</sup> July and the 24<sup>th</sup> August 2017, i.e. during the 2017 B-ICE campaign. Shown is the model prediction of INP number concentration due to marine organics (Wilson et al., 2015) and due to K-feldspar in dust based on both the A13 parameterisation (Atkinson et al., 2013; Vergara-Temprado et al., 2017) and the H19 parameterisation (Harrison et al., 2019).

Figure 4.1 shows a comparison between INP number concentrations measured in the field campaign and those simulated by GLOMAP using two INP parameterisations based on the K-feldspar content of mineral dust (A13, H19) (Atkinson et al., 2013; Harrison et al., 2019) and the Wilson et al. (2015) parameterisation based on marine organics emitted in sea spray. The shaded areas in Figure 4.1 represent the range of values simulated by GLOMAP for the time period of the B-ICE field campaign. The K-feldspar INP parameterisations have higher predicted INP concentrations than were measured in the field campaign. The A13 parameterisation over predicts INP concentrations at most temperatures by 1-2 orders of magnitude.

The simulated INP number concentrations overlaps with the new H19 parameterisation but appear to be biased high: the measured values extend to approximately one order of magnitude lower than the range simulated by GLOMAP. GLOMAP predicts that at high temperature above  $\sim 10^{\circ}\text{C}$ , marine organic INP will become important relative to K-feldspar INP. However within the temperatures where INP were measured during the B-ICE campaign, particularly between  $-20^{\circ}\text{C}$  and  $-30^{\circ}\text{C}$ , K-feldspar INP will dominate.

Figure 4.2 shows the simulated global distribution of total INP and the K-feldspar and marine INP from the A13 and the Wilson et al. (2015) parameterisations at a temperature of  $-20^{\circ}\text{C}$  over the time period of the Barbados field campaign. Regions of dust emission have the highest INP concentrations owing to the high dust, and consequently K-feldspar, concentrations in those regions. Barbados and the rest of the tropical Atlantic are in the dust export region of the Saharan desert and therefore have relatively high INP concentrations relative to other oceanic regions around the world, which are dominated by marine organic INP. The over-prediction of the measured INP by both the A13 and H19 parameterisations during B-ICE (Figure 4.1) indicates that the model is predicting too many K-feldspar-containing particles.

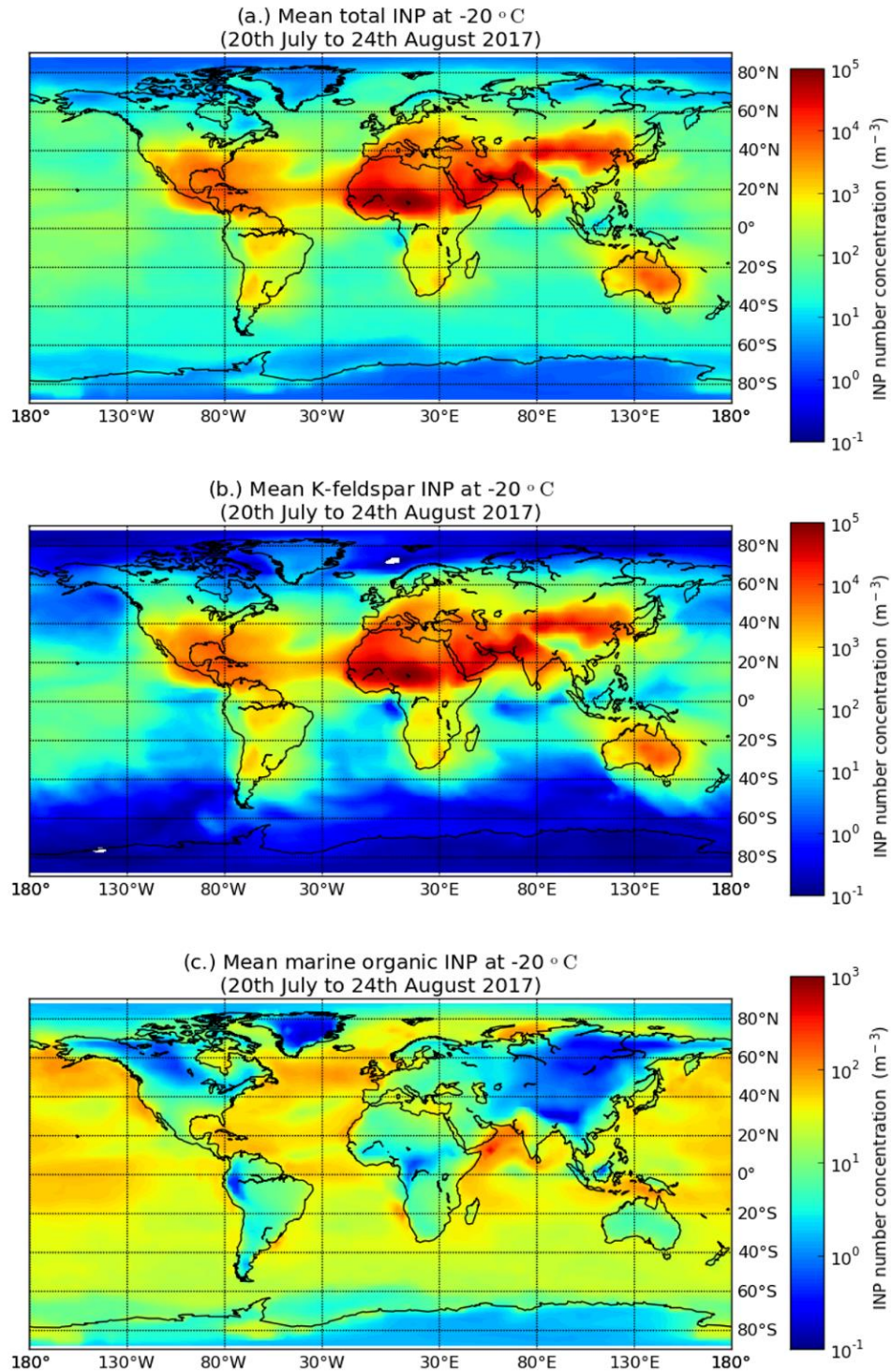


Figure 4.2. Global distribution of total INP number concentrations (the sum of INP from marine organics and K-feldspar from the A13 parameterisation) (a), INP from K-feldspar based on the A13 parameterisation (b), and INP from marine organics (c) at the surface for a temperature of  $-20\text{ }^{\circ}\text{C}$ .

I will now explore potential reasons for the over-prediction of the B-ICE K-feldspar INP number concentrations by GLOMAP. There are two potential explanations for the discrepancy between measured and simulated INP number concentrations:

1. The INP number concentration at Barbados is over-predicted by the A13 and H19 parameterisations due an over-prediction of dust concentrations at Barbados caused by the model exporting too much Saharan dust across the tropical Atlantic. An over-prediction of dust would result in an excess of feldspar particles (which are emitted as a fraction of the dust emissions) and consequently an over-prediction of K-feldspar INP particles. We test this theory by comparing the GLOMAP dust mass predictions to ground based measurements at Barbados and Miami (Zuidema et al., 2019), surface and column integrated dust mass predictions by the MERRA-2 satellite reanalysis dataset and to dust mass profiles calculated from lidar measurements during the SALTRACE ship-based field campaign (Ansmann et al., 2017).

The results show that the dust mass concentrations simulated by GLOMAP at Barbados are below or within the variability of all observational and reanalysis datasets examined and as such an over export of dust from North Africa cannot explain the over-prediction of INP number concentrations during B-ICE.

2. The INP number concentration at Barbados is over-predicted by the A13 and H19 parameterisations due an over-prediction of the K-feldspar content of dust. An over-prediction of K-feldspar could be caused by an overestimation of the K-feldspar content of dust at emission or an overestimate of the transport of dust particles containing K-feldspar across the tropical Atlantic Ocean. I examine this theory by comparing the GLOMAP predicted K-feldspar content of aerosol at Barbados to that measured during

B-ICE and to values available in the literature, as well as examining the relative content of K-feldspar in the accumulation and coarse mode dust at Barbados.

The results show that the K-feldspar content of mineral dust predicted by GLOMAP by B-ICE is larger than observations and literature values and as such may explain the over-prediction of K-feldspar INP number concentrations. However there are a number of other uncertainties and structural components of the GLOMAP model that complicate the picture and may compensate for one another. A schematic depicting the competing aspects of GLOMAP INP representation and the unquantified uncertainties is shown in Figure 4.3.

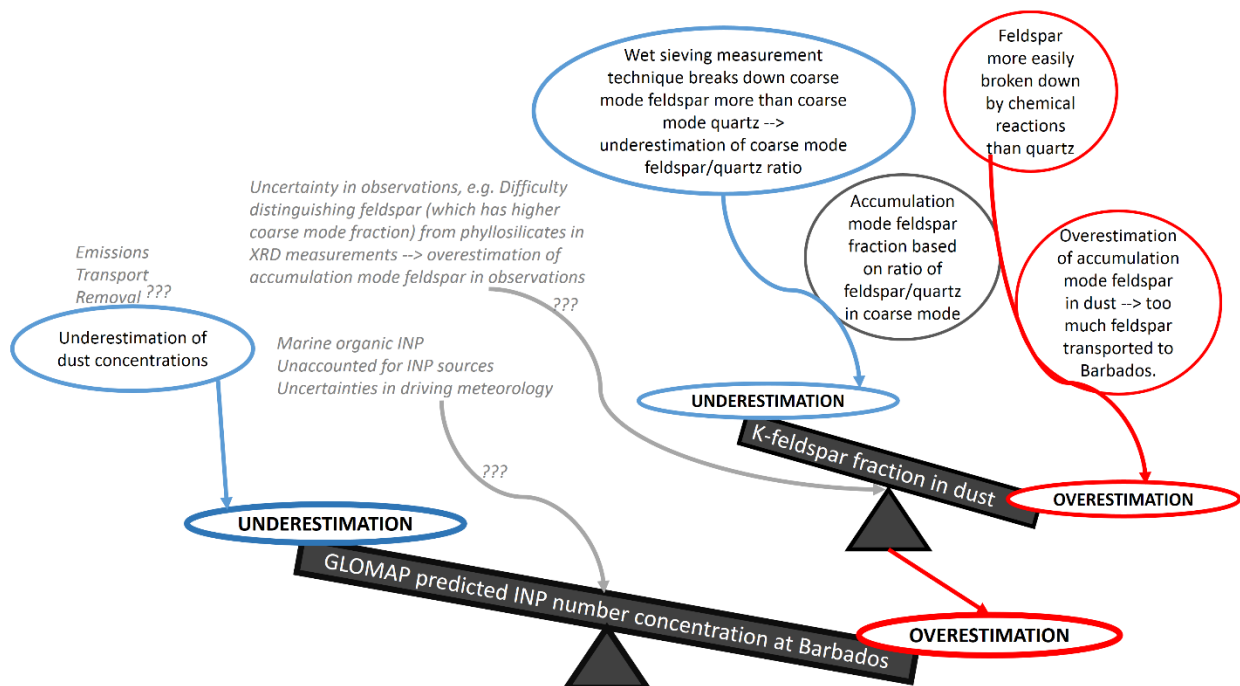


Figure 4.3. Schematic depiction of the model behaviour and uncertainties that may be contributing to the overestimation of INP number concentrations at Barbados by GLOMAP.

#### **4.4.1.1. Hypothesis 1: GLOMAP is overestimating dust export across the tropical Atlantic.**

In this section, dust mass concentrations predicted by GLOMAP are compared to a number of observational and reanalysis datasets to determine whether the over-prediction of INP number concentrations during B-ICE is due to an over-prediction of dust export from North Africa across the tropical Atlantic.

##### *Comparison to ground-based measurements*

The mean aerosol mass concentration measured during the B-ICE field campaign using an Aerosol Particle Sizer (APS) was  $20.8 \pm 11.2 \mu\text{g m}^{-3}$ . The mean is higher than the aerosol mass of  $14.8 \pm 8.2 \mu\text{g m}^{-3}$  simulated by GLOMAP and within the variability. This gives us a first indication that dust mass is not over-predicted at Barbados. The GLOMAP simulated surface dust concentrations were also compared to ground-based observations for July and August 2017 at both Barbados and Miami presented in Zuidema et al. (2019). Miami is situated at the northern edge of the SAL and thus provides a broader picture of the GLOMAP representation of Saharan dust export than if we look at Barbados alone.

A time series of daily surface dust concentrations simulated by the model and measured using filters at ground based stations at Barbados and Miami are shown in Figure 4.4. Also shown is the range of values measured throughout the entirety of the ground based stations lifetimes (1973-2017 for Barbados, and 1974-2018 for Miami) (Zuidema et al., 2019) for the time-period of the field campaign. In general the model has lower surface dust concentrations than the observations at Barbados and Miami.

In Barbados (Figure 4.4a), GLOMAP simulated some of the variability shown in the observations but generally fails to capture the magnitude of the peaks, e.g. between the 10<sup>th</sup> and the 20<sup>th</sup> of August, the observations show a peak of  $100 \mu\text{g m}^{-3}$  while GLOMAP shows a

peak of  $25 \mu\text{g m}^{-3}$ . In Miami (Figure 4.4b), peaks in dust concentrations in the observations between the 5<sup>th</sup> and 110<sup>th</sup> of July and the 5<sup>th</sup> and 12<sup>th</sup> of August are not represented at all in the model simulations.

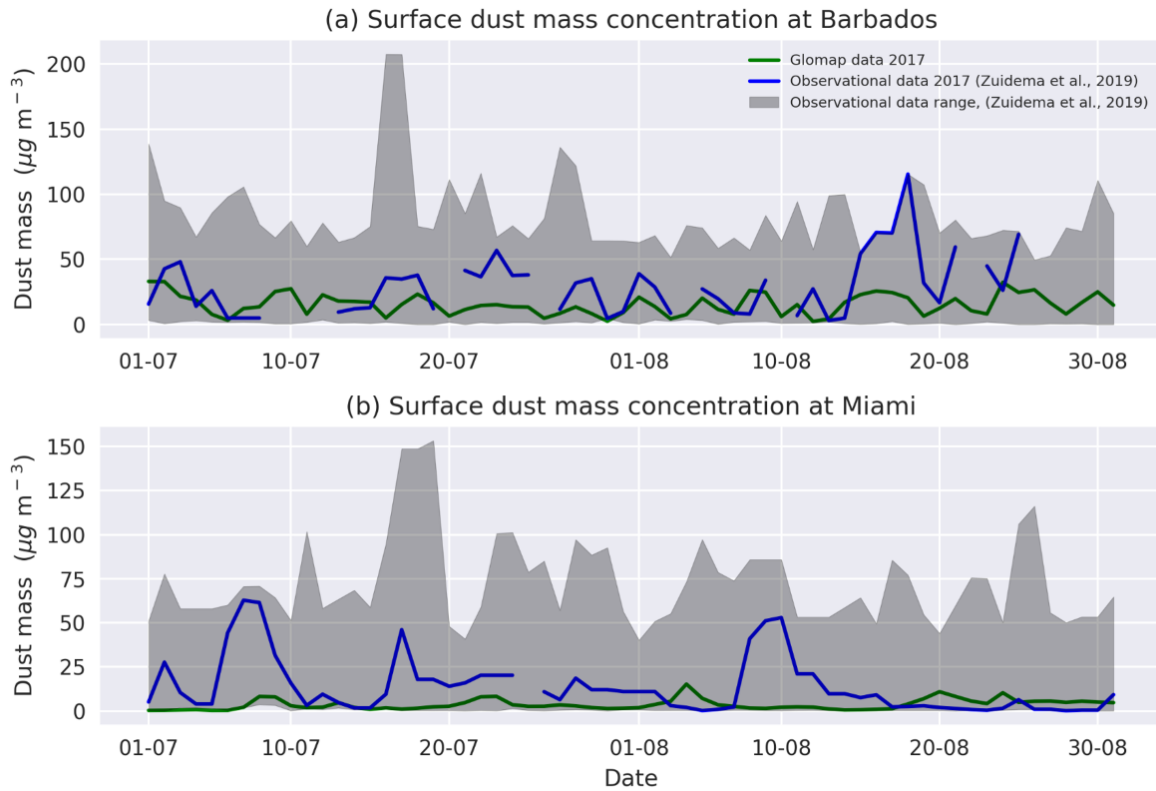


*Figure 4.4. Observed and simulated daily surface dust concentrations in July and August 2017. Surface dust mass concentrations at Barbados (a) and Miami (b) simulated by GLOMAP and observed at ground based stations (Zuidema et al., 2019). The range of dust mass concentrations observed between 1973 and 2017 (a) and between 1974 and 2018 (b) is also shown.*

This underestimate of surface dust concentrations by GLOMAP relative to the ground-based measurements is illustrated further in Figure 4.5, which shows the July and August median and interquartile ranges of the daily GLOMAP 2017 simulation alongside the interquartile ranges of the observations for 2017, 2000, and for all years within the database (1973-2017 for Barbados and 1974-2018 for Miami). The surface dust concentration at Barbados in the 2017

MERRA-2 reanalysis dataset is also shown. The MERRA-2 data are monthly means so there is only one value shown for each location in Figure 4.5.

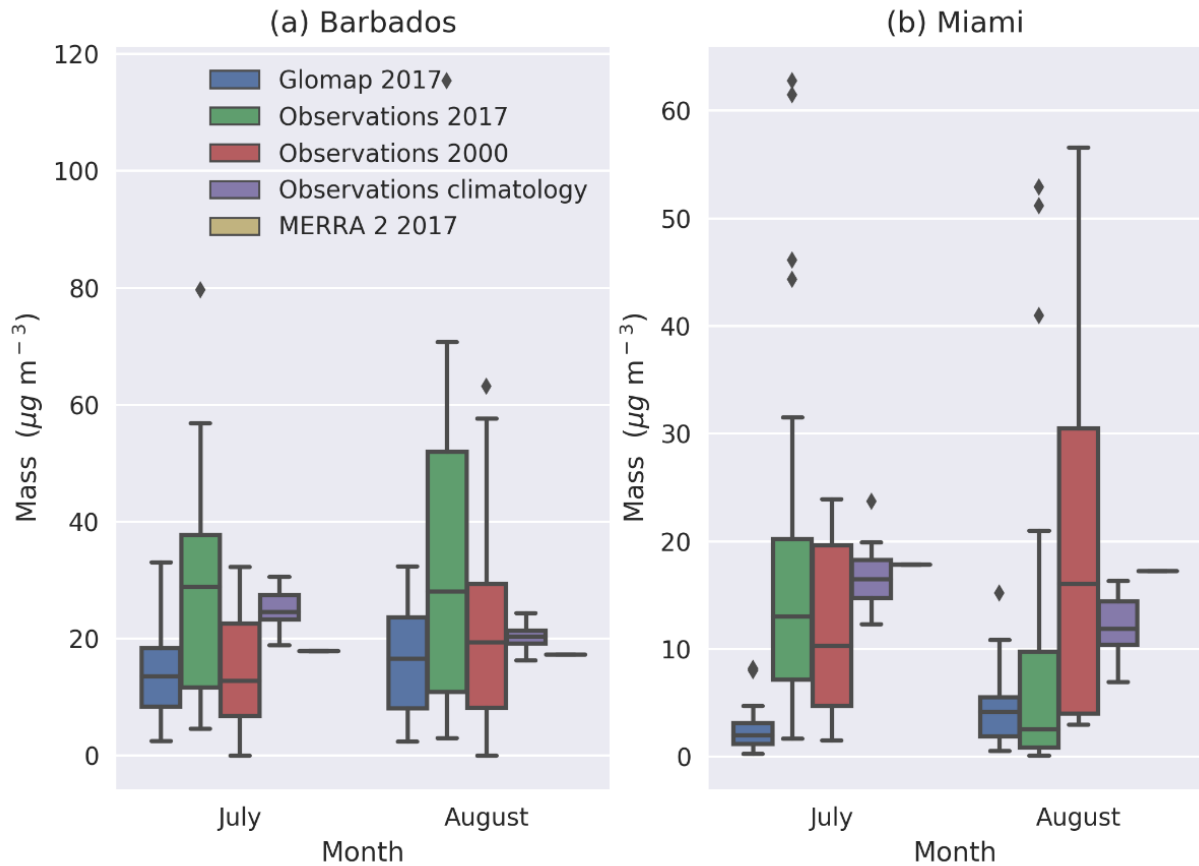


*Figure 4.5. Observed and simulated daily surface dust mass concentrations in July and August. Box plots showing the median, interquartile ranges, and outliers of surface dust mass concentrations in July and August at Barbados (a) and at Miami (b) from a 2017 GLOMAP simulation, from ground-based stations in 2017, 2000 and in all years from 1973 to 2017 (a), and from 1974 to 2018 (b). The surface dust mass concentration from MERRA-2 reanalysis for July and August 2017 is also shown. As the used MERRA-2 dataset is a monthly dataset it only contains one value for each month and as such does not have a median or an interquartile range.*

In Barbados (Figure 4.5a), the 2017 GLOMAP simulated values are within the range of the observations but with lower median and interquartile ranges for both July and August. The MERRA-2 values at Barbados are very close to the median GLOMAP simulated values. In

Miami (Figure 4.5b), the GLOMAP median and interquartile ranges are within the range of the observations for 2017 in August. However, in July, the GLOMAP simulated values are biased low, with the median sitting just inside the edge of the lower interquartile range indicating an underestimate of dust concentrations relative to the observations (as was also seen in Figure 4.5b)

The GLOMAP dust concentrations at Barbados show better agreement with the observed ground-based values from 2000 than those from 2017. This indicates that the GLOMAP representation of dust transport maybe more accurate if it used dust emission data from the year in question. Presently, the model uses AERONET emissions from 2000 for every year of simulation. However, the agreement with the 2000 observations is not universal. For example, in August at Miami, GLOMAP agrees better with the 2017 observations than the 2000 observations. Wet deposition becomes increasingly important for dust removal on the edge of the Saharan dust layer and in the Western SAL as the inversion that maintains the SAL is weakened by radiational cooling and convection becomes more common (Prospero and Carlson, 1972). Therefore, the position of Miami at the Northern edge of the SAL means that changes in dust removal by wet scavenging, which is specific to the simulated year, may be more important for the observed dust concentrations than dust emissions.

### ***Comparison to the MERRA-2 reanalysis dataset***

The surface dust mass concentration simulated by GLOMAP for July and August was compared to the MERRA-2 reanalysis dataset. The surface dust concentrations of MERRA-2 and GLOMAP in August are shown in Figure 4.6. In most locations GLOMAP has a lower surface dust concentration than MERRA-2. The largest absolute differences (Figure 4.6c) are seen in regions of emission. For example, Northern Africa has low biases of up to  $600 \mu\text{g m}^{-3}$

in some areas in the GLOMAP simulation relative to the MERRA-2 values. The largest relative differences (Figure 4.6d) between the two datasets are seen at low latitudes far from source where MERRA has higher concentrations than GLOMAP.

Regions of emission in GLOMAP, such as Australia, the African Sahel and the Southern tip of South America have dust concentrations over 100% higher than that of the MERRA-2 dataset. However, the dominant global signal is a strong negative bias of nearly 100% in almost all regions in the GLOMAP simulation relative to MERRA-2. This is particularly obvious in the Arctic and Antarctic all of which exhibit low biases in surface dust mass of greater than 80% relative to MERRA-2. However, at Barbados, Figures 4.5 and 4.6(c, d) indicate near agreement between the GLOMAP and MERRA-2 datasets in Barbados with GLOMAP exhibiting a small negative bias of ~ 10% relative to MERRA-2 (Figure 4.6d). The smallest relative differences between GLOMAP and the MERRA-2 dataset are in dust export regions where differences are generally less than 20%, for example, over the tropical Atlantic, including Barbados, and to the North West of Australia.

The picture is largely the same for the column integrated dust concentrations predicted by MERRA-2 (Figure 4.7a) and GLOMAP (Figure 4.7b). GLOMAP has higher column-integrated dust concentrations over regions of emission such as North Africa and Australia, but the global picture is one of large negative biases of nearly 100% in all regions, particularly far from dust emission regions (Figure 4.7c, d). Over the tropical Atlantic, the column-integrated dust mass concentrations are up to 25% lower than in the MERRA-2 dataset. Overall, comparison to the MERRA-2 monthly surface and column integrated dust concentration dataset does not support the hypothesis that an over export of dust from North Africa causes the over-prediction of INP number concentrations by GLOMAP relative to the B-ICE measurements

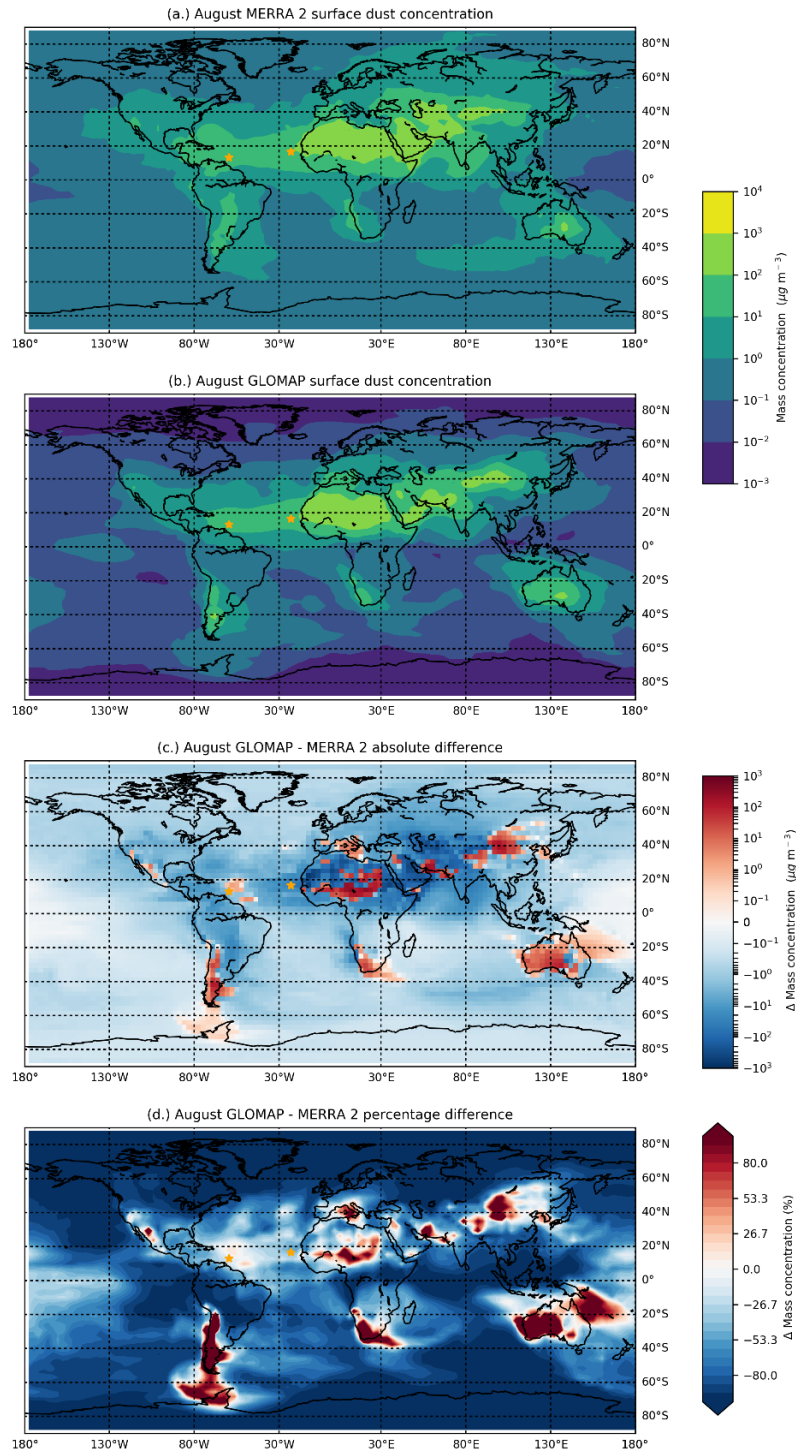


Figure 4.6. Comparison of global surface dust mass concentrations in MERRA-2 satellite reanalysis and GLOMAP for August 2017. MERRA-2 surface dust mass concentrations (a), GLOMAP surface dust concentrations (b), absolute difference between GLOMAP and MERRA-2 (c), and the percentage difference between GLOMAP and MERRA-2 (d). The location of Cape Verde and Barbados are marked by yellow stars.

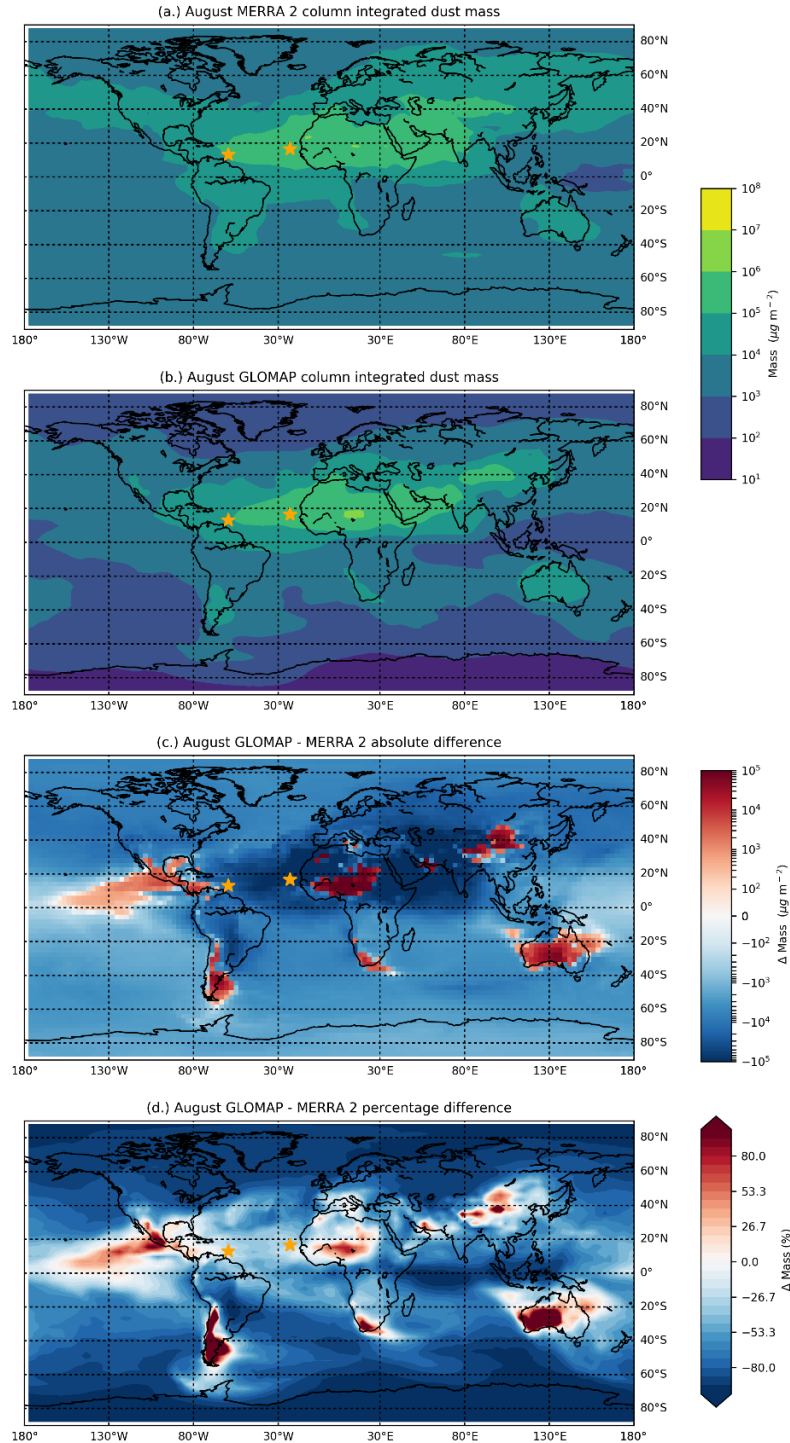


Figure 4.7. Comparison of global column integrated dust mass concentrations in MERRA-2 satellite reanalysis and GLOMAP for August 2017. MERRA-2 column integrated dust mass concentrations (a), GLOMAP column-integrated dust concentrations (b), absolute difference between GLOMAP and MERRA-2 (c) and the percentage difference between GLOMAP and MERRA-2 (d). The location of Cape Verde and Barbados are marked by yellow stars.

### *Comparison to dust mass concentration profiles measured by lidar*

In order to further assess the vertical distribution of dust in GLOMAP, the modelled dust mass concentration profiles from a simulation of May 2013 are compared to observations of dust made using a polarization/Raman lidar during the 2013 Saharan Aerosol Long-range Transport and Aerosol–Cloud Interaction Experiment (SALTRACE) (Ansmann et al., 2017; Rittmeister et al., 2017; Weinzierl et al., 2017) (Figure 4.8). The cruise travelled from the Western tropical Atlantic to Cape Verde (marked with a star in Figures 4.6 and 4.7) and undertook four lidar measurements of the dust mass profiles using the POLIPHON method along the way. The locations and dates of the measured profiles are shown on a contour plot of the integrated column dust measurements from GLOMAP between the 5<sup>th</sup> and 23<sup>rd</sup> of May 2013 in Figure A4.1 (Appendix Section 4.6). Figure 4.8 shows the lidar-observed and GLOMAP-simulated fine (or accumulation) mode (Figure 4.8, left column) and coarse mode (Figure 4.8, right column) dust mass concentration profiles. The GLOMAP profiles are the average value (red dotted line) and the range (red shading) of mass concentrations for the exact location and time of the dust profiles and the two grid boxes and daily time steps either side of this. This range is shown because exact point-to-point comparisons between modelled and observed values can be misleading if for example, GLOMAP is simulating observed dust events relatively well but with a slightly different trajectory or timing.

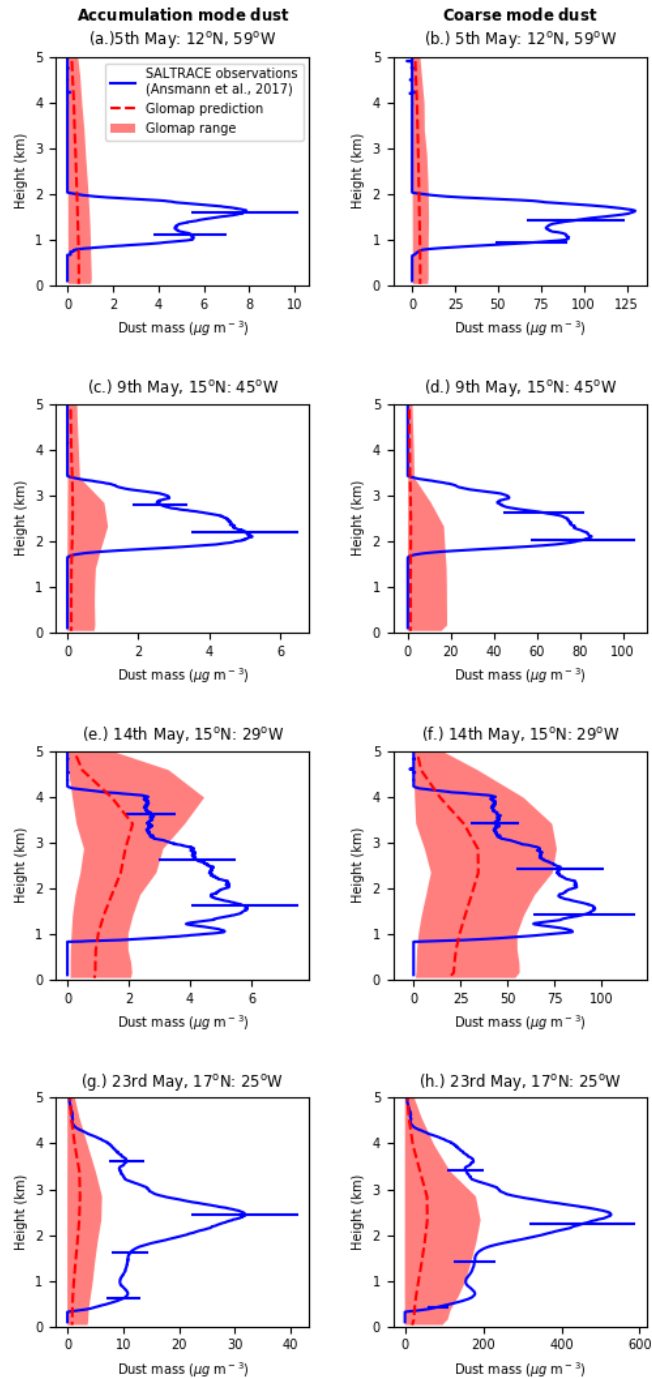


Figure 4.8. Comparison of GLOMAP dust mass concentration profiles to lidar observations from the 2013 SALTRACE ship campaign (Ansmann et al., 2017). Profiles of accumulation (a, g, e, g) and coarse (b, d, f, h) mode dust from the lidar observations (blue, with error bars shows), and GLOMAP (red line depicts mean from the 2 grid boxes and days either side of the observation location and time, while the shaded area indicates the range over this region and time). Locations of the profiles shown in a-h can be seen Figure A4.1 (Appendix Section 4.6).

The observed profiles (blue lines in Figure 4.8) indicate a relatively well-defined dust layer at all four measurement locations. The altitude and peak values of the dust layer increase at locations closer to the Sahara indicating that the Eastern tropical Atlantic is characterized by a very concentrated dust layer of over  $500 \mu\text{g m}^{-3}$  and extending from under 0.5 km to over 4 km in altitude (Figure 4.8g, h). As the dust is transported towards the Americas the dust is removed and the dust concentrations reduced due to wet and dry deposition, although it is expected that dry deposition will dominate in the SAL (Prospero and Carlson, 1972). The dust layer also descends to a maximum altitude of 2 km in the profiles taken in the Western tropical Atlantic (Figure 4.8a, b). It should be noted that the SALTRACE campaign travelled from West to East and as such the profiles shown in Figure 4.8 were likely not from the same dust event.

At all locations and dates, and for both coarse and fine mode dust, GLOMAP fails to capture the magnitude of the dust layer and consistently under-predicts the dust concentration in the SAL. The modeled values are closer to the observations in the Eastern tropical Atlantic (Figure 4.8e-h) than in the Western tropical Atlantic (Figure 4.8a-d) where no notable dust layer is observed in either coarse or fine mode dust. This indicates that dust removal processes in GLOMAP may be too strong. However the magnitude of the dust layer is also too small on the 23<sup>rd</sup> May profile close to North Africa indicating that dust emissions may also be too low.

It is obvious from Figure 4.8 that GLOMAP is failing to accurately capture the formation of and persistence of the SAL. This indicates that the model is not representing some of the complex emission and transport pathways of Saharan dust (Chiapello et al., 1995; Heinold et al., 2013; Marsham et al., 2011, 2013; Prospero and Carlson, 1972). Dust uplift can occur in numerous ways, including via nocturnal low level jets, haboobs and boundary layer convection, and most of these processes are extremely variable and occur in fractions of grid boxes of many climate and aerosol models (Heinold et al., 2013). For example, cold pool outflows can potentially generate up to 50% of summertime uplift and are poorly represented in coarse

resolution models (Marsham et al., 2011). The use of AEROCOM emissions from the year 2000 regardless of the year being simulated by GLOMAP likely inhibits the model from capturing much of the spatial and temporal heterogeneity of dust emission and SAL generation. Comparison to a number of observation and reanalysis datasets (Zuidema et al. (2019) ground-based measurements (Figure 4.4, 4.5), APS measurements conducted within the B-ICE campaign, MERRA-2 reanalysis datasets (Figure 4.6, 4.7) and observations of dust made using a polarization/Raman lidar (Figure 4.8) (Ansmann et al., 2017; Rittmeister et al., 2017; Weinzierl et al., 2017)) does not support the hypothesis that an over export of dust from the Sahara to Barbados is causing the observed over-prediction of INP number concentrations during B-ICE.

#### **4.4.1.2. Hypothesis 2: GLOMAP is over-estimating the K-feldspar content of dust at Barbados**

##### ***Model Prediction of K-feldspar content and comparison to observations and literature values***

Figure 4.1 shows that GLOMAP overestimates the observed INP concentrations at Barbados using both the A13 and H19 parameterisations. I now examine the hypothesis that the overestimation of INP concentrations during B-ICE by GLOMAP is due to an overestimation of K-feldspar content of dust at Barbados. GLOMAP estimates that 80% of aerosol mass at Barbados is composed of mineral dust (Figure 4.9a). It predicts that feldspar and K-feldspar comprise 15-25 % and 7-10 % of aerosol mass, respectively, at Barbados (Figure 4.9b, c).

A feldspar content of aerosol of 15-25% is relatively high compared to previous observations. Kandler et al. (2018) found that feldspar comprised 2-4% of silicate particles measured at Ragged Point in Barbados in the summers of 2013 and 2016, although this is likely an

underestimate as it only accounts for particles comprised solely of feldspar and not particles with mixed mineralogy. Atkinson et al. (2013) found that GLOMAP overestimated the feldspar content of dust relative to observations in regions far from source. This was attributed to the model not representing wet scavenging and thus not removing enough feldspar particles, something, which is remedied in the GLOMAP version used here (Atkinson et al., 2013; Vergara-Temprado et al., 2017). However, scavenging by ice clouds, which in GLOMAP glaciate at  $-15^{\circ}\text{C}$ , is not represented.

Evaluation of the modelled feldspar fraction in the GLOMAP simulations presented here difficult because many previous observations including those used by Atkinson et al. (2013), likely overestimated the feldspar fraction found in the accumulation mode aerosol. This is because feldspar and phyllosilicates are difficult to distinguish in observations based on X-ray diffraction (XRD) analysis (Perlwitz et al., 2015b) meaning the same volume fraction is often applied to both species (Kandler et al., 2009). Recent measurements suggest that the mass of feldspar increases relative to phyllosilicates at larger silt (coarse mode) sizes meaning that such observations and the measurements they are based on may over-predict the amount of feldspar in the clay (accumulation mode) and consequently their transport from source (Perlwitz et al., 2015b). An over-prediction of feldspar in the accumulation rather than the coarse mode will lead to increased transport of feldspar from source (Perlwitz et al., 2015b).

XRD and Scanning Electron Microscopy with Energy Dispersive Spectroscopy (SEM-EDS) analysis of the aerosol measured throughout the study period estimate the K-feldspar content of aerosol to be  $\sim 1\%$  (Harrison et al., in prep). This observation is in agreement with previous studies (Kandler et al., 2018). Adjusting the assumed K-feldspar content to aerosol mass simulated by GLOMAP from  $\sim 7\%$  to  $\sim 1\%$  greatly improves the agreement of the observed INP concentrations with the INP concentrations estimated by the H19 and A13 parameterisations (Figure 4.10).

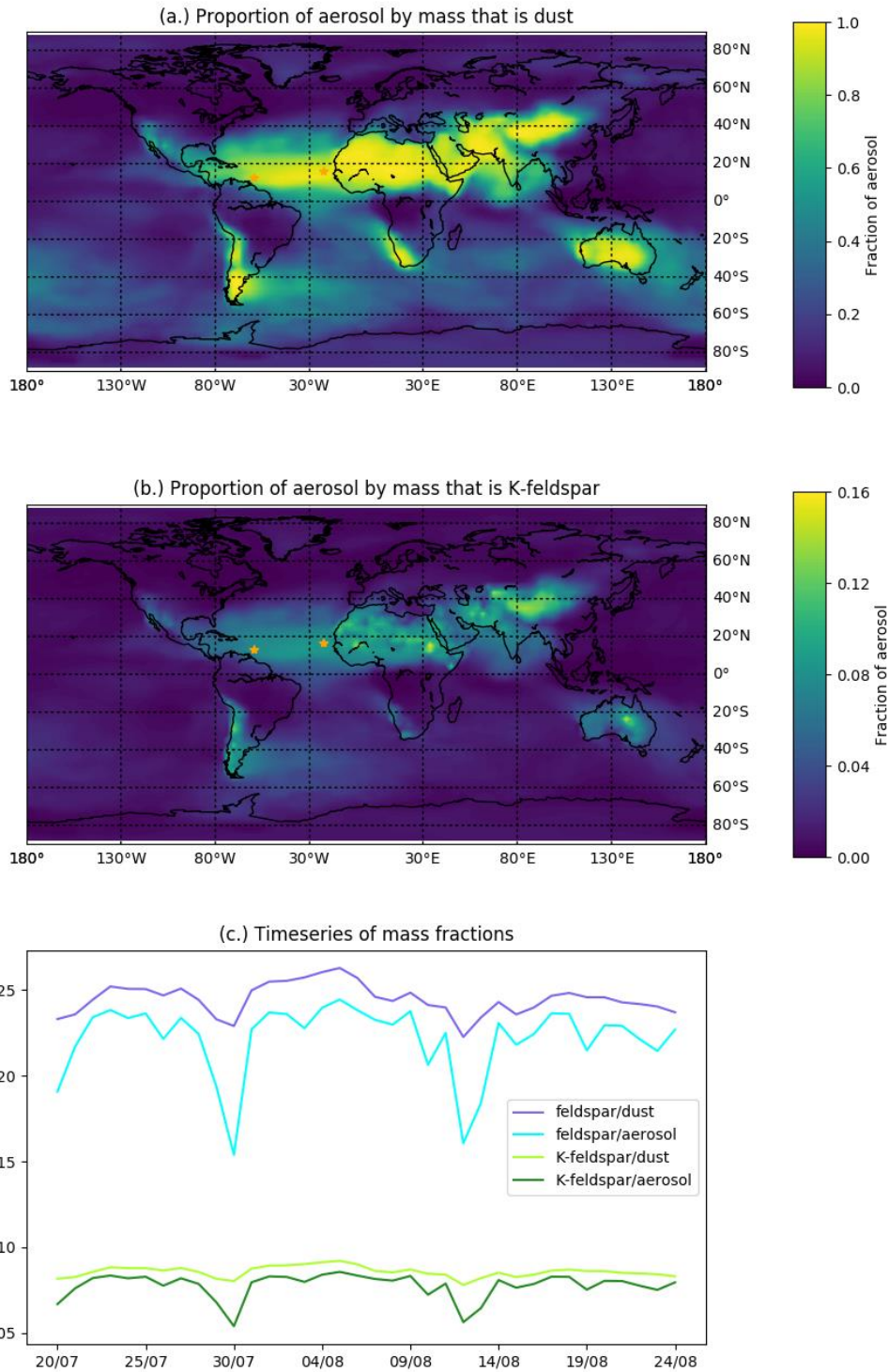
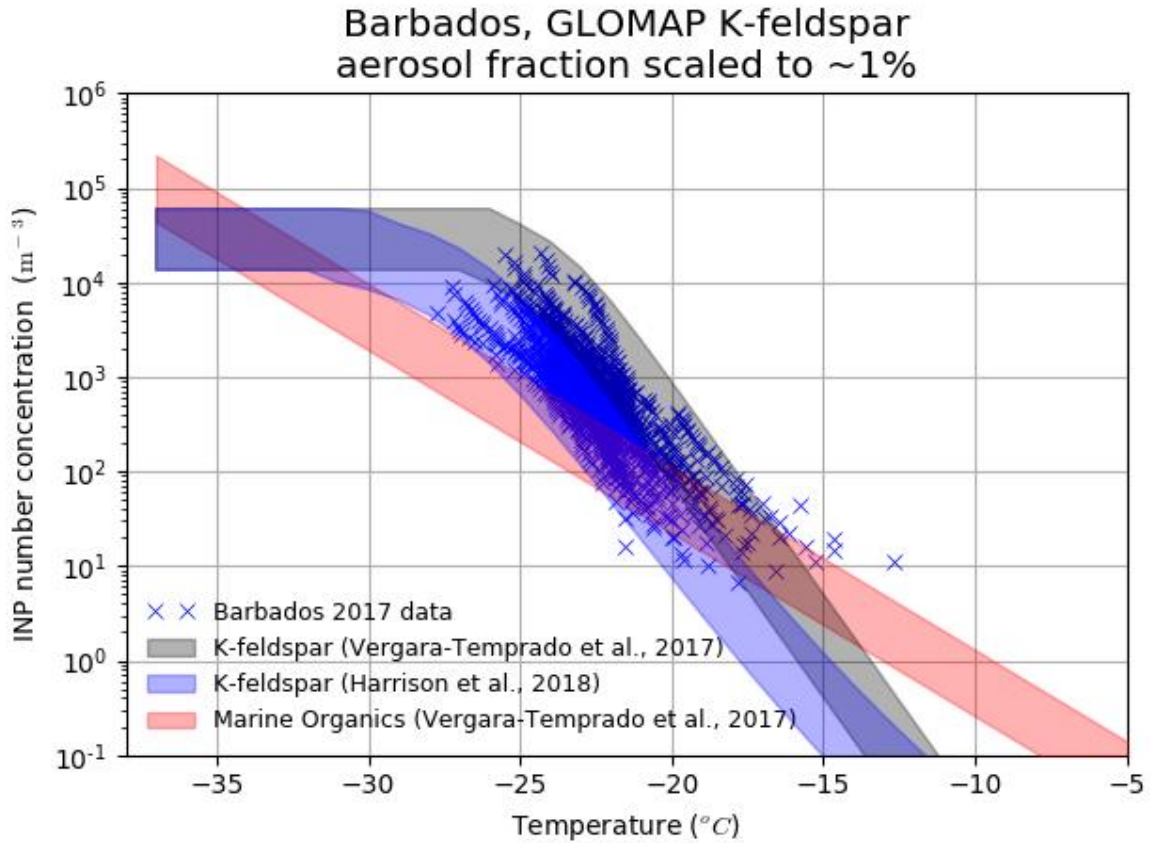


Figure 4.9. Composition of global surface aerosol. Global distribution of the mass fraction of dust in aerosol (a) and the mass fraction of K-feldspar in aerosol (b), and a timeseries of volume fractions of feldspar and K-feldspar in dust and aerosol at Ragged Point, Barbados throughout the time period of the 2017 observational campaign. The location of Cape Verde and Barbados are marked by yellow stars in b and c.



*Figure 4.10. Measured and simulated INP number concentrations at Ragged Point, Barbados between the 20th July and the 24th August 2017 adjusted from that shown in Figure 4.1 assuming a 1% volume fraction of K-feldspar in aerosol. Shown is the model prediction of INP number concentration due to marine organics (Wilson et al., 2015) and due to K-feldspar in dust based on both the A13 parameterisation (Atkinson et al., 2013; Vergara-Temprado et al., 2017) and the H19 parameterisation (Harrison et al., 2019).*

### ***Model behaviour and structure affecting simulated K-feldspar content***

I now explore how to reconcile an underestimate of dust concentrations in the boundary layer with an overestimate of feldspar and K-feldspar content (which are emitted as a fraction of mineral dust). In GLOMAP, feldspar is emitted based on a global dataset of soil mineral composition compiled by Nickovic et al. (2012). However, the global database only provides a soil feldspar content for the coarse (or silt) aerosol mode. The accumulation (or clay) mode

fraction of feldspar in soil is not specified. The fraction of feldspar in dust in the accumulation mode aerosol is therefore calculated by assuming that the ratio of feldspar to quartz is the same in both the accumulation and coarse modes (the percentage quartz in soil is reported for both clay and silt by (Nickovic et al., 2012)). This may introduce some error in the emitted feldspar fraction in dust if the percentage of feldspar in the accumulation mode relative to quartz differs to that of the coarse mode.

Harrison et al. (in prep) suggests that feldspar is more easily broken down by chemical reactions than quartz, likely leading to a lower feldspar than quartz fraction in accumulation mode dust than in the coarse mode (which is larger and more difficult to break down). Thus it is likely that the methodology used to predict feldspar emission over-predicts the feldspar content in the accumulation mode aerosol. At Barbados, 60-70% of K-feldspar INP particles are in the accumulation mode (Figure 4.11). With a more accurate distribution of feldspar between the coarse and accumulation modes, with more in the coarse mode, we would expect less feldspar INP to be transported to Barbados owing to the larger sizes of the coarse particles. It seems possible that, despite the under-prediction of dust mass, the K-feldspar INP are over-predicted at Barbados due to the model overestimating the accumulation mode feldspar.

However, other sources of error in the estimation of feldspar content have been documented and contribute further uncertainty to the values predicted by GLOMAP. The mineralogical database used to predict feldspar emission is predominately based on wet sieved samples (Perlwitz et al., 2015a, 2015b). Wet sieving is a fully dispersive technique which can disintegrate aggregates found in the original soil, which when emitted naturally due to wind erosion would not undergo this fragmentation. This leads to discrepancies between the fractions of minerals found in wet-sieved soil samples and those found in emitted aerosol populations (Perlwitz et al., 2015b). These discrepancies are not represented in aerosol models such as

GLOMAP that assume the soil mineral fractions correspond to the emitted fractions (Atkinson et al., 2013; Hoose et al., 2008; Perlwitz et al., 2015b).

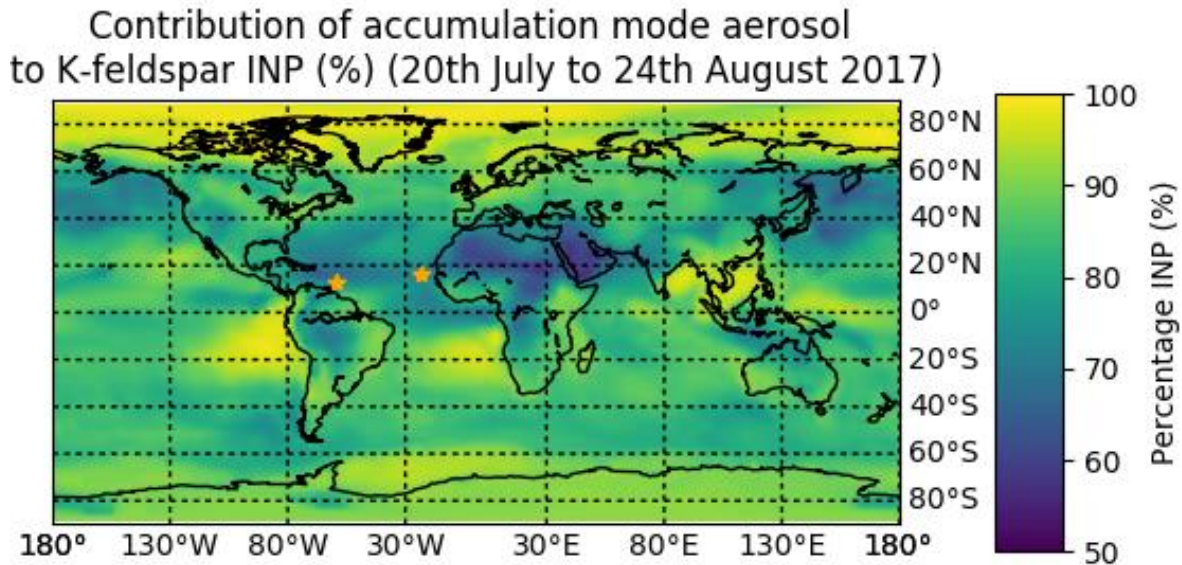


*Figure 4.11. Contribution of accumulation mode aerosol to K-feldspar INP number concentrations. Percentage contribution of INP particles from the accumulation mode aerosol to the total INP number attributed to K-feldspar using the A13 parameterisation.*

The use of wet-sieved measurements to determine emission fractions of minerals is likely to overestimate the fractions found in the clay or accumulation size mode. However, it is unlikely that this is causing any overestimate in the feldspar fraction because as stated above, the feldspar fraction in the clay mode is based on the ratio of feldspar to quartz found in the silt mode (Nickovic et al., 2012). Perlwitz et al. (2015b) suggests that quartz is the only mineral not requiring re-aggregation treatment as its large size means it is likely to survive wet sieving without disintegration. This means the ratio of feldspar and quartz from samples in the coarse mode (of which only the feldspar has had aggregates broken up and therefore measured in the accumulation mode while the quartz aggregates remain intact) would lead to an underestimation of the feldspar fraction in the accumulation mode. Therefore, while the K-feldspar concentration at Barbados is over-predicted by GLOMAP, it may be that this is compensated for by additional uncertainties in the feldspar fraction emissions dataset.

There is additional uncertainty in both dust and feldspar estimation due to the use of non-time specific dust emissions in GLOMAP. GLOMAP uses emissions prescribed from AEROCOM recommendations for 2000, regardless of the year being simulated (Atkinson et al., 2013; Vergara-Temprado et al., 2017). The source regions of feldspar are extremely heterogeneous, particularly in Northern Africa, and strong and sudden changes in the feldspar content of soil from >16% to ~2% can occur over very short distances (Nickovic et al., 2012). This means that small changes in emission locations due to the large variability in emission processes (Heinold et al., 2013; Marsham et al., 2011) may have a large effect on atmospheric feldspar and K-feldspar contents. There is also large uncertainty in dust removal processes such as wet scavenging, the examination of which is beyond the scope of this chapter.

To summarize, the overestimation of INP concentrations at Barbados may be attributed to the over-prediction of K-feldspar in the accumulation aerosol mode. This is supported by a predicted value of ~7 wt% K-feldspar in GLOMAP (Figure 4.9) compared to a measured value of ~1 wt% measured by XRD and SEM-EDS analysis throughout the study period (Harrison et al., in prep) and previous literature values (Kandler et al., 2018). This may be due to an over-prediction of the K-feldspar mass in the accumulation mode at emission due to structural uncertainties in the model. However there are many competing uncertainties and possible sources of error in the GLOMAP computation of atmospheric K-feldspar and these should ideally be addressed or quantified before the model is used in future studies to validate measured atmospheric INP number concentrations. At the very least, scientists making use of the GLOMAP model for comparison to observations of dust, K-feldspar or INP should be aware of the uncertainties inherent in the GLOMAP prediction and these should be clearly stated in any papers. A schematic depicting the competing uncertainties contributing to the over-prediction of K-feldspar INP by the GLOMAP model is shown in Figure 4.3.

#### **4.4.2. Importance of marine organic INP for the INP number concentrations at Barbados**

Analysis thus far has focussed on K-feldspar INP because the INP measured by the B-ICE campaign were predominately K-feldspar INP. We can infer this because the temperature dependence of the measured INP number concentrations matches the A13 and H19 parameterisations (Figure 4.1). Furthermore, at temperatures between  $-20$  and  $-30^{\circ}\text{C}$ , the temperature range measured by B-ICE, GLOMAP predicts that K-feldspar INP comprise greater than 90% of all INP using the A13 parameterisation. This is the case even when the K-feldspar content used to predict INP number concentrations is scaled to be 1% (as in Figure 4.10). However, marine organic INP may become more important at warm and possibly cold temperatures (Figure 4.1). Here, I examine the prevalence of marine organic INP predicted by GLOMAP in the atmosphere over the tropical Atlantic.

Figure 4.12 shows the vertical distribution of total INP concentrations for a temperatures  $-10^{\circ}\text{C}$  over North Africa and the tropical Atlantic both when the default GLOMAP predicted value of the K-feldspar content of aerosol is used and when it is scaled to match observations (see Figure 4.10). The location of Ragged Point, Barbados is marked by the black dotted line. The INP emitted from Africa ( $-20 - 0^{\circ}\text{W}$ ) is transported over the tropical Atlantic at relatively high concentrations between 3 and 4 km altitude in the SAL. The SAL moves to lower altitudes the further west it goes towards Barbados. At temperatures above  $-10^{\circ}\text{C}$ , as seen in Figures 4.1, 4.10 and 4.12, marine organic INP are more important than K-feldspar INP. In the boundary layer at Barbados,  $>70\%$  of INP at  $-10^{\circ}\text{C}$  are comprised of marine organic material on sea spray (Figure 4.12a). This rises to  $>90\%$  when the K-feldspar content of aerosol is scaled to match observations over Barbados (Figure 4.12b). More interestingly, at all altitudes up to 10 km above Barbados, and for both values of K-feldspar aerosol content, marine organics comprise

>50% of all INP at a temperature of  $-10^{\circ}\text{C}$ . This is important because it means that at ambient temperatures above Barbados, marine organics will play a significant role in heterogeneous ice formation particularly in the warmer mixed phase regime where secondary ice production mechanisms may be important.

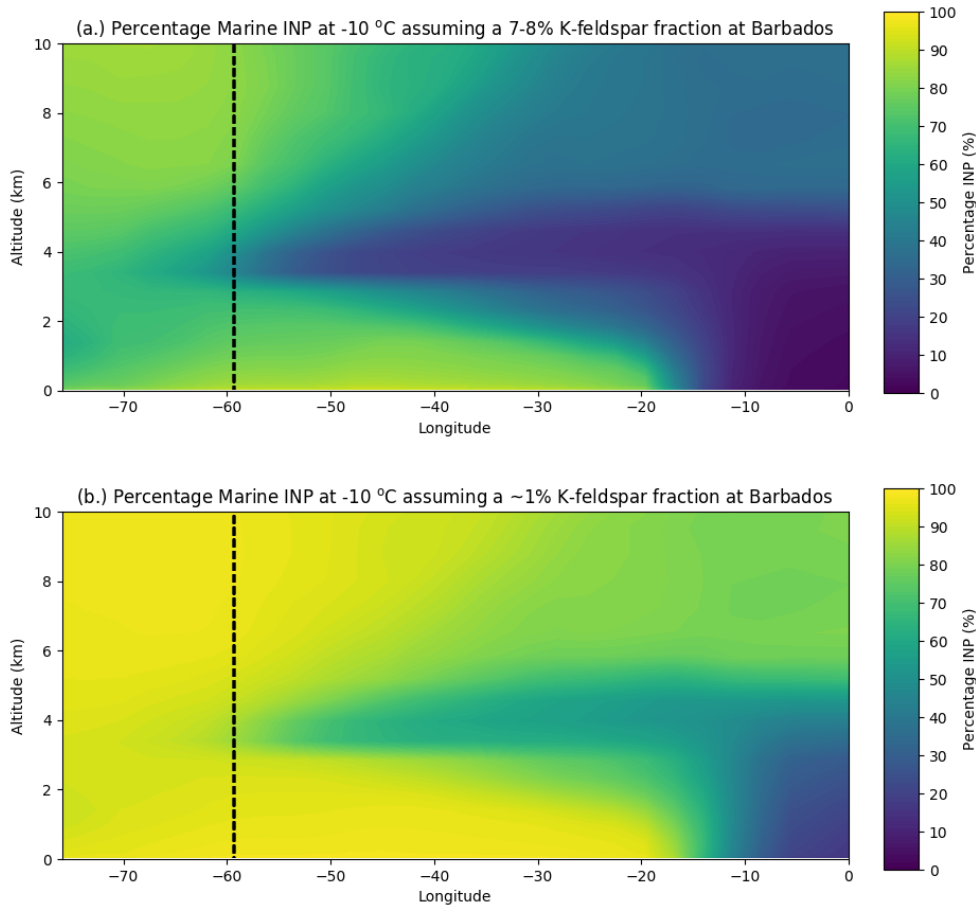


*Figure 4.12. Importance of marine organic INP. Proportion of INP number concentrations over the tropical Atlantic that are comprised of marine organic INP for a temperature of  $-10^{\circ}\text{C}$  when using the default GLOMAP prediction of K-feldspar content of aerosol of 7-8% (a) and when the K-feldspar content is scaled to be  $\sim 1\%$  in line with literature values and those measured during the B-ICE campaign (b). Shown is the mean values for latitudes  $10\text{-}20^{\circ}\text{N}$ . The K-feldspar INP in the above plots are calculated using the A13 parameterisation. The location of Barbados is shown by the black line.*

Furthermore, at  $-37^{\circ}\text{C}$ , while the model predicts that nearly all INP above 3 km and over North Africa are comprised of K-feldspar (Section 4.6: Figure A4.2a), near the surface in the middle and Western tropical Atlantic, including over Barbados, up to 25% of INP are comprised of marine organics on sea spray aerosol (Section 4.6: Figure A4.2a). This rises to  $\sim 50\%$  when the K-feldspar content of aerosol is scaled to match observations over Barbados (Section 4.6: Figure A4.2b). This finding is caveated by the fact that the Wilson et al. (2015) marine organics INP parameterisation is unconstrained below  $-27.5^{\circ}\text{C}$  and therefore the above interpretation is relatively uncertain.

Marine organics will induce most heterogeneous freezing at warm temperatures, and may contribute a substantial amount at very low temperatures (owing to the plateauing of the K-feldspar parameterisation (Figure 4.1, 4.10)) meaning they can be important at the lower and upper levels of mixed phase cloud formation). This indicates that the accurate representation of marine organic INP may be as important as the representation of K-feldspar and should be explored in more detail in future studies.

#### **4.4.3. Impact of driving meteorology on GLOMAP INP and dust predictions**

Previously, when comparing predicted INP number concentrations from GLOMAP to atmospheric observations, a simulation using meteorology from the year 2000 (Atkinson et al., 2013) or 2001 (Price et al., 2018; Vergara-Temprado et al., 2017) has been used regardless of the time period that the measurements in question were taken. It is more accurate to simulate the atmospheric state using the driving meteorology from the year of interest as there can be large variations in meteorology on annual, seasonal, and daily timescales. For the work detailed thus far the GLOMAP model was run using a driving meteorology specific to the year in

question. ERA-40 reanalysis datasets have been used to determine meteorology, including wind speed, temperature, humidity and precipitation, in previous GLOMAP simulations discussed in the literature (Atkinson et al., 2013; Price et al., 2018; Vergara-Temprado et al., 2017). However ERA-40 datasets are not available for years later than 2002 and as a result, GLOMAP was altered for this work to use the ERA-interim dataset to determine meteorology in the 2017 and 2013 simulations presented thus far. In order to test the effect, if any, of this change, I simulate the year 2001 with the ERA-interim dataset and compare the output of this simulation to that of a 2001 simulation which used ERA-40 dataset run by Vergara-Temprado et al. (2017).

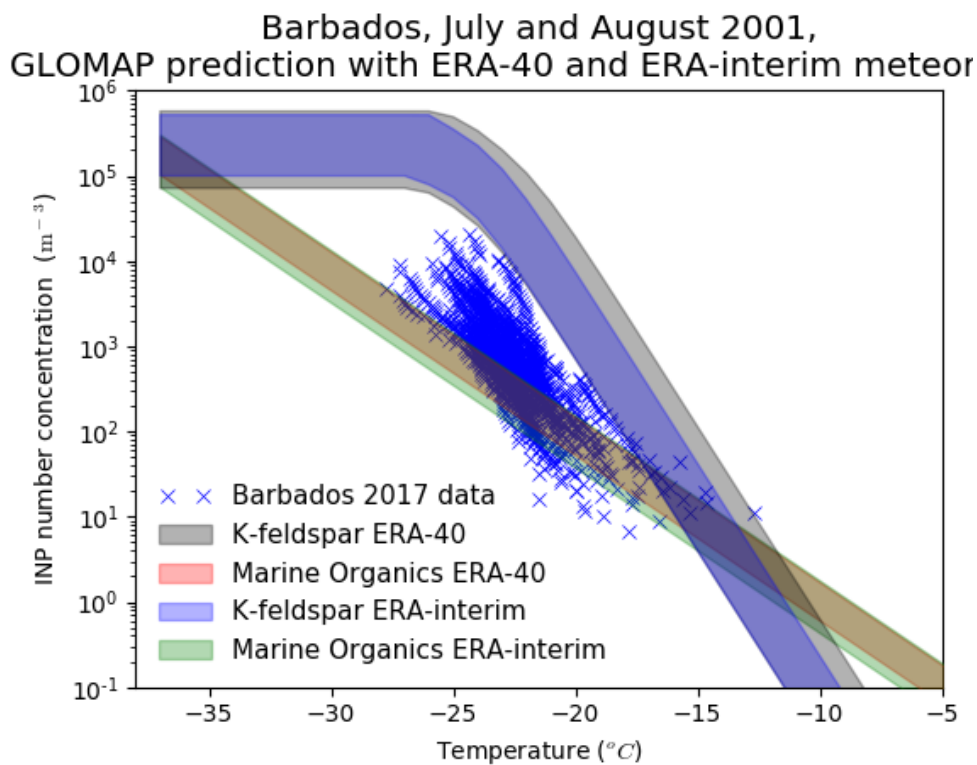


*Figure 4.13. Sensitivity of simulated INP number concentrations to driving wind dataset. Comparison of GLOMAP INP predictions for Barbados in July and August 2001 from simulations using ERA-40 and ERA-interim reanalysis winds datasets.*

#### 4.4.3.1. Sensitivity of INP spatial distribution to driving meteorology dataset

The range of INP number concentrations at the surface at Ragged Point, Barbados simulated by GLOMAP for July and August of 2001 are different depending on which driving wind dataset is used (Figure 4.13). The ERA-40 wind dataset predicts a larger range of INP concentrations over the time period for K-feldspar INP, particularly a higher maximum K-feldspar INP concentration at all temperatures and a lower minimum K-feldspar concentration at low temperatures. Conversely, the simulation using ERA-interim winds has a larger range of marine organic INP concentrations particularly a lower minimum marine organic INP concentration at all temperatures.

The surface INP number concentrations in July and August vary, not only at Barbados but globally, depending on which ERA dataset is used to determine the meteorology in GLOMAP (Figure 4.14). Figure 4.14a shows mean percentage difference in surface INP concentrations at  $-10^{\circ}\text{C}$  between latitudes  $10$  and  $20^{\circ}\text{N}$  between GLOMAP simulations using ERA-40 and ERA-interim wind datasets. We see increases in total and K-feldspar INP number concentrations in dust export regions, such as the Sahara, of up to three orders of magnitude when using the ERA-40 wind dataset. Over the tropical Atlantic, there is an increase in surface INP of between  $10$  and  $100\%$ . The simulation using ERA-40 winds seems to export more dust and therefore K-feldspar from source regions, with more K-feldspar INP (not shown) over the tropical Atlantic, and to the South East of Australia.

Figure 4.14b shows the vertical distribution of the percentage change in mean INP number concentrations between the ERA-40 and the ERA-interim wind dataset (ERA-40 - ERA-interim) for a temperature of  $-10^{\circ}\text{C}$  at latitudes between  $10$  and  $20^{\circ}\text{N}$ . We see increases in INP number concentrations in the ERA-40 simulation at all shown altitudes over the Sahara and the east and middle of the tropical Atlantic. These increases are as large as  $300\%$ . We see similar enhancements in dust mass in Figure 4.14c which shows the percentage difference in mean

mass concentration of accumulation soluble dust mass. Increases in dust mass in ERA-40 simulation relative to the ERA-interim simulation are as large as 50% in the Saharan export region. Figure 4.14 indicates that more dust and therefore K-feldspar INP are exported from the Sahara over the tropical Atlantic in the ERA-40 simulation relative to the ERA-interim simulation.

#### **4.4.3.2. Comparison of surface dust mass in simulations with different driving meteorology to observations**

We now use the ground based observations of surface dust concentrations (Zuidema et al., 2019), discussed above, to assess whether simulations using ERA-40 or ERA-interim driving meteorology give a better representation of dust export over the tropical Atlantic. In Figure 4.15, we compare the GLOMAP prediction of surface dust mass in both the ERA-40 and ERA-interim simulations to the ground based observations for each month of 2001 at Barbados (a) and Miami (b). In both locations the median and upper quartiles of the ground-based observations are nearly always higher than the GLOMAP simulations, in agreement with the 2017 comparison to surface dust mass concentrations shown in Figure 4.5. Particularly at Miami, GLOMAP underestimates the dust concentration from March to November. The difference between the observations and the nearest model prediction is nearly always greater than the difference between the two models. However, at Miami, the ERA-interim simulation seems to have higher and therefore more accurate dust mass concentrations between May and August. As Miami is situated on the outer edge of the Saharan dust outflow region, it is likely more sensitive to dust removal via wet scavenging and the more accurate representation of dust by ERA-interim in Miami is consistent with the well documented excessive precipitation over

tropical oceans in ERA-40 (Uppala et al., 2005). Conversely at Barbados the simulations are relatively similar in both the ERA-interim and ERA-40 simulations in most months.

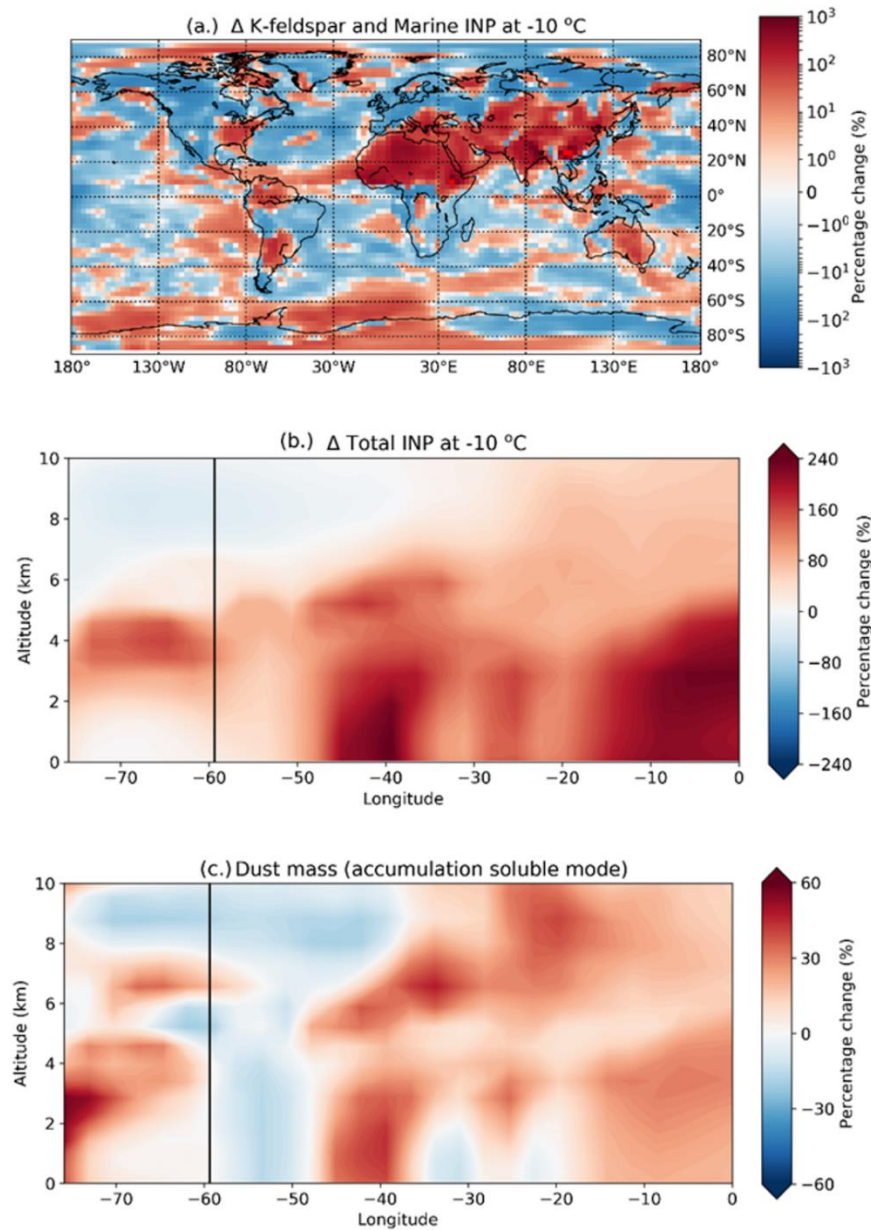
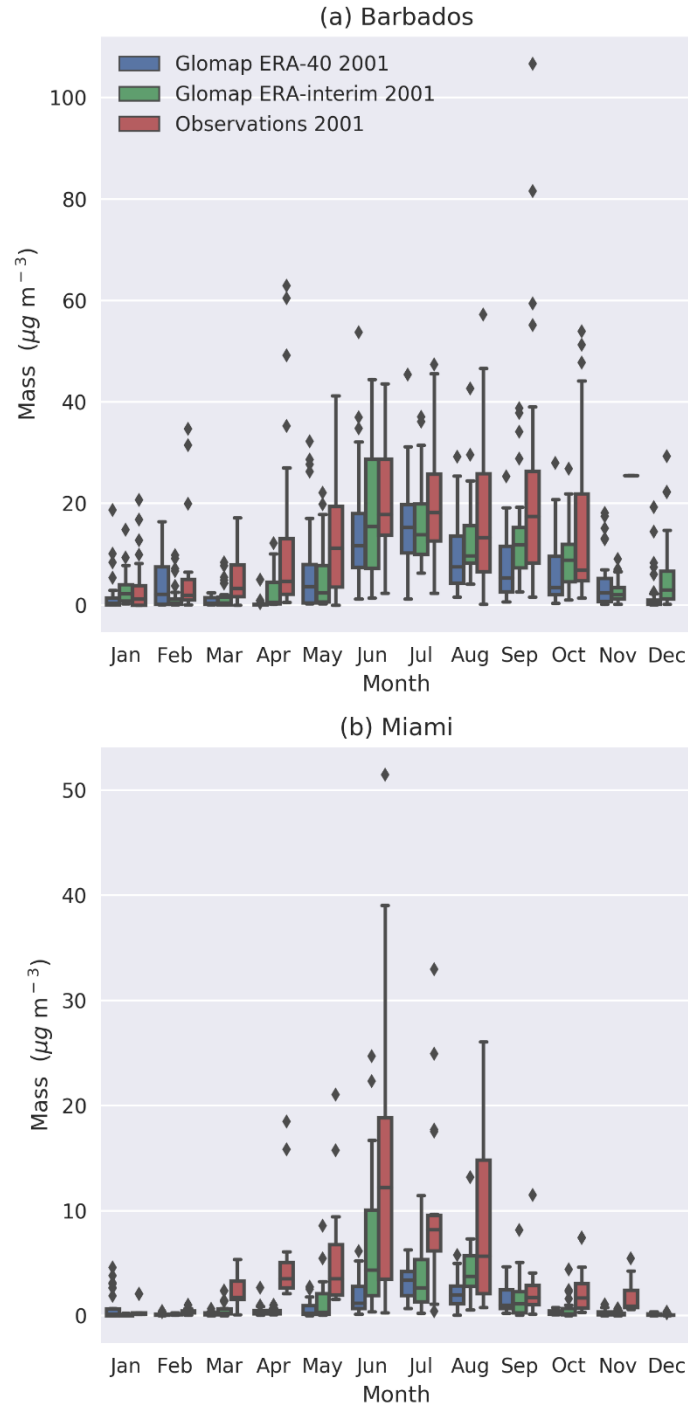


Figure 4.14. Sensitivity to driving meteorology. Shown is the mean percentage difference in surface INP concentrations (a), vertical distribution of INP concentrations between latitudes  $10$  and  $20^{\circ}\text{N}$  (b) both at  $-10\text{ }^{\circ}\text{C}$ , and vertical distribution of soluble accumulation dust mass concentrations between latitudes  $10$  and  $20^{\circ}\text{N}$  between GLOMAP simulations using ERA-40 and ERA-interim meteorology datasets. A positive value indicates the ERA-40 simulation has a higher value than the ERA-interim simulation.



*Figure 4.15. Comparison of monthly simulated and observed dust mass concentrations at Barbados and Miami for 2001. Shown is the median and interquartile ranges for dust mass simulated by GLOMAP in two simulations using ERA-40 and ERA-interim wind datasets and observed dust concentrations from ground based measurement stations (Zuidema et al., 2019) for each month in 2001.*

This analysis shows a notable effect of driving wind dataset on the INP and particle number concentrations and on the dust mass concentrations predicted globally by GLOMAP. The results indicate that changes to model structure (e.g. a switch from ERA-40 to ERA-interim reanalysis datasets when modelling 2013 instead of 2001) can have a large effect on aerosol transport and model output. While the differences caused by the wind datasets were relatively small compared to other uncertainties in the case of INP number concentrations, this may not be the case for model diagnostics that are more easily quantified and less uncertain. This work highlights the importance of validating model output against observations or previous simulations for structural changes to the model prior to using output to interpret atmospheric processes.

## **4.5. Conclusions**

An extensive comparison between INP number and dust mass concentration predictions by GLOMAP and a range of observational and reanalysis datasets in the tropical Atlantic were carried out. INP number concentrations are over-predicted in Barbados by GLOMAP in simulations using both the A13 and H19 INP parameterisations. This occurs in spite of the fact that GLOMAP under-predicts dust concentrations both at the surface and in the SAL compared to long-term surface measurements, dust mass profiles measured by lidar and relative to the MERRA-2 reanalysis dataset. The over-prediction of INP at Barbados may be explained by an over-prediction of the K-feldspar fraction of aerosol in the accumulation mode leading to too many INP particles being transported across the Atlantic. Figure 4.3 summarizes the competing model uncertainties that are affecting the predicted INP number concentrations.

Comparison to lidar measurements that span the entirety of the tropical Atlantic from Cape Verde to Barbados, and comparison to column integrated dust concentrations from the

MERRA-2 dataset, indicate that dust mass concentrations in GLOMAP at all altitudes of the SAL in both the Eastern and Western tropical Atlantic are underestimated relative to observations. The modelled dust concentration profiles are closer to observations in the Eastern tropical Atlantic, potentially inferring that over-removal of dust via wet or dry deposition is a larger problem than underestimation of emissions. In fact, comparison of GLOMAP surface and column integrated dust mass measurements to the MERRA-2 reanalysis dataset show that GLOMAP has substantially higher dust concentrations than MERRA-2 in source regions, such as over North Africa.

The enhanced GLOMAP dust concentrations relative to MERRA-2 reanalysis data in source locations may be due to the 2000 AEROCOM emissions used in all simulations presented here and in previous GLOMAP simulations analysing INP number concentrations (Dentener et al., 2006; Price et al., 2018; Vergara-Temprado et al., 2017) being higher than those of the years 2017 and 2013 analysed here. Future work should use interactive dust emissions dependent on wind speed from the year of simulation to reduce the uncertainty in INP and dust concentrations caused by the use of 2000 AEROCOM emissions.

The reasons for underestimations in dust concentrations over the tropical Atlantic relative to observations in GLOMAP are difficult to identify. The ERA-interim reanalysis dataset used to determine GLOMAP humidity, temperature, winds, and precipitation was shown to have higher precipitation rates in 1990 relative to Global Precipitation Climatology Project (a satellite reanalysis product with precipitation derived from geostationary infrared satellite imagery) values in the Western tropical Atlantic (Dee et al., 2011) which, if indicative of a systematic overestimate of precipitation in GLOMAP, may explain the large reduction in dust concentrations in GLOMAP profiles from the 14<sup>th</sup> and 23<sup>rd</sup> May 2013 relative to lidar measurements. However, this is challenging to verify owing to the uncertainties associated with all reanalysis datasets and the scarcity of direct measurements over the tropical Atlantic

(Uppala et al., 2005). The comparison to dust mass profiles measured over the tropical Atlantic during May 2013 indicates that the SAL in GLOMAP is not well developed relative to observations. This indicates that the model is not representing some of the complex and spatially variable emission and transport pathways of Saharan dust (Chiapello et al., 1995; Heinold et al., 2013; Marsham et al., 2011, 2013; Prospero and Carlson, 1972), e.g. nocturnal low level jets, haboobs or boundary layer convection (Heinold et al., 2013). This may be partly due to the use of AEROCOM emissions from the year 2000 regardless of the year being simulated. The exact reasons for the underdevelopment of the SAL by GLOMAP should be examined in more detail in the future.

The over-prediction of K-feldspar INP at Barbados in GLOMAP is likely attributable to the over-prediction of the feldspar fraction in the accumulation size mode. This is because the feldspar fraction of accumulation mode dust is derived from the feldspar to quartz ratio in coarse mode dust owing to a lack of observations. Uncertainty in the sparse existing measurements of the K-feldspar fraction in mineral dust means that quantifying the exact reason for the model overestimation of K-feldspar INP is difficult (Figure 4.3). Direct observations of size mode specific feldspar and K-feldspar fractions in dust would assist in assessing the accuracy of modelled K-feldspar fractions. This work makes clear how uncertainties can have compensating effects in global climate and numerical weather models. Tuning the K-feldspar fraction of aerosol to be 1% instead of 7-8% improved the model prediction of K-feldspar INP number concentration but the same adjustment would likely worsen the estimate of INP number concentrations close to dust emission sources where the K-feldspar fraction of dust is higher.

Sensitivity of INP and dust number concentrations to driving reanalysis dataset highlights the importance of testing the sensitivity of model output to changes that may be unrelated to the system or feature of interest. A change from the ERA-40 to the ERA-interim reanalysis dataset

was necessary to simulate the year in question. In particular, a change to the ERA-interim dataset improved the representation of the dust mass concentrations at Miami, perhaps because the ERA-interim dataset is not subject to the same excessive precipitation in the tropical Atlantic as the ERA-40 dataset (Uppala et al., 2005).

This chapter highlights the importance of the integration of direct atmospheric observations, measurements derived from satellite and remote sensing data, and model simulations for building a representative picture of atmospheric processes and particularly aerosol transport. Multiple datasets were used to examine the INP and dust concentrations over the tropical Atlantic and each one contributes information that helps us to understand dust export from Northern Africa. One of the most challenging aspects of atmospheric research is building a model that accurately represents the Earth system and proving that this is the case through extensive comparison to direct observations. Due to the lack of direct observational data in many parts of the world, modellers must rely on remotely sensed, satellite or reanalysis datasets for validation of model simulations even though many of these datasets come with their own range of biases, assumptions, and errors (Engelstaedter et al., 2006). Many regions of atmospheric importance, such as the main dust emission regions of the Sahara, are remote with limited observations available with which model data can be validated against (Engelstaedter et al., 2006). Further observations from ship campaigns such as the 2013 SALTRACE cruise (Weinzierl et al., 2017) and from flight campaigns such as the 2015 ICE-D campaign (Lloyd et al., 2019; Price et al., 2018) are critical to enhancing our understanding of atmospheric composition as well as for validating and building trust in model simulations, as well as in reanalysis datasets such as MERRA-2. This work demonstrates how observations can be used alongside remotely sensed, satellite, and reanalysis datasets to validate and examine issues in atmospheric models.

## 4.6. Appendix

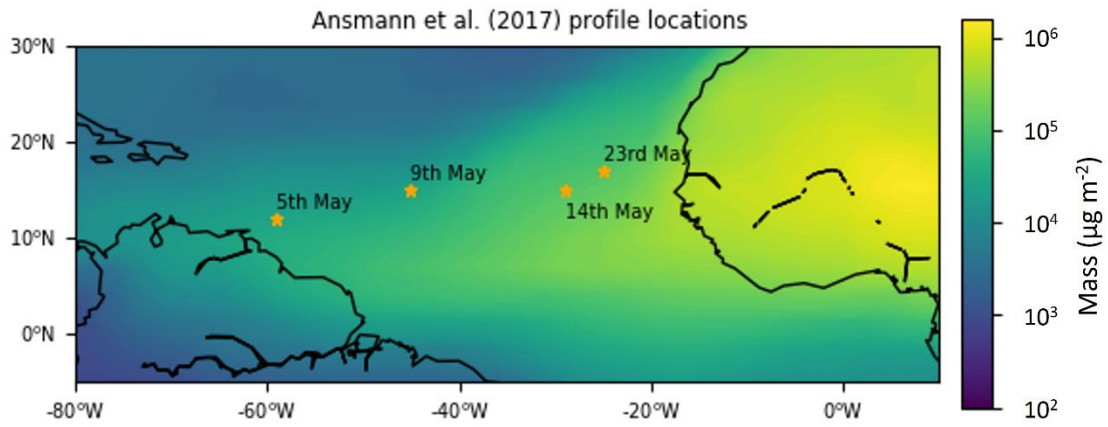


*Figure A4.1. Locations of the profiles shown in Figure 4.8 over a contour map of integrated dust mass concentrations simulated by GLOMAP for the month of May 2013.*

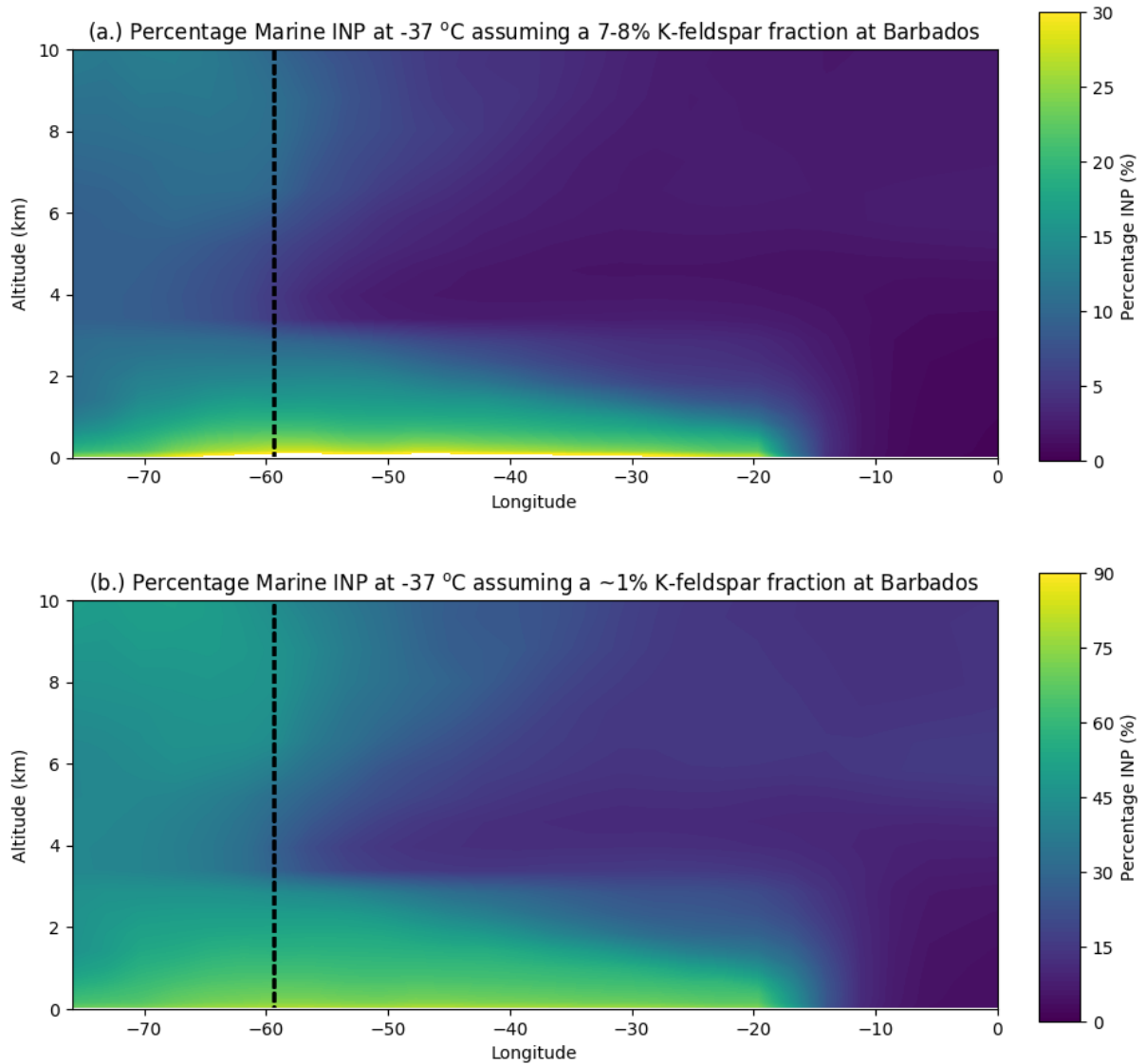


*Figure A4.2. Importance of marine organic INP. Proportion of INP number concentrations over the tropical Atlantic that are comprised of marine organic INP for a temperature of  $-37^{\circ}\text{C}$  when using the default GLOMAP prediction of K-feldspar content of aerosol of 7-8% (a) and when the K-feldspar content is scaled to be  $\sim 1\%$  in line with literature values and those measured during the B-ICE campaign (b). Shown is the mean values for latitudes  $10^{\circ}\text{N}$ – $20^{\circ}\text{N}$ . The K-feldspar INP in the above plots are calculated using the A13 parameterisation. The location of Barbados is shown by the black line.*



# Chapter 5: Conclusions

## 5.1. Summary of major findings

A number of models have been used to further our understanding of the effect of INP in convective clouds over the tropical Atlantic. First, a regional numerical weather prediction model with advanced microphysics (UM-CASIM) was used to test the effect of INP parameterisation choice on a large and complex tropical convective cloud field (Chapter 2). Second, a large eddy simulation cloud model with the same advanced microphysics (MONC-CASIM) was used to examine the interacting roles of INP number concentration, INP temperature dependence, and Hallett-Mossop splinter production rate in an idealised deep convective cloud (Chapter 3). Extensive coverage of realistic parameter space was achieved using a Latin hypercube sampling method and the importance of the three uncertain variables on the cloud properties were examined using statistical emulation and variance-based sensitivity analysis. Finally, INP transport across the tropical Atlantic, the region of interest for this thesis, was examined using a global aerosol model (GLOMAP-mode) (Chapter 4). Overall, the results further our understanding of the effects of INP in convective clouds and indicate the importance of quantifying INP number concentrations at all mixed-phase temperatures and improving the representation of cloud glaciation in climate models. A summary of the major findings of this thesis are presented below in response to the questions raised in Section 1.6.

### 5.1.1. Chapter 2: The effect of INP parameterisation choice on the radiative properties of a complex deep convective cloud field

- a) What is the radiative effect of INP and INP parameterisation choice in a complex tropical convective cloud field?

The presence of INP enhances the daylight domain-mean top-of-atmosphere (TOA) outgoing radiation (shortwave + longwave) of a complex tropical convective cloud field spanning over 600,000 km<sup>2</sup> by between 2.6 and 20.8 W m<sup>-2</sup> depending on the choice of INP parameterisation. The mean effect of including INP across all tested INP parameterisations on the daylight outgoing radiation is +9.8 W m<sup>-2</sup>. This is due to enhancements in the reflection of shortwave radiation by existing clouds (increases in cloud albedo) and increases in domain cloud fraction (predominantly due to increases in low and mid-level clouds).

The choice of INP parameterisation causes a variation of 18 W m<sup>-2</sup> in the mean outgoing radiation of the cloud field, i.e. INP parameterisation choice can have as large an impact on outgoing radiation as the exclusion of INP altogether. The difference in cloud field properties between simulations was attributed to the different temperature dependencies of INP number concentrations ( $d\log_{10}[\text{INP}]/dT$ ), i.e. the INP parameterisation slope. Outgoing radiation, along with many other macro- and microphysical properties, e.g. ice crystal water path, were significantly correlated with INP parameterisation slope, with steeper parameterisations having both a higher cloud albedo and a larger cloud fraction. This indicates that it is important to accurately represent, not only the number of aerosol particles capable of nucleating ice as indicated by Vergara-Temprado et al. (2018), but also the temperature dependence of INP number concentration which depends on aerosol composition. For example, marine organic INP (Wilson et al., 2015) have a shallower slope than mineral dust INP (e.g. Atkinson et al., 2013; Niemand et al., 2012).

- b) What is the effect of SIP (via the Hallett-Mossop process) and its interaction with INP parameterisation choice on the outgoing radiation of the cloud field?

The effect of including SIP on daylight domain-mean TOA outgoing radiation varies between -2.0 W m<sup>-2</sup> and +6.6 W m<sup>-2</sup> depending on INP parameterisation choice, i.e. the sign and

magnitude of the effect of the Hallett-Mossop process on the simulated cloud field depends on the INP parameterisation choice. Whether the Hallett-Mossop process causes increases or decreases in the domain-mean outgoing radiation depends on the cloud fraction response. Steeper INP parameterisations see an increase in anvil cloud fraction of up to 10% (+0.9% of the domain area) and thus an increase in domain outgoing radiation. This is relative to a decrease in anvil cloud of up to 40% (-3.6% of the domain area) for shallow parameterisations and a corresponding decrease in daylight domain-mean outgoing radiation.

- c) What is the relative importance of INP and SIP (via the Hallett-Mossop process) for the radiative properties of a complex convective cloud field?

The presence of the Hallett-Mossop process has a smaller effect than the INP parameterisation on the simulated cloud field. The mean effect on daylight domain-mean TOA outgoing radiation of including INP is  $+9.8 \text{ W m}^{-2}$  whereas the mean effect of including SIP via the Hallett-Mossop process is  $+2.9 \text{ W m}^{-2}$ . However the effect of the Hallett-Mossop process is dependent on the choice of INP parameterisation indicating that the interaction between SIP mechanism and INP is important for convective cloud properties. The effects of INP and INP parameterisation choice on outgoing radiation described above are evident even in the presence of the Hallett-Mossop process, refuting the hypothesis that INP is irrelevant beyond a minimum concentration needed to initiate the Hallett-Mossop process (e.g. Crawford et al., 2012; Ladino et al., 2017; Phillips et al., 2007) at least in deep convective clouds.

### 5.1.2. Chapter 3: Influence of ice-nucleating particles and Hallett-Mossop ice production rates on anvil cirrus from deep convection

- a) How does INP number concentration, INP parameterisation slope, and Hallett-Mossop splinter production rate affect the anvil properties of an idealised deep convective cloud?

Anvil ice crystal number concentration, anvil ice crystal effective radius, and anvil extent show different sensitivities to INP number concentration, INP parameterisation slope (the temperature dependence of INP number concentration between  $-38$  and  $0^{\circ}\text{C}$ ,  $d\log_{10}[\text{INP}]/dT$ ), and Hallett-Mossop splinter production rate. At high INP number concentrations, when the total number of heterogeneously formed ice crystals exceeds the number of cloud droplets reaching the homogeneous freezing level, the anvil ICNC is substantially reduced. This threshold is reached at a critical value of the peak concentration in the aerosol layer of approximately  $1\text{ cm}^{-3}$ .

The anvil ice crystal effective radius and the anvil extent are substantially enhanced at shallow INP parameterisation slopes. This is due to a regime transition at shallow INP slopes (and to some extent at high INP number concentrations) to a cloud with more extensive glaciation, stronger updraft speeds, and higher vertical mass flux and condensate divergence at the outflow level. This regime transition is driven in part by Hallett-Mossop ice production rates approximately an order of magnitude larger than those in simulations with steep INP parameterisation slopes. This increase in the Hallett-Mossop ice particle production rate occurs as a result of increased heterogeneously frozen ice crystals ‘seeding’ secondary ice production within the Hallett-Mossop region. Large anvil ice crystal effective radii in simulations with shallow INP parameterisation slopes are increased further at high INP number concentrations due an enhancement of heterogeneous freezing at the top of the mixed-phase region which

allows for further ice crystal growth relative to crystals frozen by homogeneous freezing. Conversely, a high anvil cloud fraction caused by a shallow INP parameterisation is reduced at high INP number concentrations due to reduced anvil ICNC and increased ice crystal size.

- b) What is the relative importance of INP number concentration, INP parameterisation slope, and Hallett-Mossop splinter production rate for the development and resultant anvil properties of an idealised deep convective cloud?

INP number concentration is the primary determinant of anvil ICNC which will have implications for anvil longevity beyond the simulated time period because an anvil with a lower ICNC should have a shorter lifetime. INP number concentration is also the primary determinant of column integrated heterogeneous and homogeneous ice particle production, and plays a secondary role in determining anvil ice crystal size and anvil cloud fraction. INP parameterisation slope is the primary determinant of anvil ice crystal size, anvil cloud fraction, cloud updraft enhancements, and changes in overall cloud condensate from graupel, snow, cloud droplets, and rain. INP parameterisation slope also plays a minor role in determining anvil ICNC. The only output variable affected by the Hallett-Mossop splinter production rate is the ice particle production by the Hallett-Mossop process itself, the largest changes to which occur as a result of the INP parameterisation slope. Although most cloud properties are not sensitive to the Hallett-Mossop splinter production rate, the ice particle production by the Hallett-Mossop process (determined by both the INP parameterisation slope and the Hallett-Mossop splinter production rate) is of substantial importance to many cloud properties highlighting the importance of SIP and INP interactions.

- c) Are statistical emulation and variance-based sensitivity analysis useful tools for the assessment of uncertainty in parameterisations of mixed-phase ice formation in deep convective clouds?

Statistical emulation is a powerful tool for helping to visualise and understand the relationships between cloud responses for cloud properties that vary smoothly with the uncertain input parameters. For example, statistical emulation shows excellent predictive power for parameters such as anvil ICNC and column integrated homogeneous and heterogeneous ice particle production rates which all show a strong and smooth dependence on INP number concentrations. Variance-based sensitivity analysis is also useful in these cases for identifying which input variables contribute uncertainty to the value of the cloud property in question and therefore could benefit from quantification or uncertainty reduction using observational measurements or further modelling.

Conversely, the emulator is less able to represent the variability in output variables that do not vary smoothly with the uncertain input parameters, and particularly those with sharp regime transitions. The emulator predicts the general trends of anvil ice crystal effective radius, Hallett-Mossop ice particle production, and accretion of water by ice but the surface is bumpy and the 95% confidence intervals are large so the output must be interpreted with caution. The emulator shows no predictive power for anvil cloud fraction. This is likely because the output has a complicated pattern with (i) a sharp transition to a cloud with a larger anvil at shallow INP parameterisation slopes and high INP number concentrations, (ii) a reduction in anvil extent at very high INP number concentrations within the shallow slope/high cloud fraction regime and (iii) the presence of an outlier at the corner of the parameter space with a low cloud fraction despite a high  $[INP]_{MAX}$  and shallow  $\lambda_{[INP]}$ . Therefore traditional methods of analysis should be used alongside statistical emulations where large regime shift or sharp transitions are possible in cloud output variables. Sampling using a Latin hypercube method allows insightful

use of both traditional analysis methods and statistical analysis because of the extensive coverage of parameter space that it provides relative to one-at-a-time tests.

### **5.1.3. Chapter 4: Simulation of dust and K-feldspar INP transport across the tropical Atlantic by a global aerosol model**

- a) How well does the GLOMAP aerosol model simulate the INP number concentrations measured during the 2017 Barbados Ice-nucleating particle Concentration Experiment (B-ICE) field campaign at Ragged Point, Barbados?

GLOMAP overestimates the INP number concentrations measured during the 2017 B-ICE Barbados field campaign using both the Atkinson et al. (2013) and Harrison et al. (2019) feldspar based parameterisations. The INP number concentrations in GLOMAP predicted by the Atkinson et al. (2013) are about 1-2 orders of magnitude above the measured values. The Harrison et al. (2019) parameterisation captures approximately the upper half of the measured INP number concentrations.

- b) Can discrepancies between measured and GLOMAP simulated INP number concentrations be attributed to discrepancies between measured and simulated dust export from North Africa over the tropical Atlantic?

GLOMAP does not overestimate dust concentrations over the tropical Atlantic, including at Barbados, based on comparison to a variety of observational and reanalysis datasets. As such, the overestimation of INP number concentrations at Barbados during the 2017 B-ICE campaign cannot be explained by an over-prediction of dust transport from North Africa to Barbados. Surface dust mass concentrations simulated by GLOMAP at Barbados and Miami are lower

than surface-based dust measurements (Zuidema et al., 2019) in July and August 2017 and over the entirety of 2001. Comparison to the MERRA-2 reanalysis dataset supports this finding with MERRA-2 having higher surface dust mass concentrations than GLOMAP in all regions globally except regions close to source, such as North Africa. Comparison to profiles of dust mass concentrations in the Saharan Air Layer at four locations between Cape Verde and the Caribbean (Ansmann et al., 2017) indicate that GLOMAP underestimates the dust mass concentration in the dust layer at all locations over the tropical Atlantic. This is true for both accumulation and coarse mode dust mass concentrations. The GLOMAP simulated dust profiles are closer to the observed profiles in the Easter tropical Atlantic indicating that over removal of dust, rather than weak emission, is a particular problem. Comparison to MERRA-2 integrated column dust measurements support this with lower column-integrated dust mass concentrations in all regions except dust emission source regions.

- c) Can discrepancies between measured and GLOMAP simulated INP number concentrations be attributed to discrepancies between the measured and simulated feldspar content of aerosol?

The K-feldspar content of mineral dust simulated by GLOMAP during B-ICE is larger than observations and as such may explain the over-prediction of K-feldspar INP number concentrations. XRD and SEM-EDS analysis of the aerosol measured throughout the study period estimate the K-feldspar content of aerosol at Ragged Point Barbados to be ~1% compared to a value of ~7-8% simulated by GLOMAP. Adjusting the assumed K-feldspar content in GLOMAP from ~7 to ~1% greatly improves the agreement of the observed INP concentrations with the INP concentrations estimated by the Atkinson et al. (2013) and Harrison et al. (2019) parameterisations. The overestimation of the K-feldspar fraction of aerosol at Barbados by GLOMAP is likely due to an over-prediction of the fraction of feldspar

in accumulation mode dust relative to coarse mode dust. This can be attributed to the fact that the fraction of feldspar in the accumulation mode dust is calculated from the ratio of feldspar to quartz in the coarse mode (because the global database of soil mineral composition on which feldspar emission is based does not provide a value for accumulation mode feldspar but does provide one for coarse mode feldspar, and accumulation and coarse mode quartz) (Nickovic et al., 2012). However there are a number of other uncertainties and structural components of the GLOMAP model that complicate the picture and may compensate for one another. Figure 4.3 depicts the competing aspects of GLOMAP INP representation including unquantified uncertainties.

#### **5.1.4. Overall influence of INP on convective clouds from both regional (Chapter 2) and idealised (Chapter 3) simulations**

The use of both a regional numerical weather prediction model and an idealised large eddy simulation model allows us to build a picture of the systematic ways the micro- and macro-physical convective cloud properties are affected by changes in INP number concentrations and the Hallett-Mossop process. There are a large number of similarities in the cloud response to changing INP number concentrations, and the microphysical cloud responses in particular are relatively systematic between the two studies. In both the complex cloud-field detailed in Chapter 2 and the idealised deep convective cloud described in Chapter 3, increased INP in the mixed-phase region enhance Hallett-Mossop ice particle production, snow and graupel formation and riming rates, leading to an invigoration effect, increased cloud condensate, and a higher cloud fraction at mixed-phase levels. In both regional and idealised simulations homogeneous ice particle production rates, and therefore overall ICNCs, are reduced by high INP number concentrations at the top of the mixed-phase regime.

The anvil cloud response to changes in INP is different between the two studies due to the dominance of different microphysical responses and different degrees of enhancement in mass flux between the two simulations. In the regional model, the reduction in homogeneous ice particle production and therefore anvil ICNC, along with increased consumption of liquid at lower cloud levels due to enhanced heterogeneous and secondary freezing, and more snow and graupel formation, leads to a reduction in anvil cloud fraction at shallow INP parameterisation slopes. While the idealised cloud simulated in Chapter 3 sees similar microphysical responses, the cloud invigoration effect at shallow INP parameterisation slopes due to increased mixed-phase freezing and riming events dominates over the consumption of liquid from these freezing events and leads to an increased anvil cloud fraction. This indicates that INP can have different effects depending on the environmental conditions, case study or simulation type and highlights the need for accurately representing all thermodynamic and microphysical conditions as accurately as possible to capture the cloud specific responses to perturbations.

The observed microphysical effects of INP in both the regional and idealised simulations are consistent with previous studies of deep convective clouds. For example, increased heterogeneous freezing in the mixed-phase cloud region has frequently been shown to reduce the rates of homogeneous ice production by consuming liquid at lower cloud levels (Fan et al., 2010b; Gibbons et al., 2018; van den Heever et al., 2006) which can reduce cloud anvil extent (e.g. Gibbons et al., 2018; van den Heever et al., 2006). An invigoration effect due to increased INP number concentrations has also been frequently observed (Ekman et al., 2007; Fan et al., 2010a; Gibbons et al., 2018; van den Heever et al., 2006) which can in some cases increase the availability of droplets for homogeneous ice nucleation and lead to a larger cloud anvil (e.g. Ekman et al., 2007).

In both regional and idealised simulations, the interaction of INP with SIP was important. In both cases, the rate of ice production by the Hallett-Mossop process was partly driven by the

temperature dependence of the INP parameterisation with shallow parameterisations having higher rates of secondary ice production. This indicates that INP number concentrations can be important determinants of mixed-phase ice production even when the ICNC vastly exceed the number concentration of INP (e.g. Korolev et al., 2020; Ladino et al., 2017; Lasher-Trapp et al., 2016).

In the idealised simulation, high rates of ice particle production by the Hallett-Mossop process with shallow INP parameterisations caused more extensive cloud glaciation, cloud invigoration, and a larger anvil cloud fraction. In the regional simulations, the invigoration effect is not as dominant and increased Hallett-Mossop rates reduce the availability of liquid to upper cloud levels. In simulations with shallow INP parameterisation, this reduced droplet availability causes reductions in anvil cloud fractions due to reduced droplet availability for homogeneous freezing. Conversely, in simulations with steep INP parameterisations, it causes reduced droplet availability for riming just below the homogeneous freezing level causing a reduction in ice crystal size and a consequent increase in anvil extent. The complexity and variety of these micro- and macro-physical responses to the Hallett-Mossop process depending on INP properties is consistent with non-linear interactions between the freezing mechanisms reported in the literature (e.g. Crawford et al., 2012) and highlights the importance of the interactions between INP and SIP mechanisms.

## **5.2. Key limitations of this thesis**

Both Chapter 2 and 3 examine the role of INP parameterisation and particularly that of the slope of the INP parameterisation in determining convective cloud properties. In Chapter 2, the effect of INP parameterisations commonly used in atmospheric models is tested. As such the slope of the parameterisation at low temperatures for the A13 and N12 parameterisations can

be flat because the parameterisations plateau once they reach the number concentration of dust represented in the model gridbox in question. This means that the absolute number concentration of aerosols capable of nucleating ice is not decoupled from the INP parameterisation slope in some INP parameterisations and that some cloud responses attributed to changes in the INP parameterisation slope may have in fact been caused by the absolute INP number concentration at cold temperatures.

I address this problem in Chapter 3 by treating the absolute INP number concentration and INP parameterisation slope as separate uncertain input variables and by fixing the absolute number concentration of aerosols capable of nucleating ice to be the INP number concentration at  $-38^{\circ}\text{C}$ . This allows the calculation of parameterisations that have decreasing INP number concentrations at every temperature interval from  $-38$  and  $0^{\circ}\text{C}$  based on the chosen parameterisation slope (i.e. no plateau at cold temperatures). However, this approach means that the realistic plateau of INP number concentrations at low temperatures is not represented. It also means that the simulation design is biased to representing INP parameterisations with very low INP number concentrations at temperatures above  $-38^{\circ}\text{C}$ . Additional simulations with realistic number concentrations at warmer mixed-phase temperature were added to account for this.

Future work could address both the above caveats of the work presented here by conducting a study similar to Chapter 3 using Latin hypercube sampling over four dimensions and including the temperature where INP number concentrations begin to plateau as an uncertain input parameter. This would allow for the examination of the relative importance of all aspects of the INP parameterisations and therefore which properties of the aerosol populations they are based on most require quantification for accurate representation of cloud properties. Additionally, altering the INP number concentrations within specific temperature ranges would

allow for the assessment of whether a particular temperature regime is particularly crucial for cloud development.

In both Chapters 2 and 3, the role of SIP, via the Hallett-Mossop process, was tested. However the Hallett-Mossop process is not the only SIP mechanism that has been identified in convective clouds (Field et al., 2017; Korolev et al., 2020). Other SIP mechanisms, such as droplet shattering (Lauber et al., 2018), are not represented in our simulations and their impacts have not been tested. Although comparisons to observations in Chapter 2 show good agreement between observed and simulated ICNC, the effect of other SIP mechanisms, including those occurring at temperatures below  $-10^{\circ}\text{C}$  (Field et al., 2017; Korolev et al., 2020; Lauber et al., 2018) on deep convective clouds should be tested in future studies as parameterisations become available. In particular, Lloyd et al. (2019) suggest that droplet shattering may have been occurring in the clouds sampled during the ICE-D field campaign, including those on which the simulations in Chapter 2 and 3 are based. However, as the Hallett-Mossop process is the most observed, quantified, and parameterised SIP mechanism, the results presented here give a good indication of the importance of the interaction of INP and SIP.

Chapters 2 and 3 are limited by the model representation of supersaturation with respect to liquid (using saturation adjustment) and rain freezing (using the Bigg (1953) parameterisation). While ice is allowed grow in the presence of liquid, treating supersaturation with respect to liquid explicitly in future work would allow a more accurate representation of the Wegener-Bergeron-Findeisen process. Treating rain with the same heterogeneous freezing parameterisation as cloud droplets would be more consistent with the perturbations to INP in Chapters 2 and 3 and should be examined as a possibility for future similar studies.

Chapters 2 and 3 address the effect that changes in the parameterisation of mixed-phase ice formation (through heterogeneous and Hallett-Mossop ice production) have on specific simulations of a convective cloud field and an idealised deep convective cloud. However,

convective clouds are sensitive to both meteorological and microphysical perturbations (e.g. Miltenberger et al., 2018; Miltenberger and Field, 2020; Posselt et al., 2019) and perturbations to microphysical variables that cause changes in cloud properties in one case may not have the same effects when reasonable variation in meteorological variables occurs. For example, in an ensemble of moderately deep convective clouds measured over South West England, aerosol-induced changes to the instantaneous and mean precipitation rates were only statistically significant when ensemble members were paired according to meteorological conditions but not when ensemble members with slightly different meteorological conditions are included in the analysis (Miltenberger et al., 2018a), i.e. the observed changes in precipitation rates in meteorologically paired simulations would not be evident in clouds subject to observational uncertainty or simulations with slightly varying initial or boundary conditions..

Uncertainty in initial conditions is not examined in this thesis and as such the magnitude of the reported changes due to INP and SIP relative to meteorological perturbations is not known. Future work should seek to address this with ensembles of tropical deep convective clouds with varying meteorology as well as perturbations to mixed-phase ice processes. For example, Miltenberger and Field (2020) expanded the study detailed in Chapter 2 (also in Hawker et al. (2021)) to the moderately deep convective clouds measured over South West England discussed above and found that the sensitivity of hydrometeor profiles to mixed-phase ice processes exceeds the spread of a meteorological ensemble but that the ensemble spread in cloud fraction, radiative properties, and precipitation is larger than the effects of INP and Hallett-Mossop perturbations. In particular, studies of the sensitivity of complex deep convective cloud fields, such as that of Chapter 3, to perturbations in both meteorological and microphysical ice processes should be conducted using methods such as statistical emulation and variance-based sensitivity analysis detailed in Chapter 3. To date most deep convective

studies of this nature, including that of Chapter 3, have focused on idealised simulations (e.g. Posselt et al., 2019; Wellmann et al., 2020).

In both Chapter 2 and 3, analysis is limited by the short time of the simulations. In Chapter 2, the cloud field radiative properties were analysed for the daylight hours only because the length of our simulation meant there was not a full 24 hours of simulation available once the spin up period had been removed. Ideally, the analysis would be repeated with an extended simulation that includes at least one night-time. This would mean that the observed effect of changes to the outgoing longwave radiation would be increased as outgoing shortwave radiation is zero in darkness. Furthermore, the changes in the anvil cloud detailed in Chapter 2 are opposite to the domain cloud fraction signal, with strong reductions in anvil cloud due to the presence of INP compared to increases in most other cloud types. As convectively generated anvils can persist for longer in the atmosphere than the convective clouds that form them (e.g. Luo and Rossow, 2004), it is possible that the effect of reduced anvil cloud fraction would influence the cloud field radiative properties more with a longer simulation.

In Chapter 3, the effect of the uncertain input variables on the number and size of the anvil ice crystals gives us an indication of the potential lifetime of the anvil and therefore its long-term radiative effect. Specifically, an anvil with fewer and larger ice crystals will not persist in the atmosphere as long as an anvil with more and smaller ice crystals and therefore will not affect outgoing radiation as much. However, because our simulation length is only 4 hours in length, the effects of changes in the anvil ice crystal number and size on anvil extent may not have taken full effect. For example, a shallow INP parameterisation slope causes a large increase in anvil ice crystal size and a decrease in ICNC, effects that over the anvil lifetime, and particularly once all deep convection has decayed, would be expected to decrease anvil lifetime and extent. However, at the end of the simulated time period, the effect of these anvil ice crystal changes has not been fully realised. In fact, the stronger updrafts generated by increased

freezing in the Hallett-Mossop region in simulations with shallow INP parameterisation slopes lead to increased transport of cloud mass to the top of the troposphere and a larger anvil. Ideally, the simulation would be extended to comprise the full life cycle of the generated convective anvil so that the overarching balance between the cloud invigoration and the enhanced ice crystal size effects of shallow INP parameterisations on the anvil cloud lifetime could have been assessed. Future work should seek to address this.

Both Chapters 2 and 3 showed increased updraft strength and cloud invigoration due to enhanced mixed-phase freezing. Cloud invigoration due to aerosols is most frequently discussed in relation to increased CCN concentrations or an overall aerosol increase (i.e. affecting both CCN and INP concentrations) (e.g. Altaratz et al., 2014; Fan et al., 2012; Lerach et al., 2008; Seifert and Beheng, 2006; Wang, 2005) and the relative importance and strength of cloud invigoration due to CCN and INP should be examined in future studies. Specifically, increases in CCN and INP number concentrations concurrently can have counterintuitive effects as is discussed in detail in Altaratz et al. (2014). For example, CCN concentration can increase latent heat release from condensation causing an enhancement in the flux of droplets to above the freezing level where they can freeze heterogeneously or homogeneously. However, whether this increased upward flux of droplets results in increased freezing and therefore further cloud invigoration depends on the balance between the increased availability of cloud droplets and INP and the reduced freezing efficiency of the smaller droplets (Altaratz et al., 2014; Rosenfeld and Woodley, 2000).

In Chapter 4, the model was compared to a number of observations and reanalysis datasets. Comparisons to ground-based (Zuidema et al., 2019) and lidar measurements (Ansmann et al., 2017) must be caveated with the fact that the observations presented represent the mean of multiple measurements at one point in time and space while the model values represent the mean of an average over the model grid box and timestep. Furthermore, comparisons of the

GLOMAP simulated dust mass concentrations to the MERRA-2 satellite reanalysis dataset were carried out by regridding the MERRA-2 dataset onto the GLOMAP grid, this may introduce some error into the comparison. However in most cases, the differences between the datasets were large enough for these errors to be inconsequential.

Additionally, the GLOMAP representation of dust and INP emission and transport differs from reality in a number of ways. The GLOMAP simulations presented here use AEROCOM emissions from the year 2000, regardless of the year being simulated (Dentener et al., 2006; Vergara-Temprado et al., 2017). This likely introduces errors into the dust flux, particularly because dust emissions are spatially heterogeneous based on very localised and high resolution changes in wind speed across source regions with large changes in both erodibility and mineral composition over very short distances (Nickovic et al., 2012; Sweeney et al., 2011). For example, comparison to dust mass profiles measured over the tropical Atlantic during May 2013 (Ansmann et al., 2017) shows that the Saharan Air Layer in GLOMAP is not well developed relative to observations. This implies that aspects of the complex processes that control dust uplift and transport (e.g. Heinold et al., 2013; Marsham et al., 2011; Prospero and Carlson, 1972) are not accurately captured by GLOMAP. Determining the exact reasons for differences in the Saharan Air Layer representation in GLOMAP and that observed by lidar was beyond the scope of this thesis but should be explored in future studies. Dust emission and atmospheric loading is something that is highly uncertain across most climate models (Huneeus et al., 2011; Wu et al., 2020). For example, coarse resolution models struggle to capture dust uplift by cold pools/haboobs which can account for up to 50% of summertime Saharan dust uplift (Heinold et al., 2013; Marsham et al., 2013).

### 5.3. Main implications of this research

All three research chapters of this thesis make clear the importance of quantification of INP number concentrations across the entirety of the mixed-phase temperature spectrum rather than just at one temperature, or in a narrow temperature range, as is common in many field campaigns. In Chapter 2, the temperature dependence of INP number concentrations has large effects on the outgoing radiation of a complex tropical convective cloud field. In Chapter 3, both the absolute INP number concentration and the temperature dependence of INP number concentrations, which determines the amount of heterogeneous ice nucleation in the Hallett-Mossop region, have large effects on the properties of a convectively generated anvil. In Chapter 4, we see that both K-feldspar and marine organic INP contribute to ambient INP number concentrations over Barbados and the tropical Atlantic. K-feldspar INP dominates INP number concentrations at mid-level mixed-phase temperatures between  $-20$  and  $-30^{\circ}\text{C}$  while marine organic INP are critical at warm ( $\sim -10^{\circ}\text{C}$ ) and very low ( $\sim -35^{\circ}\text{C}$ ) mixed-phase temperatures. Measuring INP over the entire mixed-phase temperature range throughout which deep convective clouds extend, from  $\sim -3$  to  $-38^{\circ}\text{C}$ , covering around 10 orders of magnitude in INP number concentration (e.g. Kanji et al., 2017), is a major experimental challenge. For example, in the ICE-D field campaign, INP concentrations at temperatures above  $-7$  and below  $-27^{\circ}\text{C}$  were not measurable due to experimental and sampling constraints (Price et al., 2018). This issue is compounded by the fact that INP spectra cannot reliably be extrapolated to higher or lower temperatures (though by necessity that is what occurs in most model simulations including those presented here) since our underpinning physical understanding of what makes an effective nucleation site is lacking (e.g. Coluzza et al., 2017; Holden et al., 2019; Kiselev et al., 2016). The large effect INP number concentrations can have on anvil cloud properties as well as the outgoing radiation of complicated deep convective cloud fields demonstrates the

importance of addressing this challenge and quantifying INP number concentrations and properties at all mixed-phase temperatures in regions dominated by deep convection.

The importance of the temperature dependence of INP number concentrations in Chapters 2 and 3 indicates that accurately representing both aerosol number and aerosol composition in atmospheric models is important for the accurate representation of deep convective cloud glaciation. Real-world INP populations will be composed of a mixture of aerosol types with biological INP, such as soil borne fungus and plant related bacteria, making significant contributions to INP number concentrations at the warmest temperatures and mineral components being more important at lower temperatures (O'Sullivan et al., 2018). Furthermore, the ice-nucleating ability of aerosols can be substantially altered by the accumulation of other species on particle surfaces, e.g. the adsorption of biological material from fungi, pollen and bacteria on mineral dust enhances particle ice-nucleating ability (Augustin-Bauditz et al., 2016; Chen et al., 2021; O'Sullivan et al., 2016).

An important finding of this thesis is the large effect that mixed-phase ice processes can have on the anvil and radiative properties of tropical convective clouds. Climate models persistently predict a glaciation of clouds at much warmer temperatures than is observed (e.g. Cesana et al., 2015; Komurcu et al., 2014). Many climate models use a simple temperature function to represent cloud glaciation and although there is suggestion that complex microphysics improves the performance of climate models in this regard, vast differences between observed and simulated glaciation temperatures in models with many different representations of cloud microphysics persist. For example, differences in the temperature where 90% of cloud is glaciated can be as large as 20°C in the tropics even when complex microphysics and prognostic liquid and ice are represented (Cesana et al., 2015). Chapters 2 and 3 highlight that changes to the mixed-phase ice processes in tropical convective clouds can substantially affect cloud fraction and outgoing radiation. Thus improvement of the representation of mixed-phase

ice processes in climate models is necessary for accurate simulation of cloud radiative forcing. Tropical convection in climate models is represented by convection parameterisations and therefore the representation of cloud glaciation is of even more simplistic than that of large-scale cloud. The results presented in this thesis indicate that as the resolution of climate models becomes finer and it becomes more common to include convective clouds in models explicitly (Neumann et al., 2019), mixed-ice processes and the effects of INP will need to be represented to accurately represent the cloud radiative effect.

Chapter 2 and 3 highlight that INP can affect the radiative properties of deep convective clouds, however many of the microphysical changes in deep convective clouds caused by INP will not be represented in the radiation schemes of climate models. Climate models do not typically represent ICNC in radiation calculations and have frequently been shown to poorly represent ice crystal mass concentrations (Baran et al., 2014; Waliser et al., 2009). The sensitivity of the cloud field in Chapter 2 and the deep convective cloud in Chapter 3 to the INP properties and the Hallett-Mossop process indicates the importance of accurately representing cloud ice properties in climate models.

This study particularly highlights the importance of the interaction of INP with SIP mechanisms, in this case the Hallett-Mossop process. In Chapter 2, the effect of the Hallett-Mossop process on the anvil cloud fraction and the domain-mean outgoing radiation was dependent on the choice of INP parameterisation. In general, cloud properties of the complex cloud field simulated in Chapter 2 and the idealised cloud in Chapter 3 were predominately altered by changes to INP rather than changes to the Hallett-Mossop process disputing the commonly held assertion that INP are only relevant in convective clouds up to a minimum threshold needed to initiate the Hallett-Mossop process (e.g. Beard, 1992; Crawford et al., 2012; Ladino et al., 2017; Phillips et al., 2007). However, initiating and ‘seeding’ the Hallett-Mossop process was an important effect of changes to INP concentrations in the Hallett-

Mossop regime in Chapters 2 and 3. In Chapter 2, parameterisations with shallower temperature dependencies and therefore more INP at warm temperatures had higher ice particle production rates by the Hallett-Mossop process. In Chapter 3, many cloud properties were controlled by the rate of ice production by the Hallett-Mossop process which in turn was determined by the temperature dependence of the INP parameterisation and the INP number concentrations within the Hallett-Mossop region. This indicated that INP could have an important role in determining cloud properties even when heterogeneous freezing is not the dominant freezing mechanism.

In summary, I find that INP parameterisation choice can have a substantial effect on the radiative properties of a large and complex tropical convective cloud field. I find that both absolute INP number concentrations and the temperature dependence of INP number concentrations at all mixed-phase temperatures are important for the anvil properties of an idealised deep convective cloud. In both a complex convective cloud-field and an idealised deep convective cloud, the interaction of INP with SIP is critically important to the cloud development. The importance of accurate representation of INP and dust export over the tropical Atlantic is also highlighted. The results presented in this thesis further our understanding of the effects of INP in convective clouds and indicate the importance of quantifying INP number concentrations at all mixed-phase temperatures and improving the representation of cloud glaciation in climate models.

## References

- Abbe, C.: The physical basis of long-range weather forecasts, *Mon. Weather Rev.*, 29(12), 551–561, 1901.
- Abdul-Razzak, H. and Ghan, S. J.: A parameterization of aerosol activation: 2. Multiple aerosol types, *J. Geophys. Res.*, 105(16), 6837–6844, doi:10.1029/1999JD901161, 2000.
- Ackerman, A. S., Toon, O. B., Stevens, D. E., Heymsfield, A. J., Ramanathan, V. and Welton, E. J.: Reduction of tropical cloudiness by soot, *Science (80-. )*, 288(5468), 1042–1047, doi:10.1126/science.288.5468.1042, 2000.
- Altaratz, O., Koren, I., Remer, L. A. and Hirsch, E.: Review: Cloud invigoration by aerosols- Coupling between microphysics and dynamics, *Atmos. Res.*, 140–141, 38–60, doi:10.1016/j.atmosres.2014.01.009, 2014.
- Anderson, N. F., Grainger, C. A. and Stith, J. L.: Characteristics of strong updrafts in precipitation systems over the central Tropical Pacific Ocean and in the Amazon, *J. Appl. Meteorol.*, 44(5), 731–738, doi:10.1175/JAM2231.1, 2005.
- Ansmann, A., Tesche, M., Althausen, D., Müller, D., Seifert, P., Freudenthaler, V., Heese, B., Wiegner, M., Pisani, G., Knippertz, P. and Dubovik, O.: Influence of Saharan dust on cloud glaciation in southern Morocco during the Saharan Mineral Dust Experiment, *J. Geophys. Res.*, 113(D4), D04210, doi:10.1029/2007JD008785, 2008.
- Ansmann, A., Rittmeister, F., Engelmann, R., Basart, S., Jorba, O., Spyrou, C., Remy, S., Skupin, A., Baars, H., Seifert, P., Senf, F. and Kanitz, T.: Profiling of Saharan dust from the Caribbean to western Africa-Part 2: Shipborne lidar measurements versus forecasts, *Atmos. Chem. Phys.*, 17, 14987–15006, doi:10.5194/acp-17-14987-2017, 2017.
- Arakawa, A.: The cumulus parameterization problem: Past, present, and future, *J. Clim.*,

17(13), 2493–2525, doi:10.1175/1520-0442(2004)017<2493:RATCPP>2.0.CO;2, 2004.

Atkinson, J. D., Murray, B. J., Woodhouse, M. T., Whale, T. F., Baustian, K. J., Carslaw, K. S., Dobbie, S., O’Sullivan, D. and Malkin, T. L.: The importance of feldspar for ice nucleation by mineral dust in mixed-phase clouds, *Nature*, 498(7454), 355–358, doi:10.1038/nature12278, 2013.

Augustin-Bauditz, S., Wex, H., Kanter, S., Ebert, M., Niedermeier, D., Stolz, F., Prager, A. and Stratmann, F.: The immersion mode ice nucleation behavior of mineral dusts: A comparison of different pure and surface modified dusts, *Geophys. Res. Lett.*, 41(20), 7375–7382, doi:10.1002/2014GL061317, 2014.

Augustin-Bauditz, S., Wex, H., Denjean, C., Hartmann, S., Schneider, J., Schmidt, S., Ebert, M. and Stratmann, F.: Laboratory-generated mixtures of mineral dust particles with biological substances: Characterization of the particle mixing state and immersion freezing behavior, *Atmos. Chem. Phys.*, 16(9), 5531–5543, doi:10.5194/acp-16-5531-2016, 2016.

Barahona, D., West, R. E. L., Stier, P., Romakkaniemi, S., Kokkola, H. and Nenes, A.: Comprehensively accounting for the effect of giant CCN in cloud activation parameterizations, *Atmos. Chem. Phys.*, 10, 2467–2473, doi:https://doi.org/10.5194/acp-10-2467-2010, 2010.

Baran, A. J., Hill, P., Furtado, K., Field, P. and Manners, J.: A Coupled Cloud Physics–Radiation Parameterization of the Bulk Optical Properties of Cirrus and Its Impact on the Met Office Unified Model Global Atmosphere 5.0 Configuration, *J. Clim.*, 27(20), 7725–7752, doi:10.1175/JCLI-D-13-00700.1, 2014.

Bauer, P., Thorpe, A. and Brunet, G.: The quiet revolution of numerical weather prediction, *Nature*, 525(7567), 47–55, doi:10.1038/nature14956, 2015.

Beard, K. V.: Ice initiation in warm-base convective clouds: An assessment of microphysical

mechanisms, *Atmos. Res.*, 28(2), 125–152, doi:10.1016/0169-8095(92)90024-5, 1992.

Bigg, E. K.: The formation of atmospheric ice crystals by the freezing of droplets, *Q. J. R. Meteorol. Soc.*, 79(342), 510–519, doi:10.1002/qj.49707934207, 1953.

Bjerknes, V.: Das Problem der Wettervorhersage betrachtet vom Standpunkt der Mechanik und Physik, *Meteor. Z.*, 21, 1–7, 1904.

De Boer, G., Morrison, H., Shupe, M. D. and Hildner, R.: Evidence of liquid dependent ice nucleation in high-latitude stratiform clouds from surface remote sensors, *Geophys. Res. Lett.*, 38(1), L01803, doi:10.1029/2010GL046016, 2011.

Bolin, B.: Numerical Forecasting with the Barotropic Model, *Tellus*, 7(1), 27–49, doi:10.1111/j.2153-3490.1955.tb01139.x, 1955.

Bond, T. C., Streets, D. G., Yarber, K. F., Nelson, S. M., Woo, J. H. and Klimont, Z.: A technology-based global inventory of black and organic carbon emissions from combustion, *J. Geophys. Res. Atmos.*, 109(14), doi:10.1029/2003JD003697, 2004.

Boose, Y., Kanji, Z. A., Kohn, M., Sierau, B., Zipori, A., Crawford, I., Lloyd, G., Bukowiecki, N., Herrmann, E., Kupiszewski, P., Steinbacher, M. and Lohmann, U.: Ice nucleating particle measurements at 241K during winter months at 3580m MSL in the swiss alps, *J. Atmos. Sci.*, 73(5), 2203–2228, doi:10.1175/JAS-D-15-0236.1, 2016a.

Boose, Y., Sierau, B., García, M. I., Rodríguez, S., Alastuey, A., Linke, C., Schnaiter, M., Kupiszewski, P., Kanji, Z. A. and Lohmann, U.: Ice nucleating particles in the Saharan Air Layer, *Atmos. Chem. Phys.*, 16(14), 9067–9087, doi:10.5194/acp-16-9067-2016, 2016b.

Bou Karam, D., Williams, E., Janiga, M., Flamant, C., McGraw-Herdeg, M., Cuesta, J., Auby, A. and Thorncroft, C.: Synoptic-scale dust emissions over the Sahara Desert initiated by a moist convective cold pool in early August 2006, *Q. J. R. Meteorol. Soc.*, 140(685), 2591–2607,

doi:10.1002/qj.2326, 2014.

Boucher, O., Randall, D., Artaxo, P., Bretherton, C., Feingold, G., Forster, P., Kerminen, V., Kondo, Y., Liao, H., Lohmann, U., Rasch, P., Satheesh, S., Sherwood, S., Stevens, B., Zhang, X., Qin, D., Plattner, G., Tignor, M., Allen, S., Boschung, J., Nauels, A., Xia, Y., Bex, V., Midgley, P., Boucher, O. and Randall, D.: Clouds and Aerosols., in *Climate Change 2013: The Physical Science Basis. Contribution of Working Group I to the Fifth Assessment Report of the Intergovernmental Panel on Climate Change*, edited by C. U. Press, Cambridge University Press, Cambridge, United Kingdom and New York, NY, USA., 2013.

Brooks, S. D., Suter, K. and Olivarez, L.: Effects of chemical aging on the ice nucleation activity of soot and polycyclic aromatic hydrocarbon aerosols, *J. Phys. Chem. A*, 118(43), 10036–10047, doi:10.1021/jp508809y, 2014.

Browse, J., Carslaw, K. S., Arnold, S. R., Pringle, K. and Boucher, O.: The scavenging processes controlling the seasonal cycle in Arctic sulphate and black carbon aerosol, *Atmos. Chem. Phys.*, 12(15), 6775–6798, doi:10.5194/acp-12-6775-2012, 2012.

Buchard, V., Randles, C. A., da Silva, A. M., Darmenov, A., Colarco, P. R., Govindaraju, R., Ferrare, R., Hair, J., Beyersdorf, A. J., Ziemba, L. D. and Yu, H.: The MERRA-2 Aerosol Reanalysis, 1980 Onward. Part II: Evaluation and Case Studies, *J. Clim.*, 30(17), 6851–6872, doi:10.1175/JCLI-D-16-0613.1, 2017.

Campbell, J. M. and Christenson, H. K.: Nucleation- and Emergence-Limited Growth of Ice from Pores, *Phys. Rev. Lett.*, 120(16), 165701, doi:10.1103/PhysRevLett.120.165701, 2018.

Campos Braga, R., Rosenfeld, D., Weigel, R., Jurkat, T., Andreae, M. O., Wendisch, M., Pöschl, U., Voigt, C., Mahnke, C., Borrmann, S., Albrecht, R. I., Molleker, S., Vila, D. A., Machado, L. A. T. and Grulich, L.: Further evidence for CCN aerosol concentrations determining the height of warm rain and ice initiation in convective clouds over the Amazon

- basin, *Atmos. Chem. Phys.*, 17, 14433–14456, doi:10.5194/acp-17-14433-2017, 2017.
- Cantrell, W. and Heymsfield, A.: Production of ice in tropospheric clouds: a review, *Bull. Am. Meteorol. Soc.*, 86(6), 795–808, doi:10.1175/BAMS-86-6-795, 2005.
- Carlton, A. G., Wiedinmyer, C. and Kroll, J. H.: A review of Secondary organic aerosol (SOA) formation from isoprene, *Atmos. Chem. Phys.*, 9(14), 4987–5005, doi:10.5194/acp-9-4987-2009, 2009.
- Carrió, G. G., van den Heever, S. C. and Cotton, W. R.: Impacts of nucleating aerosol on anvil-cirrus clouds: A modeling study, *Atmos. Res.*, 84(2), 111–131, doi:10.1016/j.atmosres.2006.06.002, 2007.
- Carslaw, K. S., Lee, L. A., Reddington, C. L., Pringle, K. J., Rap, A., Forster, P. M., Mann, G. W., Spracklen, D. V., Woodhouse, M. T., Regayre, L. A. and Pierce, J. R.: Large contribution of natural aerosols to uncertainty in indirect forcing, *Nature*, 503(7474), 67–71, doi:10.1038/nature12674, 2013.
- Cesana, G., Waliser, D. E., Jiang, X. and Li, J. L. F.: Multimodel evaluation of cloud phase transition using satellite and reanalysis data, *J. Geophys. Res.*, 120(15), 7871–7892, doi:10.1002/2014JD022932, 2015.
- Charney, J. G., Fjörtoft, R. and Neumann, J. Von: Numerical Integration of the Barotropic Vorticity Equation, *Tellus*, 2(4), 237–254, doi:10.3402/tellusa.v2i4.8607, 1950.
- Chen, J., Wu, Z., Chen, J., Reicher, N., Fang, X., Rudich, Y. and Hu, M.: Size-resolved atmospheric ice-nucleating particles during East Asian dust events, *Atmos. Chem. Phys.*, 21(5), 3491–3506, doi:10.5194/acp-21-3491-2021, 2021.
- Chen, Y., Seiki, T., Kodama, C., Satoh, M. and Noda, A. T.: Impact of Precipitating Ice Hydrometeors on Longwave Radiative Effect Estimated by a Global Cloud- System Resolving

Model, J. *Adv. Model. Earth Syst.*, 10(2), 284–296, doi:10.1002/2017MS001180, 2018.

Chiapello, I., Bergametti, G., Gomes, L., Chatenet, B., Dulac, F., Pimenta, J. and Soares, E. S.: An additional low layer transport of Sahelian and Saharan dust over the north-eastern Tropical Atlantic, *Geophys. Res. Lett.*, 22(23), 3191–3194, doi:10.1029/95GL03313, 1995.

Chiapello, I., Moulin, C. and Prospero, J. M.: Understanding the long- term variability of African dust transport across the Atlantic as recorded in both Barbados surface concentrations and large- scale Total Ozone Mapping Spectrometer (TOMS) optical thickness, *J. Geophys. Res. Atmos.*, 110(D18), doi:10.1029/2004JD005132@10.1002/(ISSN)2169-8996.MINRLDUST1, 2005.

Chin, M., Ginoux, P., Kinne, S., Torres, O., Holben, B. N., Duncan, B. N., Martin, R. V., Logan, J. A., Higurashi, A., Nakajima, T., Chin, M., Ginoux, P., Kinne, S., Torres, O., Holben, B. N., Duncan, B. N., Martin, R. V., Logan, J. A., Higurashi, A. and Nakajima, T.: Tropospheric Aerosol Optical Thickness from the GOCART Model and Comparisons with Satellite and Sun Photometer Measurements, [http://dx.doi.org/10.1175/1520-0469\(2002\)059<0461:TAOTFT>2.0.CO;2](http://dx.doi.org/10.1175/1520-0469(2002)059<0461:TAOTFT>2.0.CO;2), doi:10.1175/1520-0469(2002)059<0461:TAOTFT>2.0.CO;2, 2002.

Choobari, O. A., Zawar-Reza, P. and Sturman, A.: The global distribution of mineral dust and its impacts on the climate system: A review, *Atmos. Res.*, 138, 152–165, doi:10.1016/j.atmosres.2013.11.007, 2014.

Colarco, P., Da Silva, A., Chin, M. and Diehl, T.: Online simulations of global aerosol distributions in the NASA GEOS-4 model and comparisons to satellite and ground-based aerosol optical depth, *J. Geophys. Res. Atmos.*, 115(14), doi:10.1029/2009JD012820, 2010.

Cole-Dai, J.: Volcanoes and climate, *Wiley Interdiscip. Rev. Clim. Chang.*, 1(6), 824–839, doi:10.1002/wcc.76, 2010.

Coluzza, I., Creamean, J., Rossi, M., Wex, H., Alpert, P., Bianco, V., Boose, Y., Dellago, C., Felgitsch, L., Fröhlich-Nowoisky, J., Herrmann, H., Jungblut, S., Kanji, Z., Menzl, G., Moffett, B., Moritz, C., Mutzel, A., Pöschl, U., Schauer, M., Scheel, J., Stopelli, E., Stratmann, F., Grothe, H. and Schmale, D.: Perspectives on the Future of Ice Nucleation Research: Research Needs and Unanswered Questions Identified from Two International Workshops, *Atmosphere (Basel)*, 8(12), 138, doi:10.3390/atmos8080138, 2017.

Connolly, P. J., Choulaton, T. W., Gallagher, M. W., Bower, K. N., Flynn, M. J. and Whiteway, J. A.: Cloud-resolving simulations of intense tropical Hector thunderstorms: Implications for aerosol-cloud interactions, *Meteorol. Soc.*, 132, 3079–3106, doi:10.1256/qj.05.86, 2006.

Cooper, W. A.: Ice initiation in natural clouds, in *Precipitation enhancement—A scientific challenge*, pp. 29–32, American Meteorological Society, Boston, MA., 1986.

Corr, C. A., Ziemba, L. D., Scheuer, E., Anderson, B. E., Beyersdorf, A. J., Chen, G., Crosbie, E., Moore, R. H., Shook, M., Thornhill, K. L., Winstead, E., Lawson, R. P., Barth, M. C., Schroeder, J. R., Blake, D. R. and Dibb, J. E.: Observational evidence for the convective transport of dust over the Central United States, *J. Geophys. Res. Atmos.*, 121(3), 1306–1319, doi:10.1002/2015JD023789, 2016.

Crawford, I., Bower, K. N., Choulaton, T. W., Dearden, C., Crosier, J., Westbrook, C., Capes, G., Coe, H., Connolly, P. J., Dorsey, J. R., Gallagher, M. W., Williams, P., Trembath, J., Cui, Z. and Blyth, A.: Ice formation and development in aged, wintertime cumulus over the UK: observations and modelling, *Atmos. Chem. Phys.*, 12(11), 4963–4985, doi:10.5194/acp-12-4963-2012, 2012.

Cui, Z., Carslaw, K. S., Yin, Y. and Davies, S.: A numerical study of aerosol effects on the dynamics and microphysics of a deep convective cloud in a continental environment, *J.*

Geophys. Res., 111(D5), D05201, doi:10.1029/2005JD005981, 2006.

Dearden, C., Hill, A., Coe, H. and Choularton, T.: The role of droplet sedimentation in the evolution of low-level clouds over southern West Africa, *Atmos. Chem. Phys.*, 18(19), 14253–14269, doi:10.5194/acp-18-14253-2018, 2018.

Dee, D. P., Uppala, S. M., Simmons, A. J., Berrisford, P., Poli, P., Kobayashi, S., Andrae, U., Balmaseda, M. A., Balsamo, G., Bauer, P., Bechtold, P., Beljaars, A. C. M., van de Berg, L., Bidlot, J., Bormann, N., Delsol, C., Dragani, R., Fuentes, M., Geer, A. J., Haimberger, L., Healy, S. B., Hersbach, H., Hólm, E. V., Isaksen, L., Kållberg, P., Köhler, M., Matricardi, M., McNally, A. P., Monge-Sanz, B. M., Morcrette, J.-J., Park, B.-K., Peubey, C., de Rosnay, P., Tavolato, C., Thépaut, J.-N. and Vitart, F.: The ERA-Interim reanalysis: configuration and performance of the data assimilation system, *Q. J. R. Meteorol. Soc.*, 137(656), 553–597, doi:10.1002/qj.828, 2011.

DeMott, P. J., Sassen, K., Poellot, M. R., Baumgardner, D., Rogers, D. C., Brooks, S. D., Prenni, A. J. and Kreidenweis, S. M.: African dust aerosols as atmospheric ice nuclei, *Geophys. Res. Lett.*, 30(14), 1732–1726, doi:10.1029/2003GL017410, 2003.

DeMott, P. J., Prenni, A. J., Liu, X., Kreidenweis, S. M., Petters, M. D., Twohy, C. H., Richardson, M. S., Eidhammer, T. and Rogers, D. C.: Predicting global atmospheric ice nuclei distributions and their impacts on climate., *Proc. Natl. Acad. Sci. U. S. A.*, 107(25), 11217–22, doi:10.1073/pnas.0910818107, 2010.

DeMott, P. J., Prenni, A. J., McMeeking, G. R., Sullivan, R. C., Petters, M. D., Tobo, Y., Niemand, M., Möhler, O., Snider, J. R., Wang, Z. and Kreidenweis, S. M.: Integrating laboratory and field data to quantify the immersion freezing ice nucleation activity of mineral dust particles, *Atmos. Chem. Phys.*, 15, 393–409, doi:10.5194/acp-15-393-2015, 2015.

DeMott, P. J., Hill, T. C. J., McCluskey, C. S., Prather, K. A., Collins, D. B., Sullivan, R. C.,

Ruppel, M. J., Mason, R. H., Irish, V. E., Lee, T., Hwang, C. Y., Rhee, T. S., Snider, J. R., McMeeking, G. R., Dhaniyala, S., Lewis, E. R., Wentzell, J. J. B., Abbatt, J., Lee, C., Sultana, C. M., Ault, A. P., Axson, J. L., Martinez, M. D., Venero, I., Santos-Figueroa, G., Stokes, M. D., Deane, G. B., Mayol-Bracero, O. L., Grassian, V. H., Bertram, T. H., Bertram, A. K., Moffett, B. F. and Franc, G. D.: Sea spray aerosol as a unique source of ice nucleating particles, *Proc. Natl. Acad. Sci. U. S. A.*, 113(21), 5797–5803, doi:10.1073/pnas.1514034112, 2016.

Deng, X., Xue, H. and Meng, Z.: The effect of ice nuclei on a deep convective cloud in South China, *Atmos. Res.*, 206, 1–12, doi:10.1016/J.ATMOSRES.2018.02.013, 2018.

Dentener, F., Kinne, S., Bond, T., Boucher, O., Cofala, J., Generoso, S., Ginoux, P., Gong, S., Hoelzemann, J. J., Ito, A., Marelli, L., Penner, J. E., Putaud, J.-P., Textor, C., Schulz, M., Van Der Werf, G. R. and Wilson, J.: Emissions of primary aerosol and precursor gases in the years 2000 and 1750 prescribed data-sets for AeroCom, *Atmos. Chem. Phys.*, 6(12), 4321–4344, doi:https://doi.org/10.5194/acp-6-4321-2006, 2006.

Diehl, K., Matthias-Maser, S., Jaenicke, R. and Mitra, S. : The ice nucleating ability of pollen:: Part II. Laboratory studies in immersion and contact freezing modes, *Atmos. Res.*, 61(2), 125–133, doi:10.1016/S0169-8095(01)00132-6, 2002.

Dong, Y. Y. and Hallett, J.: Droplet accretion during rime growth and the formation of secondary ice crystals, *Q. J. R. Meteorol. Soc.*, 115(485), 127–142, doi:10.1002/qj.49711548507, 1989.

Dunion, J. P. and Velden, C. S.: The Impact of the Saharan Air Layer on Atlantic Tropical Cyclone Activity, *Bull. Am. Meteorol. Soc.*, 85(3), 353–365, doi:10.1175/BAMS-85-3-353, 2004.

Edwards, J. M. and Slingo, A.: Studies with a flexible new radiation code. I: Choosing a configuration for a large-scale model, *Q. J. R. Meteorol. Soc.*, 122(531), 689–719,

doi:10.1002/qj.49712253107, 1996.

Edwards, J. M., Havemann, S., Thelen, J. C. and Baran, A. J.: A new parametrization for the radiative properties of ice crystals: Comparison with existing schemes and impact in a GCM, *Atmos. Res.*, 83(1), 19–35, doi:10.1016/j.atmosres.2006.03.002, 2007.

Eidhammer, T., Demott, P. J. and Kreidenweis, S. M.: A comparison of heterogeneous ice nucleation parameterizations using a parcel model framework, *J. Geophys. Res. Atmos.*, 114(6), D06202, doi:10.1029/2008JD011095, 2009.

Ekman, A. M. L., Engström, A. and Wang, C.: The effect of aerosol composition and concentration on the development and anvil properties of a continental deep convective cloud, *Q. J. R. Meteorol. Soc.*, 133(627), 1439–1452, doi:10.1002/qj.108, 2007.

Emersic, C. and Connolly, P. J.: Microscopic observations of riming on an ice surface using high speed video, *Atmos. Res.*, 185, 65–72, doi:10.1016/J.ATMOSRES.2016.10.014, 2017.

Engelstaedter, S., Tegen, I. and Washington, R.: North African dust emissions and transport, *Earth-Science Rev.*, 79(1–2), 73–100, doi:10.1016/j.earscirev.2006.06.004, 2006.

Evan, A. T. and Mukhopadhyay, S.: African dust over the northern tropical Atlantic: 1955–2008, *J. Appl. Meteorol. Climatol.*, 49(11), 2213–2229, doi:10.1175/2010JAMC2485.1, 2010.

Fan, J., Zhang, R., Li, G. and Tao, W.-K.: Effects of aerosols and relative humidity on cumulus clouds, *J. Geophys. Res.*, 112(D14), D14204, doi:10.1029/2006JD008136, 2007.

Fan, J., Comstock, J. M. and Ovchinnikov, M.: The cloud condensation nuclei and ice nuclei effects on tropical anvil characteristics and water vapor of the tropical tropopause layer, *Environ. Res. Lett.*, 5(4), 044005, doi:10.1088/1748-9326/5/4/044005, 2010a.

Fan, J., Comstock, J. M., Ovchinnikov, M., McFarlane, S. A., McFarquhar, G. and Allen, G.: Tropical anvil characteristics and water vapor of the tropical tropopause layer: Impact of

heterogeneous and homogeneous freezing parameterizations, *J. Geophys. Res.*, 115(D12), D12201, doi:10.1029/2009JD012696, 2010b.

Fan, J., Rosenfeld, D., Ding, Y., Leung, L. R. and Li, Z.: Potential aerosol indirect effects on atmospheric circulation and radiative forcing through deep convection, *Geophys. Res. Lett.*, 39(9), L09806, doi:10.1029/2012GL051851, 2012.

Fan, J., Leung, L. R., Rosenfeld, D., Chen, Q., Li, Z., Zhang, J. and Yan, H.: Microphysical effects determine macrophysical response for aerosol impacts on deep convective clouds., *Proc. Natl. Acad. Sci. U. S. A.*, 110(48), E4581-90, doi:10.1073/pnas.1316830110, 2013.

Fan, J., Wang, Y., Rosenfeld, D., Liu, X., Fan, J., Wang, Y., Rosenfeld, D. and Liu, X.: Review of Aerosol–Cloud Interactions: Mechanisms, Significance, and Challenges, *J. Atmos. Sci.*, 73(11), 4221–4252, doi:10.1175/JAS-D-16-0037.1, 2016.

Feingold, G. and McComiskey, A.: ARM’s Aerosol–Cloud–Precipitation Research (Aerosol Indirect Effects), *Meteorol. Monogr.*, 57, 22.1-22.15, doi:10.1175/AMSMONOGRAPHS-D-15-0022.1, 2016.

Fernandes, K., Baethgen, W., Bernardes, S., DeFries, R., DeWitt, D. G., Goddard, L., Lavado, W., Lee, D. E., Padoch, C., Pinedo-Vasquez, M. and Uriarte, M.: North Tropical Atlantic influence on western Amazon fire season variability, *Geophys. Res. Lett.*, 38(12), n/a-n/a, doi:10.1029/2011GL047392, 2011.

Field, P. R., Möhler, O., Connolly, P., Krämer, M., Cotton, R., Heymsfield, A. J., Saathoff, H. and Schnaiter, M.: Some ice nucleation characteristics of Asian and Saharan desert dust, *Atmos. Chem. Phys.*, 6(10), 2991–3006, doi:https://doi.org/10.5194/acp-6-2991-2006, 2006.

Field, P. R., Lawson, R. P., Brown, P. R. A., Lloyd, G., Westbrook, C., Moisseev, D., Miltenberger, A., Nenes, A., Blyth, A., Choulaton, T., Connolly, P., Buehl, J., Crosier, J., Cui, Z., Dearden, C., DeMott, P., Flossmann, A., Heymsfield, A., Huang, Y., Kalesse, H., Kanji, Z.

A., Korolev, A., Kirchgaessner, A., Lasher-Trapp, S., Leisner, T., McFarquhar, G., Phillips, V., Stith, J., Sullivan, S., Field, P. R., Lawson, R. P., Brown, P. R. A., Lloyd, G., Westbrook, C., Moisseev, D., Miltenberger, A., Nenes, A., Blyth, A., Choulaton, T., Connolly, P., Buehl, J., Crosier, J., Cui, Z., Dearden, C., DeMott, P., Flossmann, A., Heymsfield, A., Huang, Y., Kalesse, H., Kanji, Z. A., Korolev, A., Kirchgaessner, A., Lasher-Trapp, S., Leisner, T., McFarquhar, G., Phillips, V., Stith, J. and Sullivan, S.: Chapter 7. Secondary ice production - current state of the science and recommendations for the future, *Meteorol. Monogr.*, 58(1), 7.1-7.20, doi:<https://doi.org/10.1175/AMSMONOGRAPHS-D-16-0014.1>, 2017.

Fountoukis, C. and Nenes, A.: Continued development of a cloud droplet formation parameterization for global climate models, *J. Geophys. Res. D Atmos.*, 110(11), 1–10, doi:[10.1029/2004JD005591](https://doi.org/10.1029/2004JD005591), 2005.

Frank, W. M.: The Structure and Energetics of the Tropical Cyclone I. Storm Structure, [http://dx.doi.org/10.1175/1520-0493\(1977\)105<1119:TSAEOT>2.0.CO;2](http://dx.doi.org/10.1175/1520-0493(1977)105<1119:TSAEOT>2.0.CO;2), 105, 1119–1134, doi:[10.1175/1520-0493\(1977\)105<1119:TSAEOT>2.0.CO;2](https://doi.org/10.1175/1520-0493(1977)105<1119:TSAEOT>2.0.CO;2), 1977.

Freedman, M. A.: Potential Sites for Ice Nucleation on Aluminosilicate Clay Minerals and Related Materials, *J. Phys. Chem. Lett.*, 6(19), 3850–3858, doi:[10.1021/acs.jpcclett.5b01326](https://doi.org/10.1021/acs.jpcclett.5b01326), 2015.

Fridlind, A. M., Ackerman, A. S., McFarquhar, G., Zhang, G., Poellot, M. R., DeMott, P. J., Prenni, A. J. and Heymsfield, A. J.: Ice properties of single-layer stratocumulus during the Mixed-Phase Arctic Cloud Experiment: 2. Model results, *J. Geophys. Res.*, 112(D24), D24202, doi:[10.1029/2007JD008646](https://doi.org/10.1029/2007JD008646), 2007.

Fu, Q., Sun, W. B., Yang, P., Fu, Q., Sun, W. B. and Yang, P.: Modeling of Scattering and Absorption by Nonspherical Cirrus Ice Particles at Thermal Infrared Wavelengths, *J. Atmos. Sci.*, 56(16), 2937–2947, doi:[10.1175/1520-0469\(1999\)056<2937:MOSAAB>2.0.CO;2](https://doi.org/10.1175/1520-0469(1999)056<2937:MOSAAB>2.0.CO;2),

1999.

Gelaro, R., McCarty, W., Suárez, M. J., Todling, R., Molod, A., Takacs, L., Randles, C. A., Darmenov, A., Bosilovich, M. G., Reichle, R., Wargan, K., Coy, L., Cullather, R., Draper, C., Akella, S., Buchard, V., Conaty, A., da Silva, A. M., Gu, W., Kim, G. K., Koster, R., Lucchesi, R., Merkova, D., Nielsen, J. E., Partyka, G., Pawson, S., Putman, W., Rienecker, M., Schubert, S. D., Sienkiewicz, M. and Zhao, B.: The modern-era retrospective analysis for research and applications, version 2 (MERRA-2), *J. Clim.*, 30(14), 5419–5454, doi:10.1175/JCLI-D-16-0758.1, 2017.

Gibbons, M., Min, Q. and Fan, J.: Investigating the impacts of Saharan dust on tropical deep convection using spectral bin microphysics, *Atmos. Chem. Phys.*, 18, 12161–12184, doi:10.5194/acp-18-12161-2018, 2018.

Gibson, E. R., Gierlus, K. M., Hudson, P. K. and Grassian, V. H.: Generation of Internally Mixed Insoluble and Soluble Aerosol Particles to Investigate the Impact of Atmospheric Aging and Heterogeneous Processing on the CCN Activity of Mineral Dust Aerosol, *Aerosol Sci. Technol.*, 41(10), 914–924, doi:10.1080/02786820701557222, 2007.

Ginoux, P., Chin, M., Tegen, I., Prospero, J. M., Holben, B., Dubovik, O. and Lin, S.-J.: Sources and distributions of dust aerosols simulated with the GOCART model, *J. Geophys. Res. Atmos.*, 106(D17), 20255–20273, doi:10.1029/2000JD000053, 2001.

Ginoux, P., Prospero, J. M., Gill, T. E., Hsu, N. C. and Zhao, M.: Global-scale attribution of anthropogenic and natural dust sources and their emission rates based on MODIS Deep Blue aerosol products, *Rev. Geophys.*, 50(3), doi:10.1029/2012RG000388, 2012.

Gläser, G., Wernli, H., Kerkweg, A. and Teubler, F.: The transatlantic dust transport from North Africa to the Americas-Its characteristics and source regions, *J. Geophys. Res. Atmos.*, 120(21), 11,231-11,252, doi:10.1002/2015JD023792, 2015.

Glassmeier, F., Hoffmann, F., Johnson, J. S., Yamaguchi, T., Carslaw, K. S. and Feingold, G.: An emulator approach to stratocumulus susceptibility, *Atmos. Chem. Phys.*, 19(15), 10191–10203, doi:10.5194/acp-19-10191-2019, 2019.

Gong, S. L.: A parameterization of sea-salt aerosol source function for sub- and super-micron particles, *Global Biogeochem. Cycles*, 17(4), doi:10.1029/2003gb002079, 2003.

Gray, M. E. B., Petch, J., Derbyshire, S. H., Brown, A. R., Lock, A. P., Swann, H. A. and Brown, P. R. A.: Version 2.3 of the Met Office Large Eddy Model: Part II. Scientific Documentation, Met O Turbul. Diffus. note, 2001.

Grini, A., Myhre, G., Zender, C. S. and Isaksen, I. S. A.: Model simulations of dust sources and transport in the global atmosphere: Effects of soil erodibility and wind speed variability, *J. Geophys. Res. D Atmos.*, 110(2), 1–14, doi:10.1029/2004JD005037, 2005.

Groß, S., Gasteiger, J., Freudenthaler, V., Müller, T., Sauer, D., Toledano, C. and Ansmann, A.: Saharan dust contribution to the Caribbean summertime boundary layer – a lidar study during SALTRACE, *Atmos. Chem. Phys.*, 16, 11535–11546, doi:10.5194/acp-16-11535-2016, 2016.

Grosvenor, D. P., Field, P. R., Hill, A. A. and Shipway, B. J.: The relative importance of macrophysical and cloud albedo changes for aerosol-induced radiative effects in closed-cell stratocumulus: insight from the modelling of a case study, *Atmos. Chem. Phys.*, 17, 5155–5183, doi:10.5194/acp-17-5155-2017, 2017.

Gu, Y., Liou, K. N., Ou, S. C. and Fovell, R.: Cirrus cloud simulations using WRF with improved radiation parameterization and increased vertical resolution, *J. Geophys. Res.*, 116(D6), D06119, doi:10.1029/2010JD014574, 2011.

Hallett, J. and Mossop, S. C.: Production of secondary ice particles during the riming process, *Nature*, 249, 26–28, doi:https://doi.org/10.1038/249026a0, 1974.

Harrison, A. D., Whale, T. F., Carpenter, M. A., Holden, M. A., Neve, L., O'Sullivan, D., Vergara Temprado, J. and Murray, B. J.: Not all feldspars are equal: a survey of ice nucleating properties across the feldspar group of minerals, *Atmos. Chem. Phys.*, 16(17), 10927–10940, doi:10.5194/acp-16-10927-2016, 2016.

Harrison, A. D., Lever, K., Sanchez-Marroquin, A., Holden, M. A., Whale, T. F., Tarn, M. D., McQuaid, J. B. and Murray, B. J.: The ice-nucleating ability of quartz immersed in water and its atmospheric importance compared to K-feldspar, *Atmos. Chem. Phys.*, 19(17), 11343–11361, doi:10.5194/acp-19-11343-2019, 2019.

Harrison, A. D., O'Sullivan, D., Adams, M. P., Porter, G. C. E., Brathwaite, C., Chewitt-Lucas, R., Hawker, R., Krueger, O. O., Neve, L., Pohlker, M. L., Pohlker, C., Poschl, U., Prospero, J. M., Sanchez-Marroquin, A., Sealy, A., Sealy, P., Tarn, M. D., S. Whitehall, J. and Murray, B. J.: Ice-nucleating activity of desert dust decreases on transport across the Atlantic, n.d.

Hawker, R., Miltenberger, A., Wilkinson, J., Hill, A., Shipway, B., Cui, Z., Cotton, R., Carslaw, K., Field, P. and Murray, B.: The temperature dependence of ice-nucleating particle concentrations affects the radiative properties of tropical convective cloud systems, *Atmos. Chem. Phys.*, 21(7), 5439–5461, doi:10.5194/acp-21-5439-2021, 2021.

van den Heever, S. C., Carrió, G. G., Cotton, W. R., DeMott, P. J. and Prenni, A. J.: Impacts of nucleating aerosol on Florida storms. Part I: Mesoscale simulations, *J. Atmos. Sci.*, 63(7), 1752–1775, doi:10.1175/JAS3713.1, 2006.

van den Heever, S. C., Stephens, G. L. and Wood, N. B.: Aerosol Indirect Effects on Tropical Convection Characteristics under Conditions of Radiative–Convective Equilibrium, *Am. Meteorol. Soc.*, 68, 699–719, doi:10.1175/2010JAS3603.1, 2011.

Heinold, B., Knippertz, P., Marsham, J. H., Fiedler, S., Dixon, N. S., Schepanski, K., Laurent, B. and Tegen, I.: The role of deep convection and nocturnal low-level jets for dust emission in

summertime West Africa: Estimates from convection-permitting simulations, *J. Geophys. Res. Atmos.*, 118(10), 4385–4400, doi:10.1002/jgrd.50402, 2013.

Herbener, S. R., van den Heever, S. C., Carrió, G. G., Saleeby, S. M. and Cotton, W. R.: Aerosol indirect effects on idealized tropical cyclone dynamics, *J. Atmos. Sci.*, 71(6), 2040–2055, doi:10.1175/JAS-D-13-0202.1, 2014.

Herbert, R. J., Murray, B. J., Dobbie, S. J. and Koop, T.: Sensitivity of liquid clouds to homogenous freezing parameterizations, *Geophys. Res. Lett.*, 42(5), 1599–1605, doi:10.1002/2014GL062729@10.1002/(ISSN)1944-8007.2015EDHIGHLIGHTS, 2015.

Heymsfield, A. and Willis, P.: Cloud conditions favoring secondary ice particle production in tropical maritime convection, *J. Atmos. Sci.*, 71(12), 4500–4526, doi:10.1175/JAS-D-14-0093.1, 2014.

Heymsfield, A. J. and Mossop, S. C.: Temperature dependence of secondary ice crystal production during soft hail growth by riming, *Q. J. R. Meteorol. Soc.*, 110(465), 765–770, doi:10.1002/qj.49711046512, 1984.

Heymsfield, A. J., Miloshevich, L. M., Schmitt, C., Bansemer, A., Twohy, C., Poellot, M. R., Fridlind, A. and Gerber, H.: Homogeneous ice nucleation in subtropical and tropical convection and its influence on cirrus anvil microphysics, *J. Atmos. Sci.*, 62(1), 41–64, doi:10.1175/JAS-3360.1, 2005.

Hill, P. G., Chiu, J. C., Allan, R. P. and Chern, J. - D.: Characterizing the Radiative Effect of Rain Using a Global Ensemble of Cloud Resolving Simulations, *J. Adv. Model. Earth Syst.*, 10(10), 2453–2470, doi:10.1029/2018MS001415, 2018.

Hiranuma, N., Hoffmann, N., Kiselev, A., Dreyer, A., Zhang, K., Kulkarni, G., Koop, T. and Möhler, O.: Influence of surface morphology on the immersion mode ice nucleation efficiency of hematite particles, *Atmos. Chem. Phys.*, 14(5), 2315–2324, doi:10.5194/acp-14-2315-2014,

2014.

Holden, M. A., Whale, T. F., Tarn, M. D., O'Sullivan, D., Walshaw, R. D., Murray, B. J., Meldrum, F. C. and Christenson, H. K.: High-speed imaging of ice nucleation in water proves the existence of active sites, *Sci. Adv.*, 5(2), eaav4316, doi:10.1126/sciadv.aav4316, 2019.

Hoose, C. and Möhler, O.: Heterogeneous ice nucleation on atmospheric aerosols: a review of results from laboratory experiments, *Atmos. Chem. Phys.*, 12, 9817–9854, doi:10.5194/acp-12-9817-2012, 2012.

Hoose, C., Lohmann, U., Erdin, R. and Tegen, I.: The global influence of dust mineralogical composition on heterogeneous ice nucleation in mixed-phase clouds, *Environ. Res. Lett.* *Environ. Res. Lett.*, 3(3), 25003–14, doi:10.1088/1748-9326/3/2/025003, 2008.

Hoose, C., Kristjánsson, J. E., Chen, J. P. and Hazra, A.: A classical-theory-based parameterization of heterogeneous ice nucleation by mineral dust, soot, and biological particles in a global climate model, *J. Atmos. Sci.*, 67(8), 2483–2503, doi:10.1175/2010JAS3425.1, 2010.

Huang, J., Chidong, Z. and Prospero, J. M.: African dust outbreaks: A satellite perspective of temporal and spatial variability over the tropical Atlantic Ocean, *J. Geophys. Res. Atmos.*, 115(5), doi:10.1029/2009JD012516, 2010.

Huang, R. J., Zhang, Y., Bozzetti, C., Ho, K. F., Cao, J. J., Han, Y., Daellenbach, K. R., Slowik, J. G., Platt, S. M., Canonaco, F., Zotter, P., Wolf, R., Pieber, S. M., Bruns, E. A., Crippa, M., Ciarelli, G., Piazzalunga, A., Schwikowski, M., Abbaszade, G., Schnelle-Kreis, J., Zimmermann, R., An, Z., Szidat, S., Baltensperger, U., El Haddad, I. and Prévôt, A. S. H.: High secondary aerosol contribution to particulate pollution during haze events in China, *Nature*, 514(7521), 218–222, doi:10.1038/nature13774, 2015.

Huang, Y., Blyth, A. M., Brown, P. R. A., Choularton, T. W., Cui, Z. and Huang, Y.: Factors

controlling secondary ice production in cumulus clouds, *Q. J. R. Meteorol. Soc.*, 143, 1021–1031, doi:10.1002/qj.2987, 2017.

Huneus, N., Schulz, M., Balkanski, Y., Griesfeller, J., Prospero, J., Kinne, S., Bauer, S., Boucher, O., Chin, M., Dentener, F., Diehl, T., Easter, R., Fillmore, D., Ghan, S., Ginoux, P., Grini, A., Horowitz, L., Koch, D., Krol, M. C., Landing, W., Liu, X., Mahowald, N., Miller, R., Morcrette, J.-J., Myhre, G., Penner, J., Perlwitz, J., Stier, P., Takemura, T. and Zender, C. S.: Global dust model intercomparison in AeroCom phase I, *Atmos. Chem. Phys.*, 11(15), 7781–7816, doi:10.5194/acp-11-7781-2011, 2011.

Jeffery, C. A. and Austin, P. H.: Homogeneous nucleation of supercooled water: Results from a new equation of state, *J. Geophys. Res. Atmos.*, 102(21), 25269–25279, doi:10.1029/97jd02243, 1997.

Jickells, T. D., An, Z. S., Andersen, K. K., Baker, A. R., Bergametti, C., Brooks, N., Cao, J. J., Boyd, P. W., Duce, R. A., Hunter, K. A., Kawahata, H., Kubilay, N., LaRoche, J., Liss, P. S., Mahowald, N., Prospero, J. M., Ridgwell, A. J., Tegen, I. and Torres, R.: Global iron connections between desert dust, ocean biogeochemistry, and climate, *Science* (80-. ), 308(5718), 67–71, doi:10.1126/science.1105959, 2005.

Johnson, B. T., Shine, K. P. and Forster, P. M.: The semi-direct aerosol effect: Impact of absorbing aerosols on marine stratocumulus, *Q. J. R. Meteorol. Soc.*, 130(599 PART B), 1407–1422, doi:10.1256/qj.03.61, 2004.

Johnson, C. E., Bellouin, N., Davison, P. S., Jones, A., Rae, J. G. L., Roberts, D. L., Woodage, M. J., Woodward, S., Or  $\tilde{O}$  Nez, C. and Savage, N. H.: CLASSIC Aerosol Scheme, Unified Model Doc. Pap. (Vn 10.3) [online] Available from: [https://code.metoffice.gov.uk/doc/um/vn10.3/papers/umdp\\_020.pdf](https://code.metoffice.gov.uk/doc/um/vn10.3/papers/umdp_020.pdf) (Accessed 9 March 2017a), 2015.

Johnson, D. B.: On the Relative Efficiency of Coalescence and Riming, *J. Atmos. Sci.*, 44(13), 1671–1680, doi:10.1175/1520-0469(1987)044<1671:OTREOC>2.0.CO;2, 1987.

Johnson, J. S., Gosling, J. P. and Kennedy, M. C.: Gaussian process emulation for second-order Monte Carlo simulations, *J. Stat. Plan. Inference*, 141(5), 1838–1848, doi:10.1016/j.jspi.2010.11.034, 2011.

Johnson, J. S., Cui, Z., Lee, L. A., Gosling, J. P., Blyth, A. M. and Carslaw, K. S.: Evaluating uncertainty in convective cloud microphysics using statistical emulation, *J. Adv. Model. Earth Syst.*, 7(1), 162–187, doi:10.1002/2014MS000383, 2015b.

Kandler, K., Schütz, L., Deutscher, C., Ebert, M., Hofmann, H., Jäckel, S., Jaenicke, R., Knippertz, P., Lieke, K., Massling, A., Petzold, A., Schladitz, A., Weinzierl, B., Wiedensohler, A., Zorn, S. and Weinbruch, S.: Size distribution, mass concentration, chemical and mineralogical composition and derived optical parameters of the boundary layer aerosol at Tinfou, Morocco, during SAMUM 2006, *Tellus, Ser. B Chem. Phys. Meteorol.*, 61(1), 32–50, doi:10.1111/j.1600-0889.2008.00385.x, 2009.

Kandler, K., Schneiders, K., Ebert, M., Hartmann, M., Weinbruch, S., Prass, M. and Pöhlker, C.: Composition and mixing state of atmospheric aerosols determined by electron microscopy: method development and application to aged Saharan dust deposition in the Caribbean boundary layer, *Atmos. Chem. Phys.*, 18(18), 13429–13455, doi:10.5194/acp-18-13429-2018, 2018.

Kanji, Z. A., Ladino, L. A., Wex, H., Boose, Y., Burkert-Kohn, M., Cziczo, D. J. and Krämer, M.: Overview of Ice Nucleating Particles, *Meteorol. Monogr.*, 58, 1.1-1.33, doi:10.1175/AMSMONOGRAPHS-D-16-0006.1, 2017.

Karydis, V. A., Capps, S. L., Russell, A. G. and Nenes, A.: Adjoint sensitivity of global cloud droplet number to aerosol and dynamical parameters, *Atmos. Chem. Phys.*, 12, 9041–9055,

doi:10.5194/acp-12-9041-2012, 2012.

Karydis, V. A., Tsimpidi, A. P., Bacer, S., Pozzer, A., Nenes, A. and Lelieveld, J.: Global impact of mineral dust on cloud droplet number concentration, *Atmos. Chem. Phys.*, 17, 5601–5621, doi:10.5194/acp-17-5601-2017, 2017.

Kelly, J. T., Chuang, C. C. and Wexler, A. S.: Influence of dust composition on cloud droplet formation, *Atmos. Environ.*, 41(14), 2904–2916, doi:10.1016/j.atmosenv.2006.12.008, 2007.

Khain, A., Lynn, B. and Shpund, J.: High resolution WRF simulations of Hurricane Irene: Sensitivity to aerosols and choice of microphysical schemes, *Atmos. Res.*, 167, 129–145, doi:10.1016/j.atmosres.2015.07.014, 2016.

Kiselev, A., Bachmann, F., Pedevilla, P., Cox, S. J., Michaelides, A., Gerthsen, D. and Leisner, T.: Active sites in heterogeneous ice nucleation—the example of K-rich feldspars, *Science* (80-. ), 355(6323), 367–371, doi:10.1126/science.aai8034, 2016.

Kishcha, P., da Silva, A. M., Starobinets, B. and Alpert, P.: Saharan dust as a causal factor of significant cloud cover along the saharan air layer in the atlantic ocean, in *Springer Proceedings in Complexity*, pp. 569–573, Springer., 2016.

Knight, C. A.: Ice Growth from the Vapor at  $-5^{\circ}\text{C}$ , *J. Atmos. Sci.*, 69(6), 2031–2040, doi:10.1175/JAS-D-11-0287.1, 2012.

Knight, C. G., Knight, S. H. E., Massey, N., Aina, T., Christensen, C., Frame, D. J., Kettleborough, J. A., Martin, A., Pascoe, S., Sanderson, B., Stainforth, D. A. and Allen, M. R.: Association of parameter, software, and hardware variation with large-scale behavior across 57,000 climate models, *Proc. Natl. Acad. Sci. U. S. A.*, 104(30), 12259–12264, doi:10.1073/pnas.0608144104, 2007.

Knippertz, P. and Todd, M. C.: Mineral dust aerosols over the Sahara: Meteorological controls

on emission and transport and implications for modeling, *Rev. Geophys.*, 50(1), RG1007, doi:10.1029/2011RG000362, 2012.

Komurcu, M., Storelvmo, T., Tan, I., Lohmann, U., Yun, Y., Penner, J. E., Wang, Y., Liu, X. and Takemura, T.: Intercomparison of the cloud water phase among global climate models, *J. Geophys. Res.*, 119(6), 3372–3400, doi:10.1002/2013JD021119, 2014.

Konwar, M., Mahes Kumar, R. S., Kulkarni, J. R., Freud, E., Goswami, B. N. and Rosenfeld, D.: Aerosol control on depth of warm rain in convective clouds, *J. Geophys. Res. Atmos.*, 117(D13), n/a-n/a, doi:10.1029/2012JD017585, 2012.

Koren, I., Kaufman, Y. J., Rosenfeld, D., Remer, L. A. and Rudich, Y.: Aerosol invigoration and restructuring of Atlantic convective clouds, *Geophys. Res. Lett.*, 32(14), n/a-n/a, doi:10.1029/2005GL023187, 2005.

Koren, I., Feingold, G. and Remer, L. A.: The invigoration of deep convective clouds over the Atlantic: aerosol effect, meteorology or retrieval artifact?, *Atmos. Chem. Phys. Atmos. Chem. Phys.*, 10, 8855–8872, doi:10.5194/acp-10-8855-2010, 2010.

Korolev, A. and Leisner, T.: Review of experimental studies of secondary ice production, *Atmos. Chem. Phys.*, 20(20), 11767–11797, doi:10.5194/acp-20-11767-2020, 2020.

Korolev, A., Heckman, I., Wolde, M., Ackerman, A. S., Fridlind, A. M., Ladino, L. A., Paul Lawson, R., Milbrandt, J. and Williams, E.: A new look at the environmental conditions favorable to secondary ice production, *Atmos. Chem. Phys.*, 20(3), 1391–1429, doi:10.5194/acp-20-1391-2020, 2020.

Kucharski, F., Bracco, A., Yoo, J. H., Molteni, F., Kucharski, F., Bracco, A., Yoo, J. H. and Molteni, F.: Low-Frequency Variability of the Indian Monsoon–ENSO Relationship and the Tropical Atlantic: The “Weakening” of the 1980s and 1990s, *J. Clim.*, 20(16), 4255–4266, doi:10.1175/JCLI4254.1, 2007.

Kucharski, F., Bracco, A., Yoo, J. H., Tompkins, A. M., Feudale, L., Ruti, P. and Dell'Aquila, A.: A Gill-Matsuno-type mechanism explains the tropical Atlantic influence on African and Indian monsoon rainfall, *Q. J. R. Meteorol. Soc.*, 135(640), 569–579, doi:10.1002/qj.406, 2009.

Kulkarni, G. and Dobbie, S.: Ice nucleation properties of mineral dust particles: determination of onset RH, IN active fraction, nucleation time-lag, and the effect of active sites on contact angles, *Atmos. Chem. Phys.*, 10(1), 95–105, doi:10.5194/acp-10-95-2010, 2010.

Kulkarni, G., Nandasiri, M., Zelenyuk, A., Beranek, J., Madaan, N., Devaraj, A., Shutthanandan, V., Thevuthasan, S. and Varga, T.: Effects of crystallographic properties on the ice nucleation properties of volcanic ash particles, *Geophys. Res. Lett.*, 42(8), 3048–3055, doi:10.1002/2015GL063270, 2015.

Kumar, P., Nenes, A. and Sokolik, I. N.: Importance of adsorption for CCN activity and hygroscopic properties of mineral dust aerosol, *Geophys. Res. Lett.*, 36(24), L24804, doi:10.1029/2009GL040827, 2009.

Kushnir, Y., Seager, R., Ting, M., Naik, N., Nakamura, J., Kushnir, Y., Seager, R., Ting, M., Naik, N. and Nakamura, J.: Mechanisms of Tropical Atlantic SST Influence on North American Precipitation Variability\*, *J. Clim.*, 23(21), 5610–5628, doi:10.1175/2010JCLI3172.1, 2010.

Lacher, L., Steinbacher, M., Bukowiecki, N., Herrmann, E., Zipori, A. and Kanji, Z. A.: Impact of air mass conditions and aerosol properties on ice nucleating particle concentrations at the High Altitude Research Station Jungfraujoch, *Atmosphere (Basel)*, 9(9), 363, doi:10.3390/atmos9090363, 2018.

Ladino, L. A., Korolev, A., Heckman, I., Wolde, M., Fridlind, A. M. and Ackerman, A. S.: On the role of ice-nucleating aerosol in the formation of ice particles in tropical mesoscale

convective systems, *Geophys. Res. Lett.*, 44(3), 1574–1582, doi:10.1002/2016GL072455, 2017.

Lasher-Trapp, S., Leon, D. C., DeMott, P. J., Villanueva-Birriel, C. M., Johnson, A. V., Moser, D. H., Tully, C. S. and Wu, W.: A Multisensor Investigation of Rime Splintering in Tropical Maritime Cumuli, *J. Atmos. Sci.*, 73(6), 2547–2564, doi:10.1175/JAS-D-15-0285.1, 2016.

Lauber, A., Kiselev, A., Pander, T., Handmann, P., Leisner, T., Lauber, A., Kiselev, A., Pander, T., Handmann, P. and Leisner, T.: Secondary Ice Formation during Freezing of Levitated Droplets, *J. Atmos. Sci.*, 75(8), 2815–2826, doi:10.1175/JAS-D-18-0052.1, 2018.

Laurent, B., Marticorena, B., Bergametti, G., Léon, J. F. and Mahowald, N. M.: Modeling mineral dust emissions from the Sahara desert using new surface properties and soil database, *J. Geophys. Res. Atmos.*, 113(14), doi:10.1029/2007JD009484, 2008.

Lawson, R. P., Woods, S., Morrison, H., Lawson, R. P., Woods, S. and Morrison, H.: The Microphysics of Ice and Precipitation Development in Tropical Cumulus Clouds, *J. Atmos. Sci.*, 72(6), 2429–2445, doi:10.1175/JAS-D-14-0274.1, 2015.

Lee, L. A., Carslaw, K. S., Pringle, K. J., Mann, G. W. and Spracklen, D. V: Emulation of a complex global aerosol model to quantify sensitivity to uncertain parameters, *Atmos. Chem. Phys.*, 11, 12253–12273, doi:10.5194/acp-11-12253-2011, 2011.

LeMone, M. A., Zipser, E. J., LeMone, M. A. and Zipser, E. J.: Cumulonimbus Vertical Velocity Events in GATE. Part I: Diameter, Intensity and Mass Flux, *J. Atmos. Sci.*, 37(11), 2444–2457, doi:10.1175/1520-0469(1980)037<2444:CVVEIG>2.0.CO;2, 1980.

Lerach, D. G., Gaudet, B. J. and Cotton, W. R.: Idealized simulations of aerosol influences on tornadogenesis, *Geophys. Res. Lett.*, 35(23), L23806, doi:10.1029/2008GL035617, 2008.

Li, X., Holland, D. M., Gerber, E. P. and Yoo, C.: Impacts of the north and tropical Atlantic

Ocean on the Antarctic Peninsula and sea ice, *Nature*, 505(7484), 538–542, doi:10.1038/nature12945, 2014.

Liu, X., Fu, Y., Cao, Z. and Jin, S.: Influence of ice nuclei parameterization schemes on the hail process, *Adv. Meteorol.*, 2018, doi:10.1155/2018/4204137, 2018.

Lloyd, G., Choulaton, T., Bower, K., Crosier, J., Gallagher, M., Flynn, M., Dorsey, J., Liu, D., Taylor, J. W., Schlenczek, O., Fugal, J., Borrmann, S., Cotton, R., Field, P. and Blyth, A.: Small Ice Particles at Slightly Supercooled Temperatures in Tropical Maritime Convection, *Atmos. Chem. Phys. Discuss.*, 1–18, doi:10.5194/acp-2019-345, 2019.

Loeppky, J. L., Sacks, J. and Welch, W. J.: Choosing the sample size of a computer experiment: A practical guide, *Technometrics*, 51(4), 366–376, doi:10.1198/TECH.2009.08040, 2009.

Lohmann, U.: Aerosol effects on clouds and climate, *Space Sci. Rev.*, 125(1–4), 129–137, doi:10.1007/s11214-006-9051-8, 2006.

Lohmann, U., Lüönd, F. and Mahrt, F.: An introduction to clouds: From the microscale to climate, Cambridge University Press, Cambridge CB2 8BS, United Kingdom., 2016.

Lopez, P.: Cloud and precipitation parameterizations in modeling and variational data assimilation: A review, *J. Atmos. Sci.*, 64(11), 3766–3784, doi:10.1175/2006JAS2030.1, 2007.

Luo, Z. and Rossow, W. B.: Characterizing tropical cirrus life cycle, evolution, and interaction with upper-tropospheric water vapor using lagrangian trajectory analysis of satellite observations, *J. Clim.*, 17(23), 4541–4563, doi:10.1175/3222.1, 2004.

Lynn, B. H., Khain, A. P., Bao, J. W., Michelson, S. A., Yuan, T., Kelman, G., Rosenfeld, D., Shpund, J., Benmoshe, N., Lynn, B. H., Khain, A. P., Bao, J. W., Michelson, S. A., Yuan, T., Kelman, G., Rosenfeld, D., Shpund, J. and Benmoshe, N.: The Sensitivity of Hurricane Irene to Aerosols and Ocean Coupling: Simulations with WRF Spectral Bin Microphysics, *J. Atmos.*

Sci., 73(2), 467–486, doi:10.1175/JAS-D-14-0150.1, 2016.

Macdonald, F. A. and Wordsworth, R.: Initiation of Snowball Earth with volcanic sulfur aerosol emissions, *Geophys. Res. Lett.*, 44(4), 1938–1946, doi:10.1002/2016GL072335@10.1002/(ISSN)1944-8007.GRLHIGHLIGHTS2017, 2017.

Mace, G. G., Deng, M., Soden, B. and Zipser, E.: Association of tropical cirrus in the 10–15-km layer with deep convective sources: An observational study combining millimeter radar data and satellite-derived trajectories, *J. Atmos. Sci.*, 63(2), 480–503, doi:10.1175/JAS3627.1, 2006.

Mahowald, N. M., Baker, A. R., Bergametti, G., Brooks, N., Duce, R. A., Jickells, T. D., Kubilay, N., Prospero, J. M. and Tegen, I.: Atmospheric global dust cycle and iron inputs to the ocean, *Global Biogeochem. Cycles*, 19(4), doi:10.1029/2004GB002402, 2005.

Mamouri, R.-E. and Ansmann, A.: Potential of polarization/Raman lidar to separate fine dust, coarse dust, maritime, and anthropogenic aerosol profiles, *Atmos. Meas. Tech*, 10, 3403–3427, doi:10.5194/amt-10-3403-2017, 2017.

Mamouri, R. E. and Ansmann, A.: Fine and coarse dust separation with polarization lidar, *Atmos. Meas. Tech*, 7, 3717–3735, doi:10.5194/amt-7-3717-2014, 2014.

Manktelow, P. T., Carslaw, K. S., Mann, G. W. and Spracklen, D. V.: The impact of dust on sulfate aerosol, CN and CCN during an East Asian dust storm, *Atmos. Chem. Phys. Discuss.*, 9(4), 14771–14823, doi:10.5194/acpd-9-14771-2009, 2009.

Mann, G. W., Carslaw, K. S., Spracklen, D. V., Ridley, D. A., Manktelow, P. T., Chipperfield, M. P., Pickering, S. J. and Johnson, C. E.: Geoscientific Model Development Description and evaluation of GLOMAP-mode: a modal global aerosol microphysics model for the UKCA composition-climate model, *Geosci. Model Dev*, 3, 519–551, doi:10.5194/gmd-3-519-2010, 2010.

Manners, J., Edwards, J. M., Hill, P. and Thelen, J.-C.: SOCRATES technical guide Suite Of Community RAdiative Transfer codes based on Edwards and Slingo, in Tech. Rep., pp. 1–87, Met Office, FitzRoy Rd, Exeter EX1 3PB, United Kingdom., 2017.

Manton, M. J., Sassen, K., Khvorostyanov, V. I., Huang, Y., Blyth, A. M., Brown, P. R. A., Choulaton, T. W., Connolly, P., Gadian, A. M., Jones, H., Latham, J., Cui, Z. and Carslaw, K.: The development of ice in a cumulus cloud over southwest England The physics of clouds in the atmosphere How important is biological ice nucleation in clouds on a global scale? The development of ice in a cumulus cloud over southwest England, *New J. Phys.* *New J. Phys.* *New J. Phys.* *New J. Phys.*, 10(10), doi:10.1088/1367-2630/10/10/105021, 2008.

Marcilli, C.: Deposition nucleation viewed as homogeneous or immersion freezing in pores and cavities, *Atmos. Chem. Phys.*, 14(4), 2071–2104, doi:10.5194/acp-14-2071-2014, 2014.

Marcilli, C., Gedamke, S., Peter, T. and Zobrist, B.: Efficiency of immersion mode ice nucleation on surrogates of mineral dust, *Atmos. Chem. Phys.*, 7, 5081–5091, doi:https://doi.org/10.5194/acp-7-5081-2007, 2007.

Marshall, L., Johnson, J. S., Mann, G. W., Lee, L., Dhomse, S. S., Regayre, L., Yoshioka, M., Carslaw, K. S. and Schmidt, A.: Exploring How Eruption Source Parameters Affect Volcanic Radiative Forcing Using Statistical Emulation, *J. Geophys. Res. Atmos.*, 124(2), 964–985, doi:10.1029/2018JD028675@10.1002/(ISSN)2169-8996.PINATUBO1, 2019.

Marsham, J. H., Knippertz, P., Dixon, N. S., Parker, D. J. and Lister, G. M. S.: The importance of the representation of deep convection for modeled dust-generating winds over West Africa during summer, *Geophys. Res. Lett.*, 38(16), n/a-n/a, doi:10.1029/2011GL048368, 2011.

Marsham, J. H., Hobby, M., Allen, C. J. T., Banks, J. R., Bart, M., Brooks, B. J., Cavazos-Guerra, C., Engelstaedter, S., Gascoyne, M., Lima, A. R., Martins, J. V., McQuaid, J. B., O’Leary, A., Ouchene, B., Ouladichir, A., Parker, D. J., Saci, A., Salah-Ferroudj, M., Todd,

M. C. and Washington, R.: Meteorology and dust in the central Sahara: Observations from Fennec supersite-1 during the June 2011 Intensive Observation Period, *J. Geophys. Res. Atmos.*, 118(10), 4069–4089, doi:10.1002/jgrd.50211, 2013.

Massie, S., Gettelman, A., Randel, W. and Baumgardner, D.: Distribution of tropical cirrus in relation to convection, *J. Geophys. Res. Atmos.*, 107(D21), AAC 19-1-AAC 19-16, doi:10.1029/2001JD001293, 2002.

Maters, E. C., Dingwell, D. B., Cimorelli, C., Müller, D., Whale, T. F. and Murray, B. J.: The importance of crystalline phases in ice nucleation by volcanic ash, *Atmos. Chem. Phys.*, 19(8), 5451–5465, doi:10.5194/acp-19-5451-2019, 2019.

Matthias, V., Bewersdorff, I., Aulinger, A. and Quante, M.: The contribution of ship emissions to air pollution in the North Sea regions, *Environ. Pollut.*, 158(6), 2241–2250, doi:10.1016/j.envpol.2010.02.013, 2010.

Mccarty, W., Coy, L., Gelaro, R., Huang, A., Merkova, D., Smith, E. B., Sienkiewicz, M., Wargan, K. and Koster, R. D.: Technical Report Series on Global Modeling and Data Assimilation, Volume 46 MERRA-2 Input Observations: Summary and Assessment. [online] Available from: <http://www.sti.nasa.gov> (Accessed 2 June 2020), 2016.

McCluskey, C. S., Ovadnevaite, J., Rinaldi, M., Atkinson, J., Belosi, F., Ceburnis, D., Marullo, S., Hill, T. C. J., Lohmann, U., Kanji, Z. A., O’Dowd, C., Kreidenweis, S. M. and DeMott, P. J.: Marine and Terrestrial Organic Ice-Nucleating Particles in Pristine Marine to Continentally Influenced Northeast Atlantic Air Masses, *J. Geophys. Res. Atmos.*, 123(11), 6196–6212, doi:10.1029/2017JD028033, 2018.

McCoy, D. T., Field, P. R., Schmidt, A., Grosvenor, D. P., A-M Bender, F., Shipway, B. J., Hill, A. A., Wilkinson, J. M. and Elsaesser, G. S.: Aerosol midlatitude cyclone indirect effects in observations and high-resolution simulations, *Atmos. Chem. Phys.*, 18, 5821–5846,

doi:10.5194/acp-18-5821-2018, 2018.

Mckay, M. D., Beckman, R. J., Conover, W. J. and Beckman W J Conover, F. J.: A Comparison of Three Methods for Selecting Values of Input Variables in the Analysis of Output From a Computer Code, *Technometrics*, 42(1), 55–61, doi:10.1080/00401706.2000.10485979, 2000.

Medeiros, B., Stevens, B., Held, I. M., Zhao, M., Williamson, D. L., Olson, J. G. and Bretherton, C. S.: Aquaplanets, climate sensitivity, and low clouds, *J. Clim.*, 21(19), 4974–4991, doi:10.1175/2008JCLI1995.1, 2008.

Meyers, M. P., DeMott, P. J., Cotton, W. R., Meyers, M. P., DeMott, P. J. and Cotton, W. R.: New primary ice-nucleation parameterizations in an explicit cloud model, *J. Appl. Meteorol.*, 31(7), 708–721, doi:10.1175/1520-0450(1992)031<0708:NPINPI>2.0.CO;2, 1992.

Mills, M. J., Schmidt, A., Easter, R., Solomon, S., Kinnison, D. E., Ghan, S. J., Neely, R. R., Marsh, D. R., Conley, A., Bardeen, C. G. and Gettelman, A.: Global volcanic aerosol properties derived from emissions, 1990–2014, using CESM1(WACCM), *J. Geophys. Res.*, 121(5), 2332–2348, doi:10.1002/2015JD024290, 2016.

Miltenberger, A. K. and Field, P. R.: Sensitivity of mixed-phase moderately deep convective clouds to parameterisations of ice formation-An ensemble perspective, *Atmos. Chem. Phys. Discuss.*, doi:<https://doi.org/10.5194/acp-2020-253>, 2020.

Miltenberger, A. K., Field, P. R., Hill, A. A., Shipway, B. J. and Wilkinson, J. M.: Aerosol-cloud interactions in mixed-phase convective clouds-Part 2: Meteorological ensemble, *Atmos. Chem. Phys*, 18, 10593–10613, doi:10.5194/acp-18-10593-2018, 2018a.

Miltenberger, A. K., Field, P. R., Hill, A. A., Rosenberg, P., Shipway, B. J., Wilkinson, J. M., Scovell, R. and Blyth, A. M.: Aerosol–cloud interactions in mixed-phase convective clouds – Part 1: Aerosol perturbations, *Atmos. Chem. Phys.*, 18(5), 3119–3145, doi:10.5194/acp-18-3119-2018, 2018b.

Min, Q.-L., Li, R., Lin, B., Joseph, E., Wang, S., Hu, Y., Morris, V. and Chang, F.: Evidence of mineral dust altering cloud microphysics and precipitation, *Atmos. Chem. Phys.*, 9(9), 3223–3231, doi:10.5194/acp-9-3223-2009, 2009.

Min, Q. and Li, R.: Longwave indirect effect of mineral dusts on ice clouds, *Atmos. Chem. Phys.*, 10, 7753–7761, doi:10.5194/acp-10-7753-2010, 2010.

Möhler, O., Field, P. R., Connolly, P., Benz, S., Saathoff, H., Schnaiter, M., Wagner, R., Cotton, R., Krämer, M., Mangold, A. and Heymsfield, A. J.: Efficiency of the deposition mode ice nucleation on mineral dust particles, *Atmos. Chem. Phys.*, 6(10), 3007–3021, doi:10.5194/acp-6-3007-2006, 2006.

Möhler, O., Benz, S., Saathoff, H., Schnaiter, M., Wagner, R., Schneider, J., Walter, S., Ebert, V. and Wagner, S.: The effect of organic coating on the heterogeneous ice nucleation efficiency of mineral dust aerosols, *Environ. Res. Lett.*, 3(2), 025007, doi:10.1088/1748-9326/3/2/025007, 2008.

Mooney, P. A., Mulligan, F. J. and Fealy, R.: Comparison of ERA-40, ERA-Interim and NCEP/NCAR reanalysis data with observed surface air temperatures over Ireland, *Int. J. Climatol.*, 31(4), 545–557, doi:10.1002/joc.2098, 2011.

Mossop, S. C.: Secondary ice particle production during rime growth: The effect of drop size distribution and rimer velocity, *Q. J. R. Meteorol. Soc.*, 111(470), 1113–1124, doi:10.1002/qj.49711147012, 1985.

Mossop, S. C., Brownscombe, J. L. and Collins, G. J.: The production of secondary ice particles during riming, *Q. J. R. Meteorol. Soc.*, 100(425), 427–436, doi:10.1002/qj.49710042514, 1974.

Murray, B. J., Carslaw, K. S. and Field, P. R.: Opinion: Cloud-phase climate feedback and the importance of ice-nucleating particles, *Atmos. Chem. Phys. Discuss.*, doi:10.5194/acp-2020-

852, 2020.

Musil, D. J., Heymsfield, A. J. and Smith, P. L.: Microphysical Characteristics of a Well-Developed Weak Echo Region in a High Plains Supercell Thunderstorm, *J. Appl. Meteorol. Climatol.*, 25(7), 1037–1051, doi:10.1175/1520-0450(1986)025<1037:MCOAWD>2.0.CO;2, 1986.

Neumann, P., Düben, P., Adamidis, P., Bauer, P., Brück, M., Kornblueh, L., Klocke, D., Stevens, B., Wedi, N. and Biercamp, J.: Assessing the scales in numerical weather and climate predictions: will exascale be the rescue?, *Philos. Trans. R. Soc. A Math. Phys. Eng. Sci.*, 377(2142), 20180148, doi:10.1098/rsta.2018.0148, 2019.

Nickovic, S., Vukovic, A., Vujadinovic, M., Djurdjevic, V. and Pejanovic, G.: Atmospheric Chemistry and Physics Technical Note: High-resolution mineralogical database of dust-productive soils for atmospheric dust modeling, *Atmos. Chem. Phys.*, 12, 845–855, doi:10.5194/acp-12-845-2012, 2012.

Niedermeier, D., Hartmann, S., Shaw, R. A., Covert, D., Mentel, T. F., Schneider, J., Poulain, L., Reitz, P., Spindler, C., Clauss, T., Kiselev, A., Hallbauer, E., Wex, H., Mildenerger, K. and Stratmann, F.: Heterogeneous freezing of droplets with immersed mineral dust particles – measurements and parameterization, *Atmos. Chem. Phys.*, 10(8), 3601–3614, doi:10.5194/acp-10-3601-2010, 2010.

Niedermeier, D., Augustin-Bauditz, S., Hartmann, S., Wex, H., Ignatius, K. and Stratmann, F.: Can we define an asymptotic value for the ice active surface site density for heterogeneous ice nucleation?, *J. Geophys. Res. Atmos.*, 120(10), 5036–5046, doi:10.1002/2014JD022814, 2015.

Niemand, M., Möhler, O., Vogel, B., Vogel, H., Hoose, C., Connolly, P., Klein, H., Bingemer, H., DeMott, P., Skrotzki, J., Leisner, T., Niemand, M., Möhler, O., Vogel, B., Vogel, H., Hoose, C., Connolly, P., Klein, H., Bingemer, H., DeMott, P., Skrotzki, J. and Leisner, T.: A

particle-surface-area-based parameterization of immersion freezing on desert dust particles, *J. Atmos. Sci.*, 69(10), 3077–3092, doi:10.1175/JAS-D-11-0249.1, 2012.

O’Sullivan, D., Murray, B. J., Ross, J. F. and Webb, M. E.: The adsorption of fungal ice-nucleating proteins on mineral dusts: a terrestrial reservoir of atmospheric ice-nucleating particles, *Atmos. Chem. Phys.*, 16(12), 7879–7887, doi:10.5194/acp-16-7879-2016, 2016.

O’Sullivan, D., Adams, M. P., Tarn, M. D., Harrison, A. D., Vergara-Temprado, J., Porter, G. C. E., Holden, M. A., Sanchez-Marroquin, A., Carotenuto, F., Whale, T. F., McQuaid, J. B., Walshaw, R., Hedges, D. H. P., Burke, I. T., Cui, Z. and Murray, B. J.: Contributions of biogenic material to the atmospheric ice-nucleating particle population in North Western Europe, *Sci. Rep.*, 8, 13821, doi:10.1038/s41598-018-31981-7, 2018.

O’Sullivan, D., Murray, B. J., Ross, J. F., Whale, T. F., Price, H. C., Atkinson, J. D., Umo, N. S. and Webb, M. E.: The relevance of nanoscale biological fragments for ice nucleation in clouds, *Sci. Rep.*, 5, 8082, doi:https://doi.org/10.1038/srep08082, 2015.

Paukert, M., Hoose, C. and Simmel, M.: Redistribution of ice nuclei between cloud and rain droplets: Parameterization and application to deep convective clouds, *J. Adv. Model. Earth Syst.*, 9(1), 514–535, doi:10.1002/2016MS000841, 2017.

Peckhaus, A., Kiselev, A., Hiron, T., Ebert, M. and Leisner, T.: A comparative study of K-rich and Na/Ca-rich feldspar ice-nucleating particles in a nanoliter droplet freezing assay, *Atmos. Chem. Phys.*, 16(18), 11477–11496, doi:10.5194/acp-16-11477-2016, 2016.

Perlwitz, J. P., Pérez García-Pando, C. and Miller, R. L.: Predicting the mineral composition of dust aerosols-Part 1: Representing key processes, *Atmos. Chem. Phys.*, 15, 11593–11627, doi:doi:10.5194/acp-15-11593-2015, 2015a.

Perlwitz, J. P., Pérez García-Pando, C. and Miller, R. L.: Predicting the mineral composition of dust aerosols - Part 2: Model evaluation and identification of key processes with

observations, *Atmos. Chem. Phys.*, 15(20), 11629–11652, doi:10.5194/acp-15-11629-2015, 2015b.

Petters, M. D. and Kreidenweis, S. M.: A single parameter representation of hygroscopic growth and cloud condensation nucleus activity., *Atmos. Chem. Phys.*, 7(8), 1961–1971, doi:https://doi.org/10.5194/acp-7-1961-2007, 2007.

Petters, M. D. and Wright, T. P.: Revisiting ice nucleation from precipitation samples, *Geophys. Res. Lett.*, 42(20), 8758–8766, doi:10.1002/2015GL065733, 2015.

Phillips, V. T. J., Choularton, T. W., Blyth, A. M. and Latham, J.: The influence of aerosol concentrations on the glaciation and precipitation of a cumulus cloud, *Q. J. R. Meteorol. Soc.*, 128(581), 951–971, doi:10.1256/0035900021643601, 2002.

Phillips, V. T. J., Andronache, C., Sherwood, S. C., Bansemer, A., Conant, W. C., Demott, P. J., Flagan, R. C., Heymsfield, A., Jonsson, H., Poellot, M., Rissman, T. A., Seinfeld, J. H., Vanreken, T., Varutbangkul, V. and Wilson, J. C.: Anvil glaciation in a deep cumulus updraught over Florida simulated with the Explicit Microphysics Model. I: Impact of various nucleation processes, *Q. J. R. Meteorol. Soc.*, 131(609), 2019–2046, doi:10.1256/qj.04.85, 2005.

Phillips, V. T. J., Donner, L. J., Garner, S. T., Phillips, V. T. J., Donner, L. J. and Garner, S. T.: Nucleation processes in deep convection simulated by a cloud-system-resolving model with double-moment bulk microphysics, *J. Atmos. Sci.*, 64(3), 738–761, doi:10.1175/JAS3869.1, 2007.

Phillips, V. T. J., Patade, S., Gutierrez, J. and Bansemer, A.: Secondary Ice Production by Fragmentation of Freezing Drops: Formulation and Theory, *J. Atmos. Sci.*, 75, 3031–3070, doi:10.1175/JAS-D-17-0190.1, 2018.

Pincus, R., Batstone, C. P., Patrick Hofmann, R. J., Taylor, K. E. and Glecker, P. J.: Evaluating

the present-day simulation of clouds, precipitation, and radiation in climate models, *J. Geophys. Res. Atmos.*, 113(14), doi:10.1029/2007JD009334, 2008.

Poku, C., Ross, A. N., Blyth, A. M., Hill, A. A. and Price, J. D.: How important are aerosol–fog interactions for the successful modelling of nocturnal radiation fog?, *Weather*, 74(7), wea.3503, doi:10.1002/wea.3503, 2019.

Posselt, D. J., He, F., Bukowski, J. and Reid, J. S.: On the relative sensitivity of a tropical deep convective storm to changes in environment and cloud microphysical parameters, *J. Atmos. Sci.*, 76(4), 1163–1185, doi:10.1175/JAS-D-18-0181.1, 2019.

Posselt, R. and Lohmann, U.: Influence of Giant CCN on warm rain processes in the ECHAM5 GCM, *Atmos. Chem. Phys.*, 8(14), 3769–3788, doi:10.5194/acp-8-3769-2008, 2008.

Prein, A. F., Langhans, W., Fosser, G., Ferrone, A., Ban, N., Goergen, K., Keller, M., Tölle, M., Gutjahr, O., Feser, F., Brisson, E., Kollet, S., Schmidli, J., Van Lipzig, N. P. M. and Leung, R.: A review on regional convection-permitting climate modeling: Demonstrations, prospects, and challenges, *Rev. Geophys.*, 53(2), 323–361, doi:10.1002/2014RG000475, 2015.

Price, H. C., Baustian, K. J., McQuaid, J. B., Blyth, A., Bower, K. N., Choulaton, T., Cotton, R. J., Cui, Z., Field, P. R., Gallagher, M., Hawker, R., Merrington, A., Miltenberger, A., Neely III, R. R., Parker, S. T., Rosenberg, P. D., Taylor, J. W., Trembath, J., Vergara-Temprado, J., Whale, T. F., Wilson, T. W., Young, G. and Murray, B. J.: Atmospheric ice-nucleating particles in the dusty tropical Atlantic, *J. Geophys. Res. Atmos.*, 123(4), 2175–2193, doi:10.1002/2017JD027560, 2018.

Prospero, J. M.: Saharan Dust Transport Over the North Atlantic Ocean and Mediterranean: An Overview, pp. 133–151, Springer Netherlands., 1996.

Prospero, J. M. and Carlson, T. N.: Vertical and areal distribution of Saharan dust over the western equatorial north Atlantic Ocean, *J. Geophys. Res.*, 77(27), 5255–5265,

doi:10.1029/JC077i027p05255, 1972.

Prospero, J. M. and Lamb, P. J.: African Droughts and Dust Transport to the Caribbean: Climate Change Implications, *Science* (80-. ), 302(5647), 1024–1027, doi:10.1126/science.1089915, 2003.

Provod, M., Marsham, J. H., Parker, D. J., Birch, C. E., Provod, M., Marsham, J. H., Parker, D. J. and Birch, C. E.: A Characterization of Cold Pools in the West African Sahel, *Mon. Weather Rev.*, 144(5), 1923–1934, doi:10.1175/MWR-D-15-0023.1, 2016.

Pruppacher, H. R. and Klett, J. D.: *Microphysics of Clouds and Precipitation*, 2nd ed., Springer Netherlands., 1978.

Pummer, B. G., Bauer, H., Bernardi, J., Bleicher, S. and Grothe, H.: Suspendable macromolecules are responsible for ice nucleation activity of birch and conifer pollen, *Atmos. Chem. Phys*, 12, doi:10.5194/acp-12-2541-2012, 2012.

Ramanathan, V. and Collins, W.: Thermodynamic regulation of ocean warming by cirrus clouds deduced from observations of the 1987 El Niño, *Nature*, 351(6321), 27–32, doi:10.1038/351027a0, 1991.

Randles, C. A., da Silva, A. M., Buchard, V., Colarco, P. R., Darmenov, A., Govindaraju, R., Smirnov, A., Holben, B., Ferrare, R., Hair, J., Shinozuka, Y. and Flynn, C. J.: The MERRA-2 aerosol reanalysis, 1980 onward. Part I: System description and data assimilation evaluation, *J. Clim.*, 30(17), 6823–6850, doi:10.1175/JCLI-D-16-0609.1, 2017.

Renno, N. O., Emanuel, K. A. and Stone, P. H.: Radiative-convective model with an explicit hydrologic cycle - 1. Formulation and sensitivity to model parameters, *J. Geophys. Res.*, 99(D7), 14429–14441, doi:10.1029/94jd00020, 1994.

Ridley, D. A., Heald, C. L. and Ford, B.: North African dust export and deposition: A satellite

- and model perspective, *J. Geophys. Res. Atmos.*, 117(2), doi:10.1029/2011JD016794, 2012.
- Rittmeister, F., Ansmann, A., Engelmann, R., Skupin, A., Baars, H., Kanitz, T. and Kinne, S.: Profiling of Saharan dust from the Caribbean to western Africa-Part 1: Layering structures and optical properties from shipborne polarization/Raman lidar observations, *Atmos. Chem. Phys.*, 17, 12963–12983, doi:10.5194/acp-17-12963-2017, 2017.
- de Rooy, W. C., Bechtold, P., Fröhlich, K., Hohenegger, C., Jonker, H., Mironov, D., Pier Siebesma, A., Teixeira, J. and Yano, J. I.: Entrainment and detrainment in cumulus convection: An overview, *Q. J. R. Meteorol. Soc.*, 139(670), 1–19, doi:10.1002/qj.1959, 2013.
- Rosenfeld, D. and Woodley, W. L.: Deep convective clouds with sustained supercooled liquid water down to - 37.5 °C, *Nature*, 405(6785), 440–442, doi:10.1038/35013030, 2000.
- Rosenfeld, D., Yu, X., Liu, G., Xu, X., Zhu, Y., Yue, Z., Dai, J., Dong, Z., Dong, Y. and Peng, Y.: Glaciation temperatures of convective clouds ingesting desert dust, air pollution and smoke from forest fires, *Geophys. Res. Lett.*, 38(21), n/a-n/a, doi:10.1029/2011GL049423, 2011.
- Saltelli, A., Tarantola, S. and Chan, K. P. S.: A quantitative model-independent method for global sensitivity analysis of model output, *Technometrics*, 41(1), 39–56, doi:10.1080/00401706.1999.10485594, 1999.
- Saltelli, A., Chan, K. and Scott, E. M.: *Sensitivity Analysis*, John Wiley, New York., 2000.
- Sanderson, B. M., Piani, C., Ingram, W. J., Stone, D. A. and Allen, M. R.: Towards constraining climate sensitivity by linear analysis of feedback patterns in thousands of perturbed-physics GCM simulations, *Clim. Dyn.*, 30(2–3), 175–190, doi:10.1007/s00382-007-0280-7, 2008.
- Sassen, K., DeMott, P. J., Prospero, J. M. and Poellot, M. R.: Saharan dust storms and indirect aerosol effects on clouds: CRYSTAL-FACE results, *Geophys. Res. Lett.*, 30(12), doi:10.1029/2003GL017371, 2003.

Saunders, C. P. . and Hosseini, A. .: A laboratory study of the effect of velocity on Hallett–Mossop ice crystal multiplication, *Atmos. Res.*, 59–60, 3–14, doi:10.1016/S0169-8095(01)00106-5, 2001.

Sauter, K., L’Ecuyer, T. S., den Heever, S. C., Twohy, C., Heidinger, A., Wanzong, S. and Wood, N.: The Observed Influence of Tropical Convection on the Saharan Dust Layer, *J. Geophys. Res. Atmos.*, 124(20), 10896–10912, doi:10.1029/2019JD031365, 2019.

Sawyer, G. M., Salerno, G. G., Le Blond, J. S., Martin, R. S., Spampinato, L., Roberts, T. J., Mather, T. A., Witt, M. L. I., Tsanev, V. I. and Oppenheimer, C.: Gas and aerosol emissions from Villarrica volcano, Chile, *J. Volcanol. Geotherm. Res.*, 203(1–2), 62–75, doi:10.1016/j.jvolgeores.2011.04.003, 2011.

Schwendike, J., Jones, S. C., Vogel, B. and Vogel, H.: Mineral dust transport toward Hurricane Helene (2006), *J. Geophys. Res. Atmos.*, 121(10), 5538–5566, doi:10.1002/2015JD024708, 2016a.

Schwendike, J., Jones, S. C., Vogel, B. and Vogel, H.: Mineral dust transport toward Hurricane Helene (2006), *J. Geophys. Res. Atmos.*, 121(10), 5538–5566, doi:10.1002/2015JD024708, 2016b.

Seifert, A. and Beheng, K. D.: A two-moment cloud microphysics parameterization for mixed-phase clouds. Part 2: Maritime vs. continental deep convective storms, *Meteorol. Atmos. Phys.*, 92(1–2), 67–82, doi:10.1007/s00703-005-0113-3, 2006.

Seinfeld, J. H. and Pandis, N. S.: *Atmospheric Chemistry and Physics: From Air Pollution to Climate Change*, 2nd ed., Wiley, New York, USA., 2006.

Shao, Y., Wyrwoll, K. H., Chappell, A., Huang, J., Lin, Z., McTainsh, G. H., Mikami, M., Tanaka, T. Y., Wang, X. and Yoon, S.: Dust cycle: An emerging core theme in Earth system science, *Aeolian Res.*, 2(4), 181–204, doi:10.1016/j.aeolia.2011.02.001, 2011.

Sherwood, S. C., Bony, S. and Dufresne, J. L.: Spread in model climate sensitivity traced to atmospheric convective mixing, *Nature*, 505(7481), 37–42, doi:10.1038/nature12829, 2014.

Shi, Y. and Liu, X.: Dust Radiative Effects on Climate by Glaciating Mixed-Phase Clouds, *Geophys. Res. Lett.*, 46(11), 6128–6137, doi:10.1029/2019GL082504, 2019.

Shi, Z. B., Woodhouse, M. T., Carslaw, K. S., Krom, M. D., Mann, G. W., Baker, A. R., Savov, I., Fones, G. R., Brooks, B., Drake, N., Jickells, T. D. and Benning, L. G.: Atmospheric Chemistry and Physics Minor effect of physical size sorting on iron solubility of transported mineral dust, *Atmos. Chem. Phys.*, 11, 8459–8469, doi:10.5194/acp-11-8459-2011, 2011.

Shipway, B. J. and Abel, S. J.: Analytical estimation of cloud droplet nucleation based on an underlying aerosol population, *Atmos. Res.*, 96(2–3), 344–355, doi:10.1016/j.atmosres.2009.10.005, 2010.

Solomon, A., de Boer, G., Creamean, J. M., McComiskey, A., Shupe, M. D., Maahn, M. and Cox, C.: The relative impact of cloud condensation nuclei and ice nucleating particle concentrations on phase partitioning in Arctic mixed-phase stratocumulus clouds, *Atmos. Chem. Phys.*, 18(23), 17047–17059, doi:10.5194/acp-18-17047-2018, 2018.

Stevens, B. and Bony, S.: What are climate models missing?, *Science* (80-. ), 340(6136), 1053–1054, doi:10.1126/science.1237554, 2013.

Stevens, R. G., Loewe, K., Dearden, C., Dimitrelos, A., Possner, A., Eirund, G. K., Raatikainen, T., Hill, A. A., Shipway, B. J., Wilkinson, J., Romakkaniemi, S., Tonttila, J., Laaksonen, A., Korhonen, H., Connolly, P., Lohmann, U., Hoose, C., Ekman, A. M. L., Carslaw, K. S. and Field, P. R.: A model intercomparison of CCN-limited tenuous clouds in the high Arctic, *Atmos. Chem. Phys.*, 18, 11041–11071, doi:10.5194/acp-18-11041-2018, 2018.

Storelvmo, T., Hoose, C. and Eriksson, P.: Global modeling of mixed-phase clouds: The albedo

and lifetime effects of aerosols, *J. Geophys. Res.*, 116(D5), D05207, doi:10.1029/2010JD014724, 2011.

Streets, D. G., Gupta, S., Waldhoff, S. T., Wang, M. Q., Bond, T. C. and Yiyun, B.: Black carbon emissions in China, *Atmos. Environ.*, 35(25), 4281–4296, doi:10.1016/S1352-2310(01)00179-0, 2001.

Sullivan, R. C., Miñambres, L., DeMott, P. J., Prenni, A. J., Carrico, C. M., Levin, E. J. T. and Kreidenweis, S. M.: Chemical processing does not always impair heterogeneous ice nucleation of mineral dust particles, *Geophys. Res. Lett.*, 37(24), n/a-n/a, doi:10.1029/2010GL045540, 2010a.

Sullivan, R. C., Petters, M. D., DeMott, P. J., Kreidenweis, S. M., Wex, H., Niedermeier, D., Hartmann, S., Clauss, T., Stratmann, F., Reitz, P. and Schneider, J.: Irreversible loss of ice nucleation active sites in mineral dust particles caused by sulphuric acid condensation, *Atmos. Chem. Phys.*, 10(23), 11471–11487, doi:doi:10.5194/acp-10-11471-2010, 2010b.

Sullivan, S. C., Hoose, C. and Nenes, A.: Investigating the contribution of secondary ice production to in-cloud ice crystal numbers, *J. Geophys. Res. Atmos.*, 122(17), 9391–9412, doi:10.1002/2017JD026546, 2017.

Sullivan, S. C., Hoose, C., Kiselev, A., Leisner, T. and Nenes, A.: Initiation of secondary ice production in clouds, *Atmos. Chem. Phys.*, 18, 1593–1610, doi:10.5194/acp-18-1593-2018, 2018.

Sweeney, M. R., McDonald, E. V. and Etyemezian, V.: Quantifying dust emissions from desert landforms, eastern Mojave Desert, USA, *Geomorphology*, 135(1–2), 21–34, doi:10.1016/j.geomorph.2011.07.022, 2011.

Takahashi, T., Nagao, Y., Kushiyama, Y., Takahashi, T., Nagao, Y. and Kushiyama, Y.: Possible High Ice Particle Production during Graupel–Graupel Collisions, *J. Atmos. Sci.*,

52(24), 4523–4527, doi:10.1175/1520-0469(1995)052<4523:PHIPPD>2.0.CO;2, 1995.

Takeishi, A. and Storelvmo, T.: A study of enhanced heterogeneous ice nucleation in simulated deep convective clouds observed during DC3, *J. Geophys. Res. Atmos.*, 123(23), 13,396–13,420, doi:10.1029/2018JD028889, 2018.

Tan, I., Storelvmo, T. and Choi, Y. S.: Spaceborne lidar observations of the ice-nucleating potential of dust, polluted dust, and smoke aerosols in mixed-phase clouds, *J. Geophys. Res.*, 119(11), 6653–6665, doi:10.1002/2013JD021333, 2014.

Tan, I., Storelvmo, T. and Zelinka, M. D.: Observational constraints on mixed-phase clouds imply higher climate sensitivity, *Science* (80-. ), 352(6282), 224–227, doi:10.1126/science.aad5300, 2016.

Tang, M., Cziczo, D. J. and Grassian, V. H.: Interactions of Water with Mineral Dust Aerosol: Water Adsorption, Hygroscopicity, Cloud Condensation, and Ice Nucleation, *Chem. Rev.*, 116(7), 4205–4259, doi:10.1021/acs.chemrev.5b00529, 2016.

Tao, W.-K., Chen, J.-P., Li, Z., Wang, C. and Zhang, C.: Impact of aerosols on convective clouds and precipitation, *Rev. Geophys.*, 50(2), doi:10.1029/2011RG000369, 2012.

Textor, C., Schulz, M., Guibert, S., Kinne, S., Balkanski, Y., Bauer, S., Berntsen, T., Berglen, T., Boucher, O., Chin, M., Dentener, F., Diehl, T., Easter, R., Feichter, H., Fillmore, D., Ghan, S., Ginoux, P., Gong, S., Grini, A., Hendricks, J., Horowitz, L., Huang, P., Isaksen, I., Iversen, T., Kloster, S., Koch, D., Kirkevåg, A., Kristjansson, J. E., Krol, M., Lauer, A., Lamarque, J. F. and Liu, X.: Analysis and quantification of the diversities of aerosol life cycles within AeroCom, *Atmos. Chem. Phys.*, 6, 1777–1813, doi:https://doi.org/10.5194/acp-6-1777-2006, 2006.

Trzeciak, T. M., Garcia-Carreras, L. and Marsham, J. H.: Cross-Saharan transport of water vapor via recycled cold pool outflows from moist convection, *Geophys. Res. Lett.*,

doi:10.1002/2016GL072108, 2017.

Twohy, C. H. and Twohy, C. H.: Measurements of Saharan Dust in Convective Clouds over the Tropical Eastern Atlantic Ocean\*, *J. Atmos. Sci.*, 72(1), 75–81, doi:10.1175/JAS-D-14-0133.1, 2015.

Twomey, S.: The nuclei of natural cloud formation part II: The supersaturation in natural clouds and the variation of cloud droplet concentration, *Geofis. Pura e Appl.*, 43(1), 243–249, doi:10.1007/BF01993560, 1959.

Twomey, S.: Aerosols, clouds and radiation, *Atmos. Environ. Part A. Gen. Top.*, 25(11), 2435–2442, doi:10.1016/0960-1686(91)90159-5, 1991.

Uppala, S. M., Kållberg, P. W., Simmons, A. J., Andrae, U., da Costa Bechtold, V., Fiorino, M., Gibson, J. K., Haseler, J., Hernandez, A., Kelly, G. A., Li, X., Onogi, K., Saarinen, S., Sokka, N., Allan, R. P., Andersson, E., Arpe, K., Balmaseda, M. A., Beljaars, A. C. M., van de Berg, L., Bidlot, J., Bormann, N., Caires, S., Chevallier, F., Dethof, A., Dragosavac, M., Fisher, M., Fuentes, M., Hagemann, S., Hólm, E., Hoskins, B. J., Isaksen, L., Janssen, P. A. E. M., Jenne, R., McNally, A. P., Mahfouf, J. F., Morcrette, J. J., Rayner, N. A., Saunders, R. W., Simon, P., Sterl, A., Trenberth, K. E., Untch, A., Vasiljevic, D., Viterbo, P. and Woollen, J.: The ERA-40 re-analysis, *Q. J. R. Meteorol. Soc.*, 131(612), 2961–3012, doi:10.1256/qj.04.176, 2005.

Vali, G., Demott, P. J., Möhler, O. and Whale, T. F.: Technical Note: A proposal for ice nucleation terminology, *Atmos. Chem. Phys.*, 15, 10263–10270, doi:10.5194/acp-15-10263-2015, 2015.

Vergara-Temprado, J., Murray, B. J., Wilson, T. W., O’sullivan, D., Browse, J., Pringle, K. J., Ardon-Dryer, K., Bertram, A. K., Burrows, S. M., Ceburnis, D., Demott, P. J., Mason, R. H., O’ Dowd, C. D., Rinaldi, M. and Carslaw, K. S.: Contribution of feldspar and marine organic

aerosols to global ice nucleating particle concentrations, *Atmos. Chem. Phys.*, 17, 3637–3658, doi:10.5194/acp-17-3637-2017, 2017.

Vergara-Temprado, J., Miltenberger, A. K., Furtado, K., Grosvenor, D. P., Shipway, B. J., Hill, A. A., Wilkinson, J. M., Field, P. R., Murray, B. J. and Carslaw, K. S.: Strong control of Southern Ocean cloud reflectivity by ice-nucleating particles., *Proc. Natl. Acad. Sci. U. S. A.*, 115(11), 2687–2692, doi:10.1073/pnas.1721627115, 2018.

Vergara Temprado, J.: Global modelling of ice-nucleating particles and impacts on mixed-phase clouds by, University of Leeds., 2017.

Vignati, E., Facchini, M. C., Rinaldi, M., Scannell, C., Ceburnis, D., Sciare, J., Kanakidou, M., Myriokefalitakis, S., Dentener, F. and O'Dowd, C. D.: Global scale emission and distribution of sea-spray aerosol: Sea-salt and organic enrichment, *Atmos. Environ.*, 44(5), 670–677, doi:10.1016/j.atmosenv.2009.11.013, 2010.

Waliser, D. E., Li, J. L. F., Woods, C. P., Austin, R. T., Bacmeister, J., Chern, J., Del Genio, A., Jiang, J. H., Kuang, Z., Meng, H., Minnis, P., Platnick, S., Rossow, W. B., Stephens, G. L., Sun-Mack, S., Tao, W. K., Tompkins, A. M., Vane, D. G., Walker, C. and Wu, D.: Cloud ice: A climate model challenge with signs and expectations of progress, *J. Geophys. Res. Atmos.*, 114(8), D00A21, doi:10.1029/2008JD010015, 2009.

Walters, D., Boutle, I., Brooks, M., Melvin, T., Stratton, R., Vosper, S., Wells, H., Williams, K., Wood, N., Allen, T., Bushell, A., Copsey, D., Earnshaw, P., Edwards, J., Gross, M., Hardiman, S., Harris, C., Heming, J., Klingaman, N., Levine, R., Manners, J., Martin, G., Milton, S., Mittermaier, M., Morcrette, C., Riddick, T., Roberts, M., Sanchez, C., Selwood, P., Stirling, A., Smith, C., Suri, D., Tennant, W., Luigi Vidale, P., Wilkinson, J., Willett, M., Woolnough, S. and Xavier, P.: The Met Office Unified Model Global Atmosphere 6.0/6.1 and JULES Global Land 6.0/6.1 configurations, *Geosci. Model Dev.*, 10(4), 1487–1520,

doi:10.5194/gmd-10-1487-2017, 2017.

Wang, C.: A modeling study of the response of tropical deep convection to the increase of cloud condensation nuclei concentration: 1. Dynamics and microphysics, *J. Geophys. Res.*, 110(D21), D21211, doi:10.1029/2004JD005720, 2005.

Weinzierl, B., Ansmann, A., Prospero, J. M., Althausen, D., Benker, N., Chouza, F., Dollner, M., Farrell, D., Fomba, W. K., Freudenthaler, V., Gasteiger, J., Groß, S., Haarig, M., Heinold, B., Kandler, K., Kristensen, T. B., Mayol-Bracero, O. L., Müller, T., Reitebuch, O., Sauer, D., Schäfler, A., Schepanski, K., Spanu, A., Tegen, I., Toledano, C. and Walser, A.: The Saharan aerosol long-range transport and aerosol-cloud-interaction experiment: Overview and selected highlights, *Bull. Am. Meteorol. Soc.*, 98(7), 1427–1451, doi:10.1175/BAMS-D-15-00142.1, 2017.

Wellmann, C., Barrett, A. I., Johnson, J. S., Kunz, M., Vogel, B., Carslaw, K. S. and Hoose, C.: Using emulators to understand the sensitivity of deep convective clouds and hail to environmental conditions, *J. Adv. Model. Earth Syst.*, 10, 3103–3122, doi:10.1029/2018MS001465, 2018.

Wellmann, C., I Barrett, A., S Johnson, J., Kunz, M., Vogel, B., S Carslaw, K. and Hoose, C.: Comparing the impact of environmental conditions and microphysics on the forecast uncertainty of deep convective clouds and hail, *Atmos. Chem. Phys.*, 20(4), 2201–2219, doi:10.5194/acp-20-2201-2020, 2020.

Welti, A. ;, Lüönd, F. ;, Stetzer, O. ;, Lohmann, U., Welti, A., Stetzer, O. and Lohmann, U.: Influence of particle size on the ice nucleating ability of mineral dusts Influence of particle size on the ice nucleating ability of mineral dusts, *Chem. Phys. Discuss*, 9, 6929–6955, doi:10.3929/ethz-b-000157041, 2009.

Welti, A., Müller, K., Fleming, Z. L. and Stratmann, F.: Concentration and variability of ice

nuclei in the subtropical maritime boundary layer, *Atmos. Chem. Phys.*, 18, 5307–5320, doi:10.5194/acp-18-5307-2018, 2018.

Westbrook, C. D. and Illingworth, A. J.: The formation of ice in a long-lived supercooled layer cloud, *Q. J. R. Meteorol. Soc.*, 139(677), 2209–2221, doi:10.1002/qj.2096, 2013.

Wilson, T. W., Ladino, L. A., Alpert, P. A., Breckels, M. N., Brooks, I. M., Browse, J., Burrows, S. M., Carslaw, K. S., Huffman, J. A., Judd, C., Kilhau, W. P., Mason, R. H., McFiggans, G., Miller, L. A., Nájera, J. J., Polishchuk, E., Rae, S., Schiller, C. L., Si, M., Temprado, J. V., Whale, T. F., Wong, J. P. S., Wurl, O., Yakobi-Hancock, J. D., Abbatt, J. P. D., Aller, J. Y., Bertram, A. K., Knopf, D. A. and Murray, B. J.: A marine biogenic source of atmospheric ice-nucleating particles, *Nature*, 525(7568), 234–238, doi:10.1038/nature14986, 2015.

Wittmann, M., Groot Zwaaftink, C. D., Steffensen Schmidt, L., Guðmundsson, S., Pálsson, F., Arnalds, O., Björnsson, H., Thorsteinsson, T. and Stohl, A.: Impact of dust deposition on the albedo of Vatnajökull ice cap, Iceland, *Cryosph.*, 11(2), 741–754, doi:10.5194/tc-11-741-2017, 2017.

Wu, C., Lin, Z. and Liu, X.: The global dust cycle and uncertainty in CMIP5 (Coupled Model Intercomparison Project phase 5) models, *Atmos. Chem. Phys.*, 20(17), 10401–10425, doi:10.5194/acp-20-10401-2020, 2020.

Xu, K.-M., Randall, D. A., Xu, K.-M. and Randall, D. A.: Updraft and Downdraft Statistics of Simulated Tropical and Midlatitude Cumulus Convection, *J. Atmos. Sci.*, 58, 1630–1649, doi:10.1175/1520-0469(2001)058<1630:UADSOS>2.0.CO;2, 2001.

Yano, J. I. I., Ziemian´ski, Mi. Z., Cullen, Mi., Termonia, Pi., Onvlee, J., Bengtsson, L., Carrassi, A., Davy, R., Deluca, A., Gray, S. L., Homar, V., Köhler, M. I., Krichak, S., Michaelides, S., Phillips, V. T. J., Soares, P. M. M. and Wyszogrodzki, A. A.: Scientific

challenges of convective-scale numerical weather prediction, *Bull. Am. Meteorol. Soc.*, 99(4), 699–710, doi:10.1175/BAMS-D-17-0125.1, 2018.

Yin, Y., Wurzler, S., Levin, Z. and Reisin, T. G.: Interactions of mineral dust particles and clouds: Effects on precipitation and cloud optical properties, *J. Geophys. Res. Atmos.*, 107(23), AAC 19-1, doi:10.1029/2001JD001544, 2002.

Yoon, J.-H. and Zeng, N.: An Atlantic influence on Amazon rainfall, *Clim. Dyn.*, 34(2–3), 249–264, doi:10.1007/s00382-009-0551-6, 2010.

Zelinka, M. D., Randall, D. A., Webb, M. J. and Klein, S. A.: Clearing clouds of uncertainty, *Nat. Clim. Chang.*, 7(10), 674–678, doi:10.1038/nclimate3402, 2017.

Zhang, H., McFarquhar, G. M., Saleeby, S. M. and Cotton, W. R.: Impacts of Saharan dust as CCN on the evolution of an idealized tropical cyclone, *Geophys. Res. Lett.*, 34(14), L14812, doi:10.1029/2007GL029876, 2007.

Zuidema, P., Alvarez, C., Kramer, S. J., Custals, L., Izaguirre, M., Sealy, P., Prospero, J. M. and Blades, E.: Is Summer African Dust Arriving Earlier to Barbados? The Updated Long-Term In Situ Dust Mass Concentration Time Series from Ragged Point, Barbados, and Miami, Florida, *Bull. Am. Meteorol. Soc.*, 100(10), 1981–1986, doi:10.1175/BAMS-D-18-0083.1, 2019.